Effets radiatifs et d'électrodynamique quantique dans l'interaction laser-matière ultra-relativiste

Mathieu Lobet

Thèse

Présentée en vue de l'obtention du grade de

Docteur de l'université de Bordeaux

Ecole doctorale Science Physique et de l'Ingénieur
Spécialité : Laser, matière et nanosciences

Réalisée au sein du

Commissariat à l'Energie Atomique et aux Energies Alternatives

En cotutelle avec le laboratoire

CELIA

Par **Mathieu LOBET**

Effets radiatifs et d'électrodynamique quantique dans l'interaction laser-matière ultra-relativiste

---

Sous la direction universitaire de Emmanuel d'HUMIÈRES
Et sous la responsabilité CEA de Laurent GREMILLET

Soutenue le 18 décembre 2015 devant le jury composé de :

Dr. TIKHONCHUCK Vladimir	CELIA, Bordeaux	Président
Dr. SILVA Luis O.	IST, Lisbon	Rapporteur
Dr. AMIRANOFF François	LULI, Palaiseau	Rapporteur
Dr. RIDGERS Christopher	University of York	Examinateur
Dr. GREMILLET Laurent	CEA, DAM, DIF, Bruyères-le-Châtel	Directeur de thèse CEA
Dr. d'HUMIÈRES Emmanuel	CELIA, Bordeaux	Directeur de thèse

Ce manuscrit de thèse est à la mémoire de mon grand père, Jacques Duruisseau, que j'ai toujours admiré et qui m'a accompagné par le passé et dans le souvenir jusqu'au bout de cette aventure.

Je dédie également ce mémoire à mes Parents, Morgane, Mikael et le reste de ma famille.

Résumé

Cette thèse a pour objet l'étude de l'interaction laser-matière dans un régime d'éclairement extrême que visent à atteindre plusieurs installations multi-pétawatt en cours de développement (CILEX-Apollon, ELI, IZEST, etc.). Pour un éclairement supérieur à $10^{22}\,\mathrm{Wcm}^{-2}$, la dynamique relativiste des électrons accélérés dans l'onde laser est modifiée par un important rayonnement Compton inverse non-linéaire. Au-delà de $10^{23}\,\mathrm{Wcm}^{-2}$, les photons γ ainsi produits peuvent, en interagissant à leur tour avec le champ laser, se désintégrer en paires électron-positron via le mécanisme de Breit-Wheeler non-linéaire. Ces mécanismes d'électrodynamique quantique, dont l'étude expérimentale était jusqu'ici l'apanage des grands accélérateurs de particles, peuvent grandement affecter les mécanismes "usuels" d'interaction laser-plasma, notamment ceux régissant l'accélération de particules chargées et, par conséquent, le bilan global de l'interaction. Afin de modéliser ce régime inédit d'interaction, qui combine processus collectifs, relativistes et d'électrodynamique quantique, nous avons enrichi des mécanismes précédents le code de simulation *particle-in-cell* CALDER développé de longue date au CEA/DIF. L'influence de ces mécanismes est d'abord explorée dans le cas d'une impulsion laser interagissant avec une cible dense de taille micrométrique. Un rendement de conversion de l'énergie laser en photons γ supérieur à 10% est observé au-dessus de $10^{23}\,\mathrm{Wcm}^{-2}$, tandis que la production d'anti-matière s'emballe, via un mécanisme de cascade, à partir de $10^{24}\,\mathrm{Wcm}^{-2}$. Dans un second temps, nous étudions la génération de positrons lors de la collision frontale entre un faisceau d'électrons ultra-relativistes issu d'un accélérateur plasma et une impulsion laser ultra-intense. Dans une dernière partie, nous considérons un scénario prospectif d'intérêt astrophysique, à savoir la collision de plasmas de paires issus de cibles solides irradiées à $10^{24}\,\mathrm{Wcm}^{-2}$ montrant la croissance rapide d'une instabilité de filamentation magnétique combinée à d'intenses effets radiatifs.

Mots-clés : interaction laser-matière, plasma, électrodynamique quantique, positron, particle-in-cell, Compton inverse non linéaire, Breit-Wheeler non linéaire, Apollon, radiation friction, Monte-Carlo, Bremsstrahlung, Bethe-Heitler, Trident

Abstract

This PhD thesis is concerned with the regime of extreme-intensity laser-matter interaction that should be accessed on upcoming multi-petawatt facilities (e.g. CILEX-Apollon, ELI, IZEST). At intensities $I_L > 10^{22}\,\mathrm{Wcm}^{-2}$, the relativistic dynamics of the laser-driven electrons becomes significantly modified by high-energy radiation emission through nonlinear inverse Compton scattering. For $I_L > 10^{23}\,\mathrm{Wcm}^{-2}$, the emitted γ-ray photons can, in turn, interact with the laser field and decay into electron-positron pairs via the nonlinear Breit-Wheeler process. These quantum electrodynamic processes, which until recently could only be explored on large-scale particle accelerators, can greatly alter the "standard" mechanisms of laser-plasma interaction, and therefore its overall energy budget. In order to model their intricate interplay with the laser-induced plasma processes, they have been implemented within the particle-in-cell code CALDER developed at CEA. In a first part, we study these QED processes in the interaction of an ultra-intense laser with a micrometric overdense target. It is found that the laser-to-γ-ray energy conversion efficiency can by far exceed 10% for intensities $I_L > 10^{23}\,\mathrm{Wcm}^{-2}$, while copious pair production (through pair cascading) kicks in for $I_L > 10^{24}\,\mathrm{Wcm}^{-2}$. In a second part, we consider positron generation in the collision between a GeV electron bunch issued from a laser-wakefield accelerator and a counterpropagating laser pulse. In a third part, we analyze a prospective scheme of astrophysical interest, consisting in the collision between two dense pair plasmas produced from solid targets irradiated at $10^{24}\,\mathrm{Wcm}^{-2}$ showing a fast-growing magnetic filamentation instability amplified by intense synchrotron emission.

keywords: laser-matter interaction, plasma, quantum electrodynamics, positron, particle-In-cell, nonlinear inverse Compton, nonlinear Breit-Wheeler, Apollon, radiation friction, Monte-Carlo, Bremsstrahlung, Bethe-Heitler, Trident

---

CEA, DAM, DIF, F-91297, Arpajon, France

CELIA, UMR 5107, Université de Bordeaux-CNRS-CEA, 33405, Talence, France

---

Présentation française de la thèse

Contexte de la thèse

L'avènement des lasers ultra-intenses, rendu possible dans les années 80 grâce, notamment, aux travaux de G. Mourou, a permis d'atteindre des champs électriques du même ordre que les champs coulombiens au sein des atomes, et donc des régimes inédits d'interaction rayonnement-matière, féconds en applications pluridisciplinaires. Les futures installations laser multi-PW Apollon, Vulcan et ELI s'inscrivent dans ce cadre, qui délivreront des impulsions ultra-brèves (quelques dizaines de femtosecondes), de forte énergie (quelques centaines de joules) et d'intensités supérieures à $10^{22}\,\mathrm{Wcm}^{-2}$. Elles donneront lieu à une physique nouvelle (en laboratoire à tout le moins), combinant effets plasmas (collectifs) et d'électrodynamique quantique (QED). Les électrons accélérés sous l'effet de l'impulsion laser atteindront en effet des énergies très importantes (supérieures à la centaine de MeV) qu'ils réémettront sous forme de rayonnement haute-fréquence (rayons X ou γ) par diffusion Compton inverse non-linéaire, en interagissant avec le champ laser, ou par Bremsstrahlung, en interagissant avec les champs atomiques. Les photons énergétiques ainsi produits pourront, à leur tour, se convertir en paires électron-positron, sous l'effet du champ laser (processus de Breit-Wheeler non-linéaire) ou des champs coulombiens atomiques (processus de Bethe-Heitler). Des paires électron-positron pourront également être créées directement (sans photons intermédiaires) par des électrons accélérés dans les champs laser ou atomique (processus Trident électromagnétique ou coulombien). Les futures installations laser constitueront la base technologique d'installations plus ambitieuses : une montée en puissance d'ELI jusqu'à 100 PW est ainsi envisagée en combinant plusieurs faisceaux de 10 PW. Afin de dimensionner et aiguiller les futures expériences, des études théoriques et numériques doivent être réalisées en amont. Il s'agit de comprendre l'influence des processus QED sur la physique connue de l'interaction laser-matière et, ce faisant, de concevoir de nouvelles configurations expérimentales exploitant ces effets. Une fois les installations opérationnelles, le savoir-faire acquis au cours de ces études aidera à l'interprétation des mesures.

Étude théorique des effets QED et implémentation numérique

Avant leurs observations en laboratoire, les effets QED peuvent d'ores et déjà être modélisés numériquement, en particulier au moyen de codes de simulation cinétiques. Parmi ceux-ci, les codes dits *particle-in-cell* (PIC) ont prouvé leur robustesse et leur efficacité, se révélant aujourd'hui les outils les mieux adaptés à l'interaction laser-matière à ultra haute-intensité (présenté au début du chapitre 6). Nous avons consacré la première partie de la thèse à l'implémentation des effets QED dans le code PIC Calder développé au CEA. Nous nous sommes restreints à la diffusion Compton inverse non-linéaire (étudiée théoriquement dans le chapitre 2) et au processus Breit-Wheeler non-linéaire (chapitre 4). Pour des intensités supérieures à $10^{22}\,\mathrm{Wcm}^{-2}$, ces mécanismes sont dominants dans des gaz ou des cibles solides suffisamment fines et de numéro atomique peu élevé. Le rayonnement des électrons se modélise diversement en fonction du régime d'émission considéré. Dans le régime d'émission dit classique (à intensité laser et/ou énergie électronique modérées), les électrons rayonnent de manière continue (les photons sont émis en grand nombre, chacun emportant une très faible fraction de l'énergie électronique). Dans ce cas, le rayonnement peut être décrit par l'ajout d'un terme de friction dans l'équation du mouvement (modèles de Lorentz-Abraham-Dirac, Landau-Lifshitz ou Sokolov), proportionnel à la puissance instantanée rayonnée (calculée de façon classique ou quantique voir ci-après). Pour des champs électromagnétiques ou des énergies électroniques très élevées (respectivement de l'ordre de $10^{14}\,\mathrm{Vm}^{-1}$ et $100\,\mathrm{MeV}$), le régime d'émission devient quantique. Les photons sont alors émis à des énergies comparables aux énergies électroniques. Les trajectoires électroniques sont ponctuées de brusques ralentissements, dont le caractère stochastique est modélisé par une méthode Monte Carlo. En pratique, la trajectoire de chaque électron est découpée en segments (séparant deux émissions successives) de longueur variable (l'épaisseur optique), tirée au sort à partir de la probabilité totale d'émission (fonctions des champs locaux et de l'énergie électronique). L'énergie du photon émis est elle-même tirée au sort dans la distribution. Les détails et validations numériques de ces implémentations font l'objet du chapitre 6 et ont été pré-publiés dans Lobet *et al.* (2015). Bien qu'étudié théoriquement, les mécanismes de Bremsstrahlung (voir Chap. 3) et de Bethe-Heitler (voir Chap. 5) n'ont pas été intégrés dans le code Calder au cours de cette thèse.

Interaction laser-solide sur cible fine

Comme première application physique, nous nous sommes intéressés aux effets QED dans l'irradiation laser de cibles solides micrométriques. Ces cibles sont couramment utilisées comme sources de particules énergétiques (électrons, ions). Soumises à un champ laser extrême, leur surface est rapidement ionisée pour former un plasma

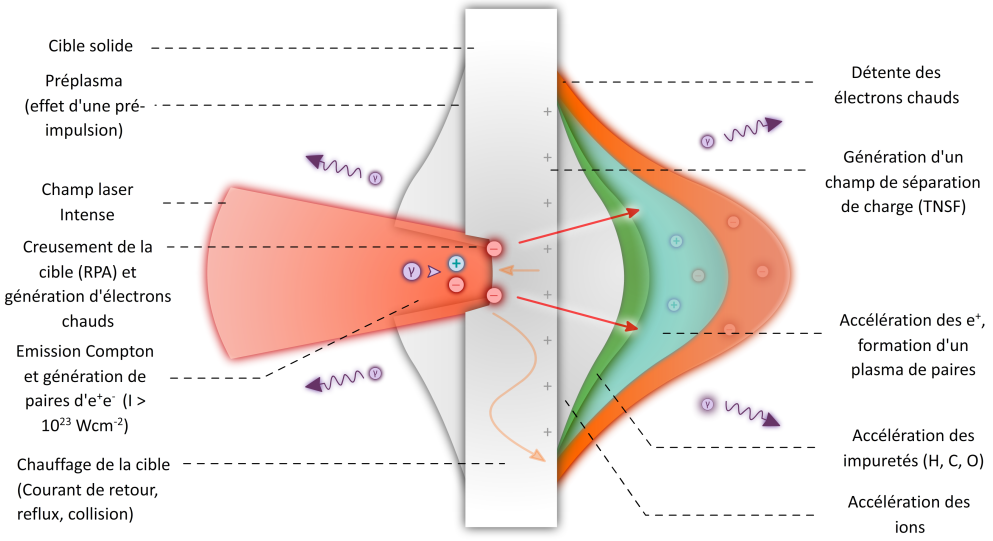

Figure 1: Schéma de l'interaction laser-solide sur cible fine en intensité extrême.

dense et chaud comme illustré sur la figure 1. Fortement accélérés par le champ laser, les électrons y rayonnent une partie de leur énergie d'oscillation par diffusion Compton inverse, émettant des photons d'une dizaine à une centaine de MeV vers l'avant et vers l'arrière. Toujours au sein du champ laser, ces derniers peuvent se désintégrer en paires électron-positron par le processus Breit-Wheeler non-linéaire. L'accélération des ions se produit aux interfaces cibles/vide par l'entremise du champ de séparation de charge induit par les électrons chauds (poussés par la pression radiative en face avant, ou s'échappant de la cible en face arrière). Les simulations montrent que les pertes radiatives réduisent l'accélération ionique en diminuant l'énergie moyenne des électrons chauds. Pour une intensité de $10^{22}\,\mathrm{Wcm}^{-2}$, les pertes radiatives représentent près de 10% de l'énergie laser à $10^{23}\,\mathrm{Wcm}^{-2}$ et près de 50% à $10^{24}\,\mathrm{Wcm}^{-2}$. La génération de paires ne devient significative qu'à partir de $5\times10^{23}\,\mathrm{Wcm}^{-2}$. Se forme alors un plasma de paires très relativiste ($\gamma\sim a_0$ pour les électrons et $\gamma\sim 2a_0$ pour les positrons, où $\gamma=\varepsilon/mc^2$ est l'énergie normalisée et a_0 l'amplitude normalisée du champ laser) et de densité sur-critique (plusieurs dizaines de fois la densité critique à $10^{24}\,\mathrm{Wcm}^{-2}$), se détendant à l'arrière de la cible. Ces résultats sont présentés dans le chapitre 7.

Collision d'un faisceau d'électrons ultra-relativistes avec un laser d'intensité extrême

Nous avons ensuite étudié la collision frontale entre un faisceau d'électrons fortement relativistes et un laser multi-PW. Cette configuration, décritre par la figure 2, semble

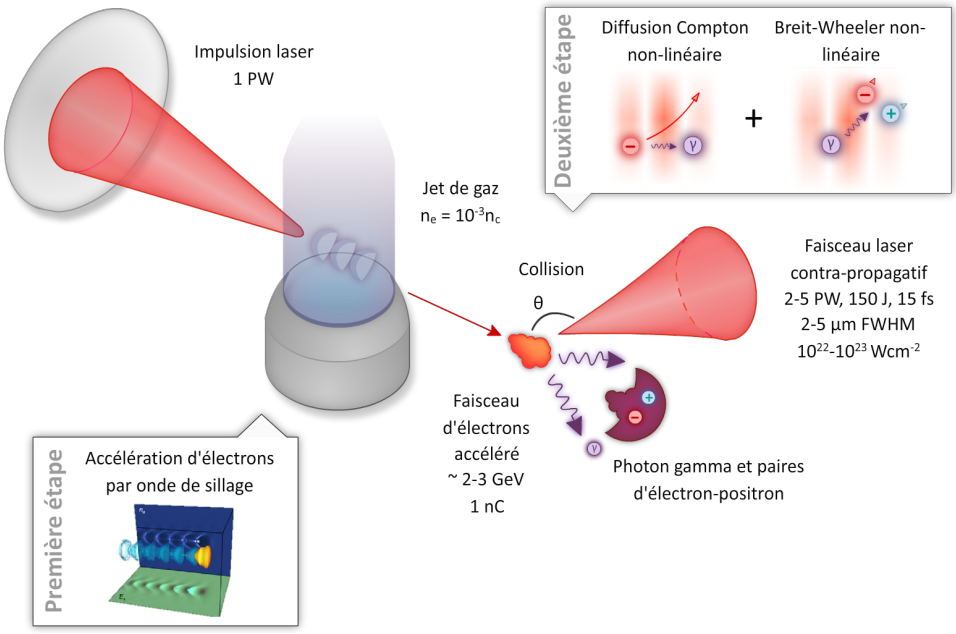

Figure 2: Schéma d'une configuration efficace pour étudier les effets QED avec les futures lasers de puissance.

l'une des plus efficaces et, par conséquent, l'une des prometteuses pour explorer les effets QED avec les futurs lasers de puissance. Le faisceau d'électrons pourrait être produit par accélération dans une onde de sillage induite par un premier laser PW dans un gaz. Le faisceau laser 1 PW (qui complète celui de 5 PW) de l'installation Apollon se prêterait idealement à un tel scenario : moyennant un profil de gaz ajusté, nos simulations montrent la possibilité de créer un faisceau de 3 GeV avec une charge de 2 nC et une divergence moyenne de 3 mrad. Lors de sa collision avec un laser d'intensité $10^{22} - 10^{23}\,\mathrm{Wcm}^{-2}$ et de durée 15 fs, ce faisceau peut rayonner jusqu'à 80% de son énergie cinétique. La distribution des photons γ émis s'étend jusqu'à environ 3 GeV, avec une moyenne autour de 33 MeV. Par la suite, ces photons se convertissent en paires électron-positron avec une probabilité d'autant plus importante que leurs énergies sont élevées. Nous avons mené une étude paramétrique avec des paramètres lasers proches des caractéristiques d'Apollon, à savoir un laser polarisé linéairement de 75 J d'énergie, 15 fs de durée et une tache focale allant de 2 à 5 μm de diamètre (les intensités résultantes vont de $10^{23}\,\mathrm{Wcm}^{-2}$ à $1.6 \times 10^{22}\,\mathrm{Wcm}^{-2}$). Les simulations prédisent que la production de paires grimpe avec l'intensité (d'une dizaine de pC à près de 0.9 nC), faisant de cette configuration l'une des meilleures sources potentielles de positrons. Leur énergie moyenne diminue avec l'intensité mais reste fortement relativiste (entre 100 et 400 MeV). Cette configuration est néanmoins marquée par une forte divergence des électrons et positrons pour deux raisons principales : les déflexions intrinsèques au rayonnement quantique (jouant principalement

dans le plan de polarisation du laser) et les effets pondéromoteurs radiaux (dus à la forte focalisation du laser). Dans le plan de polarisation, la divergence moyenne des positrons augmente avec l'intensité (de 30 à 300 mrad). Dans le plan perpendiculaire, la tendance est similaire : de l'ordre de la divergence du faisceau initial à $1.6 \times 10^{22}\,\mathrm{Wcm^{-2}}$, la divergence atteint 200 mrad à $10^{23}\,\mathrm{Wcm^{-2}}$. Notre étude démontre numériquement la faisabilité du concept, et en fait donc en une expérience de choix pour les futures installations de puissance. Selon les paramètres laser, ces sources de positrons pourraient servir d'injecteurs pour des accélérateurs conventionnels ou optiques, ainsi qu'à l'investigation de phénomènes d'astrophysique de la laboratoire. Ce travail fait l'objet du chapitre 8 de la thèse et se trouve prépublié dans Lobet *et al.* (2015).

Instabilité de Weibel dans la collision de plasmas de paires électron-positron

En physique des plasmas, une instabilité cinétique fortement étudiées est l'instabilité magnétique de Weibel qui se développe au sein de systèmes anisotropes en vitesses ou lors de la collision de jets suffisamment froids. Dans ce dernier cas, elle donne lieu à l'apparition de filaments de courant et de champs, notamment magnétiques dans la direction transverse à la dérive moyenne des plasmas. L'évolution non-linéaire de ces filaments conduit à l'isotropisation et à la thermalisation des jets, donnant lieu à la formation d'un choc capable de se propager dans le milieu amont. Un tel mécanisme pourrait avoir lieu lieu dans les restes de supernovae, où il se serait à l'origine de la production de particules et rayonnements de très hautes énergies dans les Gamma ray bursts. Ce mécanisme est décrit au début du chapitre 9. Les lasers de puissance, capables de générer des plasmas électron-ion de (relativement) grande vitesse, semblent désormais en mesure d'atteindre les conditions requises pour le développement de l'instabilité de Weibel et, in fine, la formation d'un choc (limité toutefois au régime non-relativiste). Des expériences sont actuellement menées en ce sens. En revanche, l'étude en laboratoire des instabilités électron-positron paraît hors de portée des lasers actuels en raison de la difficulté de produire des plasmas suffisamment denses et de grande échelle spatio-temporelle. La production massive de paires telle que prédite sur les futures installations laser ultra-intenses pourrait être une solution. Afin de jauger le potentiel de ces lasers, nous avons imaginé une configuration où deux cibles placées face à face (de cuivre ou aluminium, et de quelques microns d'épaisseur) seraient irradiées par deux impulsions laser d'intensité proche de $10^{24}\,\mathrm{Wcm^{-2}}$, engendrant ainsi deux plasmas de paires s'entrechoquant au centre du domaine, comme illustré par la figure 3. Nous avons simulé l'ensemble du processus, depuis la formation des plasmas jusqu'à leur collision. Celle-ci donne lieu à une instabilité de type Weibel malgré le caractère non-Maxwellien et relativement chaud des plasmas de paires (énergie de dérive de plusieurs centaines de MeV, divergence de

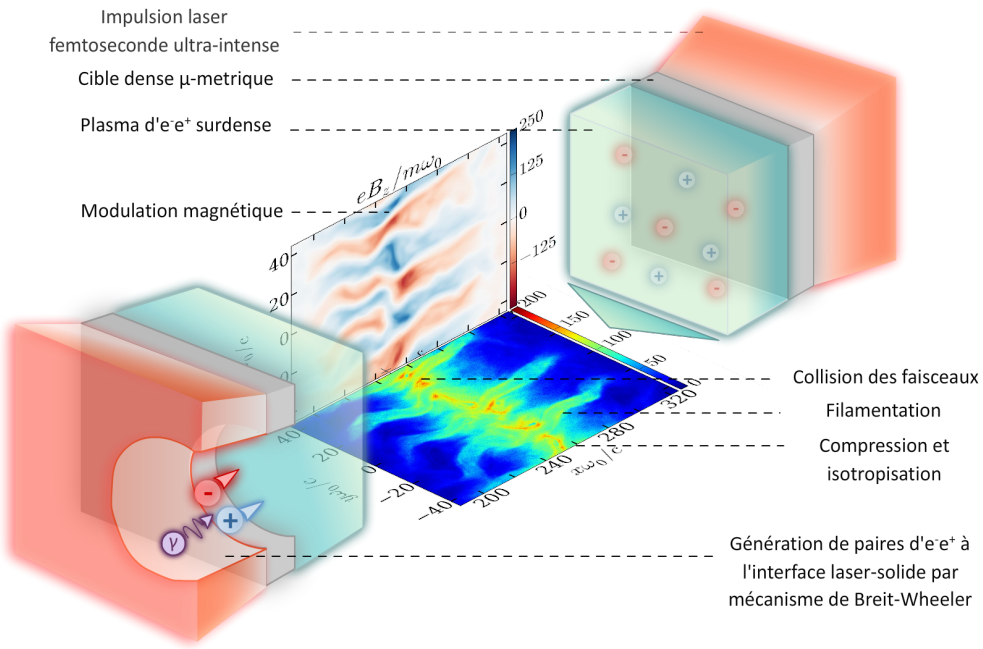

Figure 3: Schéma illustrant la configuration présentée dans cette thése pour l'étude du développement de l'instabilité Weibel dans la collision de plasmas de paires d'électron-positron.

plusieurs dizaines de radians). Cette instabilité se développe extrêmement vite (sur quelques femtosecondes) et engendre des amplitudes magnétiques considérables (de l'ordre de 10^6 T) sur de très petites échelles (quelques microns). Du fait de leur rapide isotropisation, les plasmas s'accumulent dans la région de recouvrement, jusqu'à un taux de compression d'environ 2.7 (une valeur de 3 est attendue pour un choc fort 2D relativiste). Le temps de collision, déterminé par la durée des impulsions laser (~ 100 fs), s'avère toutefois trop bref pour conduire à un choc pleinement formé (et propagatif). Fait marquant, les champs magnétiques induits par l'instabilité sont assez forts pour causer un important rayonnement synchrotron des particules. Près de 65% de l'énergie cinétique incidente est ainsi dissipée, alors que 5% seulement est convertie en énergie magnétique. En comparant ces simulations avec et sans pertes radiatives, il ressort que ces dernières accélèrent la thermalisation et l'isotropisation du milieu.

Afin de comprendre l'effet des pertes radiatives sur la formation d'un choc électron-positron sans contrainte sur la longueur des plasmas, une étude numérique a été réalisée dans une configuration plus académique considérant des plasmas denses et semi-infinis. Le refroidissement radiatif induit un ralentissement de la vitesse de choc ($\sim 0.12c$ à la fin de la simulation radiative, $t = 800$ fs, contre $0.5c$ dans le cas classique) et une augmentation continue du taux de compression (atteignant ~ 9

à $t = 800\,\mathrm{fs}$, au lieu de la valeur classique de 3) dans le milieu aval. Les pertes radiatives sont principalement actives dans la zone du précurseur (où les instabilités se développent) où les filaments magnétiques se désagrègent et se découplent des fluctuations électriques. Dans le milieu choqué (aval), les particules continuent de se refroidir sous l'effet de la turbulence magnétique résiduelle, de sorte que leur densité augmente pour équilibrer les pressions de part et d'autre du choc. De moins en moins énergétiques, ces particules sont aussi de plus en plus confinées dans le milieu comprimé : faute de pourvoir s'en échapper, elles cessent d'entretenir l'instabilité dans le milieu amont, et le choc s'essouffle progressivement. Cette configuration diffère des scénarios astrophysiques de par la force du rayonnement et sa localisation dans la zone de transition du choc (au lieu du milieu aval). Par conséquent, cette étude, première du genre, pointe la difficulté de reproduire en laboratoire des systèmes véritablement analogues aux systèmes astrophysiques. Cette difficulté est renforcée par les paramètres laser requis pour de telles expériences : une forte intensité pour une production efficace de paires, une large tache focale pour limiter les effets de la divergence des particules, une durée suffisamment longue pour permettre une croissance importance de l'instabilité, impliquant des impulsions de plus de 100 kJ, inaccessibles avant longtemps. Ces résultats ont été publiés dans Lobet *et al.* (2015).

Conclusions

Alors que l'installation laser Apollon est censée délivrer ses premiers photons d'ici 1 an, de nombreuses équipes dans le monde ont déjà mis au point de nouveaux outils de simulation, éventuellement combinés à des avancées théoriques. Succédant au travail de thèse (effectué à l'Université de Bordeaux) de Rémi Capdessus sur les effets radiatifs classiques dans l'interaction laser-matière, notre travail est le premier en France portant sur les processus proprement QED induits dans ce contexte. Il a donné lieu à l'amélioration du code PIC Calder développé au CEA, désormais capable de traiter des scénarios d'interaction à des intensités supérieures à 10^{22} Wcm^{-2}. Les méthodes numériques que nous avons mises au point et largement détaillées pourront servir dans d'autres codes PIC développés en France ou à l'étranger. Par ailleurs, les études que nous avons réalisées balayent un large spectre de conditions physiques, et permettront de guider les futures expériences dans ce régime inédit d'interaction laser-matière.

Acknowledgments

J'ai rencontré Emmanuel d'Humières mon directeur de thèse en deuxiéme année d'école d'ingénieur. Chercheur au CELIA, professeur à l'université de Bordeaux et professeur de physique des plasmas à l'ENSEIRB-MATMECA, Emmanuel avait proposé un projet de recherche intégré au cursus scolaire sur l'utilisation de GPUs pour la modélisation numérique des plasmas grâce à un code *particle-in-cell* (PIC).

Toujours intéressé par le domaine à l'issue de ce premier projet, j'ai ensuite décidé d'effectuer mon stage de deuxième sur un sujet similaire. C'est ainsi que j'ai contacté Laurent Gremillet par l'intermédiaire d'une proposition de stage déposée sur le site de l'INSTN sur l'étude de conditions limites absorbantes électromagnétiques pour le code PIC Calder. A la fin de ce travail de 4 mois, Laurent me proposait de continuer l'aventure en thèse une fois mon diplôme d'ingénieur en poche.

Au début de la dernière année d'école d'ingénieur, je suis resté en contact avec Emmanuel afin d'améliorer le code PIC démarré en seconde année. Lors des six derniers mois, j'ai effectué mon projet de fin d'étude au sien du Kansai Photon Science Institute à Nara au Japon sous la supervision de Sergei Bulanov sur l'étude des comportements non linéaires en plasma inhomogène sous-dense appliquée au concept de *flying mirror*. C'est une nouvelle fois le code PIC commencé en école d'ingénieur et parallélisé pour le coup avec MPI qui a été utilisé pour les simulations.

Ce sont donc mes deux encadrants de thèse que je souhaiterais remercier en premier lieu pour m'avoir amené depuis les premières années d'école d'ingénieur jusqu'à la fin de cette thèse. Laurent, j'ai beaucoup apprécié ton encadrement, toujours présent et disponible, pointilleux et perfectionniste mais aussi patient et pédagogue. J'ai apprécié les libertés d'initiative et d'action que tu m'as laissées tout en sachant me guider et me recadrer. Il ne faut pas oublier les à-côtés de la thèse qui font de ces annnées bien plus qu'une collaboration professionnelle, je repense bien sûr aux pistes dévalées à Orcières-Merlette, aux escapades sportives sur l'île de Porquerolles, aux restaurants judicieusement choisis à Paris et Bordeaux. Emmanuel, c'est grâce à toi que tout ça a commencé et tu m'as accompagné jusqu'au doctorat. Une fois de plus, c'est une chance d'avoir un encadrant comme toi toujours disponible même à distance, d'une extrême gentillesse, avec les bonnes idées pour se tirer des situations les plus angoissantes, avec les mots pour se remotiver, également pointilleux et très pédagogue, avec une grande ouverture. J'ai beaucoup apprécié collaborer avec toi sur divers projets du CELIA ainsi que nos nombreuses discussions

sur des sujets variés comme les prochaines technologies de calcul parallèle. A cela s'ajoute également les nombreux moments de détente en conférence, workshop et autres.

J'aimerais ensuite remercier tous les chercheurs qui ont participé de près à ma formation ainsi qu'à l'encadrement de ma thèse. Je pense à Sergei Bulanov, Tatsufumi Nakamura, Alexander Pirozhkov, James Koga, Timur Esirkepov et Masaki Kando du KPSI qui m'ont encadré lors de mon stage de fin d'étude. Je pense également à Mickael Grech au LULI avec qui nous avons énormément collaboré, ainsi qu'à Arnaud Debayle, Xavier Davoine, Roland Ducloud, Rémi Capdessus, Martin Lemoine et Xavier Ribeyre, co-auteurs de plusieurs articles.

J'aimerais remercier le CEA en tant qu'institution pour avoir financé ma thèse et accepté ma candidature. De par les conditions de travail, la force des outils et des moyens apportés (supercalculateur, contenus scientifiques, financements), réaliser sa thèse au CEA est une chance. Cette thèse est le fruit d'une collaboration entre le CEA et le laboratoire CELIA à Bordeaux, de la même façon j'aimerais remercier le CELIA en tant qu'institution pour les moyens techniques mises à disposition ainsi que pour le financement de déplacements et de conférences. Enfin, j'aimerais remercier le LULI qui nous a accueilli de nombreuses fois et mis à dispositions ses différentes salles.

Un grand merci aux chercheurs et collègues du CEA, je pense dans un premier temps à Franck Hamann et Luc Bergé pour leur soutien et leur intérêt dans ce travail. J'aimerais remercier Catherine Cherfils sans qui cette thèse n'aurait pas été cautionnée. Mes remerciements vont aussi à Brigitte Flouret pour la supervision administrative de la thèse et sa gentillesse ainsi qu'à Silvie Dulac, toujours souriante, pour son aide dans toutes les démarches. Je remercie Benoit Canaud, toujours de bonne humeur, pour ses bons conseils et prêt à tout lorsqu'il s'agit de dévaler en snowboard des pentes enneigées (de poudreuse de préférence). Que ce soit avec Charles ou Arnaud, ce sont des souvenirs que je n'oublierai pas, c'est quand tu veux pour la prochaine descente. De nouveau, je remercie Arnaud, super collègue de bureau, pour son aide scientifique, ses cours d'apnée et les nombreuses sorties. Merci à Serges Bouquet pour ses nombreuses blagues, ses conseils en littérature scientifique et sa moussaka géante. Merci à Didier grand défenseur de la pomme. Merci à Stéphanie pour ses précieux conseils sur les Etats-Unis et pour m'avoir fait découvrir sa thématique. Je remercie David pour les matchs de Badminton ainsi qu'Alexandra pour avoir partagé son intérêt pour la musique. Enfin merci aussi à Michel, Stéphane, Philippe, Christophe.

Ces trois années n'auraient pas été les mêmes sans les autres étudiants, stagiaires et thésards, ainsi que les postdocs. Je remercie donc Jérémie pour ses conseils en investissement, Nicolas pour ses avis cinématographiques, Grégoire pour les discussions politiques, Charles mon grand frère pour les sorties en hors-piste, Aurélie et Julien pour les séances de jeux, les discussions littéraires et encore une fois les descentes en ski. Merci aussi à Simon et Pedro pour leur amitié et leurs nombreuses

invitations. Un merci à Guillaume grâce à qui j'ai découvert une nouvelle facette de la culture web et vidéo-ludique (oui j'aurais pu dire culture geek). Merci à Witold avec qui j'ai partagé de nombreuses soirées de conférences. Enfin, merci également à Bastien, Vivian et Maelle.

Je remercie également tous les collègues du CELIA. Dans un premier temps les nombreux chercheurs qui m'ont aidé à avancer dans mes études et ceux avec qui j'ai collaboré, je pense à Vladimir Tikhonchuk, Xavier Ribeyre, Rachelle Nuter, Philipp Korneev, Joao Santos, Bruno Dubroca, Stéphane Brull, Oliver Jansen. Mais aussi ceux avec qui j'ai pu simplement discuter ou partager une pause-café, un restaurant, en particulier Dimitri Batani, Philippe Nicolai ainsi qu'à Emmanuel et Céline pour le soutien administratif. Un super merci aux étudiants ou anciens étudiants du CELIA qui savent accueillir les petits parisiens comme moi, en particulier, Basil, Dario, Mokrane, Mickaël, Aurore, Arnaud, Emma, Sebastien, Gabriel, Ludovic. Un remerciement spécial pour Yohann sans qui l'école d'été d'Erice et les séjours bordelais n'auraient pas été les mêmes.

J'aimerais également remercier les équipes internationales avec lesquelles nous avons collaboré. Tout d'abord, je remercie Scott Wilks dont j'ai beaucoup apprécié les discussions lors d'un séjour de quelques mois passés à nos côtés. Je remercie également le GSI et plus particulièrement Vincent Bagnoud, Paul Nemayer et Dimitri Khaghani pour m'avoir présenté leur projet et m'y avoir intégré. L'étude simulatoire de leurs expériences m'a permis de sortir des intensités extrêmes de mon sujet initial pour explorer la physique de l'interaction laser-matière à 10^{18} Wcm^{-2} avec des cibles structurées. J'espère que cette collaboration se poursuivra avec le CEA sur les expériences à venir.

J'aimerais remercier tous mes amis qui m'ont supporté (dans les deux sens du terme) pendant ces trois années de thèse, et tout particulièrement la famille Lemarquand et mon cher coloc, Charlotte et Romain, Clio et Thomas, Audrey, Hugues et Céline, János et Dóra, Misato, Irene et Lidia. Un remerciement spécial aux anciens d'Eirbot, et nouveaux membres de Rob&léon, Romain, William, Valentin, Francis, Marion, Elodie et Lucile qui ont affronté l'épreuve soporifique de la soutenance. Enfin, merci à Victor, ami de très longue date pour ne pas dire le premier, mec génial, intéressé par tout et plein de ressources qui ne cesse de m'impressionner depuis l'enfance.

Enfin, je souhaiterais remercier l'ensemble de ma famille pour leur soutien depuis le début de mes études, chose importante pour ne jamais perdre la motivation dans les moments de creux. Un gros merci à mon père et ma mère pour m'avoir apporté cette passion pour la science et la technologie ainsi que pour m'avoir aidé et soutenu dans tous mes choix. Merci à Morgane et Mikael, mon frère et ma soeur. Merci à Janine et Eric avec qui on partage toujours de bons moments. Je remercie bien sûr mes grands-parents pour leurs nombreux encouragements. Et je remercie mon petit coeur pour avoir rendu cette fin de thèse agréable.

Nomenclature

General physical constants

Parameters	Definitions
c	The speed of light in vacuum
m_e	The electron rest mass
e	The electron charge
N_A	Avogadro number
α_f	The fine structure constant
r_e	The electron radius
$\hbar$	The reduced Planck constant
n_c	The critical density relative to the laser frequency ω_0
k_B	The Boltzmann constant
E_s	The Schwinger field

Laser parameters

Parameters	Definitions
λ	The laser wavelength

ω	The laser frequency
ω_0	The critical frequency at $\lambda_0 = 1$ μm
T	The laser period
T_l	The laser duration (at half maximum in the case of a Gaussian temporal pulse shape)
I	The laser intensity
d_l	The laser focal spot diameter (at half maximum in the case of Gaussian profile)
R_l	The laser focal spot radius
η_{abs}	Laser absorption coefficient
η_{ref}	Laser reflection coefficient
E	The electric field
B	The magnetic field
E_0	The electric field amplitude
B_0	The magnetic field amplitude
a_0	The normalized laser amplitude

Matter parameters

Parameters	Definitions
m_α	In general, the mass of the particle α
q_α	In general, the charge of the particle α

ρ_α	The density for a given element α
$m_{A,\alpha}$	The atomic mass for a given element α
$\omega_p = \sqrt{e^2 n_\alpha / m_e \omega}$	The plasma frequency
l_{TF}	The Thomas-Fermi radius
l_D	The Debye length
l_r	The reduced length for the reduced screening potential
V_{TF}	Thomas-Fermi (Wentzel-Yuakwa) atomic potential
V_D	Debye screening potential
V_r	Reduced screening potential

Kinetic

Parameters	Definitions
$\mathbf{x}_\alpha$	The position vector of the particle α
v_α	The velocity of the particle α
p_α	The momentum of the particle α
γ_α	The Lorentz factor of the particle α
$\varepsilon_\alpha = \gamma_\alpha m_e c^2$	The energy of the particle α
γ_γ	The photon normalized energy
$\varepsilon_\gamma = \gamma_\gamma m_e c^2$	The photon energy

QED parameters

Parameters	Definitions
χ_α	In general, the quantum parameter of the particle α
χ_γ	The photon quantum parameter

Cross-sections and production rates

Parameters	Definitions	Described in
$d\sigma$	Total cross section	
$\frac{d\sigma}{d\gamma_{e^-}}$, $d\sigma_{\gamma_{e^-}}$	Electron energy differential cross section	
$\frac{d\sigma}{d\gamma_{\gamma}}$, $d\sigma_{\gamma_{\gamma}}$	Photon energy differential cross section	
κ_γ	Probability for a photon of energy ε_γ and quantum parameter χ_γ to decay into a pair during a given period T	
$\frac{dN^2_{Cs}}{dtd\gamma}$	Photon energy distribution rate of photons for the nonlinear inverse Compton scattering	section 2
σ_{Br}	Bremsstrahlung total cross section	section 3.3
σ_{BH}	Bethe-Heitler total cross section for any energy	section 5.1.1
σ^{NR}	Total cross section in a non-relativistic regime (Bremsstrahlung)	section 3.2.1
σ^{RE}	Total cross section in a relativistic regime (Bremsstrahlung and Bethe-Heitler)	section 3.2.2
σ^{UR}	Total cross section in a ultra-relativistic regime (Bremsstrahlung, Bethe-Heitler)	section 3.2.3
σ_{ppBW}	Cross section for the photon-photon Breit-Wheeler process	section 4.2
σ_{nBW}	Cross section for the nonlinear Breit-Wheeler process	section 4.3
$\frac{N_{Tr_e}}{dt}$	Production rate of pairs via the electromagnetic Trident	section 4.4
$\frac{N_{Tr_m}}{dt}$	Production rate of pairs via the Trident in matter	section 5.3
$\frac{N_{Tri}}{dt}$	Production rate of pairs via the Triplet process in matter	section 5.2
$\frac{N_{An}}{dt}$	Annihilation rate of pairs to two photons	section 4.5

Contents

Chapter 1

Introduction

1.1 High-intensity lasers for science

1.1.1 Plasma physics

The science of laser-matter interaction is closely related to plasma physics. Plasma is a state of matter globally neutral but locally constituted of charged particles (ions and free electrons) as well as neutral particles (Rax (2005)). Plasmas appear as the most common form of matter in the universe. However, on Earth, this state is inversely rare in the nature, which explains why it has been discovered and understood so late, after gases, liquid and solids. The closest form of plasma is located in the high layers of the atmosphere. This layer has the capacity to reflect long-wavelength radiowaves contrary to the low wavelengths which are lost in space. For this reason, international radios usually use low frequencies, the broadcast being reflected can propagate on very long distances. Then, a relatively close form of plasmas (just seven minutes far from us for who can travel at the speed of light, almost nothing compared to the size of the universe) essential to our existence and survival is the sun. Our sun, and stars in general during the first billions year of their lives, can be seen as huge balloons of hydrogen plasma. Under the conditions of pressure and temperature existing at the heart of these giant bodies, protons undergo exothermic fusion reaction leading to the production of helium, light and high-energy particles. The fusion reaction also concerns the newly generated elements giving rise to the production of a wide range of atoms, all the elements we can find naturally on our planet, such as carbon and oxygen which compose the base of living organisms, as well as metals and radioactive materials. The sun is a source of light covering a broad spectrum. Infrared, visible and ultraviolet emission contribute to make our planet so welcoming to life. The stars themselves form in large plasma clouds of hydrogen called nebula.

1.1.2 What is laser-plasma interaction?

Laser science constitutes a wide branch of physics rich of thousands of research thematics and applications. Lasers are closely related to plasma physics since they constitute a unique way to create laboratory plasmas in a wide range of states, pressure and temperatures. This branch is usually called laser-matter interaction and aims at studying the behavior of matter under extreme conditions. This research area has gained so much importance and attraction today that the most powerful, most energetic and largest laser-facilities are purely and solely dedicated to this purpose. Furthermore, it is worth noting that this field (also referred to as laser-plasma interaction) has constituted a driving force toward the development of new laser technologies, and as we will see, continues to motivate and bring solutions for the next.

1.1.3 A brief history

Lasers for Light Amplification by Stimulated Emission of Radiations are optical devices that produce spatially and temporally coherent electromagnetic radiations via the process of stimulated emission in special medium (referred to as gain medium) that allow them to get amplified (Paschotta (2008)). Lasers are characterized by a given frequency ω (i.e. a given wavelength λ) which corresponds to the energy of a single photon $\hbar\omega$ and a pulse duration T_l. Laser beams are focused and are therefore also characterized by a maximal intensity I that corresponds to the photon energy crossing a given surface per time unit (usually expressed in Wcm^{-2}) and a focal spot transverse profile with a given diameter d_l at the focused point.

The first operational laser appeared in 1960 created by Theodore H. Maiman (Maiman (1960)) following advanced previous works of Charles Hard Townes, Arthur Leonard Schawlow (Schawlow and Townes (1958)) and Gordon Gould. The laser history and technological evolutions are summarized in Fig. 1.1 taken from Mourou *et al.* (2006). During the early 60's, laser has gained a lot of attraction and the focused intensity achieved a significant growth via different improvements such as the Q-switching and the Mode-locking that enabled to respectively decrease the pulse duration to the nanosecond first and then to the picosecond and few femtoseconds. Between 1965 to 1985, the progresses toward higher intensities have undergone a period of stagnation with a maximal value close to 10^{14} Wcm^{-2} (for a power of few gigawatt). This limitation was due to the intensity threshold reached by the laser before damaging the gain medium via nonlinear optical effects such as self-focusing. During this period, the laser electric field was already comparable to interatomic electric field ($\sim 10^8$ V/m) enabling the study of nonlinear optics including photon and multi-photon ionization, optical parametric amplification, Raman and Brillouin scattering.

The technological solution came in 1985 at the University of Rochester with the works of Donna Strickland, Gérard Mourou and P. Maine (Strickland and Mourou

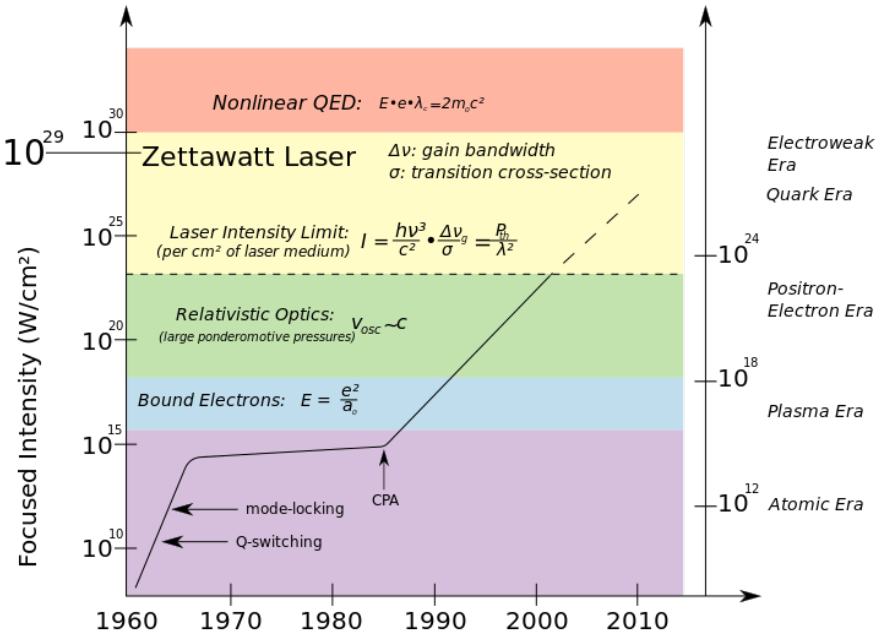

Figure 1.1: Historical evolution of the laser intensity since the creation in 1960 (from Mourou *et al.* (2006) and many others reviews on the subject).

(1985); Maine *et al.* (1988); Maine and Mourou (1988)) under the name CPA technique for Chirped Pulse Amplification. The CPA technique consists in stretching the initial pulse both temporally and spectrally by the use of a first grating to proceed the amplification and then to recompress back the pulse using a second grating. The technique has directly permitted to increase the final intensity while limiting the signal intensity through the amplification gain medium and prevent damages. This invention has paved the way to 30 years of continuous increasing in intensity and is now widely used in the main laser facilities. This has also enabled to produce affordable and easy-to-use table-top laser systems of relatively high intensities of interest for small institutions and universities.

The OPCPA for Optical Parametric Chirped Pulse Amplification technique is a variant that was developed in parallel (Piskarskas *et al.* (1986)). It consists in amplifying a seed pulse with a pump using parametric light amplification in nonlinear optical crystals. Compared with CPA, the parametric gain within a single pass through a nonlinear crystal is significantly increased reducing the number of amplification stages and complex multipass geometries.

With the possibility to exceed 10^{15} Wcm^{-2}, both techniques have opened the physical area of the laser-plasma interaction. At such an intensity, the laser field is sufficiently strong to partially ionize solid targets or fully ionize low-Z gases and create local plasmas. At a laser intensity of 10^{18} Wcm^{-2}, one enters the relativistic regime. An electron interacting in such an electromagnetic field oscillates at

relativistic velocities within one laser period. At 10^{22} Wcm^{-2}, the electromagnetic acceleration will be so strong that the electrons will start to radiate their energy. At 10^{23} Wcm^{-2}, one enters the quantum electrodynamics regime where quantum effects such as strong emission of γ-photons and generation of electron-positron pairs are expected to largely influence the laser-driven acceleration of charged particles and, as a result, the overall energy balance of the laser-target interaction. The intensity of 5×10^{29} Wcm^{-2} corresponds to the Schwinger limit. When the electric field strength ($E_s = 10^{18}$ V/m) approaches this critical limit the electron-positron pair creation from vacuum becomes possible (Sauter (1931); Schwinger (1951); Bulanov *et al.* (2011)).

1.1.4 A wide range of technologies for a wide range of applications

Laser technologies

High-power lasers from few terawatt to the petawatt (PW) level are based on CPA or OPCPA amplification technologies. For CPA, lasers are usually based on Titanium Sapphire gain medium (sapphire crystals doped with Titanium ions Rp-photonics (2015)) delivering pulse wavelength around 800 nm. The amplifying stage can also be performed with neodymium-doped gain medium (Nd:glass, Rp-photonics (2015)) or ytterbium-doped gain medium (Yb:glass, Rp-photonics (2015)) with Ti:Sa pump lasers. For OPCPA, a pre-amplifier of borate crystal can be used followed by a main amplifier of deuterated potassium dihydrophosphate crystal (DKDP). A Ti:Sa laser can be used as a seed pulse.

The current laser thresholds in term of energy and power are respectively of few megajoules and 1 petawatt. The current photography of the operational world lasers as a function of their power and energy above the terawatt level is shown in Fig. 1.2. This graph is based on the pieces of information given on the laser facility websites and interesting reviews given in Korzhimanov *et al.* (2011) and Di Piazza *et al.* (2012).

Lasers are usually divided into two main categories: high-power and high-energy lasers. High-energy lasers such as the National Ignition facility (NIF) in California, the Laser MegaJoule (LMJ) near Bordeaux, Gekko XII and Orion are huge facilities primarily dedicated to fusion energy. These facilities are composed of several lasers divided into sets with multiple beams like quads for NIF and LMJ. For the LMJ or the NIF, each beam is characterized by long pulses of several nanoseconds (20 ns for the NIF), for a power of few TW so that the final focused intensity is between 10^{14} and 10^{15} Wcm^{-2} (CEA-DAM (2015); NIF (2015)).

High-power lasers are in contrary less energetic but have a shorter duration. Again, we can distinguish two kinds of high-power lasers: the short-pulse of the order of ten femtoseconds and long-pulse lasers between 500 femtoseconds to few

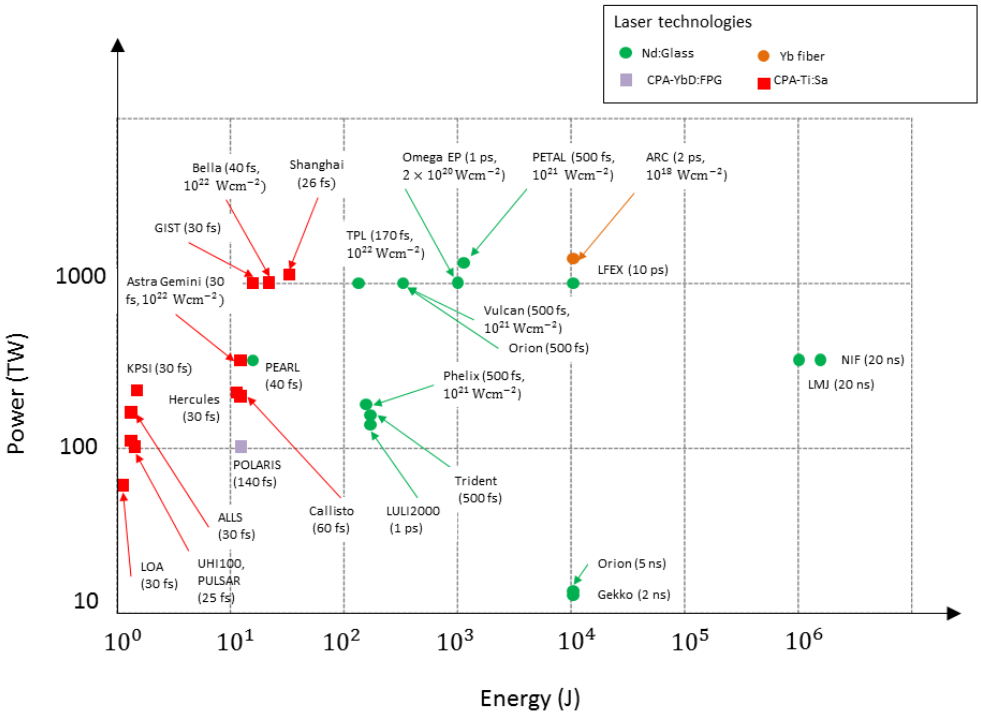

Figure 1.2: Laser facilities of power above 100 terawatts (TW) in the world as a function of their power and energy.

picoseconds.

Short pulse lasers have duration of few tens of femtoseconds and constitute the shortest ones with a composition of few cycles per pulses. The most powerful ones, around 1 petawatts, have an energy of few tens of joules such as the BELLA laser in Berkeley at 1 petawatt (BELLA (2015); Leemans *et al.* (2010)) and the 2 petawatt laser of the Shanghai Institute of Optics and fine Mechanics (Chu *et al.* (2013)). The short-pulse lasers constitute the most intense ones. The HERCULES laser of the Ann Arbor University holds the record of focused intensity at 2×10^{22} Wcm^{-2} (Yanovsky *et al.* (2008)) in a tiny focal spot diameter of 1.3 μm although this intensity has never been used in experimental conditions.

Long-pulse high-power lasers are in between the two previous classes. They usually deliver a final energy on target of hundred of joules to few kilojoules and as shown in Fig. 1.2 mainly use Nd:glass amplifying technologies. Their durations of 500 femtoseconds to few picoseconds enable to reach intensities on target close to 10^{21} Wcm^{-2}

Laser-matter interaction can be performed with undercritical (or underdense) targets such as gas jets. In this case, the laser frequency is higher than the plasma frequency $\omega > \omega_p$ and the laser can propagate in the medium. The interaction with

solid targets, foams and clusters is said to be overcritical. The plasma frequency which increases with the plasma electron density becomes higher than the laser frequency and the plasma becomes reflective. At extreme intensity, this vision is too simplistic because of relativistic effects.

Particle acceleration in laser-matter interaction

Short pulse lasers can be used to accelerate electrons at extreme energies above the GeV level. Laser-based accelerators use the accelerating potential of the Langmuir wave created in the wake of a short pulse propagating in a gas jet (Esarey *et al.* (2009)). This is the so-called Laser-Wakefield Acceleration regime (LWFA). They have the advantage to provide a significant charge of high-energy electrons in a small acceleration distance of few millimeters to few centimeters (in capillary discharge waveguide Leemans *et al.* (2014)). So far, the final energy was limited by the size of the accelerating medium and the power of the laser pulses. In the all-optical multistage acceleration, several laser beams will be combined to reach even higher energies of expected values of few tens of GeV. A first laser, as in the case of a single stage, will be used to create a high-energy electron beam. This electron beam is hence transported and injected inside a second plasma wakefield, that constitutes the second acceleration stage of the process, created in a dielectric capillary tube with a second laser (Kim *et al.* (2013); Wang *et al.* (2013)). In principle, the acceleration stages could be multiplied. Compact LWFA-based accelerators (Malka *et al.* (2008)) are therefore expected to compete with huge and expensive linear radio-frequency conventional accelerators which require several hundred of meters to reach the same final energy (acceleration of few tens of MeV/m, such as the superconducting RF systems at the Desy laboratory in Germany, compared to several hundred of GeV/m for PW lasers). Some challenges nonetheless remain. LWFA electron beams suffer from a higher divergence and a broader energy spectrum in comparison with RF accelerators. The beam properties can also vary shot to shot in addition to the transportation and synchronization issues still under exploration. Laser-based accelerators could be used to design compact free-electron laser facilities. The resulting electron beam could be sent inside undulators as for conventional facilities (as the European XFEL, the SLAC in Stanford) to form a synchrotron source of X-rays (McNeil and Thompson (2010)). Long-pulse high-power lasers are in contrary not adapted to such a scheme because of their durations exceed the plasma wavelength.

High-power lasers in general (including both short and longer pulses) constitute promising sources of fast ions (Macchi *et al.* (2013)). As for the electrons, fast ions are currently produced in large linear or circular accelerators. In this domain, lasers can not pretend to reach the same level of efficiency. The most powerful facility is the Large Hadron Collider (LHC) at the CERN. This complex structure of multiple circular rings where the largest is of 27 km of circumference is able to accelerate protons to 6.5 TeV and lead 208 isotopes to 2.8 TeV (CERN (2009)). The second largest

facility is the FERMILAB accelerator in the United States with a maximal proton energy of 980 GeV (Lebedev and Shiltsev (2014)). In comparison, the maximal proton energy ever reached with a laser is of 120 MeV in the so-called Breakout Afterburner configuration. Fast ions were first generated at modest intensity of 10^{18} Wcm^{-2} via the Target Normal Sheath Acceleration (TNSA) in solid thin-foils. When the laser strikes the target front side, it generates fast electrons that form expanding flows both at the front and the rear. A charge differential appears with the immobile ions and a charge separation field, accelerating for positively charged particles, settles. The strength of the sheath field depends on the laser properties and the target length scale. To simplify, the field is as strong as the laser intensity is intense but it also depends on the laser contrast and the duration. Thin foils (between few μm to few tens of μm) are better because of the hot electron dilution (d'Humières *et al.* (2005)). Target surfaces contain impurities made of organic molecules for instance, therefore with hydrogen, carbon or oxygen. The protons that constitute the highest charge-to-mass ratio ions are the first to be snatched and accelerated as more efficiently as they are located near the maximum of the field. Rear proton and ion acceleration was evidenced experimentally in many papers (Snavely *et al.* (2000), Hatchett *et al.* (2000), Allen *et al.* (2004) and Romagnani *et al.* (2005)). Heavier ions, and target ions, can also be accelerated at longer time. The TNSA only benefits the target ions if the surface is cleaned from impurities, this can be performed by pre-heating the target surface (Hegelich *et al.* (2002)). TNSA acceleration constitutes an efficient source for proton-imaging already used in many laser experiments to probe electric and magnetic fields in plasmas (Borghesi *et al.* (2002)). TNSA was itself observed and studied with TNSA-accelerated protons. Detecting how the protons are scattered and deposit their energy is another used information. This has partly motivated the building of PW lasers on Inertial Confinement Fusion facilities such as PETAL on the LMJ and ARC on the NIF.

The Radiation Pressure Acceleration (RPA) is another regime of ion acceleration more efficient than the TNSA at ultra-high intensity. The laser radiation pressure is so high that it pushes inward the overdense front surface of the target. In the case of a tiny focal spot, the laser digs a hole in the target (Schlegel *et al.* (2009); Robinson *et al.* (2009); Naumova *et al.* (2009); Robinson (2011)). This is commonly named Hole Boring (HB) process. The TNSA and the RPA are further discussed in Chapter 7.

The Light Sail regime (LS) uses an extremely thin foil of thickness below the laser wavelength to maximize the effect of the laser radiation pressure acceleration. Using a circularly wave, the electrons are accelerated as a whole by the ponderomotive force, therefore inducing a uniform charge separation accelerating field with the ions. If the ions reach relativistic energies in less than a laser period they can follow the electron sheet and undergo a constant acceleration (Esirkepov *et al.* (2004); Macchi *et al.* (2005); Bulanov *et al.* (2010)).

The Breakout Afterburner (BOA) is a regime of acceleration happening in the

relativistic transparency regime. As the target becomes transparent, the laser penetrates and heats volumetrically the electrons leading to an enhanced ion acceleration field (Yin *et al.* (2006)). This mechanism claims to have a record of accelerated protons at around 120 MeV (Hegelich (2011)).

Applications

As a source of coherent X-rays, lasers have potential applications in molecular imaging for biology and material science (Rousse *et al.* (2001); Chapman *et al.* (2006)). Molecular imaging requires bright sources sufficiently short to not deteriorate the compounds during the exposure. Using trains of electron bunches, several X-ray flashes can be produced of interest to film ultrafast processes such as the formation of molecules. The time scale of a molecular reaction is between the nanosecond and the picosecond, and the flash duration of few femtoseconds for the fastest facilities such as the SLAC. In a larger extent, as a source of high-frequency radiations in different range of frequencies from radiowaves to γ-rays, lasers have imaging applications in medicine, material engineering and public security.

Laser-based ion accelerators have first potential application as a source for first injector stage of larger conventional accelerators. In this case, high-repetition rates are required with final energies of few tens of MeV. A promising and motivating application for laser ion acceleration is medical application and in particular hadrontherapy in oncology (Ma and Lomax (2012); Nunes (2015); Amaldi and Kraft (2005)). Hadrontherapy is a medical use of ions to treat tumors. Cancers are conventionally irradiated by multiple beams of X-rays focused from many angles on the ill tissues in order to deposit the maximum of energy in this part of the body and the less as possible in the surrounding healthy cells. Hadrontherapy offers a more accurate way to treat tumors with weaker non-desirable effects. Ions penetrating the tissues, they transfer energy all along their propagation with a deposition peak just before stopping. This property is called the Bragg peak. The first patients were treated experimentally in particle accelerators originally dedicated to particle science such as the Gesellschaft f'ur Schwerionenforschung Institute (GSI) in Darmstadt. Clinical ion accelerator facilities, only dedicated to cure cancers, have been built in the last few years such as in Heidelberg in Germany. Despite a better efficiency than X-rays, these techniques remain very expensive. This is where the lasers can eventually be competitive but there remains a long way to go. Hadrontherapy is performed with hydrogen ions, and preferably with carbon ions with respective required energy above 250 and 400 MeV. A high-repetition rate, stability and repetitiveness of the process is of great importance.

As already mentioned, proton imaging can be used to probe thin objects (West and Sherwood (1972)) and is already used in laser-plasma experiments to probe magnetic and electric fields allowing for spatial and temporal evolution studies. Protons and ions, with localized energy depositions, are also interesting for medical imaging

allowing for a better accuracy than X-rays.

With high-power lasers, high-energy density environment with conditions of pressure and temperature similar to many astrophysical objects can be reproduced in the laboratory. This branch is usually refered to as High Energy Density Physics (HEDP) and laboratory astrophysics. In a large extent, laboratory astrophysics is the reproduction of powerful astrophysical events at the laboratory-scale (Ryutov and Remington (2007); Bouquet *et al.* (2010)). The understanding of supernovae requires complex hydrodynamics and radiative modeling and laser experiments contribute to improve the models (opacity calculation for instance). Lasers can be used to study the formation of shocks such as accretion shocks (Falize *et al.* (2011)) and collisionless shocks that may happen in active galaxy nuclei, supernovae remnants and pulsar wind nebulae. Collision of laser-driven plasma flows will enable to study various kind of instabilities such as the Weibel filamentation (Quinn *et al.* (2012)). The Weibel/filamentation instability (further studied in Chapter 9) could be responsible for collisionless shock formation, generation of nonthermal particles and high-frequency radiations. It is a potential candidate to explain the Gamma ray bursts and afterglows, i.e. the observation of short-duration intense flash of radiations coming from localized points in the sky (Fishman and Meegan (1995); Piran (2005); Waxman (2006)).

1.2 The forthcoming high-power laser facilities and related challenges

Le petawatt level will be soon overtaken by the forthcoming generation of multi-petawatt lasers. Among the different projects, Apollon built in Saclay will be soon operational at the first level of 2 petawatts to progressively increase in power to reach the final level of 10 petawatts. This laser aims at reaching the maximal intensity of 10^{23} Wcm^{-2} by focusing an energy of 150 Joules in few micrometer-scale focal spot and a duration of 15 femtoseconds with a repetition rate of one shot per minute (Apollon (2015)). The multi-PW beam line will be coupled with an other 1-PW laser. Vulcan-10 PW is a similar project under construction in United Kingdom at the Rutherford Appleton Laboratory (RAL). It will have an energy of 300 Joules for a duration of 30 femtoseconds and will also be combined with a 1-PW laser (Vulcan (2015)). The Extreme Light Infrastructure (ELI) project is a large-scale facility conducted by the European Union and under-development on three different sites in Eastern Europe (ELI (2015)). In Romania near Bucharest, a first facility will be dedicated to nuclear physics, another will be built in Szeged in Hungary for attosecond physics and finally a third one will be erected in Prague in Czech Republic for high-energy particles and high-frequency radiations. All these facilities will be equipped with several beam lines including two 10-PW lasers of 200 Joules compressed in a duration of 20 femtoseconds. This version of ELI constitutes the

first step of a second project of upgrade to the level of 100-PW. Such a power will be reached by the combination of several 10-PW lasers with the aim to reach a focused intensity of 10^{24} Wcm^{-2}. We can also mention the project PEtawatt pARametric Laser (PEARL-10) as an upgrade of the current laser to 10-PW in Nizhny Novgorod in Russia. At the same location, the XCELS infrastructure is a 200-PW project based on the combination of several beams of hundred of joules (Bashinov *et al.* (2014); XCELS (2015)).

Long-term projects with the goal to reach the exawatt already exist. In the IZEST project, a megajoule-laser like the NIF and the LMJ would be compressed to reach extreme intensities of 10^{25} Wcm^{-2} (Mourou *et al.* (2012); Mourou and Tajima (2014); IZEST (2013)).

As already mentioned in section 1.1.3 and Fig. 1.1, some physical processes irrelevant so far in laser-plasma interaction will arise due to the strong field including radiative and quantum electrodynamics effects. These effects are presented in the next sections.

1.2.1 High-frequency radiation emission in laser-matter interaction

They are many different sources of radiations in laser-matter interaction, with a wide range of properties (frequency from the U.V. to the γ-rays, short pulses to single-cycle waves, chirp...) governed by various physical effects and depending on the target and the laser properties.

Source of radiations in laser-matter interaction

Emission of radiations is inherent to the laser-matter interaction from the ionization intensity threshold close to 10^{14}-10^{15} Wcm^{-2} (Batani *et al.* (2012)). At such an intensity, the laser potential is of the order of the atomic one and therefore perturbs the electron dynamics around the atoms, for instance by tunnelling and recombination after having oscillated in the laser field. Such a mechanism can be responsible for radiation emissions of harmonics of the laser frequency (Winterfeldt *et al.* (2008); Teubner and Gibbon (2009)), attosecond pulses (Krausz and Ivanov (2009)), extreme-ultraviolet and soft X-rays. In the relativistic regime, from 10^{18} Wcm^{-2}, gases are completely ionized and it is almost the case for dense low-Z materials such as carbon. The free electrons can be accelerated to relativistic energies within a laser period. Whereas X-ray emission from the ionization is still observable, other emission processes appear. Atomic high-order harmonic generation suppressed at such an intensity is changed for harmonics generation from the reflection of the laser on the steep and dense oscillating surface of a foil (Debayle *et al.* (2013)). In a gas jet, a laser wake wave is created with betatron emission of the oscillating injected electrons inside the cavity (Rousse *et al.* (2004); Kiselev *et al.* (2004); Corde *et al.* (2013)). In

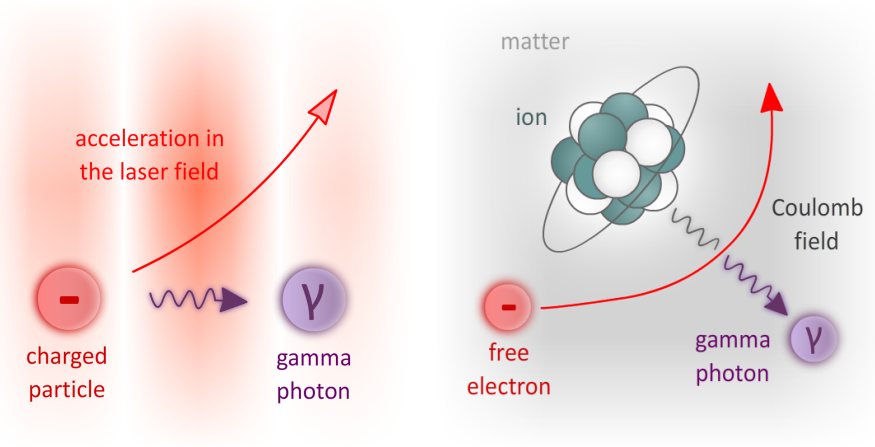

Figure 1.3: Scheme of the nonlinear Compton Scattering (a) and the Bremsstrahlung (b) emission processes.

dense target, the fast electrons lose energy inside the matter when they closely interact with the Coulomb field of the atoms via the so-called Bremsstrahlung process described in Fig. 1.3b. It preferably occurs in high-Z targets. With present laser technologies, Bremsstrahlung emission is one of the brightest source of X and γ-rays (Kmetec *et al.* (1992); Galy *et al.* (2007); Henderson *et al.* (2014); Schumaker *et al.* (2014)). With a laser close to 10^{21} Wcm^{-2} focused on a gold target, the conversion into γ-rays is estimated to be few % of the laser with photons generated up to few tens of MeV and an angular divergence of 30 degrees in Henderson *et al.* (2014).

Sources of high-frequency radiations in extreme intensity

In extreme intensity, the radiation losses will be induced by nonlinear inverse Compton scattering effect of the electron deflected in the laser field as described in Fig. 1.3a. The Compton scattering is the collision between an electron and a photon that results in a transfer of energy from the second to the first one. The inverse Compton scattering is therefore the transfer of energy from an electron to the photon. The nonlinear inverse Compton scattering can be seen as the collision with the multiple low-energy photons of the laser ($e^- + n\omega \rightarrow e^- + \gamma$). An efficient configuration to observe this mechanism in the laboratory consists in colliding a high-energy electron beam with a counter-propagating high-intensity laser as experimentally done in Sarri *et al.* (2014). A counter-traveling configuration maximizes the process whereas electrons co-propagating with the laser pulse would not radiate. Another but close configuration consists in using a laser to generate the fast electrons via laser wakefield acceleration and a mirror to make the electron beam interacting with the reflected pulse (Phuoc *et al.* (2012); Chen *et al.* (2013); Tsai *et al.* (2015)). At intensity between 10^{21} Wcm^{-2} and 10^{22} Wcm^{-2}, for GeV electrons, the emission

will take place in the classical regime. This means that the particles will continuously radiate many photons of relatively low energy in comparison with their kinetic energy. Above 10^{22} Wcm^{-2}, the emission will become quantum meaning that the emitted photons will bring away a significant fraction of the electron kinetic energy. Therefore, the electrons will undergo strong recoil. Other signatures of the quantum emission is a broadening of the spectrum accompanying the cooling of the beam energy (Sokolov *et al.* (2010); Neitz and Di Piazza (2013)) and a significant straggled scattering (Green and Harvey (2014)) due to the stochastic nature of the process. Future high-power lasers will therefore constitute significant sources of hard X-rays and γ-rays of interest for the imaging applications cited in section 1.1.4 (Mackenroth and Di Piazza (2011); Bulanov *et al.* (2013); Vranic *et al.* (2014); Blackburn *et al.* (2014); Blackburn (2015); Harvey *et al.* (2015)). They will enable to study the radiation cooling effects from the classical to the quantum regime in order to validate the different theories.

In laser thin-foil interaction, the high-frequency radiation emission of strongly accelerated electrons will take place at the laser solid interface in the superimposition of the incident wave and the reflected one. The radiation losses will reduce the average energy of the electrons and therefore modify the ponderomotive scalings of the literature valid until 10^{21} Wcm^{-2}. Numerical simulations have already shown that the cooldown of the electrons affect the target normal sheath acceleration and the laser radiation pressure acceleration. The maximal ion and proton energies are reduced in comparison with non-radiative theoretical prediction and simulations (Zhidkov *et al.* (2002); Nakamura *et al.* (2012); Capdessus *et al.* (2013); Brady *et al.* (2014); Ji *et al.* (2014),Ji *et al.* (2014); Capdessus and McKenna (2015)).

The radiation losses will also affect the electron dynamics in underdense (Brady *et al.* (2012)) and near-critical plasmas (Liu *et al.* (2013); Ji *et al.* (2014); Zhu *et al.* (2015); d'Humières *et al.* (2015)).

1.2.2 Generation of electron-positron pairs in laser-matter interaction

The positron, the anti-particle of the electron of same mass m_e and opposite charge, was first predicted in Dirac (928a) and Dirac (928b) and then discovered experimentally by Anderson (1932, 1933). Anti-matter can be generated in many ways. Positrons can be naturaly produced in nuclear decays. Anti-matter can also be produced in the collision of particles as performed in large colliders. Positrons are also the product of the cosmic rays (extreme-energy particles emitted from powerful events in the universe) when they interact with the earth atmosphere.

The first described process of electron pair production is the so-called photon-photon Breit-Wheeler process in which an electron-positron pair arises from the decay of two colliding photons ($\gamma + \gamma \rightarrow e^- + e^+$) (Dirac (1930); Breit and Wheeler (1934)) as drawn in Fig. 1.4. On Earth this mechanism is still one of the most difficult to be

confirmed experimentally. But in the universe, the photon-photon Breit-Wheeler is of considerable importance for the absorption of high-energy photons traveling cosmic distances (Nikishov (1964); Gould and Schréder (1967)). Recently, new schemes have been proposed in order to observe these mechanisms at the laboratory scale. The first idea has been studied by Pike *et al.* (2014) and Thomas (2014) and consists of colliding γ-photons produced via Bremsstrahlung in a high-temperature radiation bath produced inside a laser-heated hohlraum. If in principle this could be achieved with present laser technologies, some difficulties arise from different technical and physical aspects. The first one is the detection and the distinguishing of the created electron-positron pairs produced in very few numbers in a very noisy environment where pairs will be also produced by the Bethe-Heitler mechanism inside the high-Z target for the γ-photon production and probably inside the hohlraum. Another

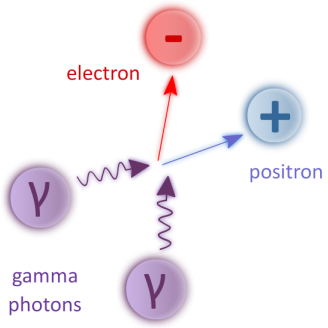

Figure 1.4: Scheme of the photon-photon Breit-Wheeler process.

configuration has been recently proposed based on the significant emission of γ-photon foreseen with the next generation of extreme-intensity lasers. It consists in the collision of two counter-streaming flows of γ-photons created from irradiated thin-foils with two focused multi-petawatt lasers (Ribeyre *et al.* (2015)).

In laser-matter interaction, the production of pairs with present laser technologies is the most efficient in the collision of high-energy electrons and γ-photons with high-Z atoms. The different mechanisms are described in the following section 1.2.2. The quantum electrodynamics processes in strong field will be introduced in section 1.2.2.

Generation of electron-positron pairs in the matter

In the vicinity of the field of a nucleus, a γ-photon of energy above twice the rest mass of an electron and a positron ($2m_ec^2 \sim 1.022$ MeV) in the laboratory frame can decay into pair by interaction with the Coulomb field ($\gamma + Z \rightarrow e^- + e^+ + Z$) as schematically presented in Fig. 1.5a (Bethe and Heitler (1934)). The Bethe-Heitler photon decay into an electron-positron pair occurs with high-probability in high-Z targets. In relativistic laser matter-interaction, the generation of anti-matter is

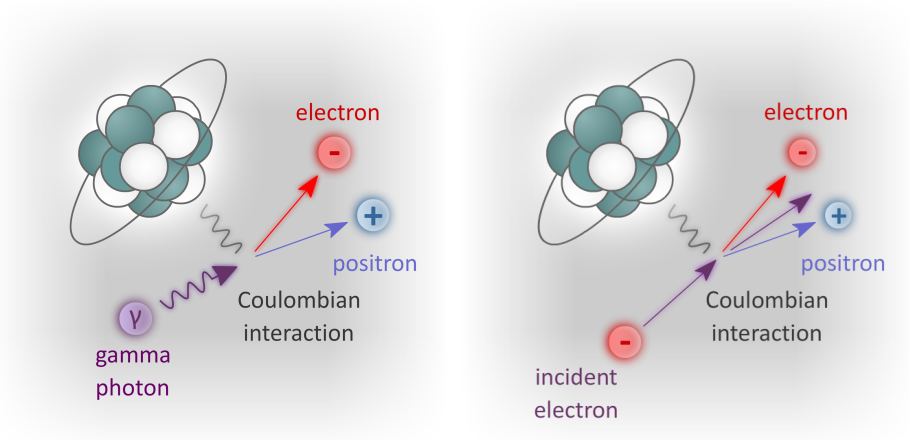

Figure 1.5: Scheme of the Bethe-Heitler process (a) and the Coulomb Trident (b).

the consequence of two successive mechanisms: the production of γ-photon via the Bremsstrahlung and their conversion via the Bethe-Heitler process. These mechanisms have a great potential in the creation of laser-based sources of positron beams and pair plasmas. A significant pair production can be achieved by direct interaction of an ultra-intense laser with a thin foil. The hot electrons created at the laser-solid interface dilute in the matter, produce Bremsstrahlung γ-photons that decay into pairs. Experiments on recent facilities (ORION,TITAN,OMEGA EP) have been performed by Chen *et al.* (2009, 2011, 2015). The high-energy electrons can also be generated with a laser (in a laser wakefield accelerator for instance) prior to their collision with a high-Z converter. This configuration has proved its efficiency by generating a highly-collimated almost-neutral relativistic pair beam (Sarri *et al.* (2013),Sarri *et al.* (2013),Sarri *et al.* (2015)).

The Coulomb Trident is the direct creation of an electron-positron pair from the collision of a high-energy electron with a nucleus ($e^- + Z \rightarrow 2e^- + e^+ + Z$) and can be seen as the combination of the Bremsstralhung and the Bethe-Heitler processes into a single one as presented in Fig. 1.5b. The Bethe-Heitler itself dominates the Trident but requires a source of γ-photons. With the Bremsstrahlung, the Bremstrahlung+Bethe-Heitler dominates the Trident in thick high-Z targets (of several millimeters, of gold for instance) but can be comparable in thinner foils (several tens of micrometers according to Myatt *et al.* (2009)).

The Triplet is the production of pairs resulting from the collision of a γ-photon with an electron. This can happen with the bound electrons in the atoms ($\gamma + e^- \rightarrow e^- + e^+ + e^-$). The Triplet pair production approaches the Bethe-Heitler pair yield in low-Z targets and reveals almost equivalent for high-energy photons in hydrogen.

Electron-positron pair production at extreme intensity

In the vacuum, the electromagnetic field becomes nonlinear from the Schwinger electric field $E_s = 1.3 \times 10^{18}$ V/m corresponding to an intensity of 10^{29} Wcm^{-2} for $\lambda = 1$ μm. In such a field, spontaneous apparitions of electron-positron pairs from the nonlinear vacuum are possible. If this field is not reachable in the laboratory frame, it will be very close in the boosted frame of highly-accelerated electrons. At 10^{24} Wcm$^{-}2$, a Lorentz factor of $\gamma \sim 10^5$ is required to reach the Schwinger limit. This is the reason why quantum electrodynamics effects and in particular strong-field pair generation will be accessible with the forthcoming extreme-intensity lasers (Heinzl and Ilderton (2009); Di Piazza *et al.* (2012)).

The nonlinear Breit-Wheeler process is the decay of a γ-photon in interaction with a strong field ($\gamma + n\omega \rightarrow e^+ + e^-$) as drawn in Fig. 1.6a. A source of γ-photon

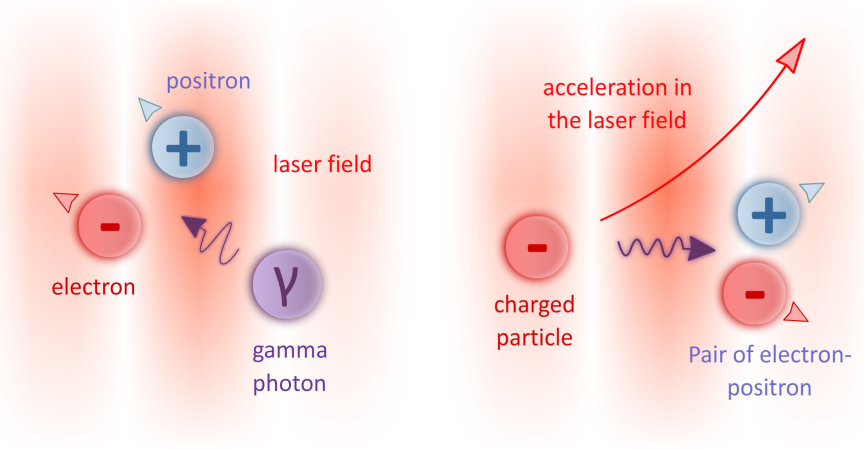

Figure 1.6: The nonlinear Breit-wheeler process (a) and the electromagnetic Trident (b).

is required that can be provided by the nonlinear Compton Scattering. This process has been observed experimentally on the SLAC facility in the collision of a 46.6 GeV (corresponding to a Lorentz factor of $\gamma \sim 9 \times 10^4$) electron beam and a counter-propagating laser of intensity close to 10^{19} Wcm^{-2} (Bula *et al.* (1996); Burke *et al.* (1997); Bamber *et al.* (1999)) despite a very small number of detected positrons. Such an experimental configuration will be accessible in an all-optical scheme with the multi-PW lasers. A first beam could be used for the generation of a high-energy electron beam of several GeV in a LWFA and a second beam could be focused on it to extreme intensities to trigger quantum electrodynamics effects. The electrons will first emit γ-photons via the nonlinear Compton scattering that will subsequently decay into pairs (Sokolov *et al.* (2010); Bulanov *et al.* (2013), this scenario is further studied in chapter 8)

As for pair production in the matter, the nonlinear Breit-Wheeler has a Trident

equivalent. An electron-positron pair can arise from the direct deflection of a high-energy electron in the laser field as illustrated in Fig. 1.6b.

In extreme-intensity laser-solid interaction, the electron-positron pair generation occurs in the vacuum at the laser-solid interface where the high-energy photons are created. The γ-photons emitted toward the laser can decay into pairs via the non-linear Breit-Wheeler process which is the dominant mechanisms above 10^{23} Wcm^{-2}. Emitted toward the target, the photons can also decay into pairs via the Bethe-Heitler. Numerical studies of interaction with thin-foils predict the production of overdense pair plasmas from intensities of 10^{24} Wcm^{-2} (Bell and Kirk (2008), Bulanov *et al.* (2010), Ridgers *et al.* (2012), Ridgers *et al.* (2013), Ji *et al.* (2014), Ji *et al.* (2014), Brady *et al.* (2014) and Nakamura and Hayakawa (2015); Luo *et al.* (2015)).

Another studied phenomenon is the pair cascading that consists in the exponential growth of the number of pairs from a seed electron irradiated by multiple laser beams of extreme intensities. Inside the superimposition of the multiple beam, the field is so high that the electrons are accelerated from several hundred of MeV to GeV energies in less than a laser period and deflected. γ-photons are generated in every direction and rapidly decay into pairs that in turn gain energy and radiate. For high-enough intensities, the production of overdense, neutral and extremely hot pair plasmas is expected (Narozhny *et al.* (2004); Kirk *et al.* (2009); Elkina *et al.* (2011); Nerush *et al.* (2011); Mironov *et al.* (2014); Narozhny and Fedotov (2014); Tang *et al.* (2014); Gelfer *et al.* (2015)).

1.2.3 Application to the next generation of high-power lasers

The next generation of high-power lasers will enable to continue the current studies. Despite the radiation losses, higher proton and ion energies are expected in laser-thin foil interaction both in the TNSA and in the RPA regime. Higher electron energies will also be accessible using laser wakefield accelerators with larger focal spots.

Via the radiation emission of the highly-accelerated electrons, they will constitute interesting bright sources of X-rays and γ-rays. One of the most attracting challenge is the experimental observation of the transition between the classical and the quantum emission regime. Experimental evidence of the radiation damping on the electron dynamics will first help to discriminate the numerous models developed so far. Then, the transition to the quantum regime will be highlighted by observation of the stochastic effects (straggling, scattering) and is essential to validate the theory.

Another challenge is the strong-field QED via the electron-positron pair generation. High-power lasers will constitute one of the most efficient way to generate antimatter. These lasers could constitute a positron injector for optical accelerators (Vieira and Mendonça (2014)), conventional accelerators and plasma-based accelerators (Blue *et al.* (2003); Hogan *et al.* (2010); Yi *et al.* (2014)).

The study of the massive pair generation is also highly motivated by laboratory astrophysical purposes. The experimental study of Weibel-mediated shocks in the collision of electron-positron pair plasmas, or between a pair plasma flow and an inert ion plasma (fireball) unattainable so far owing to the difficulty to generate dense-enough plasmas, is a current hot topic. Today's most promising scenarii are the Bethe-Heitler + Bremsstrahlung processes in high-Z thick-foil pair generation (Chen *et al.* (2011)) explored via numerical simulations in Chen *et al.* (2015) and the laser wakefield accelerated electron beam directed in high-Z converters also studied numerically in the fireball configuration in Sarri *et al.* (2015) (these scenarii are further described in chapter 9).

1.3 Presentation of this work

The study of the radiative and quantum electrodynamics effects requires to improve the theoretical models and the numerical simulation codes. In laser-matter interaction, parallelized simulation codes are needed for any range of intensities to capture all the complexity of the physics in 2D or 3D including classical and relativistic plasma physics, nonlinear optics, photo-ionization, collisions, etc. Radiative and QED will be supplemental sources of complexity making even harder the simplification and the modeling of the different systems and numerical simulation appears more than ever essential. This thesis takes part in the intense efforts ongoing worldwide to simulate and better understand these novel mechanisms in the field of the laser-matter interaction. Numerical simulation is a key tool to explore unprecedented regimes of interaction and novel configurations. Before the facilities are operational, they enable to design the future experiments and to find some applications. Once ready, the fully-prepared codes will help to understand experimental results.

The manuscript is divided into two parts. The first one is dedicated to the study of the radiative and quantum electrodynamics effects presented in section 1.2.1 and section 1.2.2, and is composed of five chapters. In the first four chapters, the high-frequency radiation emission in strong field (Chapter 2), the radiation emission in the matter (Chapter 3), electron-positron pair generation in strong field (Chapter 4) and electron-positron pair generation in the matter (Chapter 5) will be respectively analyzed. The cross sections of each process are described in their different regimes of validity in order to be implemented in our simulation code. In high-intensity laser-matter interaction in which a kinetic description is required, Particle-In-Cell (PIC) codes became widely used in the whole community. The classical Particle-In-Cell method is described in chapter 6. The PIC code Calder developed at the CEA, DAM, DIF has been enriched of the classical and the quantum radiation processes as well as the nonlinear Breit-Wheeler pair generation. The implementation choices and algorithms are also explained, and simulation tests are presented in this chapter.

The second part is focused on the numerical applications of the code and is composed of three chapters. The first one (Chapter 7) deals with the interaction between

extreme intensity lasers (from 10^{22} Wcm^{-2} to 10^{24} Wcm^{-2}) and thin-foils. Presented simulations enable to understand this fundamental interaction and to ensure that our results are in a good agreement with the literature. In the following chapter (Chapter 8), the configuration involving the collision between a high-energy electron beam and a counter-propagating extreme-intensity laser pulse is explored with the forthcoming laser parameters. An all-optical configuration is considered as it will be experimentally possible with the Apollon laser. The first stage of the concept, consisting in the high-energy electron beam generation using a laser wakefield accelerator, is simulated and optimized considering different gas profiles with the long-focused petawatt laser beam. The collision with the multi-PW beam is then studied and demonstrates the collimated bright γ-photon emission in addition to a significant electron-positron pair production. The variation of the beam properties with different intensities, focal spot sizes, durations, and collision angles is parametrically analyzed.

In the last chapter (9), we will demonstrate the capability of extreme-intensity lasers to generate relativistic overdense pair plasmas of interest for the study of electron-positron instabilities relevant for astrophysical scenarii. We present the first self-consistent numerical PIC study of the interaction of two counter-streaming, relativistic pair flows driven from laser-irradiated thin-foils. Fast-growing Weibel instabilities are found to induce ultra-fast thermalization of the pair jets through the buildup of a $\sim 10^6$ Teslas magnetostatic barrier. The associated gamma-ray generation, as well as the subsequent ion-ion interaction are analyzed in detail.

Part I

Radiative and QED effects in laser-matter interaction: description and implementation

Chapter 2

High-frequency radiation emission in a strong field

The interaction between light quanta and particles can occur in different ways. In the case of low photon energies compared to the particle rest mass energy, the colliding photons are scattered without any energy transfer. This elastic interaction is referred to as Thomson scattering. By contrast, in the case of high-energy photons, the photon energy can be partially or totally transferred to the colliding particle. This inelastic process is called the Compton scattering. These processes mainly concern the interaction with electrons since the rest mass energy is accessible with present technologies although it is theoretically possible with heavier charged particles. In the case of moving electrons, the inverse processes are possible. For a photon colliding with an electron of higher kinetic energy, the scattered photon can gain energy (frequency upshift). This process is the inverse Compton scattering. In a laser field, electrons oscillating in the electric field are responsible for the scattering of the laser photons. The electrons are therefore assimilated as dipoles radiating at the laser frequency. When the electron motion becomes relativistic, the scattered light is emitted with frequency up-shift due to the Doppler effect (also referred to as the nonlinear inverse Compton scattering). In general, any traveling charge particle under acceleration or deflection radiates its energy and the radiated energy is as strong as the initial kinetic energy of the particle is high.

This process constitutes the base of many sources of high-frequency radiations and can be hidden behind different names such as synchrotron, betatron, ondulator or wriggler emission depending on the nature of the field and the resulting emission properties (see sect. 1.2.1 in the introduction). For all these applications, the same mathematical formalism can be applied. In this chapter, we describe in the first section the principle of the inverse Compton scattering and the physical equations in the classical and quantum regimes. Then, we study the inverse process, the Compton scattering of charged particles by high-frequency photons.

2.1 Nonlinear inverse Compton Scattering

2.1.1 Physical model

Electrons interacting with an extremely intense laser field can be strongly accelerated so that they radiate their kinetic energy (Blumenthal and Gould, 1970). The importance of the quantum electrodynamics effects on a relativistic particle of mass m and charge q interacting with a monochromatic plane wave depends on the quantum Lorentz-invariant parameter χ (Ritus, 1985) :

$$\chi = \frac{|q|\,\hbar}{m^3c^3}\,|F_{\mu\nu}p^\nu|, \tag{2.1}$$

also referred to as the quantum nonlinearity parameter. Similarly, the quantum effects on a photon of energy $\hbar\omega$ and momentum $\hbar\mathbf{k}$ are quantified by the parameter

$$\chi_\gamma = \frac{e\hbar^2}{m^3c^3}\,|F_{\mu\nu}k^\nu|. \tag{2.2}$$

Here, p^ν is the particle four-momentum, $\hbar k^\nu$ the photon four-momentum and $F^{\mu\nu}$ the electromagnetic field tensor which is defined as follows :

$$F_{\mu\nu} = \begin{pmatrix} 0 & E_x/c & E_y/c & E_z/c \\ -E_x/c & 0 & -B_z & B_y \\ -E_y/c & B_z & 0 & -B_x \\ -E_z/c & -B_y & B_x & 0 \end{pmatrix} \tag{2.3}$$

Two other Lorentz-invariant parameters are important, namely the electromagnetic field invariants, defined as

$$F = \frac{|E^2 - B^2|}{E_s^2} \qquad G = \frac{|\mathbf{E}\cdot\mathbf{B}|}{E_s^2} \tag{2.4}$$

In an arbitrary external electromagnetic field, the model remains valid assuming that :

1. The laser field is uniform and quasistatic during the QED interaction.
2. The laser field is much weaker than the Schwinger field $E_s = m_e^2c^3/e\hbar \simeq 1.3\times10^{18}$ V/m, beyond which the electromagnetic field can no longer be treated classically (Schwinger (1951)).

Assumption (1) requires that the time scale over which the QED processes occur remains smaller than the variation time of the field. Another assumption is the incoherent nature of the emission. In the case of a plane wave, the coherence time associated with the synchrotron radiation is the period over which an electron is

deflected by an angle $\theta \sim 1/\gamma_{e^-}$. In the classical case, where B_0 and E_0 are the magnetic and electric field amplitudes

$$t_{coh}^{cl} = \frac{d}{c} = \frac{R}{c\gamma_e} = \frac{m}{eB_0} \sim \frac{mc}{eE_0}. \tag{2.5}$$

where d is the crossed distance after a rotation of angle θ and radius R. A non-coherent emission requires the coherence time to be longer than the laser period T_0 which is fulfilled provided that $eB/m\omega_0 \gg 1$. The result is similar in the quantum regime: $t_{coh} \sim (E_s/E_0)(\hbar/mc) \sim c/eE_0$. The Lorentz-invariant strength parameter of the laser wave, also referred to as the normalized laser amplitude, is

$$a_0 \quad = \frac{eE_0}{m_e c\omega_0}. \tag{2.6}$$

Therefore, the quasi-static field approximation corresponds to $a_0 \gg 1$. The electromagnetic field can be then considered as uniform and constant during the emission process, making valid the radiated spectrum formula described in the next section (Ritus, 1985). For a bunch of electrons oscillating in a laser field, the coherent nature of the emission process depends on the distance between the emitting particles $d_{e^-e^-}$ relative to the emission wave length $d_{e^-e^-} < \lambda$. The distance depends on the electronic density n_{e^-} as $d_{e^-e^-} = (1/n_{e^-})^{1/3}$. In a ionized gas, the density is close to $10^{-3}n_c \sim 10^{18}$ cm^{-3}, giving $d_{e^-e^-} \sim 10^{-2}$ μm. In a solid target, $n_{e^-} \sim 1000n_c \sim 10^{24}$ cm^{-3} so that $d_{e^-e^-} \sim 10^{-4}$ μm. The process of coherent emission is therefore restricted to relatively modest photon energies (up to few keV in solids), below the energy range (from hard X-rays to γ-rays) considered in this thesis.

The energy-differential production rate of photons of normalized energy γ_γ generated by an electron of energy γ_e in a strong plane electromagnetic field was first calculated by Nikishov (1964),Nikishov and Ritus (1964),Reiss (1962) and Nikishov and Ritus (1967).

$$\frac{d^2N_{Cs}}{dtd\gamma_\gamma}(\gamma_e, \gamma_\gamma) \quad = \quad \frac{P_{cl}}{\gamma_\gamma mc^2} S(\gamma_e, \gamma_\gamma), \tag{2.7}$$

where P_{cl} is the classical radiated power, also defined as the dipole emission intensity,

$$P_{cl} = \frac{2}{3}\frac{q^2}{m^2c^3} |f_{l,\mu} \cdot f_l^\mu|. \tag{2.8}$$

For an electron, it corresponds to

$$P_{cl} \quad = \quad \frac{\tau_0 e^2 |F_{\mu\nu}p^\nu|^2}{m_e^3} \tag{2.9}$$

$$= \quad \frac{\tau_0 e^2 E_s^2 \chi_e^2}{m_e} \tag{2.10}$$

$$= \quad \frac{2}{3}\frac{\alpha_f m_e c^2}{\tau_c}\chi_e^2 \tag{2.11}$$

Here, $\alpha_f = e^2/(4\pi\varepsilon_0)\hbar c$ is the fine structure constant and $\tau_c = \hbar/m_e c^2$ the Compton time. The function S ((Nikishov and Ritus, 1964; Landau and Lifshitz, 2012)) is defined as

$$S(\gamma_e, \gamma_\gamma) = -\frac{\sqrt{3}}{2\pi}\frac{\gamma_\gamma}{\gamma_e^2 \chi_e^2}\left[\int_{2y}^{+\infty} K_{1/3}(s)ds - (2+3\chi_\gamma y)\, K_{2/3}(2y)\right]. \tag{2.12}$$

An alternative expression of S is given in Erber (1966) and used by Kirk *et al.* (2009):

$$S(\gamma_e, \gamma_\gamma) = \frac{1}{2\pi^2}\frac{\gamma_\gamma^2}{\gamma_e^3 \chi_e^3}\sum_{i=1}^{3} m_i(x) J_i(y) \tag{2.13}$$

where $x = \gamma_\gamma/\gamma_e$, $y = \gamma_\gamma/\left[3\chi_e(\gamma_e - \gamma_\gamma)\right]$ (provided that the emitted energy is below the particle kinetic energy $\gamma_\gamma \leq \gamma_e - 1$) and

$$m_1(x) = 1 + (1-x)^{-2}, \tag{2.14}$$

$$m_2(x) = 2(1-x)^{-1}, \tag{2.15}$$

$$m_3(x) = x^2(1-x)^{-2}, \tag{2.16}$$

$$J_1(y) = \frac{1}{3y^2}\int_y^\infty \frac{u}{\sqrt{(u/y)^{2/3}-1}} K_{2/3}^2(u)du, \tag{2.17}$$

$$J_2(y) = \frac{1}{3y}\int_y^\infty \left(\frac{u}{y}\right)^{1/3}\sqrt{(u/y)^{2/3}-1}\, K_{1/3}^2(u)du, \tag{2.18}$$

$$J_3(y) = \frac{1}{3y^2}\int_y^\infty \frac{u}{\sqrt{(u/y)^{2/3}-1}} K_{1/3}^2(u)du \tag{2.19}$$

where K_ν refers to the modified Bessel as a function of real order ν.

Under the condition $a_0 \gg 1$, the accelerated electrons in an intense laser field can become highly relativistic so that $\gamma_e \sim a_0$. The photons are then emitted along the electron trajectory with an angular spread $\sim 1/\gamma_e$. Furthermore, under relativistic motion, the contribution of the longitudinal field in the parameter χ_{e^-} can be neglected, thus yielding:

$$\chi_{e^-} = \frac{\gamma_{e^-}}{E_s}\left|(\beta\cdot\mathbf{E})^2 - (\mathbf{E}+\mathbf{v}\times\mathbf{B})^2\right|^{1/2} \tag{2.20}$$

$$= \frac{\gamma_e}{E_s}\left[{\mathbf{E}_\parallel}^2/\gamma_{e^-}^2 + (\mathbf{E}_\perp + \mathbf{v}\times\mathbf{B})^2\right]^{1/2} \tag{2.21}$$

$$\simeq \frac{\gamma_e}{E_s}\left|\mathbf{E}_\perp + \mathbf{v}\times\mathbf{B}\right|, \tag{2.22}$$

where $\beta = \mathbf{v}/c$ is the normalized velocity and $\mathbf{E}_\perp$ the electric field orthogonal to the propagation direction. Similarly, the photon quantum parameter can be written

$$\chi_\gamma = \frac{\gamma_\gamma}{E_s} \left| \mathbf{E}_\perp + \mathbf{c} \times \mathbf{B} \right| . \tag{2.23}$$

The electron and the photon quantum parameter can be related to the electron and the photon energies according to the formula

$$\chi_{e^-\gamma_\gamma} \sim \chi_\gamma \gamma_{e^-} \tag{2.24}$$

assuming the photon is emitted along the electron velocity in the same direction to the electron. This expression tends to be exact when the parallel field $E_\parallel$ is null and the particle is highly-relativistic $\gamma_{e^-} \gg 1$.

The total photon emission rate is simply the integration of Eq. 2.7 over the photon energy that can be computed numerically or asymptotically approached:

$$\frac{dN_{Cs}}{dt} = \int_0^{\gamma_{e^-}-1} \frac{d^2 N_{Cs}}{dt d\gamma} d\gamma \tag{2.25}$$

For high-χ values, an asymptotic expression has been calculated to be equal to

$$\frac{dN_{Cs}}{dt} \underset{\chi \to +\infty}{\longrightarrow} 1.46 \frac{\alpha_f}{\tau_c} \frac{\chi_{e^-}^{2/3}}{\gamma_{e^-}} \tag{2.26}$$

The energy-differential radiated power can be simply written

$$\frac{dP_{Cs}}{d\gamma_\gamma} = \gamma_\gamma m_{e^-} c^2 \frac{d^2 N_{Cs}}{dt d\gamma_\gamma} = P_{cl} S\left(\gamma_e, \gamma_\gamma\right) \tag{2.27}$$

and therefore, the total radiated power corresponds to

$$P_{Cs} = \int_0^{\gamma_{e^-}-1} \gamma m_{e^-} c^2 \frac{d^2 N_{Cs}}{dt d\gamma_\gamma} d\gamma_\gamma = P_{cl} \int_0^{\gamma_{e^-}-1} S\left(\gamma_e, \gamma_\gamma\right) d\gamma \tag{2.28}$$

$$\tag{2.29}$$

In Kirk *et al.* (2009), the radiated power is expressed in a slightly different form as a function of the so-called synchrotron emissivity function $F(\chi_{e^-}, \chi_\gamma)$

$$P_{Cs} = \frac{\sqrt{3}}{2\pi} \frac{\alpha_f m_{e^-} c^2}{\tau_c} \int_0^{\chi_{e^-}} F(\chi_{e^-}, \chi_\gamma) d\chi_\gamma \tag{2.30}$$

where

$$F(\chi_{e^-}, \chi_\gamma) = \frac{2\chi_\gamma}{3\chi_{e^-}^2} \left(\int_{2y}^{+\infty} K_{1/3}(s) ds - (2 + 3\chi_\gamma y) K_{2/3}(2y) \right) \tag{2.31}$$

The radiated power can be calculated using the following approximation $g(\chi_{e^-})$ given by

$$g(\chi_{e^-}) = \frac{3\sqrt{3}}{4\pi\chi_{e^-}^2}\int_0^{\chi_{e^-}} F(\chi_{e^-},\chi_\gamma)d\chi_\gamma \tag{2.32}$$

$$= \left[1+4.8\,(1+\chi_{e^-})\log(1+1.7\chi_{e^-})+2.44\chi_{e^-}^2\right]^{-2/3} \tag{2.33}$$

This function is referred to as the quantum correction to the classical radiated power so that

$$P_{Cs} = P_{cl}g\left(\chi_{e^-}\right) \tag{2.34}$$

For an electron interacting with a constant magnetic field, the production rate of photons dN_{Cs}/dt as a function of the electron quantum parameter χ_{e^-} and the radiated photon energy γ_γ (Eq. 2.7) is shown in Fig. 2.1a for a normalized field amplitude $B/B_0 = 500$ ($\sim 5\times10^6$ T). For a given quantum parameter χ_{e^-}, the production rate of photons is a decreasing function of the photon energy. The total photon emission rate is plotted in Fig. 2.1b for a similar field amplitude $B/B_0 = 500$ as a function of the electron quantum parameter. The total photon emission rate is obtained from numerical integration of Eq. 2.25. The lower integration bound is chosen so that the calculation has converged to a value equal here to $10^{-15}\left(\gamma_{e^-}-1\right)$. In Fig. 2.1b is also shown the production rate of photons of energy up to $2m_{e^-}c^2$ and the asymptotic expression Eq. 2.26. The evolution of the photon emission rate, integrated from $10^{-15}\left(\gamma_{e^-}-1\right)$ to $\gamma_{e^-}-1$ as a function of the field amplitude and electron energy is displayed in Fig. 2.1c. These figures show two regimes of photon emission. In the low-χ region, $\chi_{e^-}\leq 10^{-2}$, the total production rate of photon is maximal (Fig. 2.1b) and the photon energy distribution (Fig. 2.1a) for a given χ value reveals that the production rate of photons is significant for relatively low photon energies compared to the electron kinetic energy, $\gamma_\gamma < 10^{-1}\left(\gamma_{e^-}-1\right)$. This means that photon energies of the order of the electron kinetic energy has negligible probability to be produced. For high-χ values, $\chi_{e^-}\geq 1$, the total number of photons generated per time unit is a decreasing function of χ_{e^-} (Fig. 2.1a). Nonetheless, the creation of photons of energy close to the electron kinetic energy rises so that the probability to generate such a photon is not negligible anymore (Fig. 2.1b). In parallel, the amount of low-ratio photon energy $\gamma_\gamma/\left(\gamma_e-1\right)$ diminishes.

The photon-energy differential radiated power is plotted in Fig. 2.2a as a function of the electron quantum parameter and the emitted photon energies for a field amplitude $B/B_0 = 500$. The total radiated power, after numerical integration of Eq. 2.29 and using the fitting function (Eq. 2.33) are shown in Fig. 2.2b. The quantum correction $g(\chi_{e^-})$ is also plotted in green. We observe that the numerical integration and the radiated power from the quantum correction match perfectly in the range of parameters studied here. The radiated power is a rising function of the quantum parameter: the stronger are the field and the particle energies, the stronger

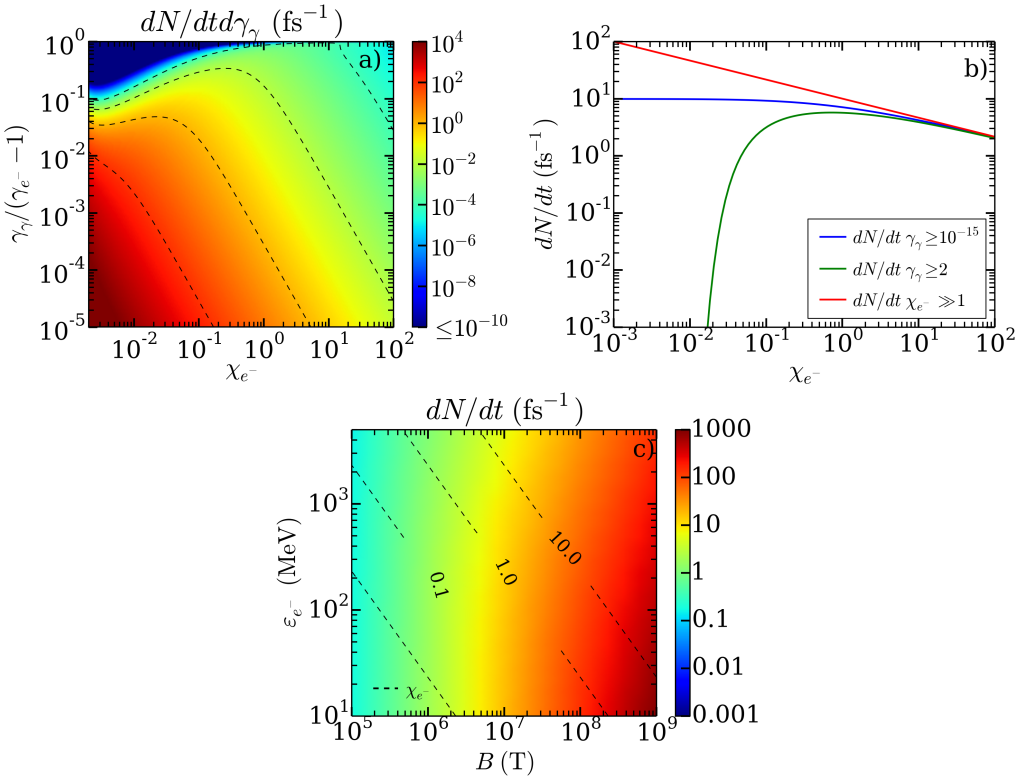

Figure 2.1: (a) - Energy-differential photon emission rate $\frac{d^2N_{Cs}}{dtd\gamma_\gamma}$ (Eq. 2.7) as a function of the electron quantum parameter χ_{e^-} and the ratio of the photon energy over the emitting electron kinetic energy. The dashed contours correspond to 10^{-4}, 10^{-2}, 10^0 and 10^2. (b) - Photon emission rate $\frac{dN_{Cs}}{dt}$ given by numerical integration of Eq. 2.7 for photon of energies above 1 MeV (blue curve), above $10^{-15}\gamma_{e^-}m_ec^2$ (green curve) and the asymptote limit in the high-χ region (red curve) as a function of the quantum parameter (here, the electron energy varies whereas the field is set at $B = 5.5 \times 10^6$ T). (c) - Photon emission rate in a constant magnetic field as a function of the magnetic field amplitude B and the electron energy ε_{e^-}. The dashed contour lines represent the electron quantum parameter parameter χ_{e^-}.

the radiation losses are. For instance, if we consider an electron of energy 500 MeV ($\gamma_e \simeq 10^3$) traveling in a constant electric field $B/B_0 = 500$, one obtains $\chi_{e^-} \simeq 0.5$ and a radiated power (Fig. 2.2b) approximately equal to 100 MeV.fs^{-1}. As above, two regimes of interaction can be identified. In the low-χ region, the maximal radiated power is between $\gamma_\gamma = 10^{-3}\,(\gamma_{e^-} - 1)$ and $\gamma_\gamma = 10^{-2}\,(\gamma_{e^-} - 1)$ (Fig. 2.2a). In the high-χ region, $\chi_{e^-} \geq 1$, the radiated power goes to the highest photon energy close to the electron kinetic one which shows that the radiation losses will be mainly governed by the emission of high-frequency photons.

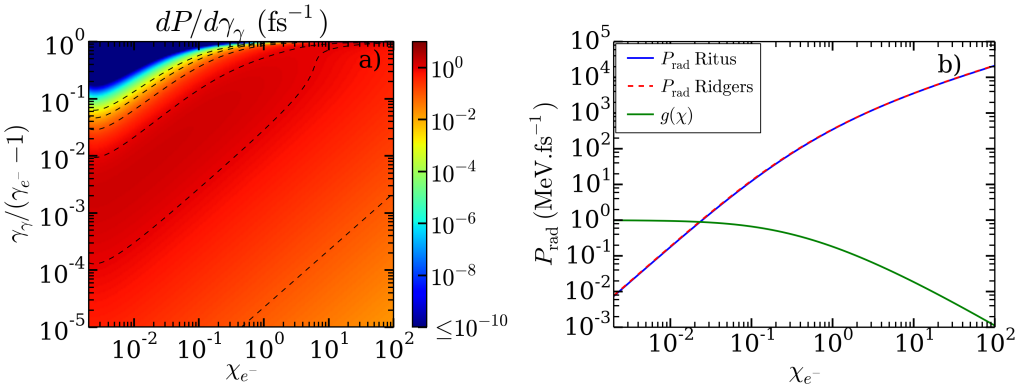

Figure 2.2: (a) - Photon-energy radiated-power distribution for the inverse nonlinear Compton scattering, $\dfrac{dP_{Cs}}{d\gamma_\gamma}$, as a function of the electron quantum parameter χ_{e^-} and the photon energy normalized to the electron kinetic energy $\gamma_\gamma/(\gamma_{e^-}-1)$. The dashed contours correspond to 10^{-3}, 10^{-2}, 10^{-1} and 10^0. (b) - The total radiated power P_{Cs} from the numerical integration of Eq. 2.29 (blue) and the approximate quantum correction given by Eq. 2.33 (dashed red line). The quantum correction $g(\chi_{e^-})$ is plotted in green.

The modeling of the radiation losses will be different in the two aforementioned regimes. The low-χ region is usually referred to as the classical regime. Since electrons radiate many photons of small energies in comparison to their kinetic one, the deceleration can be seen as continuous. The radiation losses can thus be treated via a friction term, depending on the radiated power, added to the equations of motion. In the so called classical limit $\chi_{e^-} \ll 1$, the S function is reduced to the well-known form (Erber, 1966; Blumenthal and Gould, 1970) :

$$S(\omega) = \frac{3^{5/2}}{8\pi}\frac{\omega}{\omega_{cr}}\int_{\omega/\omega_{cr}}^{\infty} K_{5/3}(t)dt \tag{2.35}$$

where ω/ω_{cr} is approximately the frequency limit of the spectrum. We have

$$\omega_{cr} = \frac{3}{2}\gamma_{e^-}^3\omega_r = \frac{3\gamma_{e^-}\chi_{e^-}}{(2+3\chi_{e^-})} \tag{2.36}$$

where $\omega_r = |\mathbf{p}_{e^-} \times \mathbf{F}_L|/p_{e^-}^2$ is the instantaneous electron rotation frequency. In the classical limit, $\chi_{e^-} \ll 1$ (but $\gamma_{e^-} \gg 1$), the limit frequency can be approximated by $\omega_{cr} \simeq 3/2\gamma_e^-\chi_{e^-}$. The maximal radiated power is located at $\gamma_{\gamma,\max} \sim 1/3\omega_{cr}\hbar/m_ec^2 \sim 1/2\gamma_{e^-}\chi_{e^-}$ in the classical spectrum in a good agreement with Fig. 2.2a. We can similarly define the limit energy $\varepsilon_{cr} = \hbar\omega_{cr} = \gamma_{cr}mc^2$. In Fig. 2.2, we can observe that the quantum correction tends to 1 in the classical regime, which means that the

radiated power is close to the classical power P_{cl} independently of χ_{e^-}. The classical radiation regime is described in greater detail in the next section 2.1.2.

The high-χ region is the so-called quantum regime. Because the electrons are more likely to emit photons of energy close to their kinetic energy, it means that the continuous (soft and smooth) approach is not appropriate anymore. Electrons of high-χ values will undergo strong recoil and therefore exhibit straggled deceleration (Shen and White (1972); Neitz and Di Piazza (2013)). The energy losses can be seen as series of discrete energy jumps corresponding to the emitted photon energy. In this regime, the radiation loss is extremely fast as shown in Fig. 2.2b so that the electrons can lose more than half of their energy in a few tens of femtoseconds. Since in the quantum regime, electron have energies of hundreds of MeV to several GeV, the consequent radiated spectrum is strongly energetic in the same range of energies. In the quantum regime, the discrete emission should be modeled with a Monte-Carlo scheme (Duclous *et al.* (2011)).

For intermediate values of χ close to 10^{-1}, we are in the semi-quantum regime where both descriptions can be applied. In this case, we can extend the continuous description by using a quantum correction on the radiated power.

For an electron interacting with a constant magnetic field, the radiated spectra are shown in Figs. 2.3(a,b,c) for $\chi_{e^-} = 0.01$, 0.1 and 1 (γ_{e^-} =46, 152 and 485, $B/B_0 =$ 90, 270 and 850). The plots present both the classical (Eq. 2.35) and quantum spectra (Eq. 2.27). The location of the maximal radiated power $\gamma_{\varepsilon_{\max}}$ is indicated in green for the classical curve and in orange for the quantum one. The comparison between the classical and the quantum formulae shows that for $\chi_{e^-} = 0.01$ (Fig. 2.3a) (the limit of the classical regime), the distributions are nearly the same. In a strict classical regime $\chi_{e^-} \sim 0.001$, the spectra are perfectly similar. In the semi-quantum, going to the quantum regime ($\chi_{e^-} \sim 0.1$), Fig. 2.3b demonstrates that the classical distribution gets wrong in the high-energy domain, allowing for the emission of photons of energies exceeding the electron's. This inconsistency is all the more pronounced as χ_{e^-} is high as shown by Fig. 2.3c and the use of the quantum formula is required for a correct description of the photon spectrum. It is worth noting the increasing steepness of the spectrum at $\gamma_\gamma \to \gamma_{e^-} - 1$ as χ_{e^-} is increased, hence leading to the emission of photons of energies larger and larger.

The photon energy maximizing the radiated power is usually estimated as $\gamma_{\gamma,\varepsilon_{\max}} \sim 0.3\omega_{cr}\hbar/m_e c^2$ in the classical regime. This is not satisfactory for high χ values where this approximation tends to over-estimate the photon energy, and even exceed the upper bound of $\gamma_{e^-} - 1$ as shown in Fig. 2.3. In Fig. 2.4a, the value of $\gamma_{\varepsilon_{\max}}$ is mapped as a function of the electron energy and quantum parameter. It confirms that for high χ values, in the quantum regime, the photon energy at maximal radiated power approaches the electron kinetic energy. Moreover, it shows that the behavior of $\gamma_{\gamma,\varepsilon_{\max}}/(\gamma_{e^-} - 1)$ is mainly dependent on χ_{e^-}, γ_{e^-} only plays a role of displacing of the emitted photon energy. We can therefore calculate a fitting function of the average function $\kappa(\chi) = \langle \gamma_{\gamma,\varepsilon_{\max}}/(\gamma_{e^-} - 1) \rangle_{\gamma_{e^-}}$ displayed in Fig. 2.4(right).

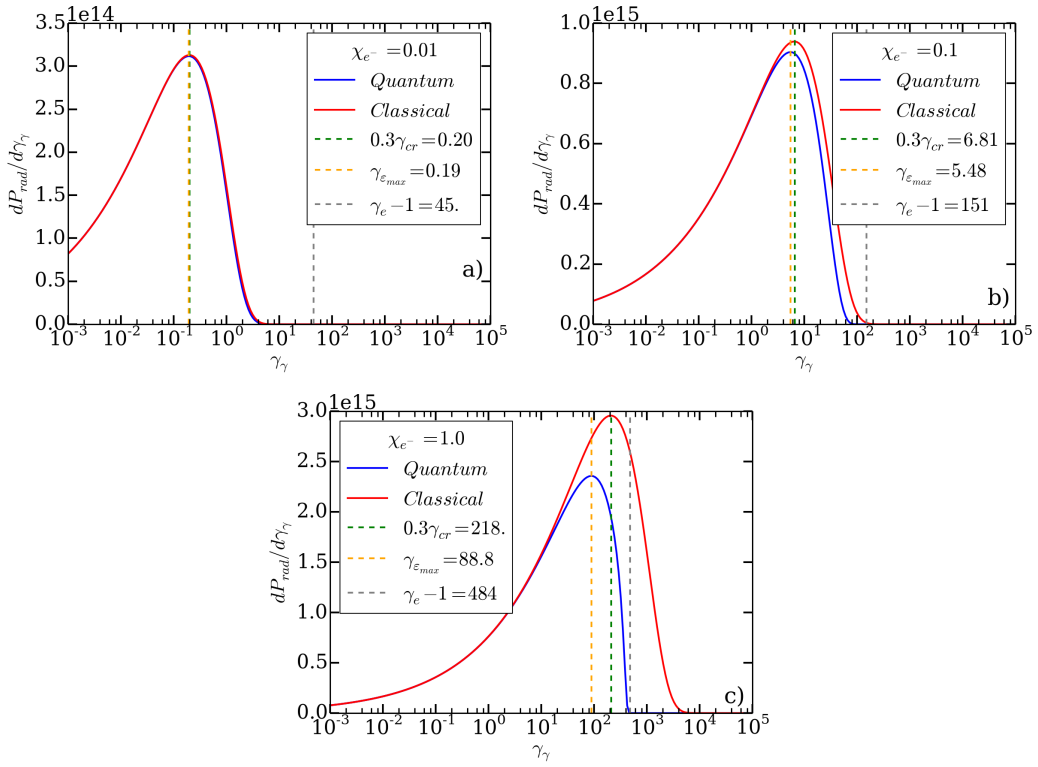

Figure 2.3: Energy distribution of the radiated power in the quantum (Eq. 2.27, blue curves) and the classical (Eq. 2.35, red curves) regimes for $\chi_e = 0.01$ (a), $\chi_e = 0.1$ (b) and $\chi_e = 1$ (c). The orange and green dashed lines indicate the photon energy at position of maximal radiated power respectively in the quantum and the classical regime. The grey line is at the electron kinetic energy.

Here, the fit is a polynomial function of high order (20^{th} order in this case) in order to well describe the behavior of κ.

2.1.2 Continuous radiation loss

The models of continuous radiation are based on the notion of self-force and consists in a modification of the momentum equations by the addition of radiation friction terms. An accelerated charged particle creates an own electromagnetic field that will interact with itself. In the case of strongly accelerated charged particles, this self-generated field is sufficiently strong to decelerate them in terms of radiation. The first expression of the self-force was calculated by Lorentz (1909) and then generalized in the relativistic regime by Abraham and Föppl (1908) and Dirac (1938), usually cited as the Lorentz-Abraham-Dirac (LAD) equations. The LAD suffers from unphysical effects owing to the assumption of point-like charged particle. For instance, the

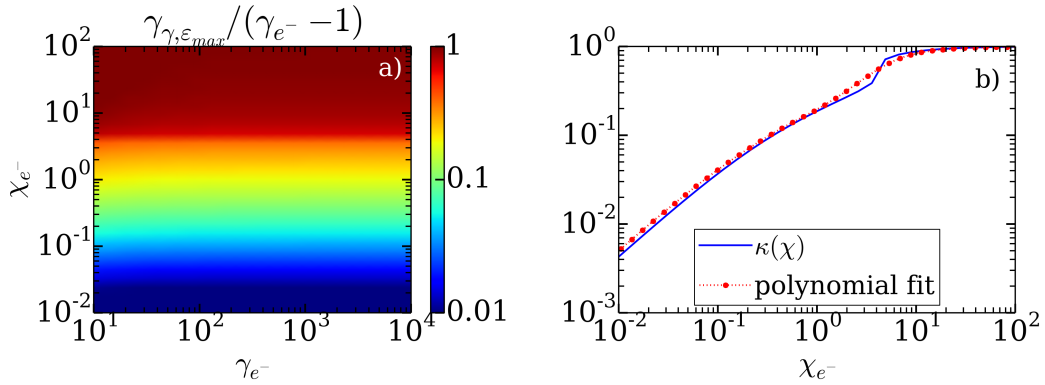

Figure 2.4: (a) - Evolution of the normalized photon energy $\gamma_{\gamma,\varepsilon_{\max}}/(\gamma_{e^-}-1)$ maximizing the radiated power spectrum as a function of the electron energy γ_{e^-} and the quantum parameter χ_{e^-}. (b) - Average evolution of the photon normalized energy $\gamma_{\gamma,\varepsilon_{\max}}/(\gamma_{e^-}-1)$ as a function of χ_{e^-} (blue) and the numerical polynomial fit (red).

model does not verify the principle of inertia, so that the radiation reaction term does not vanish when the external force acting on the particle is null, leading to a spurious force (Rohrlich (1997); Spohn (2000)). An interesting discussion on the mathematical formalism and the limit of the LAD can be found in Rohrlich (2000) and Rohrlich (2001).

In order to correct the LAD equations, different solutions have been proposed by different authors (Landau and Lifshitz (1975); Mo and Papas (1971); Ford and O'Connell (1991, 1993); Sokolov (2009)). The Landau-Lifshitz (LL) equation was obtained from a perturbative expansion of the LAD equations (Landau and Lifshitz (1975)). It assumes that the radiation force stays small relative to the Lorentz one. In Rohrlich (1997), the LAD model has been also revisited considering the particle as a charged sphere rather than a point. The LAD and the LL model are both analyzed and compared with exact solutions of the electron motion in different scenario in Bulanov *et al.* (2011). In Rivera and Villarroel (2002), it has been pointed out that the LL approximation is not exact and, by solving the runaway solution problem of the LAD, introduces a very small error on the correct radiation rate. An unphysical result is also discussed in Domínguez *et al.* (2006).

In the following, we will adopt the recent model of Sokolov ((Sokolov, 2009; Sokolov *et al.*, 2009)). Using four-vector notation, the equations governing the motion of a relativistic particle can be written

$$\frac{dp^\mu}{d\tau} = f_l^\mu + f_{rad}^\mu \tag{2.37}$$

$$\frac{dx^\mu}{d\tau} = \frac{p^\mu}{m} + \tau_0 \frac{P_{rad}}{P_{cl}} \frac{f_l^\mu}{m} \tag{2.38}$$

where $f_l^\mu = qF_\nu^\mu p^\nu/m$ is the Lorentz force four-vector and $f_{rad}^\mu = Ip^\mu/mc^2$ the ra-

diation friction force. In the comoving Lorentz frame, τ is the proper time defined by $\gamma = dt/d\tau$. The emission radiated power $P_{\rm rad}$ is defined as the average of the emitted photon energy $\hbar\omega$ weighted by the photon rate production $dN_{ph}/d\tau d\omega$ in the comovoving Lorentz frame. Thus, we have

$$P_{\rm rad} = \int_{\omega_{min}}^{\infty} \hbar\omega \frac{dN_{ph}}{d\tau d\omega} d\omega = g(\chi_e) P_{cl} \tag{2.39}$$

In the comoving frame, the non-relativistic radiated power, also defined as the dipole emission intensity P_{cl}, has been given previously for an electron (also valid for a positron)

$$P_{cl} = \frac{\tau_0 e^2 \left|F_{\mu\nu} p^\nu\right|^2}{m_e^3} = \frac{\tau_0 e^2 E_s^2 \chi_{e^-}^2}{m_e} \tag{2.40}$$

where $\tau_0 = 2r_e/3c$ and r_e is the electron radius. The function $g(\chi_{e^-})$ is the quantum correction to the total power emitted by an electron of parameter χ_{e^-},

$$g(\chi_e) = \frac{3\sqrt{(}3)}{4\pi\chi_e^2} \int_0^\infty F(\chi_e, \chi_\gamma) d\chi_\gamma. \tag{2.41}$$

In the classical regime corresponding to $\chi_{e^-} \ll 1$, the quantum correction is $g(\chi_{e^-}) \simeq 1$ so that the emission intensity can be approximated by P_{cl}.

In terms of three vector formulation, Eqs 2.38 become

$$\frac{d\mathbf{p}}{dt} = \mathbf{f}_l + q\left(\delta\mathbf{v} \times \mathbf{B}\right) - P_{\rm rad} \frac{\mathbf{p}}{\gamma m c^2} \tag{2.42}$$

$$\frac{d\mathbf{x}}{dt} = \mathbf{v} + \delta\mathbf{v} \tag{2.43}$$

where

$$\delta\mathbf{v} = \frac{\tau_0}{m} \frac{\mathbf{f}_l - \mathbf{v}\left(\mathbf{v}\cdot\mathbf{E}\right)}{1 + \tau_0(\mathbf{v}\cdot\mathbf{E})/mc^2}. \tag{2.44}$$

In this case, the classical Larmor radiated power can be written

$$P_{cl} = \gamma^2 \left(\delta v \cdot \mathbf{f}_L\right). \tag{2.45}$$

To illustrate this radiation model, we consider the interaction of an electron with a counter-propagating circularly polarized electromagnetic pulse. The pulse has a Gaussian temporal profile of duration 33 fs at half maximum. In the first case, the electron has an initial longitudinal momentum $p_{x,0}/m_e c^2 = 100$ and the pulse a maximum amplitude of $a_0 = 10$. Therefore, the quantum parameter reaches a maximum of $\chi_{e^-} \sim 0.005$ (at $\omega_0 t \sim 90$) corresponding to a weak emission regime. The time evolutions of the different components of Eqs. (2.42) and (2.43) are plotted

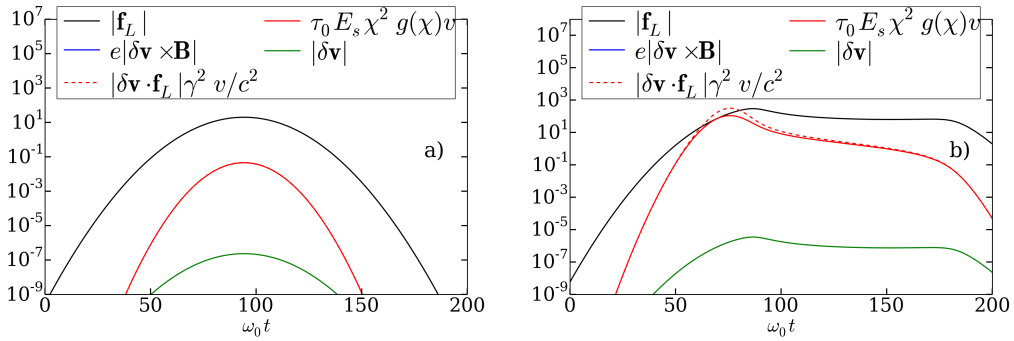

Figure 2.5: Time evolution of the norm of the different components of Eq. (2.43), Eq. (2.44) and Eq. (2.42) for two cases of interaction of a free electron with a counter-propagating circular electromagnetic pulse. In (a), the electron has an initial longitudinal momentum of $p_{x,0} = 100 m_e c$ and the normalized field amplitude is equal to $a_0 = 10$. In (b), the electron has an initial longitudinal momentum of $p_{x,0} = 2000 m_e c$ and the normalized field amplitude is equal to $a_0 = 200$.

in Fig 2.5. It shows that the Lorentz force dominates the radiation damping by almost a factor 100. The classical Larmor and the quantum formulas give the same results. In this interaction, the term $(\delta\mathbf{v} \times \mathbf{B})$ is null and $\delta\mathbf{v}$ negligible.

In the second case, the electron has an initial longitudinal momentum $p_{x,0}/m_e c^2 = 2000$ and the pulse a maximum amplitude of $a_0 = 200$. Here, the quantum parameter reaches $\chi_{e^-} \sim 0.4$ (at $\omega_0 t \sim 65$). In such a regime, the quantum correction is necessary as shown in Fig. 2.5. The Larmor formula in this interaction regime tends to overestimate the radiation reaction and when $\chi_{e^-} > 0.1$, the quantum radiation reaction is comparable to the Lorentz force. The term $\delta\mathbf{v}$ is still negligible.

A number of authors have addressed the influence of the radiation loss in laser-plasma interaction at intensities $I > 10^{21}$ W.cm^{-2} ($\chi_e \sim 10^{-3}$ for a laser driven particle) using the continuous emission description implemented in a particle-in-cell code. Most of these studies have focused on the variation of the laser absorption and the ion acceleration in thin foil targets and dense plasma slabs (Zhidkov *et al.*, 2002; Tamburini *et al.*, 2010, 2012; Capdessus *et al.*, 2012; Nakamura *et al.*, 2012; Ridgers *et al.*, 2012; Ji *et al.*, 2014).

2.2 Compton scattering

Photons travelling in the matter can be scattered by charged particles (especially electrons and positrons). In the low energy limit $\varepsilon_\gamma \ll m_e c^2$, the photons undergo an elastic collision (The energy is conserved during the collision). The process is referred to as Thomson scattering. In the opposite high energy limit, an energy transfer occurs. The particle trajectories can be strongly deflected and the re-emitted

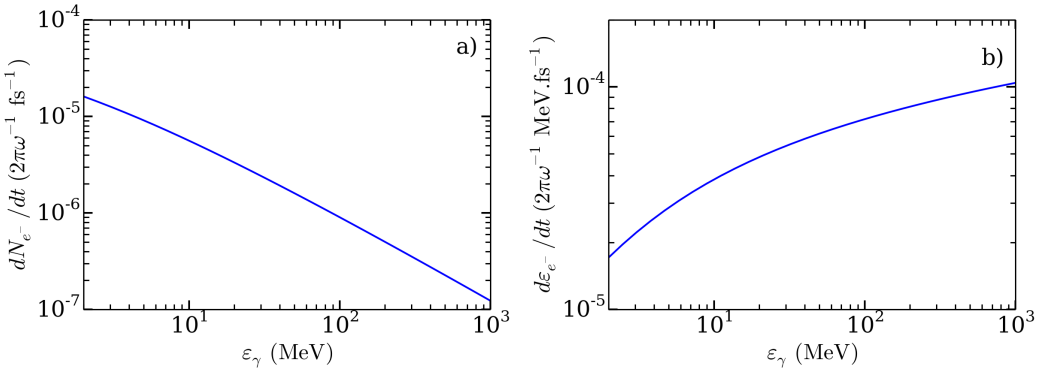

Figure 2.6: Number of Compton scattering events (a) and energy gain (b) per laser period for $\lambda = 1$ μm undergone by an electron in a constant, homogeneous flow of photons of energy ε_γ and density $n_\gamma = 10^3 n_c$.

photon has a lower energy (Blumenthal and Gould, 1970; Madau and Thompson, 2000; Zampieri *et al.*, 2003).

In laser-matter interaction, gamma photons generated by synchrotron radiation have sufficient energies to deflect the electrons through Compton scattering.

Let us consider an electron moving in the direction $\mathbf{k}_{e^-}$ with energy ε_{e^-}, colliding with a photon of energy ε_γ propagating in the direction $\mathbf{k}_\gamma$ so that $\mathbf{k}_{e^-}\cdot\mathbf{k}_\gamma = \cos\theta$. After scattering, the particle trajectories do not necessarily remain in the plane $(\mathbf{k}_{e^-}, \mathbf{k}_\gamma)$. The scattered energies and angles are respectively defined by $\varepsilon_{e^-,s}$, θ_s and ϕ_s as shown in Fig. Expressed in the electron's proper frame, the probability for the photon to be scattered with angular deflection χ'_s, φ'_s and photon energy $\varepsilon'_{\gamma,s}$ is given by the Klein-Nishina differential cross section

$$\frac{d\sigma_{KN}}{d\chi'_s} = \frac{3}{16\pi}\sigma_T\tau^2\left(\frac{1}{\tau} + \tau - \sin^2\chi_s\right), \tag{2.46}$$

where τ is the ratio of the photon energies before and after scattering

$$\tau = \frac{\varepsilon'_{\gamma,s}}{\varepsilon'_\gamma} = \frac{1}{1 + \left(\varepsilon'_\gamma/m_e c^2\right)\left(1 - \cos\chi'_s\right)}. \tag{2.47}$$

The Klein-Nishina cross section shows that the probability to be deflected does not depend on the azimutal deflection φ'_s. From Lorentz transformation, the photon energy in the laboratory frame K and the electron's frame are related by $\varepsilon'_\gamma = \varepsilon_\gamma\gamma_{e^-}\left(1 - \beta_{e^-}\cos\theta\right)$ and $\varepsilon_\gamma = \varepsilon'_\gamma\gamma_e\left(1 + \beta_e\cos\theta'\right)$. Then, one obtains the angular relations

$$\cos\theta' = \left(\frac{\cos\theta - \beta_e}{1 - \beta_e\cos\theta}\right) \qquad \sin\theta' = \frac{\tan\theta}{\gamma_e}\cos\theta'. \tag{2.48}$$

The propagation unit vector of the photon after scattering in the electron's frame is

$$\mathbf{k}'_{\gamma,s} = \begin{cases} \cos\chi'_s \sin\theta' + \sin\chi'_s \cos\varphi' \cos\theta' & (e_1) \\ \cos\chi'_s \cos\varphi' - \sin\chi'_s \cos\varphi' \sin\theta' & (e_2) \\ -\sin\chi'_s \sin\varphi'_s & (e_3) \end{cases} \tag{2.49}$$

From Lorentz transformation, one easily gets the direction of the scattered photon in the laboratory frame.

The number of Compton scattering events per unit time dt undergone by an electron in the laboratory in a wind of photons of density n_γ and distribution f_γ is given by

$$\frac{dN_{e^-}}{dt} = \int c\sigma_{KN} \left(1 - \beta_e \cos\theta\right) n_\gamma f_\gamma(\varepsilon_\gamma) \sin(\chi_s) dp_e d\varepsilon_\gamma d\theta d\chi'_s d\varphi \tag{2.50}$$

where p_e is the electron momentum. We denote $\Delta\varepsilon = \varepsilon_\gamma - \varepsilon_{\gamma,s}$ the variation in the photon energy. The evolution of the electron energy is therefore described by the equation

$$\frac{d\varepsilon_{e^-}}{dt} = \int \Delta\varepsilon c\sigma_{KN} \left(1 - \beta_e \cos\theta\right) n_\gamma f_\gamma(\varepsilon_\gamma) \sin(\chi_s) d\varepsilon_\gamma d\theta d\chi'_s d\varphi. \tag{2.51}$$

The energy transfer is maximized for a head-on collision $\theta = \pi$. In this case, the photon angular deflection χ is small. We consider the ideal case of a mono-energetic unidirectional flow of photons of density $n_\gamma = 10^3 n_c$ and energy ranging from 2 to 10^3 MeV (of the order of what we can get in a strong laser field, $I_\gamma = n_\gamma \varepsilon_\gamma c$ between $10^{22}\mathrm{Wcm}^{-2}$ and $5 \times 10^{24}\mathrm{Wcm}^{-2}$) striking an electron at rest. The number of Compton scattering event and the energy transfer to the electron per laser period is given in Fig. 2.6. The curves have been obtained from numerical integration of Eq. 2.50 and Eq. 2.51. We find that the higher is the photon energy, the lower is the number of collisions (i.e. the probability for collision per time unit). A collision with a photon of higher energy will transfer a stronger energy to the electrons (Fig. 2.6b), but this corresponds to a decreasing fraction of the incident γ energy. Under the considered conditions, the acceleration of an electron initially at rest to an energy of 1 MeV takes a minimum of $\sim 10^4$ laser periods (30 ps) that is much longer than by direct interaction with an intense laser field. As a consequence, the force acting on an electron due to Compton scattering turns out to be negligible compared to those of an intense laser field. The typical laser-interaction time of several picoseconds is not sufficient to allow electrons to reach even relativistic energies by this process. If we now consider one photon traveling in a dense thin foil ($n_{e^-} \sim 100 - 1000 n_c$), we can similarly infer that the optical depth to one Compton scattering is well-above the μm scale typical of the targets used in laser experiments.

Chapter 3

Radiative process in the matter

Bremsstrahlung is a mechanism of high-frequency photon emission in inelastic collisions between charged particles ($e^- + Z \rightarrow e^- + Z + \gamma$). It preferably occurs in high-Z dense matter between ions and free electrons, or between electrons. In laser-matter interaction, the hot electrons injected deep into the target are held responsible for bremsstrahlung emission of X and γ-rays.

3.1 Modelling the Bremsstrahlung emission

Analytically calculated cross-sections available in the literature are derived from approximate wave functions depending on the nature of the collision and their applicability depends on the material and the particle energies.

3.1.1 The Born-approximation

In the Born approximation, an analytic evaluation of the Bremsstrahlung cross section can be made using free-particle wave-function (Bethe and Heitler (1934)). A widely-used review has been done in Koch and Motz (1959) focusing on the Bremsstrahlung cross sections in the Born approximation in several energy and screening regimes. The Born approximation is valid when

$$2\pi\frac{Ze^2}{\hbar v_i} \ll 1 \qquad 2\pi\frac{Ze^2}{\hbar v_f} \ll 1 \tag{3.1}$$

where v_i and v_s are the particle velocity before and after the collision. For a given material, the kinetic energy has to be large enough to satisfy these conditions. The Born approximation suffers from a lack of accuracy for small electron energies and in the high-energy limit, and for high-Z materials.

3.1.2 Numerical calculations

Several references provide numerical fits for different energy ranges of the differential and total cross-sections. In Seltzer and Berger (1985) and Seltzer and Berger (1986), the authors have tabulated the cross section differential in photon energy for electron energies ranging from 1 keV to 10 GeV, and for different materials ($6 \leq Z \leq 100$) in the case of neutral atoms. For electron energies below 2 MeV, the authors have used the results of Refs Tseng and Pratt (1971) and Pratt *et al.* (1977) and performed a numerical integration of the Dirac equation in which electron wave functions have been approached by a partial-wave series in a screened potential. For energies above 50 MeV, the analytic Born approximation calculation of Davies *et al.* (1954) has been exploited. Finally, the authors have interpolated the whole data in order to fill the gap between non-relativistic and relativistic electron energies and therefore obtain continuous cross sections. Although the tabulation discretization is not sufficiently accurate to be used in a code, they provide a suitable database to check and compare our following results. The cross sections have been moreover calculated in the hypothesis of an isolated atom.

3.1.3 Screening effects

In the case of an isolated atom, in neutral or weakly ionized matter, the Coulomb interaction between the fast electrons and the nuclei is partially screened by the bound electrons. The Coulomb potential has to be modified in consequence to account for this effect.

A simple, widely used modeling of the atomic potential is given by the Wentzel-Yukawa format,

$$V_{WY}(r) = \frac{Ze}{r} \exp\left(-r/l_{TF}\right) \tag{3.2}$$

where l_{TF} is the screening radius taken to be equal to the Thomas-Fermi radius

$$l_{TF} = 0.885 \frac{\hbar^2}{m_e e^2} Z^{-1/3} \tag{3.3}$$

A more accurate fit of the Thomas-Fermi potential has been obtained in Moliere (1947) and is constituted of three exponential potentials:

$$V_M(r) = \frac{Ze}{r} \left[0.35 \exp\left(-0.3r/l_{TF}\right) + 0.55 \exp\left(-1.2r/l_{TF}\right) + 0.1 \exp\left(-6r/l_{TF}\right)\right] \tag{3.4}$$

In a significantly ionized plasma, the Debye screening provided by the free electrons and occurring relatively far from the ions, should also be taken into account. Far from the partially ionized atom, we expect a potential of the form

$$V_D(r) = \frac{Ze}{r} \exp\left(-r/l_D\right), \qquad l_D = \sqrt{\frac{k_B T \varepsilon_0}{n_i e^2 Z^* \left(Z^* - 1\right)}} \tag{3.5}$$

where l_D is the Debye-Huckel length approximated in a plasma where all the species have the same temperature T and Z^* is the ionization rate. In practice, the Debye length is minimized by the interatomic distance $l_D = \max\left(k_B T\varepsilon_0/n_i e^2 Z^*\left(Z^*-1\right), r_i\right)$. We call V_{WYD} the multi-screening potential. When the matter is neutral, $V_{WYD} \to V_{WY}$, when the matter is fully ionized, $V_{WYD} \to V_D$, when $r \ll l_{TF}$, $V_{WYD} \to V_{WY}$ and when $r > l_D$, $V_{WYD} \to V_D$. As a consequence, V_{WYD} can be approximated by (Nardi and Zinamon (1978); Nardi *et al.* (2007))

$$V_{WYD}(r) = Ze\left[\left(1-\frac{Z*}{Z}\right)V_{WY}(r) + \frac{Z*}{Z}V_D(r)\right]. \tag{3.6}$$

In the above formula, the close-distance Wenkel-Yukawa potential V_{WY} can be changed to a more sophisticated potential, as derived by Molière for instance.

Screening effects uppon Bremsstralung processes can be estimated by realizing that the maximum impact parameter, $r_{\max}$, is inversely proportional to the minimum momentum transfer to the atom $\delta_{p,min}$. The momentum transfer to the atom corresponds to

$$\begin{aligned}\delta_p &= \left(\mathbf{p}_{e,i} - \mathbf{p}_{e,s} - \mathbf{p}_\gamma\right)\cdot\mathbf{n}_r &(3.7)\\ &= \left[p_{e,i}^2 + p_{e,s}^2 + p_\gamma^2 - 2p_{e,i}p_\gamma\cos\theta_i + 2p_{e,s}p_\gamma\cos\theta_s - 2p_{e,s}p_{e,s}\left(\cos\theta_s\cos\theta_i + \sin\theta_s\sin\theta_i\cos\phi_s\right)\right]^{1/2} &(3.8)\end{aligned}$$

$\mathbf{n}_r$ being the direction of $\mathbf{r}$, $p_\gamma = k\hbar$ the momentum transfer to the Bremsstrahlung photon (and k the photon wave number), $p_{e,i}$ the incident electron momentum and $p_{e,s}$ the scattered momentum. Thus, the maximum impact parameter writes

$$r_{max} = \frac{\hbar}{\delta_{p,min}} = \frac{\hbar}{p_{e,i} - p_{e,s} - p_\gamma} \sim \frac{2\hbar\gamma_{e,i}\gamma_{e,s}}{p_\gamma} \text{ for } \gamma_{\mathrm{e,i}} \gg 1 \tag{3.9}$$

where $\gamma_{e,i}$ and $\gamma_{e,s}$ are respectively the Lorentz factor for the incident and the scattered electron. By comparing $r_{\max}$ to l_{TF} and l_D, one can then determine how strong are the Debye and atomic (Thomas-Fermi) screenings. For a screening potential of characteristic length l, the screening effect has no influence if $r_{\max}/l \ll 1$.

In Figure 3.2, $r_{\max}$ is compared with the characteristic lengths l_{TF} (red) and $l_D(T)$ (blue dashed curves) in a silver target ($Z = 47$) as a function of the temperature. The parameter $r_{\max}$ is plotted for $\gamma_\gamma = 0.1, 0.5$ and $0.9(\gamma_{e,i} - 1)$, p_s is calculated by energy balance. The ionization rate is calculated from the plasma temperature using fit obtained by More (1985). As displayed in tab 3.1, aluminium gets fully ionized for $T \geq 10$ keV. Coulomb screening is dominant for non-relativistic and ultra-relativistic electron energies and is amplified when little energy is given to the photon. Overall, Debye screening turns out to be weak in most of the considered electron energy range. Its domain of influence is resticted to ultra-relativistic electrons and weak photon energies in relatively low temperature plasmas. We can also define $\Gamma = l_{TF}/r_{\max}$. When $\Gamma \leq 1$, the Coulomb screening should be taken into account.

T (keV)	0.001	0.01	0.1	1	10	100
Z^*	5	5	12	35	46	47

Figure 3.1: Ionization rate $Z*$ as a function of the plasma temperature in silver according to the scaling of More (1985) .

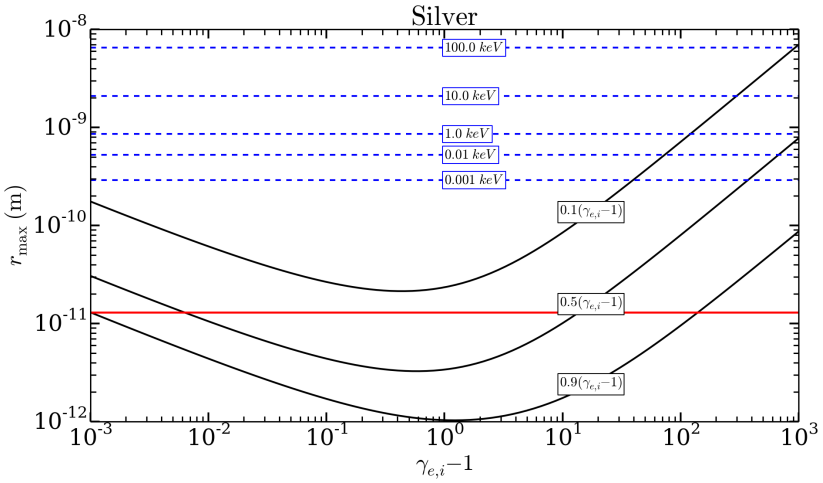

Figure 3.2: Parameter $r_{\max}$ as a function of the initial electron energy $\gamma_{e,i}$ for different photon energies $\gamma_\gamma = 0.1, 0.5$ and $0.9(\gamma_{e,i} - 1)$ (black lines). The red line indicates the Thomas-Fermi radius l_{TF} for $Z = 47$. The dashed blue lines represent the Debye lengths for plasma temperatures ranging from 1 eV to 100 keV.

3.2 Cross-sections differential in photon energy

An analytical Bremsstrahlung cross section valid for a few keV to hundreds of MeV electron energies does not exist. Several expressions have been calculated in the different regimes. Here, we distinguish three regimes of interaction, the non-relativistic ($\gamma_{e,i} \leq 1$), the relativistic ($1 < \gamma_{e,i} < 100$) and the ultra-relativistic case ($\gamma_{e,i} > 100$). In the following sections, the photon-energy differential cross section is written interchangeably in both ways $\frac{d\sigma}{d\gamma}$ and $d\sigma_\gamma$.

3.2.1 Non-relativistic case

From quantum theory, the non-relativistic (or weakly-relativistic should we say) electron-ion Bremsstrahlung cross section in the Born approximation can be written

(Heitler (1954)) as

$$\frac{d\sigma}{d\gamma_\gamma} = \frac{64\pi^4 r_e^2 \alpha_f}{3\gamma_\gamma p_{e,i}^2} \int_{\delta_{p,-}}^{\delta_{p,+}} |\bar{V}(u)|^2 u^3 du \tag{3.10}$$

where $\delta_{p,\pm} = p_i \pm p_f$ are the maximum and minimum momentum transfers to the nucleus, $\bar{V}$ is the Fourier transform of the atomic potential,

$$\bar{V}(u) = \frac{1}{(2\pi)^3} \int_\Omega V(\mathbf{r}) \exp(i\mathbf{ur}) d\mathbf{r}. \tag{3.11}$$

The screening effects can be taken into account in this formula using specific potentials. Let us first consider the case of a single exponential Wentzel-Yukawa atomic potential $V(r) = (q/r)\exp(-r/l)$.

$$\bar{V}(u) = \frac{q}{(2\pi)^3} \int_\Omega \frac{1}{r} \exp(-r/l) \exp(i\mathbf{ur}) d\mathbf{r} \tag{3.12}$$

$$= \frac{q}{(2\pi)^3} \int_0^{+\infty} \int_0^{\pi} \int_0^{2\pi} \frac{1}{r} \exp\left(-\frac{r}{l}\right) \exp(iur\cos\theta) r^2 \sin(\theta) dr d\theta d\phi \tag{3.13}$$

Integrating over $\phi \in [0, 2\pi]$ and $\cos\theta \in [-1, 1]$, it becomes

$$\bar{V}(u) = \frac{q}{(2\pi)^2} \int_0^{+\infty} \exp\left(-\frac{r}{l}\right) \frac{1}{iur^2} \left[\exp(-iur) - \exp(iur)\right] r^2 dr \tag{3.14}$$

$$= -\frac{q}{(2\pi^2)} \int_0^{+\infty} \exp\left(-\frac{r}{l}\right) \frac{\sin ur}{u} dr \tag{3.15}$$

$$= -\frac{q}{(2\pi^2)} \frac{l^2}{u^2 l^2 + 1} \tag{3.16}$$

For a potential expression of the form $V(r) = \sum_i q_i e^{-r/l_i}$, l_i and q_i being the i-th respective screening radius and charge factor, the Fourier transform becomes

$$\bar{V}(u) = \frac{1}{2\pi^2} \sum_{i=1}^{N} q_i \frac{l_i^2}{l_i^2 u^2 + 1} \tag{3.17}$$

Injecting Eq. 3.16 in Eq. 3.10, the non-relativistic, screening cross section reads

$$\frac{d\sigma^{NR-WY}}{d\gamma_\gamma} = \frac{16 r_e^2 Z^2 \alpha_f}{3\gamma_\gamma p_{e,i}^2} g(k_m, k_p, q, l) \tag{3.18}$$

where the integration over $[k_m, k_p]$ gives

$$g(k_m, k_p, q, l) = \frac{q^2}{2} \left[\ln \frac{k_p^2 l^2 + 1}{k_m^2 l^2 + 1} + \frac{1}{k_p^2 l^2 + 1} - \frac{1}{k_m^2 l^2 + 1}\right] \tag{3.19}$$

In a plasma, we propose to use Eq. 3.6 in order to calculate the non-relativistic Bremsstrahlung cross-section including both the Wentzel-Yukawa potential and the Debye screening effects (Rozsnyai (1979)):

$$\frac{d\sigma^{NR-WYD}}{d\gamma_\gamma} = \frac{16 r_e^2 Z^2 \alpha_f}{3\gamma_\gamma p^2} \left(g(k_m, k_p, q, l) + g(k_m, k_p, q_d, l_d) + \Gamma_c \right) \tag{3.20}$$

where $q = (1 - Z^*/Z)$, $q_d = Z^*/Z$ and Γ_c is a coupling term so that

$$\Gamma_c = \frac{q q_d}{l_d^2 - l^2} \left(l^2 \ln \frac{k_m^2 l_d^2 + 1}{k_p^2 l_d^2 + 1} + l_d^2 \ln \frac{k_p^2 l^2 + 1}{k_m^2 l^2 + 1} \right) \tag{3.21}$$

When $l_d \to \infty$, the function $g(k_m, k_p, q_d, l_d)$ becomes

$$g(k_m, k_p, q_d, l_d) \to q^2 \ln \frac{k_p}{k_m} \tag{3.22}$$

and the coupling term Γ_c becomes

$$\Gamma_c \to q(1 - q) \ln \frac{k_m^2 l^2 + 1}{k_p^2 l^2 + 1} \tag{3.23}$$

An alternative potential has been proposed by Avdonina and Pratt (1993); Lamoureux and Avdonina (1997). The corresponding cross-section ($d\sigma_{\gamma_\gamma}^{NR-LA}$) is the solution of the following screening potential

$$V(r) = \frac{Ze}{r} \left(\frac{Z^*}{Z} - (1 - \frac{Z^*}{Z}) \exp(-r/l) \right). \tag{3.24}$$

Far from the nucleus, the potential tends to a pure Coulomb potential of interaction between the free electron and the ion. In these references, the authors have used a different screening radius approximated from the Hartree-Fock-Slater atomic potential. They have calculated numerically the coefficient obtained from the second order expansion of the ionic potential 3.24 Bunaciu *et al.* (1980), using the numerical result of the Hartree-Fock-Slater potential, to obtain the following numerical fit

$$l_{LA} = r_b \sqrt{\frac{1 - Z^*/Z}{0.798 Z \left(1 - (Z^*/Z)^\alpha\right)}} \qquad \alpha = Z\,(1/3 - 0.002Z) + 1 \tag{3.25}$$

giving a fairly good approximation of the potential in the inner region of the ion.

In the unscreened case, $l \to +\infty$, the non-relativistic cross section differential in photon energy simplifies and is given as formula 3BN(a) in Koch and Motz (1959).

In the high-energy transfer limit, a multiplicative Coulomb correction factor has been obtained by Elwert by comparison of the non-relativistic Sommerfield calculation with the non-relativistic born approximation. This factor improves the cross-section when the emitted photon energy approaches the initial electron kinetic energy

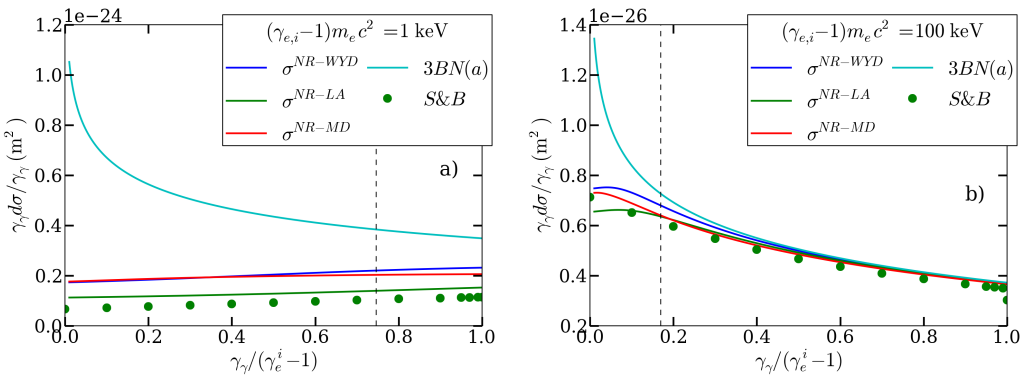

Figure 3.3: Comparison of the non-relativistic cross-sections $\gamma d\sigma_{\gamma\gamma}^{NR-WYD}$, $\gamma d\sigma_{\gamma\gamma}^{NR-LA}$, $\gamma_\gamma d\sigma_{\gamma\gamma}^{NR-MD}$, the non-screened formula 3BN(a) from Koch and Motz (1959) and the numerical fits of Seltzer and Berger (1986) for two electron energies 1 keV (a) and 100 keV (b). The dashed line corresponds to parameter $\Gamma = 2$.

$(\gamma_\gamma/(\gamma_{e,i}-1) \to 1)$. The finite value of the spectrum tends to zero otherwise. The Elwert factor depends on the incident and scattered electron velocities $\beta_{e,i}$ and $\beta_{e,s}$:

$$f_E = \frac{\beta_{e,i}\,(1-\exp-(2\pi Z\alpha_f/\beta_{e,i}))}{\beta_{e,s}\,(1-\exp-(2\pi Z\alpha_f/\beta_{e,s}))}. \tag{3.26}$$

Although it is strictly valid if $(\alpha_f Z)(\beta_{e,s}^{-1}-\beta_{e,i}^{-1}) \ll 1$, the correction can be used in the whole non-relativistic energy range in good agreement with the numerically computed cross sections. Nonetheless, the Elwert correction is mathematically divergent when $\gamma_\gamma \to (\gamma_{e,i}-1)$.

The different cross-sections analyzed in this section are compared in Figures 3.3 for silver and initial electron energies of 1 keV and 100 keV. The analytic solution given in Lamoureux and Avdonina (1997) and our solution $\sigma_{\gamma\gamma}^{NR-WYD}$ are presented. Here, the matter is assumed neutral, and as a consequence, the Debye screening plays no role. The non-relativistic cross section with the Molière screening potential, $d\sigma_{\gamma\gamma}^{NR-MD}$, is obtained by numerical integration. The comparison is made with the numerical values tabulated by Seltzer and Berger (1986) using the results of Lee *et al.* (1976). The solution without screening, labeled 3BN(a) in Koch and Motz (1959), is also plotted. The figures show that the analytic cross-sections, $\sigma_{\gamma\gamma}^{NR-WYD}$ and $\sigma_{\gamma\gamma}^{NR-LA}$, and the numerical one $\sigma_{\gamma\gamma}^{NR-MD}$ have the same behaviors and relatively close values for electron energies from 1 keV to 2 MeV. The comparison between $\sigma_{\gamma\gamma}^{NR-WYD}$ and the numerical values of Seltzer and Berger (1986) for γ_e between 1 keV and 2 MeV gives an average relative error of 35% (with maximum of 160% for electron kinetic energy of 1 keV and minimum of 0.4% for 1 MeV).

The ionization effects on the cross-section $d\sigma_{\gamma\gamma}^{NR-WYD}$ are illustrated in figures 3.4. As for the previous figures, initial electron energies of 1 keV and 100 keV are

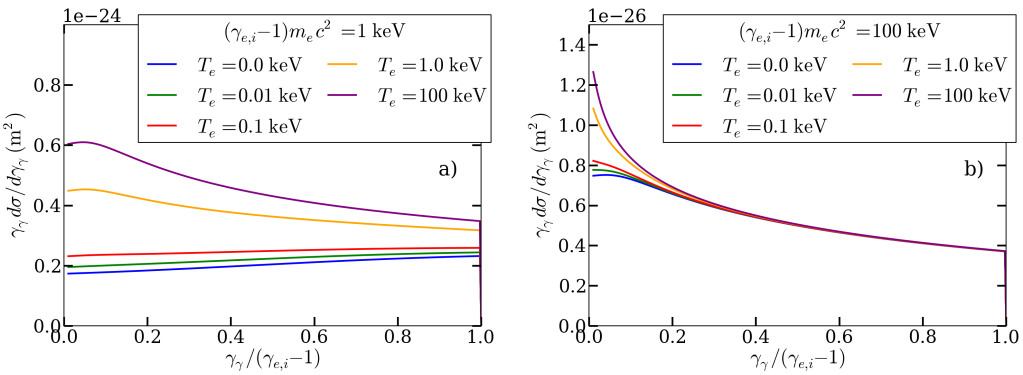

Figure 3.4: Cross-section $d\sigma_{\gamma_\gamma}^{NR-WYD}$ including the effect of the Debye screening for different plasma temperatures (and consequently different degrees of ionization) for two initial electron energies 1 keV (a) and 100 keV (b) in silver.

considered, for plasma temperatures ranging from 0.01 keV to 100 keV. Overall, the cross sections increase with the plasma temperature. The blue curves correspond to the neutral case ($Z^* = 0$, with vanishing Debye screening). As predicted by Figure 3.2, the Debye screening appears more significant for small electron kinetic energies and weak emitted photon energy. At 1 keV, the cross-section are well distinguishable whatever the emitted photon energy. At 100 keV, they are similar for strong photon emission $\gamma_\gamma/(\gamma_{e,i}-1) > 0.5$.

3.2.2 Relativistic case

In the Born approximation, the Bremsstrahlung relativistic cross-section differential in energy for arbitrary screening can be written (Davies *et al.* (1954); Koch and Motz (1959)) as

$$\frac{d\sigma}{d\gamma_\gamma} = \frac{4Z^2 r_e^2 \alpha_f}{\gamma_\gamma}\left[\left(1+\left(\frac{\gamma_{e,s}}{\gamma_{e,i}}\right)^2\right)(I_1+1) - \left(\frac{2}{3}\frac{\gamma_{e,s}}{\gamma_{e,i}}\right)\left(I_2+\frac{5}{6}\right)\right] \quad (3.27)$$

$$I_1 = \int_\delta^1 (u-\delta)^2 \frac{(1-F(u))^2}{u^3} du \quad (3.28)$$

$$I_2 = \int_\delta^1 \left(u^3 - 6\delta^2 u \ln\frac{u}{\delta} + 3\delta^2 u - 4\delta^3\right)\left(\frac{1-F(u,Z)}{u^2}\right)^2 du \quad (3.29)$$

where $\delta = \gamma_\gamma/(2\gamma_{e,i}\gamma_{e,s})$ is the minimum momentum transfer to the nucleus and $F(Z,u)$ the bound electron form factor. The potential is related to the form factor

according to

$$\bar{V}(u) = \frac{1}{(2\pi)^3}\int_\Omega V(\mathbf{r})\exp(i\mathbf{ur})d^3\mathbf{r} \quad (3.30)$$

$$= \frac{-1}{(2\pi)^3 u^2}\int_\Omega \nabla^2 V(\mathbf{r})\exp(i\mathbf{ur})d^3\mathbf{r}. \quad (3.31)$$

Using the Poisson equation,

$$= \frac{Z}{(2\pi)^3}\frac{F_n - F_e}{u^2} \quad (3.32)$$

where F_n is the nucleus form factor.

$$F_n = \frac{1}{Z}\int_\Omega 4\pi\rho_n \exp(i\mathbf{ur})d^3\mathbf{r} \quad (3.33)$$

The nucleus can be considered as a punctual charge,

$$F_n = \int_\Omega 4\pi e\delta(r)\exp(i\mathbf{ur})d^3\mathbf{r} \sim 1 \quad (3.34)$$

Using the Wentzel-Yukawa potential with a screening length l, we have

$$\frac{(1-F_e)}{u^2} = \frac{l^2}{u^2 l^2 + 1} \quad (3.35)$$

When $\Gamma \gg 1$, the Coulomb screening is small and consequently $F_e(q, Z) \to 0$.

As for the non-relativistic case, the relativistic screening cross-section using the Wentzel-Yukawa potential has an exact solution.

$$I_1 = q^2\left(l\delta\arctan(l\delta) + \frac{1}{2}\ln\frac{1+l^2}{1+l^2\delta^2} - l\delta\arctan l - \frac{l^2}{2}\frac{(1-\delta^2)^2}{1+l^2}\right) \quad (3.36)$$

$$\frac{2}{q^2}I_2 = 4l^3\delta^3\arctan(l\delta) + \left(1+3l^2\delta^2\right)\ln\left(\frac{1+l^2}{1+l^2\delta^2}\right) + \frac{6l^4\delta^2}{1+l^2}\ln\delta - 4l^3\delta^3\arctan l + \frac{l^2(\delta^2-1)(\delta+1-4l^2\delta^2)}{1+l^2} \quad (3.37)$$

If I_2 mathematically has a finite limit when $\delta \to 0$,

$$I_2 = \frac{1}{2}\frac{q^2}{1+l^2}\left(\left(1+l^2\right)\ln 1 + l^2 - l^2\right). \quad (3.38)$$

The term $6l^4\delta^2\ln(\delta)$ poses a numerical problem. A straightforward solution consists in testing the condition $6l^4\delta^2 < \epsilon$ where ϵ is chosen so that the logarithm term

contributes negligibly to the full cross section. One can also determine an ϵ so that $\delta > \epsilon$ implies that $6l^4\delta^2 \ln(\delta)$ has not reached the floating-point limit.

The cross section is not integrable when using series of exponential potential, particularly when including the Debye screening (Eq. 3.6), due to the term $\ln(x/\delta)$ in I_2. In the following, we propose an alternative approximate method in order to reduce the double exponential expression, Eq. 3.6, to an effective single-exponential form

$$V_r = \frac{q_r}{r} \exp(-r/l_r) \tag{3.39}$$

where q_r is the effective charge, and l_r the effective screening distance. The idea is to make the double and the single exponential formulae match in the limit $\delta \to 0$ ($\gamma_e \gg 1$), in which one has

$$I = \lim_{\delta\to 0} I_1 = \lim_{\delta\to 0} I_2 = \int_0^1 u^3 \left(\frac{1 - F(u,Z)}{u^2}\right)^2 du. \tag{3.40}$$

The latter expression has an analytic solution for the Wentzel-Yukawa-Debye potential (Eq. 3.6). The reduced parameter l_r is determined by solving the equation

$$\frac{d\sigma_{WYD}}{d\gamma_\gamma}(\delta = 0) = \frac{d\sigma_r}{d\gamma_\gamma}(\delta = 0), \tag{3.41}$$

where $\frac{d\sigma_r}{d\gamma_\gamma}$ is the energy-differential cross section with the reduced potential V_r. The reduced solution is therefore ensured to work in the low photon energy limit. We define I_{WYD} the limiting form of I_1 and I_2 using the Wentzel-Yukawa-Debye potential (Eq. 3.6)

$$I_{WYD}(Z, Z^*, l_{TF}, l_D) = \frac{1}{2}\frac{q^2\left(-l^2 + \ln(1+l^2) + \ln(1+l^2)\, l^2\right)}{1+l^2} \tag{3.42}$$

$$+\frac{1}{2}\frac{{q_D}^2\left(-l^2 + \ln\left(1+{l_D}^2\right) + \ln\left(1+{l_D}^2\right){l_D}^2\right)}{1+{l_D}^2} \tag{3.43}$$

$$\frac{q\, q_D\, \left({l_D}^2 \ln(1+l^2) - l^2 \ln\left({l_D}^2+1\right)\right)}{-l^2+{l_D}^2} \tag{3.44}$$

Here, q_{TF} and q_D refer to the normalized charges respectively associated with the Thomas-Fermi and the Debye potentials. Thus, Eq. 3.41 is equivalent to

$$I_{WYD}(Z, Z^*, l_{TF}, l_D) = \frac{1}{2}\frac{q_r^2\left(\ln(1+l_r^2)\,(1+l_r^2) - l_r^2\right)}{l_r^2+1} \tag{3.45}$$

where the right side is the result of the integration of Eq. 3.40 with the reduced single-exponential potential. Setting $a = 2I_{WYD}/q_r^2$, with $q_r = Ze$ and $x = l_r^2$, the above equation becomes

$$a(x+1) = \ln(x+1)(x+1) - x \tag{3.46}$$

The solution x_s can be written as

$$x_s = \exp\left(W_0\left(-\exp -1 - 2a\right) + 1 + 2a\right) - 1 \tag{3.47}$$

where W_0 is the Lambert function. Because the coefficient a is positive, W_0 is well defined on $[-1/e, 0]$ and x is positive. The sought for effective screening distance is therefore equal to $l_r = \sqrt{x_s}$.

The energy differential cross sections using the reduced potential V_r, the Wentzel-Yukawa $d\sigma_{\gamma_\gamma}^{RE-WYD}$, the Molière potential and the numerical results of Seltzer and Berger (1986) are plotted in Fig. 3.5 for electron energies of 5 and 40 MeV in neutral silver. Both the Wentzel-Yukawa and the Molière curves are obtained by Gauss-Legendre numerical integration. In general, the different cross-sections are in good agreement with the data of Seltzer and Berger (1986). Without ionization effects, $l_r = l_{WY}$, $d\sigma_{\gamma_\gamma}^{WYD}$ and $d\sigma_{\gamma_\gamma}^{r}$ are therefore similar (well confirmed by the curves). For electron energies close to 2 MeV, the results of Seltzer and Berger are well reproduced by the Molière potential, particularly for photon energies below $0.6(\gamma_{e,i} - 1)$. In the high energy tail of the spectrum ($\gamma_\gamma \to 1$), the different cross-sections tend to converge, but somewhat differ from the Seltzer and Berger values.

For electron energies above the threshold of 2 MeV, as the electron energy increases, the Bremsstrahlung cross-sections remain similar in the low-energy part of the spectrum ($\gamma_\gamma/(\gamma_{e,i} - 1) < 0.5$) whereas they grow in the high-energy part ($\gamma_\gamma/(\gamma_{e,i} - 1) > 0.5$). For an energy of 40 MeV, the maximum around 2.8×10^{-27} m^2 for $\gamma_\gamma/(\gamma_{e,i} - 1) \to 0$ is similar to the lower electron energy. The intermediate photon energy region $0.2 \leq \gamma_\gamma/(\gamma_{e,i} - 1) \geq 0.8$ however increases. A slightly decreasing plateau appears followed by an abrupt decrease for $\gamma_\gamma/(\gamma_{e,i} - 1) \to 1$. The screening threshold $\Gamma = 1$ moves to the high-frequency part of the spectrum (only the low-frequency emission is therefore affected by the Coulomb screening). The relative error between Seltzer and Berger and the reduced model has an average value of 40 % for a maximum of 150 % (near the threshold $\gamma_\gamma/\left(\gamma_{e,i} - 1\right) = 1$) and a minimum of 0.6 % for an electron energy between 2 and 50 MeV.

The influence of the Debye screening on the relativistic cross-section $d\sigma_\gamma^{RE-r}$ and $d\sigma_\gamma^{RE-WYD}$ (obtained by numerical integration) is shown in Fig. 3.6 for different plasma temperatures in silver for initial electron energy 5 and 40 MeV. As expected in Fig. 3.2, the cross-section is mainly affected by the Debye screening for relatively low photon energies. Close to $\varepsilon_e \sim 1$ MeV, screening effects are minimum, therefore, the Debye screening is more significant as the electron energy increases. The reduced potential shows good agreements with the numerical evaluation of $d\sigma_\gamma^{RE-WYD}$. The relative error, computed for electron energies between 2 MeV and 50 MeV, a plasma temperature T between 0.01,and 100 keV and a photon energy exceeding 1 keV has an average value of 0.05 %, with a maximum of 6 % for $T_e \sim 0.17$ keV. When $\delta \to 0$ (corresponding to $\gamma_\gamma \to 0$) the cross-section $d\sigma_\gamma^{RE-r}$ closely matches $d\sigma_\gamma^{RE-WYD}$.

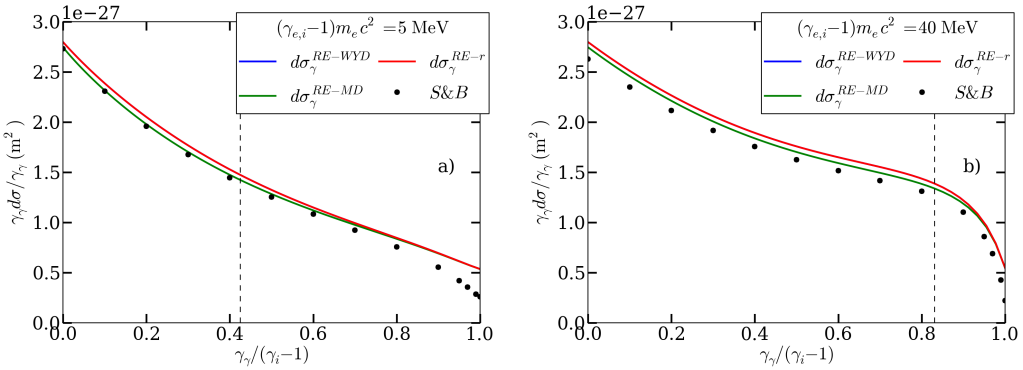

Figure 3.5: Comparison of the relativistic cross-sections $\gamma d\sigma_{\gamma\gamma}^{RE-WYD}$, $\gamma d\sigma_{\gamma\gamma}^{RE-MD}$, $\gamma d\sigma_{\gamma\gamma}^{RE-r}$ and the numerical fits of Seltzer and Berger (1986) for incident electron energies 5 MeV (a) and 40 MeV (b). The dashed line corresponds to screening parameter $\Gamma = 1$.

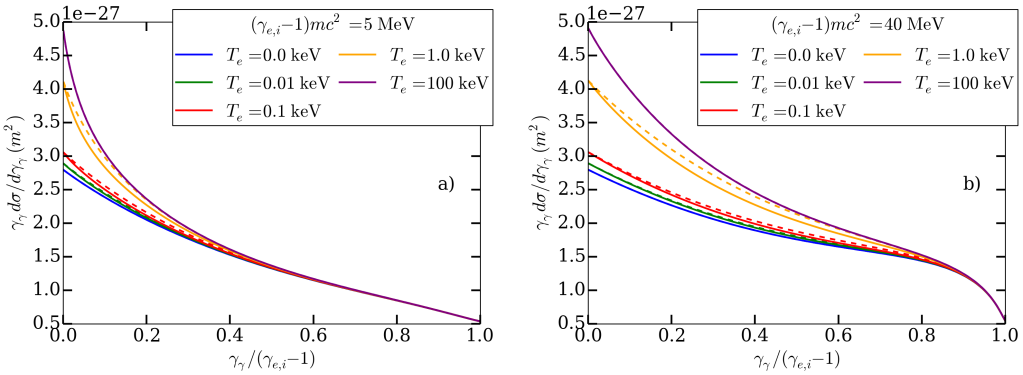

Figure 3.6: Cross section $\gamma d\sigma_{\gamma\gamma}^{RE-WYD}$ (solid line) and $\gamma d\sigma_{\gamma\gamma}^{RE-r}$ (dashed line) for different plasma temperatures (and consequently different degrees of ionization) for two initial electron energies 5 MeV (a) and 40 MeV (b) in silver.

3.2.3 Ultra-relativistic case

In the ultra-relativistic case (referred to as UR for the cross section, $\gamma \gg 1$), the energy-differential cross section in the Born approximation consists of adding a Coulomb correction

$$C = \frac{4Z^2 r_e^2 \alpha_f}{\gamma_\gamma} \left[\left(1 + \left(\frac{\gamma_{e,s}}{\gamma_{e,i}} \right)^2 \right) - \left(\frac{2}{3} \frac{\gamma_{e,s}}{\gamma_{e,i}} \right) \right] f(Z) \tag{3.48}$$

to the relativistic formula. With arbitrary screening, it can be written as

$$\frac{d\sigma}{d\gamma_\gamma} = \frac{4Z^2 r_e^2 \alpha_f}{\gamma_\gamma}\left[\left(1+\left(\frac{\gamma_{e,s}}{\gamma_{e,i}}\right)^2\right)(I_1+1+f)-\left(\frac{2}{3}\frac{\gamma_{e,s}}{\gamma_{e,i}}\right)\left(I_2+\frac{5}{6}+f\right)\right] \quad (3.49)$$

where I_1 and I_2 are defined is in Eqs. 3.36 and 3.37. The function f is defined as (Davies *et al.* (1954))

$$f(Z) = \sum_{i=1}^{n} \frac{(\alpha Z)^2}{i(i^2+(\alpha Z)^2)} \quad (3.50)$$

The sum can be conveniently evaluated as

$$f(Z) = \frac{a^2}{1+a^2}\sum_{i=1}^{n}(-a^2)^n\left(\zeta(2n+1)-1\right) \quad (3.51)$$

where ζ is the Riemann function. An expansion to order $n = 4$ is sufficient to get a good approximation until $Z \leq 235$.

The results obtained for the moderately relativistic cross sections are therefore still valid in the ultra-relativistic regime when taking into account the Coulomb correction. Here, σ_γ^{UR-r}, σ_γ^{UR-WYD} and σ_γ^{UR-MD} refer to the energy-differential cross section using respectively the reduced potential V_r, the Wentzel-yukawa-Debye potential (Eq. 3.6) and the Molièrere potential (Eq. 3.4).

Figure 3.7 compares the cross sections σ_γ^{UR-r}, σ_γ^{UR-WYD}, σ_γ^{UR-MD} and the numerical results of Seltzer and Berger in neutral silver and for initial electron energies of 100 and 500 MeV. As described in the previous sections, the high-energy cross sections increase with the initial electron energy while the low energy cross sections remain constant at around 2.7×10^{-27} m^2. The cross-section σ_γ^{UR-r} is in overall good agreement with the Seltzer and Berger results. The relative error has an average value of 0.16, a maximum of 1.5 (near the threshold of $\gamma_\gamma/(\gamma_{e,i}-1)=1$ for $\varepsilon_{e,i}\sim$ 500 MeV) and a minimum of 0.07 (near $\gamma_\gamma/(\gamma_{e,i}-1)\to 0$, for $\varepsilon_{e,i}\sim 80$ MeV) for an electron energy between 50 and 500 MeV.

The comparison of σ_γ^{UR-WYD} and σ_γ^{UR-r} as a function of the plasma temperature is shown in Fig. 3.8 for $T\in[0.01,100]$ keV. As expected from Fig. 3.2, the effects of the Debye screening effect impact the cross-section for $\gamma_\gamma/(\gamma_i-1)\leq 0.9$. The cross-sections with the reduced and the Wentzel-Yukawa-Debye potentials exhibit very close results. The relative error between these two cross-sections, calculated for a temperature between 0.01 and 100 keV, for an electron energy between 50 and 500 MeV and for a photon energy above 1 keV, is in average of 10^{-3} with a maximum of 7×10^{-2}.

3.2.4 Cross section gathering

In order to get tabulated values of the energy-differential cross sections valid for any electron energy taking into account both the Coulomb and the Debye screening, we

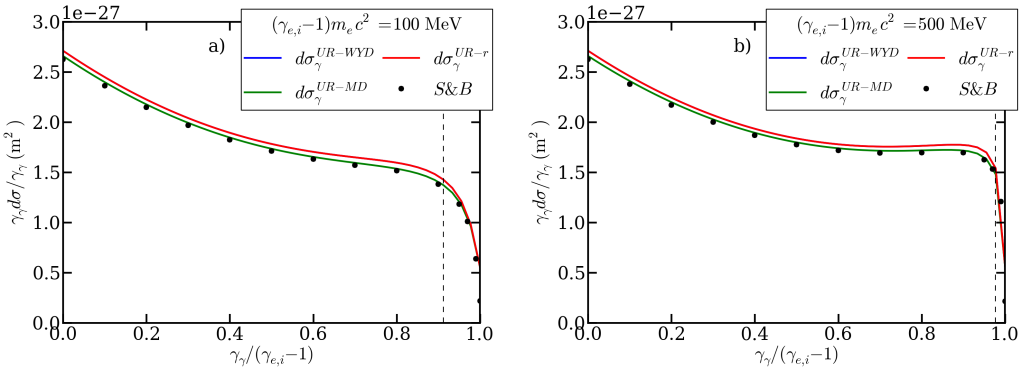

Figure 3.7: Comparison of the cross-sections in the ultra-relativistic regime $\gamma d\sigma_{\gamma_\gamma}^{UR-WYD}$, $\gamma d\sigma_{\gamma_\gamma}^{UR-MD}$, $\gamma d\sigma_{\gamma_\gamma}^{UR-r}$ and the tabulated data of Seltzer and Berger (1986) for incident electron energies 100 MeV (a) and 500 MeV (b). The dashed line corresponds to screening parameter $\Gamma = 1$.

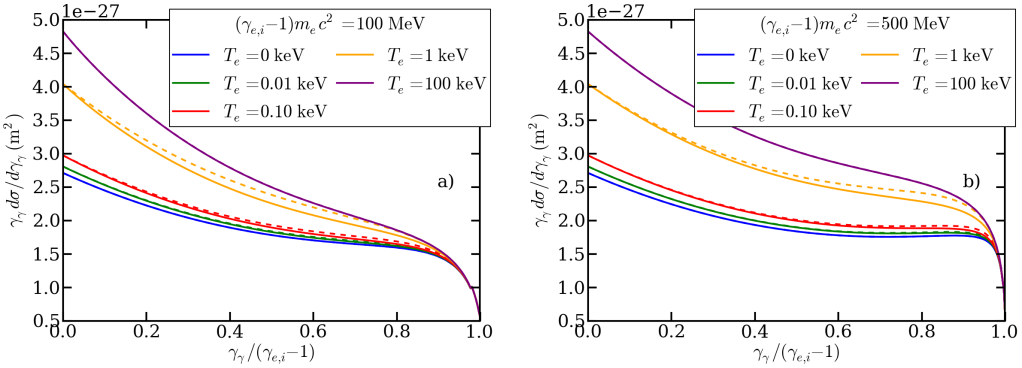

Figure 3.8: Cross sections $\gamma d\sigma_{\gamma_\gamma}^{UR-WYD}$ (solid line) and $\gamma d\sigma_{\gamma_\gamma}^{UR-r}$ (dashed line) for different plasma temperatures (and consequently different degrees of ionization) for two initial electron energies 100 MeV (a) and 500 MeV (b) in silver.

build a composite cross-section $d\sigma_\gamma$ resulting from the merging of the previous results from the non-relativistic case to the ultra-relativistic regime.

$$\frac{d\sigma^{BR}}{d\gamma} = \begin{cases} d\sigma_\gamma^{NR-WYD} & \gamma_i \leq 2 \\ d\sigma_\gamma^{RE-r} & 2 < \gamma_i \leq 100 \\ d\sigma_\gamma^{UR-r} & \gamma_i \end{cases} \tag{3.52}$$

A summary of the previous results and discussions is presented in Figs. 3.9. It clearly shows that the energy cross section is maximum for low electron energy. The cross-section is minimized for an average electron energy between 1 and 10 MeV and

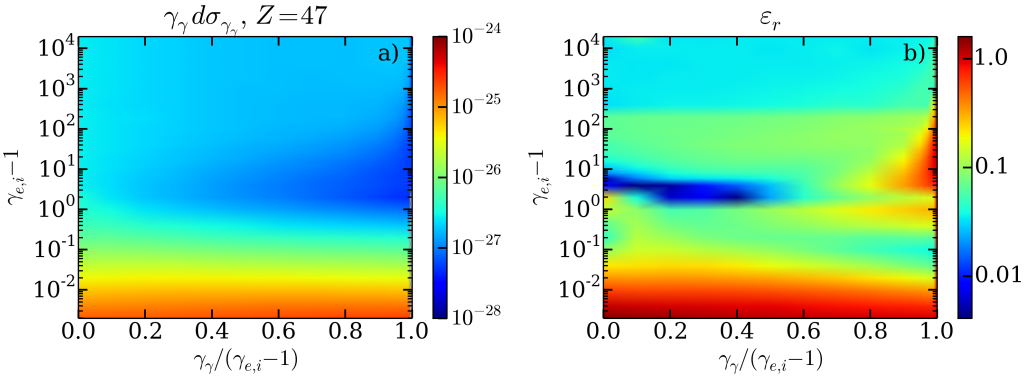

Figure 3.9: (a) - Cross-section $\gamma d\sigma_\gamma$ as a function of the initial electron kinetic energy and the emitted photon energy γ_γ in neutral silver. (b) - Relative error ε_r between $\gamma d\sigma_\gamma$ and the Seltzer and Berger data.

a photon energy close to the electron kinetic energy.

The relative error, $\varepsilon_r = |d\sigma^{S\&B} - d\sigma^{BR-r}|/d\sigma^{S\&B}$, between the results of Seltzer and our global function is shown in Fig. 3.9b. Again, we can see that the difference is highest, up to 100%, in the non-relativistic regime. An important difference exists in the region where the cross-section is minimized, nonetheless the general behavior is the same for the two cases.

Our global reduced model for a plasma temperature of 1 keV is also shown in Fig. 3.10. From comparison with Fig. 3.9a, the temperature is seen to globally increase the cross-section. This increase is more pronounced in the non-relativistic and the ultra-relativistic cases and for relatively low photon energies ($\gamma_\gamma/(\gamma_{e,i}-1)$ close to 0.). Nonetheless, the cross-section is not modified by more than an order of magnitude. The maximum error between the global reduced model $d\sigma_\gamma^{BR-r}$ and the numerically evaluated Wentzel-Yukawa-Debye cross sections $d\sigma_\gamma^{BR-WYD}$ attains $\sim 5 \times 10^{-2}$ in the ultra-relativistic regime for a plasma of temperature $T_e \sim 1$ keV.

3.3 Bremsstrahlung integrated quantities

3.3.1 Total Bremsstrahlung cross sections

The radiative cross section is defined as

$$\Phi = \int_0^{\gamma_{e,i}-1} \gamma_\gamma \frac{d\sigma}{d\gamma} d\gamma \tag{3.53}$$

and the total cross section as

$$\Phi = \int_0^{\gamma_{e,i}-1} \frac{d\sigma}{d\gamma} d\gamma \tag{3.54}$$

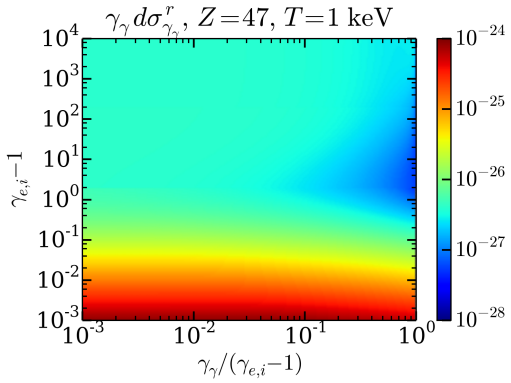

Figure 3.10: Cross-section $\gamma d\sigma_\gamma$ in silver at a temperature of 1 keV.

Both quantities are presented in Fig. 3.11 and Fig. 3.12 in neutral silver. They are obtained from numerical integration of the energy-differential cross sections. As the latter diverges for $\gamma_\gamma \to 0$, we have to suppose a minimum threshold $\gamma_{\gamma,\min}$ so that the energy radiated below this limit is negligible:

$$\frac{\Phi(\gamma_{e,i}) - \int_{\gamma_{\gamma,\min}}^{\gamma_{e,i}-1} \frac{\gamma d\sigma^r}{d\gamma} d\gamma}{\Phi(\gamma_{e,i})} \ll 1 \tag{3.55}$$

The discontinuities visible in Figs. 3.11 and 3.12 and shown by the dashed red lines correspond to the boundaries of the different energy domains involved in Eq. 3.52. These discontinuities can be flattened using smoothing functions without affecting the behaviors and the average values of the cross sections.

The total cross sections are maximized in the non-relativistic regime with a two orders of magnitude decrease between $\gamma_{e,i}-1 = 10^{-3}$ and 10, and a plateau, at higher energies. The probability for photon emission during a Bremsstrahlung emission is therefore the most significant in this part. The radiated power is directly proportional to the radiation cross-section. As a consequence, Fig. 3.11 shows that despite a lower probability for photon emission, the higher is the electron energy, the higher is the total radiated energy (because the average photon energy will be higher).

3.3.2 Optical depth and estimations

The optical depth, i.e. the typical distance to photon emission, can be simply estimated using the total cross section

$$L_{Br} = (\sigma_{Br} n_\alpha)^{-1} \tag{3.56}$$

where n_α is the material atomic density. The optical depth is shown in Fig. 3.13 for

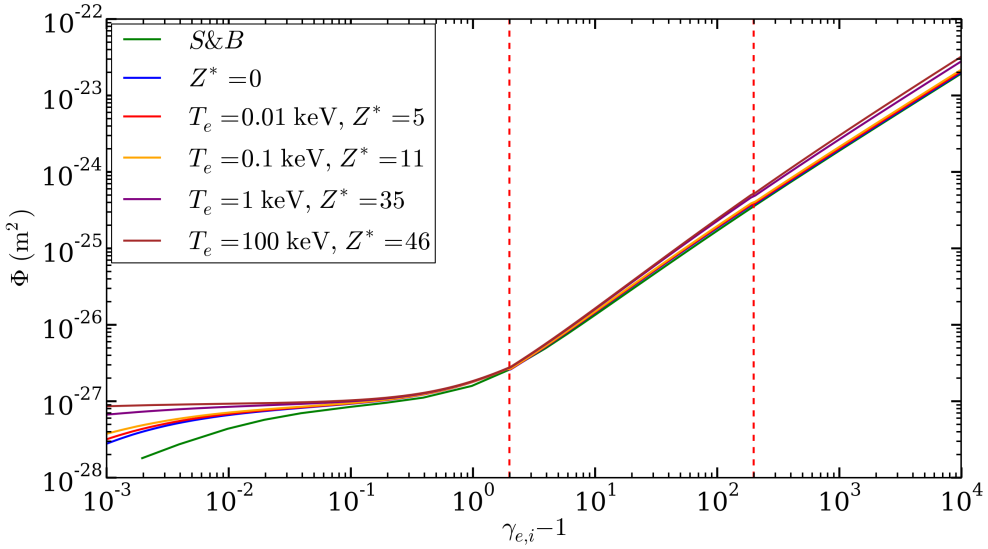

Figure 3.11: Radiative cross section Φ^{BR-r} in silver as a function of the normalized electron kinetic energy $\gamma_{e,i} - 1$ and the electron temperature T_e. The Seltzer and Berger (S&B) data are plotted in green.

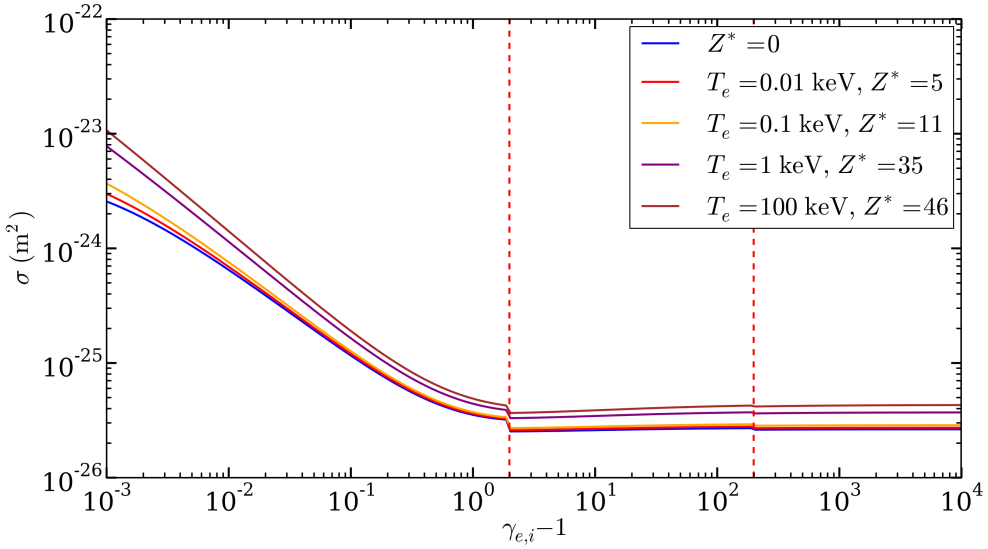

Figure 3.12: Total Bremsstrahlung cross section in silver as a function of the normalized electron kinetic energy $\gamma_{e,i} - 1$ and the electron temperature T_e.

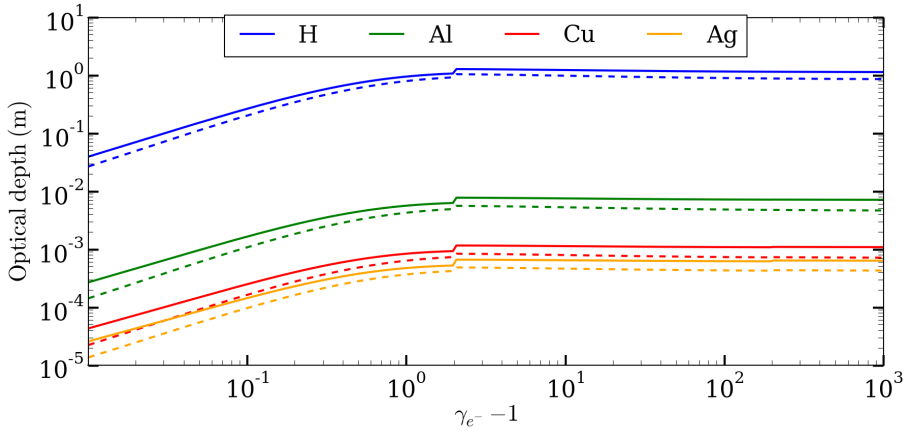

Figure 3.13: Distance (Optical depth) in m to photon emission for hydrogen (H), aluminium (Al), copper (Cu) and silver (Ag) depending on the normalized electron initial kinetic energy.

Material	H	Al	Cu	Ag
Z	1	13	29	47
density (kg.m$^-$3)	0.09	2.7	8.96	10.50
particle density ($\times 10^{27}$m$^-$3)	54	60	85	59

Figure 3.14: Properties of the materials considered in Fig. 3.13.

various materials and electron energies described in tab. 3.14. As expected, from the evolution of the silver cross-section in Fig. 3.12, the optical depth increases with the initial electron kinetic energy. Since the cross section saturates for highly relativistic electrons ($\gamma_{e^-} \gg 1$), the optical depth also stabilizes for high energies. Even if the screening distances are different in each material, the behavior of the optical depth as a function of the initial electron energy is approximately the same for each of them. The cross-section depends on the atomic number Z^2 and the particle density depends on the inverse of the atomic mass m_A also related to the atomic number. Consequently, the optical depth $L_{Br} \propto \frac{m_A}{Z^2 \rho N_A}$ well diminishes proportionally as the Z increases and the material becomes heavier. In order to get an efficient emission of high-frequency radiation via the Bremsstrahlung, mm to cm high-Z targets are usually considered experimentally which is consistent with the optical depth obtained in Fig. 3.13.

Chapter 4

Pair production in a strong field

4.1 Presentation of the different mechanisms

The production of electron-positron pairs in the collision of two photons ($\gamma + \gamma \rightarrow e^- + e^+$), and its inverse process, namely the two-photon pair annihilation ($e^- + e^+ \rightarrow \gamma + \gamma$), were first described by Dirac (1930) and Breit and Wheeler (1934). Although the so-called photon-photon Breit-wheeler process was one of the first processes of positron creation discovered, its experimental validation has yet to be performed. Indeed, this mechanism is theoretically characterized by a very weak probability and requires an extremely bright and collimated source of γ-photons to obtain a significant number of pairs. In many configurations, this mechanism is dominated by other more efficient pair creation processes. Recently, an experimental setup has been proposed on megajoule facilities such as the NIF and the LMJ to test this process. It consists first in the generation of a directed and bright Bremsstrahlung source of γ-photon via the irradiation of a thin foil by an intense laser. The photons are then directed into a bath of x-rays created inside an irradiated hohlraum. The authors have estimated a production of 10^4 pairs per shot (Pike *et al.* (2014); Thomas (2014)).

The nonlinear Breit-Wheeler ($\gamma + n\omega_0 \rightarrow e^- + e^+$), also referred to as the multi-photon Breit-Wheeler, corresponds to the decay of a high-energy photon interacting with a strong electromagnetic field. This physical process has been observed experimentally using the SLAC 47 GeV electron beam made to collide with a terawatt laser pulse ((Burke *et al.*, 1997; Bamber *et al.*, 1999)). The most favorable scenario consists in the collision of high-energy electrons with a counter-propagating laser wave. Electrons first radiate γ-photons via nonlinear Compton scattering (see chapter 2), which subsequently decay into pairs via the nonlinear Breit-Wheeler process. With present laser technologies, the electron beam needs an energy of several tens of GeV to lead to viable and sufficient pair creation.

Pair generation in a strong external field may also stem from the electromagnetic Trident process through which a pair is directly generated from a high-energy

deflected electron ($e^- + n\omega_0 \rightarrow e^- + e^- + e^+$). It can be seen as the combination of the nonlinear Compton emission and the nonlinear Breit-Wheeler in a single process. The nonlinear Breit-Wheeler, represented in terms of Feynman diagrams in Fig. 4.2, is a first order process in the fine structure constant α_f whereas the Trident is a second order process $\propto \alpha_f^2$. The pairs of electron-positron can also annihilate into one or several photons. The most probable is the two-photon annihilation ($e^- + e^+ \rightarrow \gamma_1 + \gamma_2$).

In this Chapter, we present the cross-section and some numerical calculations of the previously described mechanisms of electron-positron pair creation in a strong field. The electron-positron pair annihilation is also studied in the last part.

4.2 The photon-photon Breit-Wheeler process

The first proposed mechanism of pair creation from the collision of two photons was the Breit-Wheeler process. We consider two photons of respective normalized energies $\gamma_{\gamma,1}$ and $\gamma_{\gamma,2}$ colliding at an angle α as described in Fig. 4.1. Pair creation is possible only if in the center of mass frame, the total energy provided by the photons is twice the rest mass energy of an electron. In the center-of-mass frame of the system we have $p^*_{e^+} + p^*_{e^-} = \hbar\left(k^*_1 + k^*_2\right)$ where $p^*_{e^+}$ and $p^*_{e^-}$ are the particle momenta and k^*_1, k^*_2 the photon wave vectors. In this frame of reference, the photon energies are equal $\gamma^*_{\gamma,1} = \gamma^*_{\gamma,2}$ and their momenta equal and opposite $k^*_1 = -k^*_2$ so that the particle momenta respect the similar properties $p_{e^+} = -p_{e^-}$ and $\gamma_{e^+} = \gamma_{e^-}$. The cross section for pair production σ_{ppbw} can be written (Nikishov (1964); Gould and Schréder (1967); Jauch and Rohrlich (1955); Ruffini *et al.* (2010))

$$\sigma^*_{ppbw} = \pi \frac{r_e^2}{\gamma^{*2}} \left[2\beta^* \left(\beta^{*2} - 2\right) + \left(3 - \beta^{*4}\right) \ln\left(\frac{1+\beta^*}{1-\beta^*}\right) \right] \tag{4.1}$$

where $\beta^* = \frac{|p^*|}{\gamma^* m_e c}$, $|p^*| = p_{e^+} = p_{e^-}$. We have as a function of the photon energies and collision angle

$$\beta^* = \sqrt{1 - \frac{1}{s}} \qquad s = \frac{1}{2}\gamma_1\gamma_2\left(1 - \cos\left(\alpha\right)\right). \tag{4.2}$$

The probability per time unit for a first photon propagating in a photon cloud of density distribution function $n_{\gamma,2}(\gamma_\gamma, \theta, \varphi)$ to decay in a pair is given by

$$\frac{dN_{ppBW}}{dt} = \int_{\gamma_{\gamma,2}} \int_{\Omega} n_{\gamma,2}(\gamma_{\gamma,2}, \theta, \varphi) \sigma_{ppBW} c \left(1 - \cos\left(\alpha\right)\right) d\gamma_{\gamma,2} d\Omega \tag{4.3}$$

where Ω is the collision solid angle, $d\Omega = \sin\theta d\theta d\varphi$ the element of solid angle in the propagation direction of the element of the photon distribution.

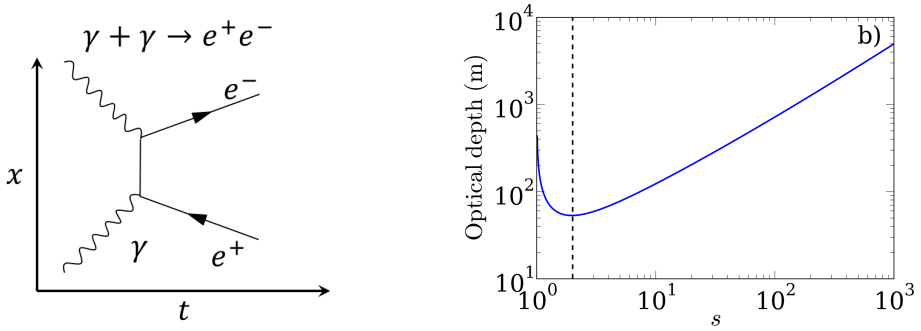

Figure 4.1: (a) - Feynman diagram of the photon-photon Breit Wheeler pair conversion. (b) - Optical depth as a function of the parameter s for a photon propagating in a cloud of photons of density n_c. The black dashed line corresponds to $s = 2$.

The number of pairs created over a period T of a first unidirectional photon beam of $N_{\gamma,1}$ photons entering an infinitely large second photon cloud of density $n_{\gamma,2}(\gamma_\gamma, \theta, \varphi)$ therefore corresponds to

$$N_{ppBW} = \int_{\gamma_{\gamma,1}} \frac{dN_{\gamma,1}}{d\gamma_{\gamma,1}} \left[1 - \exp\left(\int_T \frac{dN_{ppBW}}{dt} dt\right)\right] d\gamma_{\gamma,1} \tag{4.4}$$

Here, we have only considered inter-beam collisions. In the Universe, the photon-photon Breit-Wheeler process concerns the high-energy photons (up to 10^6 MeV) propagating in the intergalactic thermal photon bath of energy density less than a few eV per m^3, corresponding to an average photon energy $\langle \varepsilon_\gamma \rangle \sim 10^{-3}$ eV (Nikishov (1964); Gould and Schréder (1966)). The galactic bath can be modeled as a Planck distribution $n_\gamma(\gamma_\gamma) = \left(\gamma_\gamma^2 m^2 c/\pi^2 \hbar^3\right) \left(e^{\gamma_\gamma mc^2/T} - 1\right)^{-1}$ where T is the blackbody photon gas temperature. A similar laser-driven scenario involving the interaction of high-energy photons with a Planckian photon distribution has been proposed by Pike *et al.* (2014) (see also Thomas (2014) and Introduction).

From Eq 4.3, we can estimate the optical depth of a photon traveling in a photon gas at the critical density $n_\gamma = n_c$. The function is plotted in Fig. 4.1 as a function of the parameter s (see Eq. 4.2). It shows that the probability for two photons to decay into a pair is maximized for $s = 2$ and is not possible for $s \leq 1$. This means for instance that in a direct collision ($\alpha = \pi$), if a photon is at twice the electron rest mass energy, the other should be at least at the electron rest mass energy and at twice this energy for the highest probability. However, because of a very large optical depth ($> 10^2$ meters), even in a dense photon bath ($n_\gamma \sim n_c$), this process is usually dominated by other pair creation mechanisms (shown in the next sections for the generation of pairs in a strong field and in chapter 5 for the generation of pairs in the matter) and is difficult to observe.

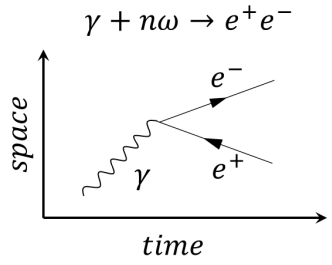

Figure 4.2: Feynman diagram of the multiphoton Breit-Wheeler pair creation

4.3 The multiphoton Breit-Wheeler process

4.3.1 Presentation of the cross sections

The theoretical formalism is similar to the nonlinear Compton Scattering and can be found in many papers (Reiss, 1962; Nikishov and Ritus, 1964, 1967; Erber, 1966; Ritus, 1985; Ruffini *et al.*, 2010; Landau and Lifshitz, 2012). The significance of QED processes on a photon propagating in an electromagnetic field is given by the Lorentz invariant χ_γ already defined in (2.2):

$$\chi_\gamma = \frac{\gamma_\gamma}{E_s} \left| \mathbf{E}_\perp + \mathbf{c} \times \mathbf{B} \right| \tag{4.5}$$

where $\mathbf{E}_\perp$ is the electric field orthogonal to the photon propagation direction and $\mathbf{B}$ the magnetic field. Here, $\gamma_\gamma = \varepsilon_\gamma / m_e c^2$ is both the Lorentz factor and the normalized energy of the photon. As for the nonlinear Compton scattering, assumptions 1 and 2 remain necessary, the field should be considered uniform and quasistatic during the process and the field much weaker than the Schwinger limit ($1 \ll a_0 \ll eE_s/m_e\omega c$).

The energy distribution of the production rate of pairs by a hard photon is

$$\frac{dN_{nBW}}{d\chi_e dt} = \frac{\alpha_f m_e^2 c^4}{\pi\sqrt{3}\hbar\varepsilon_\gamma\chi_\gamma} \int_x^{+\infty} \sqrt{s} K_{1/3}\left(\frac{2}{3}s^{3/2}\right) ds - \left(\left(2 - \chi_\gamma x^{3/2}\right) K_{2/3}\left(\frac{2}{3}x^{3/2}\right)\right) \tag{4.6}$$

where $x = (\chi_\gamma/\chi_{e^+}\chi_{e^-})^{2/3}$. The parameters χ_{e^-} and χ_{e^+} are the respective Lorentz invariant of the electron and the positron after pair creation. One has $\chi_{e^+} = \chi_\gamma - \chi_{e^-}$ and $\varepsilon_e = \varepsilon_e \chi_e / \chi_\gamma$, χ_e denotes interchangeably χ_{e^-} or χ_{e^+}. Function (4.6) is symmetric in χ_e.

The total production rate of pairs can be put in the form

$$\frac{dN_{nBW}}{dt} = \frac{\alpha_f m_e^2 c^4}{\hbar\varepsilon_\gamma} \chi_\gamma T_{nBW}(\chi_\gamma) \tag{4.7}$$

where the auxiliary dimensionless function $T_{nBW}(\chi_\gamma)$ can be written

$$T_{nBW}(\chi_e, \chi_\gamma) = \frac{1}{\pi\sqrt{3}\chi_\gamma^2} \int_0^{+\infty} \int_x^{+\infty} \sqrt{s} K_{1/3}\left(\frac{2}{3}s^{3/2}\right) ds - \left(\left(2 - \chi_\gamma x^{3/2}\right) K_{2/3}\left(\frac{2}{3}x^{3/2}\right)\right) d\chi_e \tag{4.8}$$

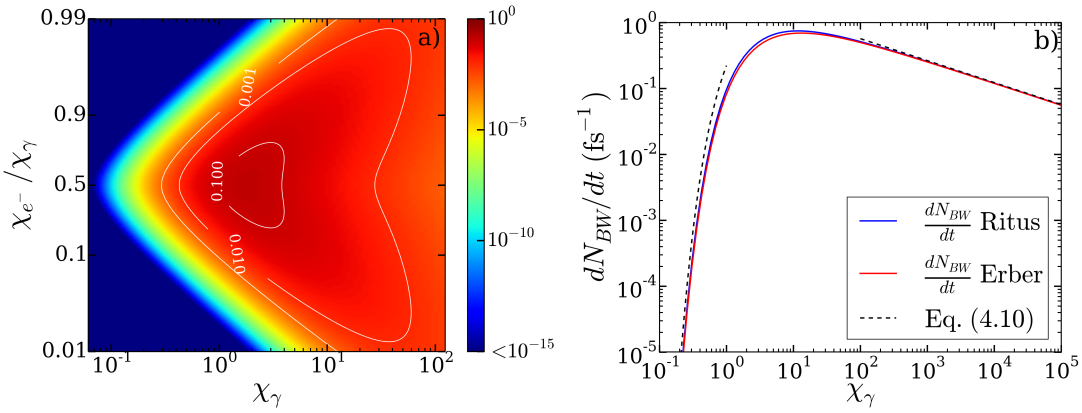

Figure 4.3: (a) - Normalized pair creation energy distribution given by Eq. 4.6. (b) - Normalized total pair production distribution. The blue curve is a plot of Eq. 4.7. The red one is the Erber approximation given by Eq. 4.9. Black curves are asymptotic approximations.

An alternative approximate expression of the function T_{nBW} has been proposed by Erber (1966)

$$T_{nBW}(\chi_\gamma) = \frac{0.16}{\chi_\gamma} K_{1/3}^2\left(\frac{4}{3\chi_\gamma}\right). \tag{4.9}$$

The function (4.8) presents the following asymptotic forms

$$T_{nBW}(\chi_\gamma) \sim \begin{cases} \exp\left(-8/3\chi_\gamma\right) & \text{if } \chi_\gamma \ll 1 \\ 0.38\chi_\gamma^{-1/3} & \text{if } \chi_\gamma \gg 1 \end{cases} \tag{4.10}$$

A photon of energy γ_γ traveling in a constant electric field E_0 has a Lorentz parameter equal to $\chi_\gamma = \gamma_\gamma E_0/E_s$. For a field of amplitude $a_0 = 500$, the energy distribution rate of pair creation is plotted in Fig. 4.3 as a function of χ_γ. The symmetry of the distribution with respect to $\chi_e/\chi_\gamma = 1/2$ is clearly seen in Fig. 4.3a. The maximum probability corresponds to equal electron-positron energies $\chi_e^+ = \chi_e^- = \chi_\gamma/2$. The energy dispersion increases with χ_γ.

The total pair production rate is displayed in Fig. 4.3b comparing Eq. (4.8), Eq. (4.9) and asymptotic formula (4.10). The probability of pair production peaks at $\chi_\gamma \sim 10$. It rapidly drops below $\chi \leq 1$ and much more slowly beyond $\chi_\gamma \sim 100$.

4.3.2 Estimation of pair production in laser-matter interaction

Let us now estimate the pair production rate during the interaction of an electron with an intense laser field, similarly to what has been done in Bell and Kirk (2008).

We first consider an electron of total energy $\gamma_{e^-} m_e c^2$ propagating in the opposite direction of the laser field (along the x direction). We neglect the transverse oscillation of the electron ($p_y = p_z = 0$) and we average the laser field over a period for the calculation of the quantum parameter. The laser is considered linearly polarized. Pair cascading, i.e. the possibility for pairs to induce new pairs, is here neglected. The electron quantum parameter is

$$\chi_{e^-} = \frac{\gamma_{e^-} E_0}{\sqrt{2} E_s} = \frac{\gamma_{e^-} m_e \omega_0 c a_0}{e\sqrt{2} E_s} \tag{4.11}$$

where $E_0 = cB_0$ is the electric field amplitude (B_0 the magnetic field amplitude) and a_0 the normalized laser field. The number of of γ-photons created per laser period T is

$$\begin{aligned} N_{\gamma,\gamma>2} &= \int_0^T \int_2^{+\infty} \frac{dN_\gamma}{d\gamma_\gamma dt} d\gamma_\gamma dt & (4.12) \\ &\sim \frac{dN_\gamma}{dt} \left(\langle \chi_\gamma \rangle\right) T & (4.13) \end{aligned}$$

where $\langle \chi_\gamma \rangle$ is the average photon quantum parameter which can be calculated via the photon energy at the maximum of the classical power spectrum $\langle \gamma_\gamma \rangle \sim 0.3 \hbar \omega_{cr} / (m_{e^-} c^2)$. In our case, we prefer using the quantum-corrected function given in section 2.1. The probability for γ-photons to decay into a pair during a laser period can be approximated by

$$\kappa_\gamma(\chi_\gamma) = 1 - \exp \int_0^T \frac{dN_{nBW}}{dt} dt \sim 1 - \exp\left(- \left\langle \frac{dN_{nBW}}{dt} \right\rangle T \right) \tag{4.14}$$

As a consequence, the total production of pairs by an electron is equal to

$$\begin{aligned} N_{nBW} &= \int_0^T \int_2^{+\infty} \frac{dN_\gamma}{d\gamma_\gamma dt} \kappa_\gamma(\chi_\gamma) d\gamma_\gamma & (4.15) \\ &\sim \langle N_{\gamma,\gamma>2} \rangle \kappa_\gamma(\langle \chi_\gamma \rangle) & (4.16) \end{aligned}$$

Here, the total pair production is calculated from numerical integration of the full cross-sections. The electron quantum parameter and the number of emitted γ-photons are shown in Fig. 4.4. The maximum intensity of the upcoming Apollon laser, $I \simeq 10^{23}$ Wcm^{-2}, is indicated by the red dashed line. Figure 4.4b shows that the production of γ-photons required for pair production increases with the laser intensity. In the limit of the laser Apollon, we predict a production rate of 10 γ-photons during a laser period. For multi-GeV photons, the number of produced photons can slightly decrease compared to the lower electron energies: fewer photons are emitted with higher individual energies. The average total radiated energy $\varepsilon_{rad} \sim P_{rad} T$ divided by the initial electron energy is shown in Fig. 4.5a. The photon

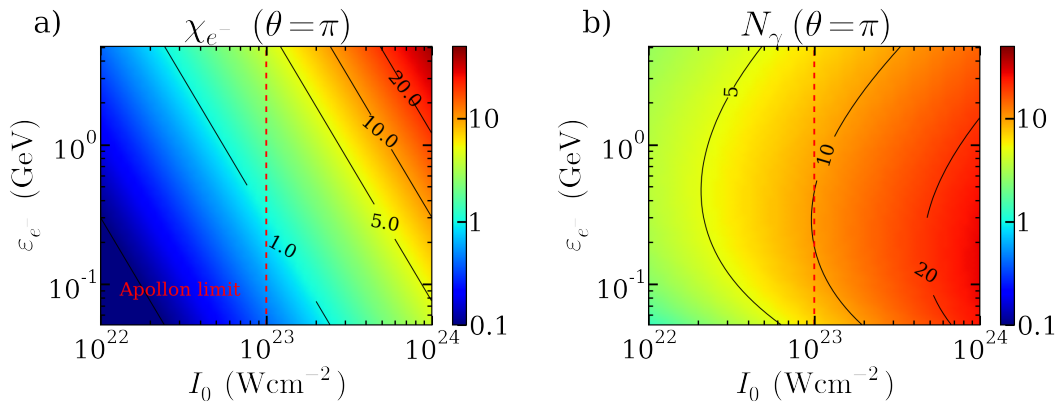

Figure 4.4: (a) Approximated electron quantum parameter χ_{e^-} as a function of the laser intensity and the electron energy. (b) Number of photons of energy up to 1 MeV produced during a laser period by an electron. The red dashed line corresponds to the expected maximum intensity of the Apollon laser.

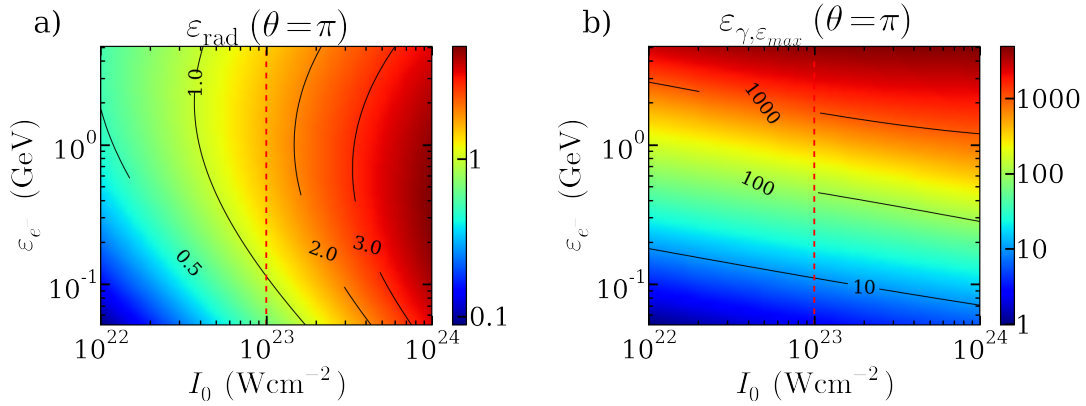

Figure 4.5: (a) - Radiated energy during a laser period for a single electron. (b) - Photon energy at the maximum of the radiated spectrum $\varepsilon_{\gamma,\varepsilon_{max}}$.

energy at the maximum of the energy spectrum is in Fig. 4.5b. Finally, the pair production rate for an electron during a laser period is given in Fig. 4.6. According to this simple modeling, in this regime, the pair yield per electron per laser wavelength shows that an efficient production requires both a GeV electron and an intensity above 10^{23} Wcm^{-2}. Under these conditions of energy and intensities, an electron will produce less than a pair during a laser period. With a higher intensity or a higher electron energy, several pairs can emerge per electron so that the final generated electron-positron pair plasma is almost neutral. Furthermore, in this regime of interaction, the pair cascading may significantly enhance the total yield.

For laser intensities under 10^{21} Wcm^{-2}, the experimental observation of the non-

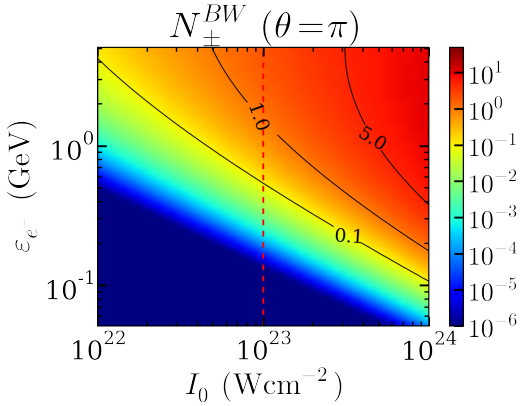

Figure 4.6: (a) - Number of nonlinear Breit-Wheeler pair produced per laser period by a single electron.

linear Breit-Wheeler process requires electron beam energies above several tens of GeV. On the forthcoming high-power laser facilities, the nonlinear Breit-Wheeler pair creation will be achievable provided GeV electron can be generated (Fig. 4.6). An all-optical scheme, based on laser wakefield acceleration (LWFA), will be studied in Chapter 8.

This scenario is not the only one considered. The nonlinear Breit-Wheeler may be accessible at lower intensities using multiple laser beams. In Wu and Xue (2014), the collision of a probe photon with a low and a high-frequency plane wave at intensity 10^{18} Wcm^{-2} propagating in the same direction is considered.

4.4 Electromagnetic Trident pair production

The electromagnetic Trident process is the direct e^-e^+ pair emission by an accelerated electron in an electromagnetic field through a virtual photon ($e' + n\omega_0 \rightarrow e^- + e^+ + e'$). This process can be seen as the combination of the Compton emission of a high-frequency photon and its conversion into a pair via the multiphoton Breit-Wheeler mechanism. The Trident pair production rate can be estimated on the basis of the Fermi-Weizsäcker-Williams approximation depending on the electron quantum parameter χ_{e^-} (Erber (1966))

$$\frac{dN_T^{\pm}}{dt} = \frac{0.32}{\pi}\frac{mc^2}{\hbar}\alpha_f^2\chi_{e^-}S(\chi_{e^-}). \tag{4.17}$$

The integral function S is given by

$$S(\chi) = \int_0^{+\infty} u^{-2}W(u/\chi)K_{1/3}^2(4/3u). \tag{4.18}$$

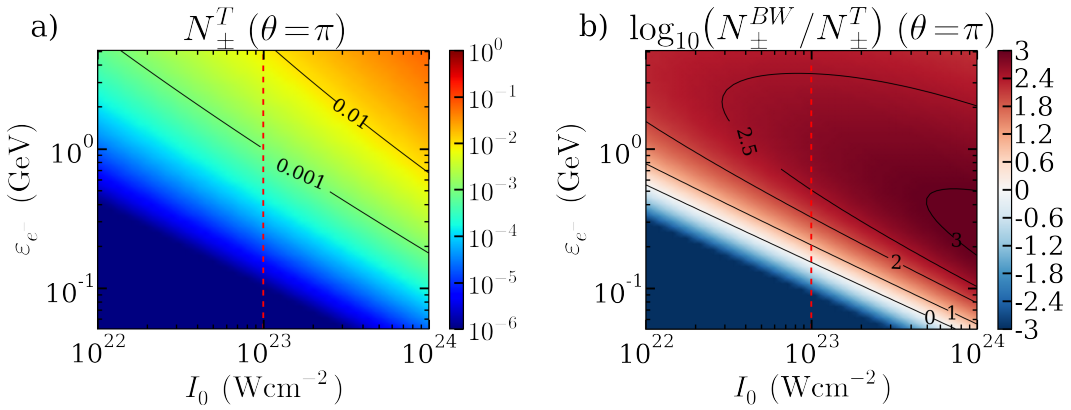

Figure 4.7: (a) - Trident pair production rate as a function of the laser intensity I and the electron energy γ_{e^-}. (b) - Comparison of the Trident and the Breit-Wheeler production rates.

where

$$W(x) \;=\; xK_0(x)K_1(x) - \left(x^2/2\right)\left[K_1^2(x) - K_0^2(x)\right], \tag{4.19}$$

K_α being a modified Bessel function of the second kind of order α.

In a constant magnetic or electric field, the quantum parameter simply becomes $\chi_{e^-} \sim \frac{\gamma_{e^-}E}{E_s} \sim \frac{\gamma_{e^-}cB}{E_s} \sim \gamma_{e^-}a_0\times 2.46\times 10^{-6}$, directly proportional to the field amplitude and the particle energy. The Trident pair production rate in a constant electric field of amplitude a_0 by an electron of energy γ_{e^-} is displayed in Fig. 4.7.

The relative efficiency of the Trident and the nonlinear Breit-Wheeler processes can be estimated from their limiting expression in χ_{e^-}. We first remark that the Trident process is of second order in α_f (since a virtual photon is involved). The Trident pair production rate becomes in the limits of χ

$$S(\chi) \sim \begin{cases} (\pi^{5/2}/16)(3\chi)^{1/4}\exp\left(-8/(3\chi)^{-1/2}\right) & \text{if } \chi_\gamma \ll 1 \\ (\pi^2/2)\ln\chi & \text{if } \chi_\gamma \gg 1 \end{cases} \tag{4.20}$$

One can check that the approximation for $\chi \ll 1$ is still in a good agreement with the cross sections when χ approaches unity. When $\chi \ll 1$, the multiphoton Breit-Wheeler pair production rate decreases faster than the electromagnetic Trident so that the latter can be dominant. When $\chi \gg 1$, the Trident rises logarithmically whereas the Breit-Wheeler slowly decreases again (see Fig. 4.3). The Trident can be therefore dominant again in the extreme regimes of interaction.

One can also compare the efficiency of the electromagnetic Trident with the Compton-emission and the nonlinear Breit-Wheeler process from a similar electron initial state. The number of pairs per laser periods via the Trident process is equal

to

$$N_T = \int_0^T \frac{dN_T}{dt} \sim \frac{dN_T}{dt}(\gamma_{e^-})T \tag{4.21}$$

Here, we make the assumption that T is sufficiently short not to affect the electron energy during the emission which is a strong hypothesis for GeV electrons. Again, pair cascading is neglected.

The ratio between the electromagnetic Trident and the nonlinear Breit-Wheeler pair production during a laser period is shown in Fig. 4.7b. The Trident process dominates the pair production for $\varepsilon[\text{GeV}] \leq -0.27(I_{22})^{-0.0074}$. This is simply due to the fact that the nonlinear Compton scattering does not produce sufficiently energetic photons $\gamma_\gamma \leq \gamma_{e^-} - 1$ which are therefore converted with difficulty into pairs via the multiphoton Breit-Wheeler, even if χ_{e^-} approaches unity. Nonetheless, Fig. 4.7a shows that the Trident production rate of pairs is relatively small even when this mechanism dominates. In our domain of interest, $\chi \sim 1, \gamma \sim a_0$, the multiphoton Breit-wheeler pair production rate is three orders of magnitude larger than the Trident's.

4.5 Pair annihilation

4.5.1 Pair annihilation in a pair plasma

Pair annihilation is the process of positron-electron recombination into one or several photons. It can be shown that the two-photon process is the most likely (Heitler (1954)) for given particle energies (for instance, the three-photon pair annihilation is 370 times lower than the two-photon process).

The two-photon pair annihilation cross section has been calculated from quantum theory solving the Dirac wave equation with linear perturbation (Dirac (1930); Svensson (1982); Ruffini *et al.* (2010); Landau and Lifshitz (2012); Heitler (1954)).

Let us consider the collision between a positron and an electron with respective normalized velocities β_{e^+} and β_{e^-}. In the center of momentum frame (COM) of the two particles, the total annihilation cross section depends on the COM frame velocity $\beta_* = v_*/c$

$$\sigma_{An,*} = \frac{\pi r_e^2}{4\gamma_*^2\beta_*}\left(\frac{3-\beta_*^4}{\beta_*}\log\frac{1+\beta_*}{1-\beta_*} - 2\left(2-\beta_*^2\right)\right). \tag{4.22}$$

The cross section is a diminishing function of the colliding velocity. For relativistic velocities, it becomes

$$\sigma^* = \frac{\pi r_e^2}{4\gamma_*^2\beta_*}\left(2\log 2\gamma_* - 2\right). \tag{4.23}$$

In the laboratory frame, the annihilation probability per time unit for a positron (or an electron) traveling in an electron (positron) cloud of density distribution $n_{e^-} f(\mathbf{p}_{e^-})$ writes

$$\frac{dN_{An}}{dt}(\gamma_{e^+}) = \iint n_{e^-} f(\mathbf{p}_{e^-}) \frac{\gamma_*^2}{\gamma_{e^+}\gamma_{e^-}} 2\beta_* c\sigma_*(\beta_*) d\mathbf{p}_{e^-} \quad (4.24)$$

$$= n_{e^-} \int_{\gamma_{e^-}\in[1,+\infty]} \int_\Omega f(\mathbf{p}_{e^-}) \frac{\gamma_*^2}{\gamma_{e^+}\gamma_{e^-}} 2\beta_* c\sigma_*(\beta_*) d\Omega \quad (4.25)$$

where $2\gamma_*^2 - 1 = \gamma_+\gamma_- (1 - \beta_+\beta_- \cos\theta)$, $d\Omega = \sin\theta d\theta d\phi$ and p_{e^-} is the electron momentum. For an isotropic distribution, it becomes

$$\frac{dN_{An}}{dt}(\gamma_{e^+}) = 4\pi n_{e^-} \int_{\gamma_{e^-}\in[1,+\infty]} f(\gamma_{e^-}) d\gamma_{e^-} \int_0^\pi \frac{\gamma_*^2}{\gamma_{e^+}\gamma_{e^-}} \beta_* c\sigma_*(\beta_*) \sin\theta d\theta \quad (4.26)$$

where θ is the angle between the two particles propagation direction in the collision plane. It can be written $\frac{dN}{dt} = n_- \langle v\sigma \rangle$ where $\langle v\sigma \rangle$ is the distribution average reaction rate.

In the collision with a mono-energetic unidirectional electron beam, the probability per unit of time simply becomes

$$\frac{dN_{An}}{dt}(\gamma_{e^+}, \gamma_{e^-}) = n_{e^-} \frac{\gamma_*^2}{\gamma_{e^+}\gamma_{e^-}} 2\beta_* c\sigma_*(\beta_*) \quad (4.27)$$

In the case of a head-on collision ($\theta = \pi$, giving the highest annihilation rate), Fig. 4.8 shows, using Eq. 4.27 the evolution of the positron expected lifespan in a cloud of electrons at the critical density $n_{e^-} = n_c$. The lifespan in this case is directly proportional. The annihilation probability increases with decreasing electron-positron energies. In the non-relativistic limit, one has $\langle v\sigma \rangle \sim c\pi r_e^2$. For a density of $n_{e^-} = n_c$, the positron has thus a characteristic lifetime of several hundreds of nanoseconds, which is much larger than the femtosecond/picosecond time scale of ultra-intense laser experiments.

For a cloud of electrons (positrons) characterized by a Maxwell-Jüttner distribution,

$$f = \frac{1}{TK_2(1/T_\pm)} \gamma^2 \beta \exp(-\gamma/T_\pm) \quad (4.28)$$

Figure 4.8c shows the average optical depth for pair annihilation for an incident positron (incident electron) as a function of the positron energy γ_{e^+} and the cloud temperature $T_\pm$. The dashed lines correspond to the case of a head-on collision with a mono-directional plasma of energy $\gamma = T_\pm$. As expected the annihilation distance increases with the particle energy and the plasma temperature. The annihilation distance in a Maxwellian cloud is slightly longer than the mono-energetic case.

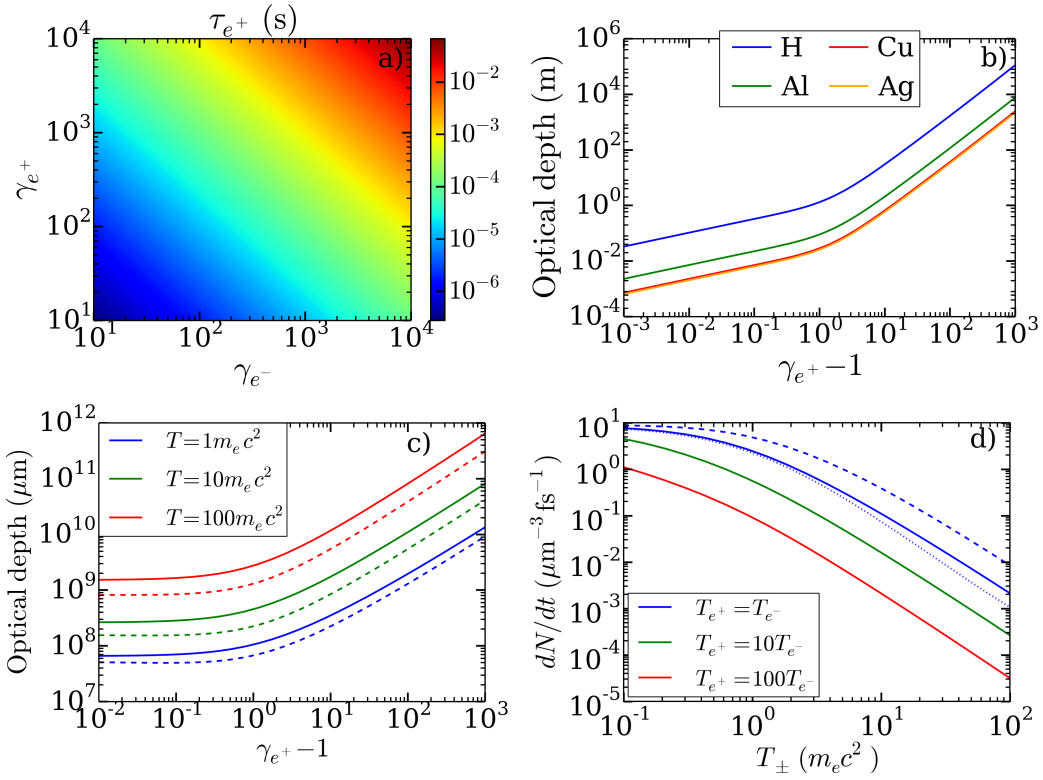

Figure 4.8: (a) - Lifespan of a positron of energy γ_{e^+} propagating in a mono-energetic cloud of electrons at γ_{e^-} at the critical density $n_{e^-} = n_c$. (b) - Optical depth (m) to pair annihilation in hydrogen, aluminium, copper and silver. (c) - Annihilation distance (optical depth) of a positron propagating in a Maxwellian plasma at temperature $T_\pm = 1, 10, 100 m_e c^2$. The dashed lines correspond to the case of the head-on collision of a particle with a counter-streaming cloud of electrons with energy $\gamma_{e^-} = T_{e^-}$. (d) - Annihilation rate in μm^{-3}fs^{-1} inside a Maxwellian pair plasma of temperature ratio $T_{e^+}/T_{e^-} = 1, 10, 100$. Again, the dashed line corresponds to the collision of two mono-directional counter-streaming pair plasmas at similar energy $\gamma = T_\pm$. The dotted line corresponds to the collision with an angle of 0.01 rad of two beams of energy $\gamma = T_\pm$.

In a thermalized and isotropized pair plasma of temperatures T_{e^-} and T_{e^+} respectively for the electrons and the positrons, at the density $n_{e^-} = n_{e^+} = n_c \sim 1.1 \times 10^{27}$ m^{-3} for $\lambda = 1$ μm, the pair annihilation rate per unit volume is

$$\frac{dn_{An}}{dt}(T_{e^-}, T_{e^+}) = 4\pi n_{e^-} n_{e^+} \int_1^{+\infty} f(\gamma_{e^-}) d\gamma_{e^-} \int_1^{+\infty} f(\gamma_{e^+}) d\gamma_{e^+} \int_{-1}^{1} \frac{\gamma_*^2}{\gamma_{e^+}\gamma_{e^-}} \beta_* c \sigma_* (\beta_*, \mu) d\mu \quad (4.20)$$

where $\mu = \cos\theta$. Using numerical integration, we plot dn_{An}/dt in Fig. 4.8d for different temperature ratios between the electrons and the positrons. For comparison,

the dashed line corresponds to the collision of two counter-streaming mono-energetic pair plasmas at the critical density with energy $\gamma_{e^\pm} = T_{e^\pm}$. All curves show a rapid decrease of the annihilation rate with the temperature. The head-on collision has the highest annihilation rate. For the relativistic-temperature case, we are interested in, the annihilation rate is below 1 event per μm^3 per fs, so that it can be neglected.

4.5.2 Pair annihilation in the matter

Pair annihilation can also happen with atomic electrons. W. Heitler has given a simple approximation considering the Dirac cross section (Heitler (1954) (p. 268-275) and Geant4 (2012); Nelson *et al.* (1985)). Each atom is composed of Z electrons at rest so that the probability for a positron to be annihilated in a given material of atom density n_α and atomic number Z_α is given by

$$\frac{dN_{An}}{dt} = \sigma_{An}\left(\gamma_{e^-} = 1\right) n_\alpha Z_\alpha v_{e^+} \tag{4.30}$$

$$= n_\alpha Z_\alpha \pi r_e^2 c \frac{\sqrt{\gamma_{e^+} - 1}}{\gamma_{e^+}\sqrt{\gamma_{e^+} + 1}} \left[\frac{\gamma_{e^+}^2 + 4\gamma_{e^+} + 1}{\gamma_{e^+}^2 - 1} \log\left(\gamma_{e^+} + \sqrt{\gamma_{e^+}^2 - 1}\right) - \frac{\gamma_{e^+} + 3}{\sqrt{\gamma_{e^+}^2 - 1}}\right] \tag{4.31}$$

where $\sigma_{An}\left(\gamma_{e^-} = 1\right)$ is the Dirac cross-section for an electron at rest. The effect of the Coulomb field is neglected. The optical depth to pair annihilation in hydrogen, aluminium, copper and silver are plotted in Fig. 4.8b. The optical depth increases with the particle energy. A positron of $\gamma_{e^+} \sim 10^2$ will travel 30 meters before being annihilated in copper whereas in hydrogen, the distance is of around 1500 meters. For non-relativistic positrons, the distance is of few millimeters in copper to few centimeters in hydrogen. The annihilation should have an effect in the case of extremely dense high-Z materials of mm-scale thickness in the non-relativistic regimes which can be the case in Bethe-Heitler experiment of pair production with lasers.

Chapter 5

Pair production in matter

In matter, pair creation occurs when high-energy photons interact with the field around a nucleus ($\gamma + Z \rightarrow e^- + e^+ + Z$). This process is referred to as Bethe-Heitler (BH) pair production. Pair production is also possible in the field of an electron ($\gamma + e^- \rightarrow e^- + e^+ + e^-$) and this process is called Triplet production, incoherent pair production or pair production with excitation or ionization (when the collision happens with a bound electron). Pair production can also arise directly from the collision of an electron with a nuclei via the so-called Trident process ($e^- + Z \rightarrow e^- + e^+ + e^- + Z$ (in contrast to the previously discussed electromagnetic Trident process). A thorough review on pair production in matter can be found in Hubbell (006a).

5.1 Bethe-Heitler pair production

First calculations of the Bethe-Heitler pair production were made after the discovery of the positron by C. D. Anderson (Nishina and Tomonaga (1933); Oppenheimer and Plesset (1933); Heitler and Sauter (1933)). As for the Bremsstrahlung, the calculation of the Bethe-Heitler cross section can be made in the Born approximation (Bethe and Heitler (1934)), where the wave functions of the created positron and electron are calculated to first order. The Born approximation is valid provided

$$2\pi \frac{Ze^2}{\hbar v_{e^-}} \ll 1 \qquad 2\pi \frac{Ze^2}{\hbar v_{e^+}} \ll 1 \tag{5.1}$$

In other words, the Born approximation is adapted to low Z material and high-energy particles. In practice, the Born approximation constitutes a good approximation even for higher Z materials. In the contrary case, exact calculations or partial wave functions should be considered. In Motz *et al.* (1969), the authors make a complete inventory of the various analytical Bethe-Heitler and Trident cross sections before 1969. Born approximation and exact calculations are considered, in the classical and relativistic regime, with and without screening, for large and small recoil angle, with

and without atomic excitation, with and without photon polarization. In our case, the atomic excitation and the polarization is not taken into account. We suppose that the recoil energy of the target particle is negligible.

The photon should carry sufficient energy to be converted into a pair. The threshold is given from energy and momentum conservation in the center of mass frame of the collision so that

$$\gamma_\gamma > 2\left(1 + m_{e^-}/m_n\right) \sim 2 \tag{5.2}$$

where m_n is the nucleus mass. The maximum recoil for the positron or the electron corresponds to (Motz *et al.* (1969))

$$\cos(\theta_{max}) = \frac{2}{p_\gamma}\sqrt{1 + p_\gamma\left(m_e/m_n\right)}. \tag{5.3}$$

When $p_\gamma \gg 1$, θ_{max} tends to $\pi/2$. The minimum momentum transfer to the nucleus corresponds to

$$p_{n,min} = \sqrt{p_\pm^2 + p_\gamma^2 - 2p_\pm p_\gamma \cos\theta_\pm} - \sqrt{\left(p_\gamma - \gamma_\pm\right)^2 - 1}. \tag{5.4}$$

As for the Bremsstrahlung we consider $r_{\max} = \hbar/p_{n,\min}$ as the impact factor which enables us to quantify the importance of the screening. The evolution of the impact factor as a function of the photon energy and the recoil angle is shown in Fig. 5.1 for Silver and for two different positron energies $\gamma_{e^+} = 0.1\gamma_\gamma$ and $0.9\gamma_\gamma$. For a given recoil angle, the $r_{\max}$ function has the shape of a bell. As the positron (or electron) recoil angle decreases ($\theta \to 0$), the position in photon energy and the value of the maximum increase. The solid black line corresponds to the contour of the Thomas-Fermi radius l_{TF}. Impact factors above l_{TF} correspond to interaction cases where screening by the bound electrons has to be taken into account. The dashed line corresponds to the Debye length for $T = 1$ eV. We can see that the Debye screening is significant only for the creation of highly collimated pairs and for photons of high energies $\gamma_\gamma > 10^3$. The dotted line plots the maximal recoil angle.

5.1.1 Cross section differential in energy

The relativistic Bethe-Heitler energy-differential cross section for an arbitrary screening in the Born approximation is taken from Motz *et al.* (1969). This formula is equivalent to the Bremsstrahlung cross-section (inverse process) Eq. 3.29 in Chapter 3. This cross-section, that we name σ_{BH-RE}, can be written

$$\frac{d\sigma_{BH-RE}}{d\gamma_{e^+}} = \frac{4Z^2 r_e^2 \alpha_f}{\gamma_\gamma^3}\left[\left(\gamma_{e^+}^2 + \gamma_{e^-}^2\right)\left(1 + I_1\right) + \frac{2}{3}\gamma_{e^+}\gamma_{e^-}\left(I_2 + \frac{5}{6}\right)\right] \tag{5.5}$$

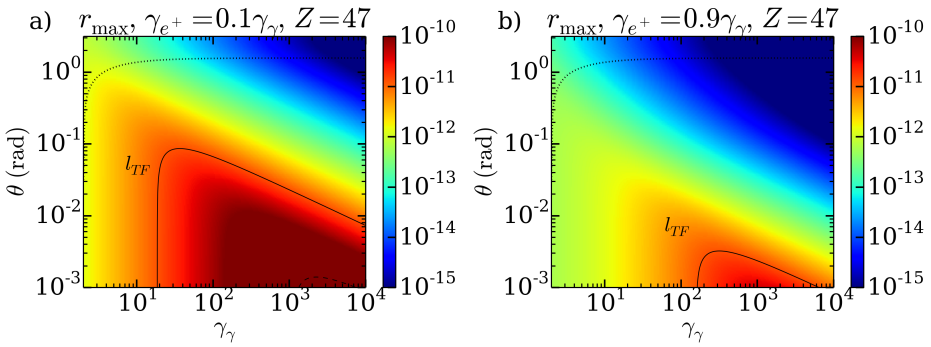

Figure 5.1: Colormaps of the impact factor $r_{\max}$ in silver as a function of the photon energy γ_γ and the positron emission angle θ for positron energy $\gamma_{e^+} = 0.1\gamma_\gamma$ and $0.9\gamma_\gamma$. The solid black line corresponds to the Thomas-Fermi radius, the dashed line to the Debye length for $T = 1$eV and the point line to the maximal angle θ_{max}.

where the integral function I_1 and I_2 are defined similarly to the Bremsstrahlung case

$$I_1 = \int_\delta^1 (u-\delta)^2 \frac{(1-F(u))^2}{u^3} du \tag{5.6}$$

$$I_2 = \int_\delta^1 \left(u^3 - 6\delta^2 u \ln\frac{u}{\delta} + 3\delta^2 u - 4\delta^3\right)\left(\frac{1-F(u,Z)}{u^2}\right)^2 du. \tag{5.7}$$

Here, $\delta = \gamma_\gamma/(2\gamma_{e^-}\gamma_{e^+})$ where γ_{e^-} and γ_{e^+} are respectively the electron and the positron energies.

Using the Wentzel-Yukawa potential, I_1 and I_2 have exact solutions (see section 3.2.2, Eqs. 3.36 and 3.37). We can also include the Debye potential using Eq. 3.6 and use the same reduced solution as for the Bremsstrahlung. In this case, the cross-section with the reduced length l_r will be referred to as σ_{BH-R}.

The behavior of the Bethe-Heitler energy-differential cross sections is shown in Fig. 5.2 for different photon energies (10 MeV, 100 MeV and 1000 MeV) and plasma temperatures in silver ($Z = 47$). The degree of ionization for each considered temperature is given in section 3.1 in Tab. 3.1. The curves are perfectly symmetric with respect to $\gamma_{e^-}/\gamma_\gamma = 1/2$. The cross section has a plateau-like shape centered on $\gamma_{e^+}/\gamma_{e^-} = 1/2$ of height (respectively width) decreasing (respectively increasing) with rising photon energy. At high photon energy (1000 MeV), the plateau extends from $\gamma_{e^+} \to 1$ and $\gamma_{e^+} \to \gamma_\gamma - 1$. Ionization tends to increase the cross section leading to variations of a few % at 10 MeV up to ~ 60 % at 1000 MeV.

The total cross-section for the reduced case is calculated by numerical integration. The result is shown in Figs 5.3 for aluminium and silver for the neutral (red line) and the fully ionized (orange line) cases. The results are compared with the Bethe-Heitler Coulomb screened point nucleus cross-section for extreme-relativistic energies

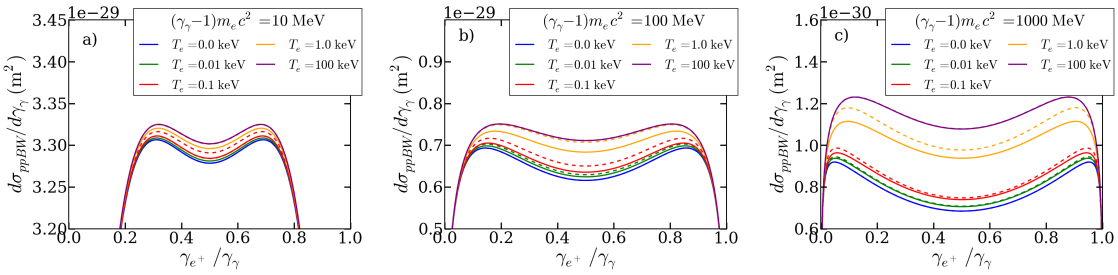

Figure 5.2: Cross-section differential in positron energy for three photon energies 10 MeV (a) 100 MeV (b) and 1000 MeV (c). The solid lines correspond to the cross-section $d\sigma^{BH-RE}_{\gamma_{e+}}$ and the dashed lines to $d\sigma^{BH-r}_{\gamma_{e+}}$ for different plasma temperatures T.

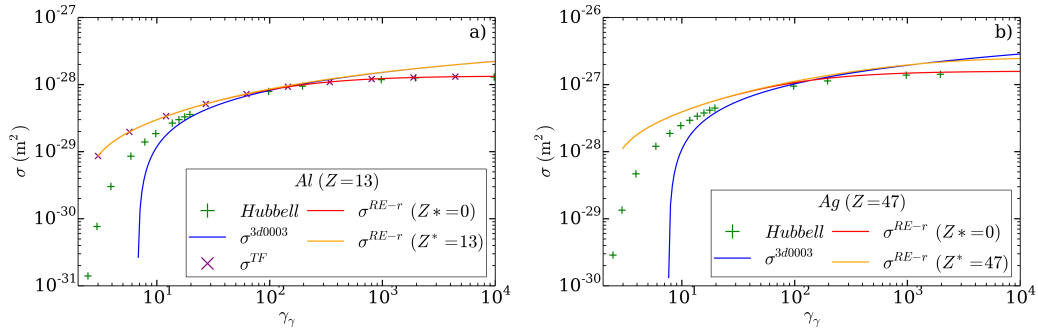

Figure 5.3: Total cross sections using (3D-0003 in Motz *et al.* (1969)) the screened point nucleus for extreme-relativistic energies from Bethe and Heitler (blue line), using the numerical calculations of Hubbell (Hubbell *et al.* (1980)) (green markers) and using the reduced cross-section for the minimal (red line) and the maximal (orange line) ionization rate for aluminium (Z=13, left) and silver (Z=47, right).

(3D-0003 in Motz *et al.* (1969)) and the results obtained numerically in Hubbell *et al.* (1980), Hubbell (006b) and Hubbell (006a). Hubbell has tabulated the cross-section for energies between 1 and 100 MeV and for Z between 1 and 100 mixing different approximations and different corrections (see references). The curves first demonstrate that the probability to decay into pairs increases with the photon energy. In the region $\gamma_\gamma < 100$, the reduced cross-section overestimates the results obtained by Hubbell and the screened point nucleus cross-section is clearly not adapted and falls down rapidly. The ionization degree, in this region, has no impact on the cross-sections. In the high-energy limit $\gamma_\gamma > 100$, the cross section rises with Z^*. In this region, the reduced cross-section with $Z^* = 0$ closely matches the results of Hubbell. With $Z^* = 13$, the reduced cross section approaches the screened point nucleus cross section.

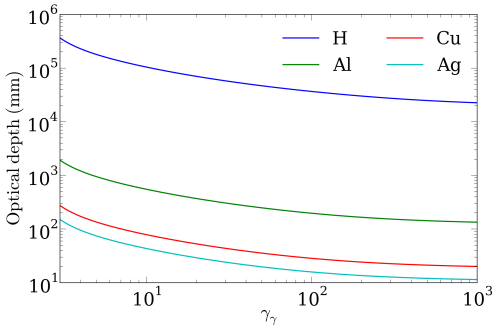

Figure 5.4: Estimation of the optical depth to pair generation in different materials (hydrogen (Z=1), aluminium (Z=13), copper (Z=26), silver (Z=47)) as a function of the photon energy.

The optical depth to pair decay is given by

$$L_{BH} = (\sigma_{BH} n_\alpha)^{-1} = \left(\sigma_{BH} \frac{\rho_\alpha N_A}{A_\alpha}\right)^{-1} \tag{5.8}$$

where n_α is the material number density (in m^{-3}), ρ_α the mass density, A the relative atomic mass and N_A the Avogadro number. The optical depth in different neutral ($Z^* = 0$) materials including hydrogen, aluminium, copper and silver is plotted in Fig 5.4. As expected, the lower the photon energy, the lower the cross-section and the longer the optical depth. The ratio between the cross section in a given material and that in hydrogen is equal to $0.09 Z^2 \rho_\alpha / A_\alpha$ and this can be checked on the numerical calculations of the optical depth, Coulomb screening having a weak impact on the optical depth. A photon of energy 10 MeV will require 10^2 m of hydrogen and 5 cm of silver to decay into pairs.

As for the Bremsstrahlung emission, these results demonstrate that in laboratory experiments of pair generation via the Bethe-Heitler mechanism, dense and high-Z targets (silver, gold) of thickness ranging from several millimeters to several centimeters are needed to get significant pair yield.

5.2 Triplet pair production

As already described, the Triplet pair production occurs in the collision of a photon with an electron. The Triplet pair production has a higher photon energy threshold of 4 $m_e c^2$ contrary to the threshold of 2 $m_e c^2$ for the Bethe-Heitler mechanism. Exhaustive reviews on this mechanism have been published by Motz *et al.* (1969) and Hubbell *et al.* (1980). In addition to screening effects, the Triplet mechanism is affected by the photon-electron interaction (the secondary electrons gain energy during

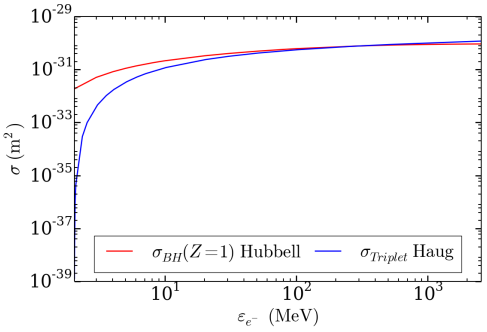

Figure 5.5: Total cross-section for the triplet pair production taken from the numerically-calculated values of Haug and for the Bethe-Heitler cross-section in hydrogen from the numerical results of Hubbell.

the collision process or Compton scattering, negligible at high photon energy), the exchange effect from the two electrons (negligible at high photon energy), retardation and radiative correction effects. The first calculations of the cross sections (neglecting screening) were performed by Ghizzetti (1947), Borsellino (1947)) (more accurate at high energy $\gamma_\gamma > 16$) and Votruba (1948) (valid near the threshold, taking into account $\gamma - e^-$ interaction, exchange and retardation). Numerical calculations were made by Mork (1967) who proposed a correction to the Borsellino-Ghizzetti cross section at intermediate energies $4 < \gamma_\gamma < 16$. Later, Haug (1975) performed numerical calculations without the screening effects for energies γ_γ ranging from 4 to 5000 $m_e c^2$. The Triplet cross section is approximately Z^2 times lower than the Bethe-Heitler cross section. Nonetheless, the probability for pair creation also depends on the electron density Z times higher that the ion density, which is consequently only Z times lower than the Bethe-Heitler probability. In a low-Z materials, the Triplet process can therefore approach the production rate of the Bethe-Heitler. The results obtained by E. Haug are drawn in Fig. 5.5 and compared to the Bethe-Heitler cross section in hydrogen. The Bethe-Heitler cross section for hydrogen is of the same order of magnitude as the Trident for energies up to 10 MeV. Moreover, the Triplet pair production appears higher for energies up to 200 MeV. In astrophysics, both mechanisms can contribute to limiting the propagation of high-energy photons. In hot astrophysical plasmas (with a temperature close to 500 keV) the Triplet pair production could dominate the Bethe-Heitler process (Haug (2004)).

In order to take into account screening effects and drawing upon the Bethe-Heitler formalism in the Born approximation, Wheeler and Lamb derived a cross section valid for high-energies using the incoherent scattering function (see Hubbell *et al.* (1975)) calculated by Heisenberg (1931) and Bewilogua (1931). Hubbell *et al.* proposed a correction factor usable with the results of Haug. Numeral estimates show that the screening factor does not modify the unscreened cross-section by more that an order

of magnitude. The screening effects are significant at high photon energies and in high-Z materials. Other formulations which extend Borsellino's energy differential cross section have also been proposed (Jost *et al.* (1950)).

5.3 Trident pair production in matter

The direct production of pairs from an electron interacting with the Coulomb field of a nucleus is referred to as the Trident. The Trident cross section was first calculated by Bhabha (1935). In this paper, the author considered the collision of two arbitrary particles of charge $Z_1 e$ and $Z_2 e$. The collision of an electron with a nucleus is therefore just a particular case. The cross sections were calculated in the Born approximation in which the particle interaction is treated as a perturbation. J. H. Bhabha derived both the total and the pair energy-differential cross sections in different regimes of interaction, depending on the properties of the incident particle and the final energy of the pair (close to $m_e c^2$, the case of a heavy initial particle) and the screening effects. Calculated using the Thomas-Fermi approximation, screening effects were found to be negligible for a non-relativistic generated pair and for a relativistic incident electron when

$$\frac{\gamma_{e^+}\gamma_{e^-}}{(\gamma_{e^+}+\gamma_{e^-})} \ll \frac{1}{2\alpha_f} Z^{-1/2} m_e c^2. \tag{5.9}$$

However, Bhabha's formula suffers from a lack of accuracy hardly assessable due to different approximations (Shearer *et al.* (1973)). In this paper, the cross section near threshold was numerically evaluated to obtain a more accurate fitting expression. Using a different approximation, Murota *et al.* (1956) derived an other form for the cross sections in the relativistic case. More recently, Gryaznykh *et al.* (1998) computed a fitting approximation using the calculation of Baĭer and Fadin (1971) valid between the threshold values of $2m_e c^2$ and $200m_e c^2$ without screening effects:

$$\sigma_{Tr} = 5.22 \times 10^{-34} Z^2 \log^3 \left(\frac{2.3 + (\gamma_{e^+,i} - 1) m_e c^2}{3.52} \right) \tag{5.10}$$

where $\gamma_{e^-,i}$ is the incident electron energy. In this process, the incident electron should have an energy above $3m_e c^2$. They also provide an approximation for the generated positron average energy

$$\langle \gamma_{e^+} \rangle \sim (\gamma_{e^+,i} - 1) \left(\frac{1}{3} - 0.0565 \log \left(\frac{\gamma_{e^+,i} - 1}{3 m_{e^-} c^3} \right) \right). \tag{5.11}$$

The total cross section, Eq. 5.10, is plotted in Fig. 5.6 for aluminium and silver as a function of the incident electron energy The Trident is compared to the Bethe-Heitler (Eq. 5.5) in section 5.1 with a Wentzel-Yukawa screening potential. In the latter case, the abscissa refers to the incident photon energy γ_γ. The Bethe-Heitler cross

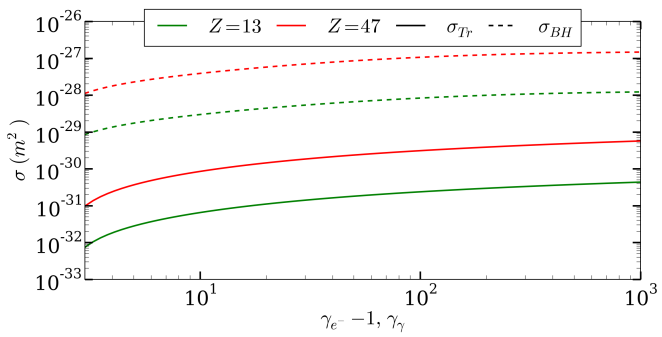

Figure 5.6: Total cross-section for the Trident pair production σ_{Tr} (solid line) as a function of the normalized incident kinetic electron energy $\gamma_{e^-} - 1$ for aluminium (Z=13, blue) and silver (Z=47, red). The Trident cross sections are compared to the Bethe-Heitler without Debye screening (dashed line).

section is larger by 3 orders of magnitude, yet the two mechanisms cannot be directly compared since the Bethe-Heitler efficiency actually depends on the high-frequency photon yield. A meaningful comparison can only be made by describing the photon production in specific configurations.

A common laser-matter configuration is the irradiation of high-Z targets of hundred of micrometers to several millimeters thickness at laser intensities from 10^{18} to 10^{21} Wcm^{-2}. The laser interaction generates hot electrons with energies above the MeV level which propagate through the target to the read side and generate Bremsstrahlung photons. The γ-photons can then generate pairs via the Bethe-Heitler process. The electrostatic confinement of most of the hot electrons enhances the Bremsstrahlung losses and the resulting pair production. In this configuration, the pairs can also be generated via the Trident directly from the hot electrons. Usually, high-Z targets with optimal $Z^2 n_i$ ratios are selected to maximize these effects. This configuration has been explored by several groups as a new source of positrons (Becker (1991); Gryaznykh *et al.* (1998); Gahn *et al.* (2000, 2002)). In Myatt *et al.* (2009), pair production both from the Trident and Bethe-Heitler conversion of the Bremsstrahlung photons is analyzed for different target thicknesses and laser intensities. By modeling the hot electrons as a Maxwellian of temperature given in the scalings of Wilks *et al.* (1992) or Beg *et al.* (1997), it is found that Trident process may dominate pair production in thin (< 20 μm) gold foils ($Z = 79$) irradiated by a kJ-class laser. In thin foils, the electron refluxing can increase the Bremsstrahlung emission and therefore enhance the Bethe-Heitler pair yield efficiency.

The possibility to generate pair plasmas with thick-foil irradiation has been studied experimentally in different campaigns by Chen et al. (Chen *et al.* (2009, 2011, 2015)). The experiments have been carried out on different laser facilities including Titan, Orion and Omega EP with intensities ranging from 10^{18} to 10^{20} Wcm^{-2}.

Millimeter thick gold foils were used so that Bremsstrahlung and Bethe-Heitler pair production were the dominant processes. Pair flows were obtained composed of 10^{10} to 10^{12} positrons with a maximal density close to 10^{13} cm^{-3} on target.

Chapter 6

The Particle-In-Cell description for the numerical simulation of laser-plasma interaction

6.1 Modeling Plasma Physics

The most basic method to solve the behavior of a plasma would require to follow the trajectory of each particle of a studied system and their interaction with the particles nearby in the Debye sphere. With more than 10^6 particles in a volume of 1 μm^{-3} in a simple hydrogen plasma (at $n_c = 0.001 n_c$), and more than 10^{11} in a solid target, we rapidly understand that such a method is not feasible due to its computation cost.

In the kinetic description offered by the Vlasov equations, the distribution function $f_\alpha(t, \mathbf{x}, \mathbf{v}_\alpha)$ is used to describe the amount of charged particles of species α, mass m_α and charge q_α having the velocity $\mathbf{v}_\alpha$ at the position $\mathbf{x}$ and time t. In a plasma, the charged particles move under the effect of the Lorentz force $\mathbf{F} = q_\alpha \left(\mathbf{E} + \mathbf{v} \times \mathbf{B}\right)$ where $\mathbf{E}$ and $\mathbf{B}$ are respectively the electric and the magnetic field seen by the particle. Considering particles of species α, the Vlasov equation is usually expressed as follows

$$\frac{\partial f_\alpha}{\partial t} + \mathbf{v}_\alpha \cdot \nabla f_\alpha + \mathbf{F} \cdot \frac{\partial f}{\partial \mathbf{p}_\alpha} = g_\alpha(t). \tag{6.1}$$

For a collision-less plasma, the term $g(t)$ is reduced to zero. To generalize the motion of the particles in the relativistic case, we introduce the Lorentz factor $\gamma_\alpha = \sqrt{1 + \frac{p_\alpha^2}{m_\alpha^2 c^2}}$ so that $\mathbf{v}_\alpha = \frac{\mathbf{p}_\alpha}{m_\alpha \gamma_\alpha}$.

To describe entirely the electromagnetic interaction occurring between the charged particles of the plasma, the Vlasov kinetic equation needs to be coupled with the

Maxwell equations

$$\nabla \times \mathbf{B} = \mu_0 \mathbf{j} + \frac{1}{c^2} \frac{\partial \mathbf{E}}{\partial t} \tag{6.2}$$

$$\nabla \times \mathbf{E} = -\frac{\partial \mathbf{B}}{\partial t} \tag{6.3}$$

$$\nabla \cdot \mathbf{E} = \frac{\rho}{\varepsilon_0} \tag{6.4}$$

$$\nabla \cdot \mathbf{B} = 0 \tag{6.5}$$

with ρ the charge density and $\mathbf{j}$ the current density vector.

Integrating the Vlasov equation leads to the plasma fluid description and the magneto-hydrodynamics equations. Fluids are then described by the momenta: the density, the local mean velocity $\mathbf{u}$ and the pressure p. The first order momentum equation corresponds to the continuity equation describing the local charge conservation in the plasma

$$\frac{\partial \rho}{\partial t} + \nabla \cdot (\rho \mathbf{u}) = 0. \tag{6.6}$$

The second momentum equation describes the motion of the fluid

$$\partial_t \mathbf{p} + \mathbf{u} \cdot \nabla \mathbf{p} = q \left(\mathbf{E} + \mathbf{u} \times \mathbf{B} \right). \tag{6.7}$$

In laser-matter interaction, a kinetic approach is required to describe correctly the dominant collective and relativistic effects. The direct calculation of the Vlasov equation in 2D and 3D is numerically extremely expensive both in memory and in computational power since they require to solve the distribution functions for every species in every directions of the phase space (x, y, z, p_x, p_y, p_z).

The Particle-In-Cell description, usually referred to as the PIC method, was first imagined in the fifties in order to solve hydrodynamic problems (Harlow and Evans (1955); Amsden (1969)). In plasma physics, Particle-In-Cell methods became popular in the sixties thanks to the work of pioneers as J. M. Dawson, O. Buneman, R. W. Hockey and others (Dawson (1983); Buneman (1993); Hockney and Eastwood (1988); Birdsall and Langdon (2005)). They revealed relatively easy to program, to parallelize and particularly efficient in term of computational time to solve problems of plasma physics in comparison with pure Eulerian resolutions. On the most powerful super-computers, 3D simulations are now accessible for some specific applications (for short pulse interaction for instance with small targets or in dilute gas jets) and is becoming more and more usual.

The Particle-in-Cell codes then proved to be well adapted to the simulation of high-intensity laser-plasma interaction. The basic scheme of this method is composed of a time loop of four steps. They are described in Fig. 6.1. First, the species distribution $f_\alpha(\mathbf{x}, \mathbf{p})$ are discretized both in space and momentum into a finite number of pieces that are called super-particles (or macro-particles). The super-particles

have a weight w_p, some kinetic properties as for a classical particle $\mathbf{v}_p$, $\mathbf{p}_p$, a position on the grid $\mathbf{x_p} = (x_p, y_p, z_p)$ and a shape factor $S(x)$ that determines the spatial profile of the particle. The sum of all the super-particles spatially allocated in the whole domain of simulation enables to rebuild the distribution. Moreover, the initial space-momentum distribution is considered to initialize the super-particle position and momentum. The construction can be ordered or locally randomized. The super-particles move in the domain depending on their momentum and the local fields according to the relativistic motion equations as for a classical particle. This can be demonstrated showing that a piece of distribution is conserved all along the characteristics $(\mathbf{x}, \mathbf{p})$ (Drouin (2009)). This step is represented by the blue panel in Fig. 6.1 and is described in section 6.3. The initial electromagnetic field can be determined using the Poisson equation (6.4) and the Maxwell-Faraday equation (6.3) from the initial distributions.

The electromagnetic fields are solved using a spatial and time discretization of the Maxwell equations. This step is represented by the green panel in Fig. 6.1 and is further described in section 6.2.

In order to calculate the current induced by the movement of the super-particles for the calculation of the fields, an interpolation technique is used depending on the considered shape factor. This step constitutes the transfer of information from the matter to the Maxwell grid shown via the orange panel in Fig. 6.1. Inversely, the newly calculated fields have to be considered to push the particles to their next positions. The fields from the Maxwell grid seen by the super-particles at their positions are also determined by an interpolation technique depending on the shape factor. This constitutes the last step in pink in Fig. 6.1. The interpolation is described in section 6.4.

The Particle-In-Cell approach can be applied on a wide range of issues with its basic form but also has the advantage to be quite easily enriched with many physical models including the binary collision between particles, ionization processes, inelastic collision (Bremsstrahlung) and recently quantum electrodynamics effects.

Among the most famous codes, we can quote Osiris developed by people from the IST and UCLA (Fonseca *et al.* (2002)), Epoch an opensource code developed at the University of Warwick that was one of the first to include radiative and QED effects (Bennett (2015)), PIConGPU an opensource very-efficient code developed at the Helmhotz Zentrum Dresden Rossendorf and optimized for GPU clusters (Burau *et al.* (2010)), Warp, Remp, Tristan, Smilei, Picls, VLPL (Pukhov (1999)), Picante (Sgattoni *et al.* (2015)), LSP an hybrid PIC code, Aladyn (Benedetti *et al.* (2008)), PICsar, VPIC (Bowers *et al.* (2008)), Vorpal (Nieter and Cary (2004)), PSC (Ruhl (2005)), Ocean developped by R. Nuter at the laboratory CELIA in Bordeaux, ELMIS (Gonoskov (2013)), Picador (Bastrakov *et al.* (2012)) and CHIPIC (Zhou *et al.* (2009)).

Intense efforts have been made to optimize and parallelize the PIC scheme on different kind of architectures including both GPUs (Hönig *et al.* (2010); Bastrakov

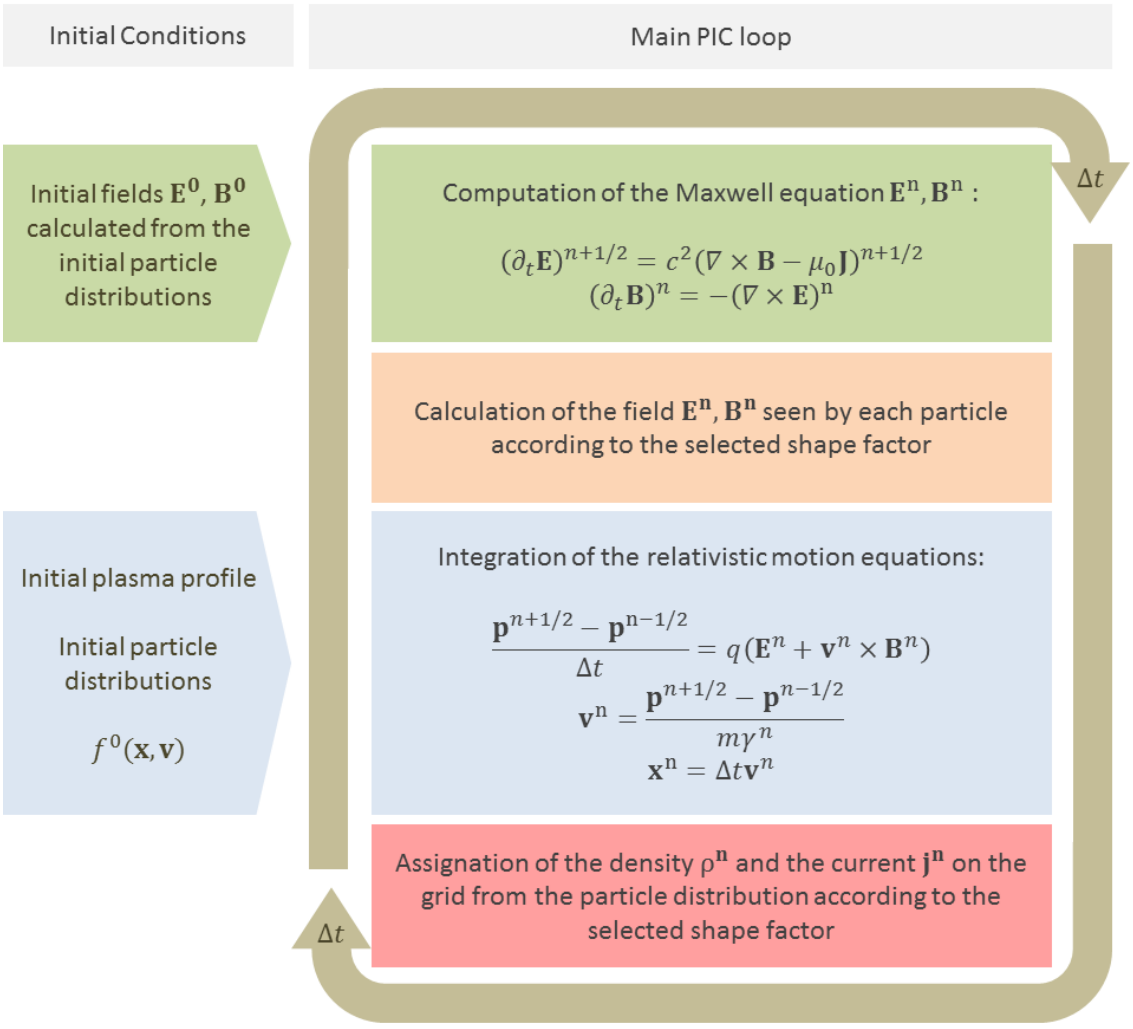

Figure 6.1: The successive steps making up a classical PIC iteration.

et al. (2012)), CPUs (Bastrakov *et al.* (2012); Germaschewski *et al.* (2013), Fonseca *et al.* (2013)) and more recently on the next generation of Intel MIC processors (Nakashima (2015); Surmin *et al.* (2015)). Recent reviews on the PIC method can be found in the literature (Tskhakaya *et al.* (2007)).

In this thesis, we use the PIC code Calder developed at the CEA, DAM, DIF (Lefebvre *et al.* (2003)).

6.2 The electromagnetic solver

6.2.1 The solver of K. Yee

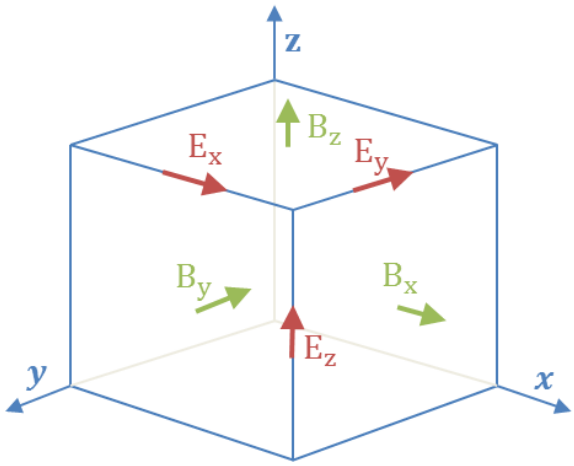

Figure 6.2: The K. Yee cartesian discretization of the Maxwell equations.

Maxwell equations can be solved using a wide range of numerical methods. In the field of laser-plasma interaction, many Particle-In-Cell codes have adopted the finite difference time domain method of K. Yee (Yee *et al.* (1966)) due to the simplicity of its implementation and its relative computational rapidity. As described in Fig. 6.2 for a Cartesian space discretization, fields are carefully decomposed and distributed on the space grid (on the example, a three dimension grid) so that the partial space derivative in the Maxwell Equation becomes centered differences. Electric field and magnetic field are solved turn by turn every half time steps so that the partial time derivatives are also centered differences. The discretization scheme is written

$$(\partial_t \mathbf{E})^{n+1/2} = c^2 \left(\nabla \times \mathbf{B} - \mu_0 J\right)^{n+1/2} \tag{6.8}$$

$$(\partial_t \mathbf{B})^{n} = -\left(\nabla \times \mathbf{E}\right)^{n}. \tag{6.9}$$

The time derivative is calculated at the first order so that

$$(\partial_t \mathbf{F})^{n+1/2} \equiv \frac{\mathbf{F}^{n+1} - \mathbf{F}^{n}}{\Delta t} \tag{6.10}$$

The space operator ∇ is classically defined as follows

$$\nabla = (\partial_x, \partial_y, \partial_z,). \tag{6.11}$$

$$\tag{6.12}$$

The partial space derivative is defined as

$$\partial_x F_{i+1/2,j,k} = \left(F_{i+1,j,k} - F_{i,j,k}\right)/\Delta x \tag{6.13}$$

For a plane electromagnetic wave, the respect of the Courant-Friedrichs-Lewy condition

$$1 \geq (c\Delta t)^2 \left(\frac{1}{\Delta x^2} + \frac{1}{\Delta y^2} + \frac{1}{\Delta z^2} \right) \tag{6.14}$$

ensures no de-phasing between electric and magnetic fields. The relative error on the frequency ω is of order two in space and time due to the centered method. In one dimension, this numerical dispersion can be avoided for $c = \Delta x/\Delta t$.

6.2.2 Numerical Čerenkov and improved Maxwell solvers

The Vavilov-Čerenkov effect is the emission of electromagnetic radiation when a charged particle travels faster than the phase velocity of the light in dielectric media in which the speed of light is below c. In the vacuum the emission is not possible since we always have $v_{e^-} < v_\phi$. The FDTD dispersion, given by

$$\left(\frac{\sin \omega \Delta t/2}{c\Delta t} \right)^2 = \left(\frac{\sin k_x \Delta x/2}{c\Delta x} \right)^2 + \left(\frac{\sin k_y \Delta y/2}{c\Delta y} \right)^2 + \left(\frac{\sin k_z \Delta z/2}{c\Delta z} \right)^2 \tag{6.15}$$

for a wave of the form $\exp(i\mathbf{k} \cdot \mathbf{r} - i\omega t)$, does not reproduce the expected physical dispersion. The method exhibits numerical artefacts along the grid axis directions. The dispersion is only respected in the diagonal directions. The Yee method allows for some modes to travel with a velocity v_ϕ below the speed of light c in the vacuum. In the case of the propagation of relativistic electrons so that $v_{e^-} > v_\phi$, the numerical scheme induces a numerical Čerenkov effect even in the vacuum. For instance, this is the case in simulation of laser accelerated particles. Furthermore, the self-fields are also incorrect.

In order to fight against the numerical Čerenkov and improve the control on the dispersion, the FDTD scheme has been modified in various ways. It has been first improved by the addition of anisotropic coefficients on the differential operators (Pukhov (1999); Juntunen and Tsiboukis (2000); Vay *et al.* (2011); Cowan *et al.* (2013); Lehe *et al.* (2013)). The Čerenkov can also be reduced by artificially increasing the numerical value of the speed of light in vacuum c. Implicit methods have also been developed (Zagorodnov *et al.* (2003); Zagorodnov and Weiland (2005); Drouin (2009)) with better dispersion but in PIC codes, explicit schemes are still widely used for their computational efficiency. The Maxwell equations can also be solved with spectral solvers in the Fourier domain. These solvers perfectly respect the dispersion but are more expensive than explicit methods. Another way to suppress the spurious Čerenkov consists on filtering the radiations (Greenwood *et al.* (2002, 2004); Vay *et al.* (2011)). Despite efficient, this method can also affect the physics. The use of high-order explicit scheme, finite volume and finite element Maxwell solvers for PIC codes has been studied in Fochesato and Bouche (2006).

6.3 Integration of the Newton-Lorentz motion equations

The relativistic Newton-Lorentz equations of motion governing the behavior of a super-particle in an arbitrary local electric $\mathbf{E}$ and magnetic field $\mathbf{B}$ can be written

$$\frac{d\mathbf{p}_\alpha}{dt} = q_\alpha \left(\mathbf{E} + \mathbf{v}_\alpha \times \mathbf{B}\right) \tag{6.16}$$

$$\mathbf{p} = m_\alpha \gamma \mathbf{v}_\alpha \tag{6.17}$$

Different numerical schemes, explicit or implicit, can be used to integrate the motion equations. One of the most popular and extensively scheme used so far in Particle-In-Cell codes is the method of Boris which consists in a separate update of the velocities and the new particle positions every half time step. Such a method is usually referred to as a leap-frog integrator. These methods, although developed more than 40 years ago, have proved to be fast, easy to implement and robust.

6.3.1 The Boris Scheme

The Boris particle pusher is a centered-difference second-order explicit method developed in the seventies (Boris (1970),Boris (1970),Birdsall and Langdon (2005); Tajima (2004)), following the work of Buneman (1993) which can be written as follows in its relativistic form

$$\frac{\mathbf{p}^{n+1/2} - \mathbf{p}^{n-1/2}}{\Delta t} = q_\alpha \left(\mathbf{E}^n + \frac{1}{c}\frac{\mathbf{p}^{n+1/2} + \mathbf{p}^{n-1/2}}{2\gamma^n m_\alpha} \times \mathbf{B}^n\right) \tag{6.18}$$

$$\gamma^n = \sqrt{1 + \left(p^{n-1/2} + \Delta t \frac{qE^n}{2m}\right)} \tag{6.19}$$

$$\mathbf{v}^{n+1/2} = \frac{\mathbf{p}^{n+1/2}}{m\gamma^{n+1/2}} \tag{6.20}$$

$$\mathbf{x}^{n+1} = \mathbf{x}^n + \Delta t \mathbf{v}^{n+1/2} \tag{6.21}$$

where n is the discrete time step and Δt the time difference so that $t = n\Delta t$.

In this scheme, the velocities are calculated at half-time $t + \Delta t/2$ whereas the electric acceleration and the magnetic rotation is determined using the quantities at the step time t. The position is updated using a simple explicit Euler integration from the half-time velocities. More specifically, the Boris scheme, also referred to as the *Boris rotation*, consists of a separated treatment of the accelerating action of the electric field and the rotational action of the magnetic field. It can be split up into three steps, the first one is the effect of the electric acceleration during a half time step, the second is referred to as the magnetic rotation and the third one corresponds to the second half timestep electric acceleration.

$$p^- = p^{n-1/2} + \Delta t \frac{qE^n}{2m} \tag{6.22}$$

$$p^+ - p^- = \Delta t \frac{q}{2m} \left(\frac{p^+ + p^-}{\gamma^n} \right) \times \mathbf{B^n} \tag{6.23}$$

$$p^{n+1/2} = p^+ + \Delta t \frac{qE^n}{2m} \tag{6.24}$$

The *Boris rotation* algorithm is a numerically efficient way to solve the previous system which can be simply understood geometrically. The first step of the magnetic rotation is the calculation of an intermediate vector $\mathbf{p'}$

$$\mathbf{p'} = \mathbf{p^-} + \mathbf{p^-} \times \mathbf{b} \tag{6.25}$$

This vector is then used to determine the momentum after the rotation $\mathbf{p^+}$

$$\mathbf{p^+} = \mathbf{p^-} + \mathbf{p'} \times \mathbf{s} \tag{6.26}$$

where

$$\mathbf{s} = \frac{2\mathbf{b}}{1 + b^2} \tag{6.27}$$

and

$$\mathbf{b} = q \frac{\mathbf{B}^n \Delta t}{2m}. \tag{6.28}$$

The magnetic rotation, Eq. 6.23, can be put to the following linear matrix equation $\mathbf{p}^+ = A\mathbf{p}^-$ where

$$A = \frac{2}{1 + b^2} \begin{bmatrix} -b_z^2 - b_y^2 & b_z + b_x b_y & -b_y + b_z b_x \\ b_x b_y - b_z & -b_x^2 - b_z^2 & b_x + b_z b_y \\ b_y + b_x b_z & -b_x + b_y b_z & -b_x^2 - b_y^2 \end{bmatrix}. \tag{6.29}$$

6.3.2 The J. L. Vay Scheme

Another leap-frog pusher has been published in Vay (2008) following the same base of J. P. Boris in order to address modeling issues of ultra-relativistic beam propagation and interaction with plasma background. For instance, in high-energy accelerators, particle beams travel near the speed of light with Lorentz factor close to 1 and the force from their own current-magnetic field compensates the electric field repulsion. This condition can be simply written $\mathbf{E} + \mathbf{v} \times \mathbf{B}$. Assuming that the pusher does an exact calculation, the particle velocity should remain unchanged as long as the electric field cancels the magnetic rotation. This condition in terms of discrete notation becomes

$$\mathbf{E} + \mathbf{v^{n-1/2}} \times \mathbf{B} = \mathbf{E} + \mathbf{v^{n+1/2}} \times \mathbf{B} \tag{6.30}$$

If we apply this condition to the Boris scheme 6.21-6.18, supposing $p^{n+1/2} = p^{n-1/2}$, the system has a solution only if $\mathbf{E} = \mathbf{B} = 0$. As a consequence, the condition can not be satisfied for non zero electromagnetic fields leading to the apparition of a spurious force.

J. L. Vay has proposed to change the calculation of the velocity in Eq. 6.18 by

$$\mathbf{v^n} = \frac{\mathbf{v}^{n+1/2} - \mathbf{v}^{n-1/2}}{2} \tag{6.31}$$

so that it becomes

$$\frac{\mathbf{p}^{n+1/2} - \mathbf{p}^{n-1/2}}{\Delta t} = q_\alpha \left(\mathbf{E}^n + \frac{\mathbf{v}^{n+1/2} + \mathbf{v}^{n-1/2}}{2} \times \mathbf{B}^n \right) \tag{6.32}$$

With this form, the condition 6.30 is perfectly respected. In particle beam simulations, the particle interactions are preferably performed in the boosted frame moving at the average beam velocity. J. L. Vay has demonstrated the robustness of his scheme in moving frame with constant electric and magnetic fields. However, no study has been devoted to the propagation of particles in a plane wave. This will be numerically addressed in the next part.

6.3.3 Comparison between the methods of J. L. Vay and J. P. Boris in plane waves

We compare the two methods in the case of a single charged particle moving in a plane wave both for linear and circular polarization, which, as we know, can be solved analytically. The accuracy of the schemes depends both on the discritization and the wave amplitude a_0. The particle considered is an electron. The comparison is made with different time steps dt determined so that the number of points per laser period N_p ranges from 10 to 1000. We considered three normalized laser amplitudes a_0 of 0.1, 1 and 10. In a plane wave, an electron has an oscillating trajectory and the period which depend on the amplitude of the pulse. The study is consequently made over a propagating distance of 5 oscillations, the required interaction time and number of iterations are therefore adjusted for each case.

We first start with the case of the circular polarization. The comparison of the evolution of the relative error on the energy and the position between the two schemes and the analytical calculation is shown in Fig. 6.3. For an amplitude below the relativistic threshold $a_0 \leq 1$, the trajectory of the particle is in average well described using the two schemes even with a few numbers of iterations per laser period. The Boris scheme is slightly better than the one of J. L. Vay. Nonetheless, for 10 points per laser period, the relative error on the trajectories given by both schemes are already significant and proves that we are reaching the minimum threshold for a correct description even for low intensities. For an intensity of $a_0 = 10$, the scheme of J. L. Vay reveals to be extremely good, even with a low discretization. This behavior is highlighted by the figure 6.4 in which the particle trajectories are plotted

with a time discretization of 50 points per laser period for two laser amplitudes of 0.01 and 10. In both cases, the scheme of J. L. Vay perfectly matches the analytical trajectory. However, as the laser amplitude increases, the trajectory described by the Boris scheme exhibits a slow drift, as clearly shown for the case $a_0 = 10$.

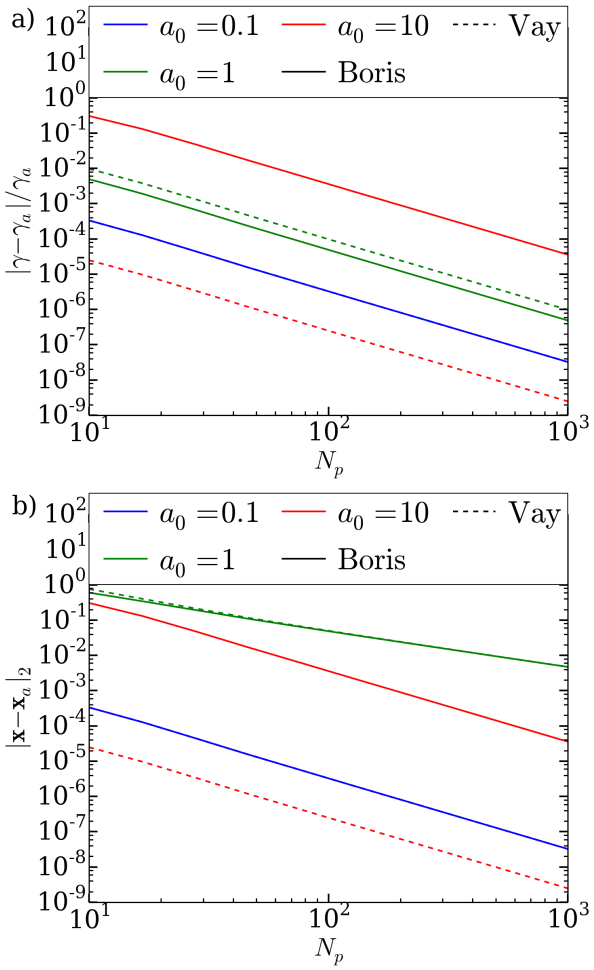

Figure 6.3: a) - Relative errors on the γ factor between the analytical γ_a and the numerically calculated trajectories of an electron in a circular plane wave using both the scheme of J. L. Vay (dashed line) and J. P. Boris (solid line) as a function of the number of points to describe a laser period N_p. b) - Relative error on the position $|\mathbf{x} - \mathbf{x_a}|_2$ with the similar parameters.

We now turn to the linear polarization case. Here, the energy given by the schemes of J. L. Vay and J. P. Boris are compared with the energy calculated analytically at the position obtained numerically. The linear trajectories can be integrated in the proper time of the particle but the direct calculation in the laboratory time is not possible, we therefore compare a semi-analytical calculation of the position (using a 4-th order Range-Kuta) with the positions obtained with the considered leap-frog

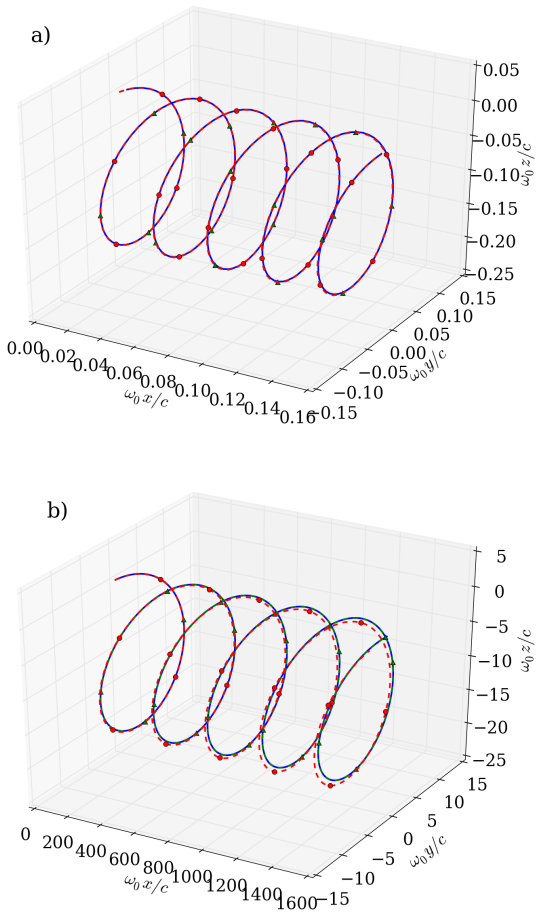

Figure 6.4: Particle trajectories in a circular plane wave calculated with the scheme of J. P. Boris (red dashed line), J. L. Vay (green dashed line) and analytically (blue) with 50 points per laser period and laser amplitudes of $a_0 = 0.1$ (a) and $a_0 = 10$ (b).

pushers where the positions are obtained from the numerically integration of the exact momenta. The energy and position comparisons are given in Fig. 6.5. The exact position is nonetheless plotted in the following trajectory curves.

Figures 6.5 show that both schemes are less accurate as the number of points per laser period diminishes and the laser amplitude increases. For low discretization, both schemes exhibit wrong trajectories, this can be seen in Figure 6.6.

Simulating single particle trajectories in plane waves, and to some extent in any electromagnetic wave, requires to be careful with the time-discretization, particularly when the field amplitude reaches the relativistic threshold of $a_0 = 1$. Our study demonstrates that for extremely-high intensities, with $a_0 \gg 1$, a correct description of the trajectories would require up to several hundred of points per laser period which is a severe constraint for 3D PIC studies. Furthermore, the error induced

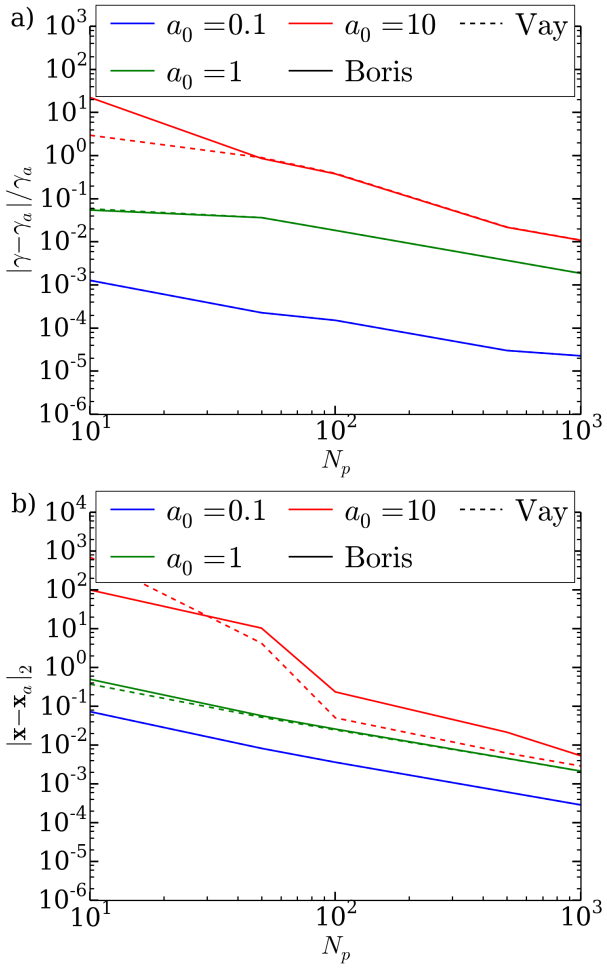

Figure 6.5: a) - Relative error on the γ factor between the analytical γ_a and the numerically calculated trajectories of an electron in a linear plane wave using both the scheme of J. L. Vay (dashed line) and J. P. Boris (solid line) as a function of the number of points to describe a laser period N_p. b) - Relative error on the position $|\mathbf{x} - \mathbf{x_a}|_2$ with the similar parameters.

by the particle pusher is increased by the finite-difference Maxwell solver and the interpolation process on the Maxwell grid to get the fields seen by the particle at its position. All these constraints and approximations make the PIC approach a bad candidate to simulate few particles interaction with electromagnetic fields. Nonetheless, inside a plasma, particles mainly act collectively under the low-frequency fields induced by charge separation effects or inner instabilities. Particles usually interact on a short distance with the laser fields since their trajectories are rapidly modified by the collective effect. In such a configuration, the PIC approach reveals an efficient tool to simulate overall behaviors where single particle trajectories weakly matter.

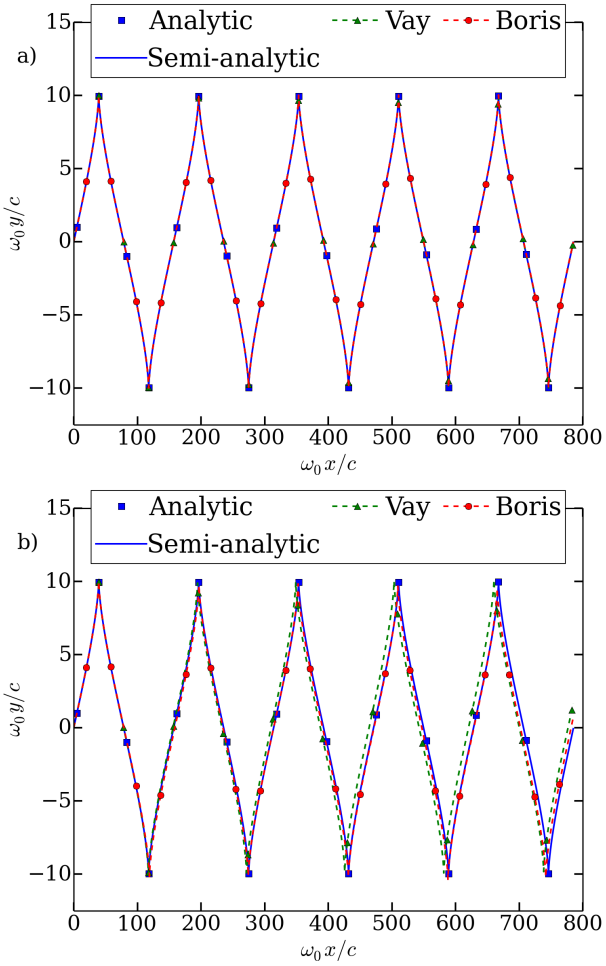

Figure 6.6: Particle trajectories in a linear plane wave calculated with the scheme of J. P. Boris (red dashed line), J. L. Vay (green dashed line), the semi-analytically (blue line) and analytically (blue markers) with a laser amplitude of $a_0 = 10$ and discretizations of 100 (a) and 50 (b) points per laser period.

6.4 The particle current and the field interpolation

The current assignation and the field interpolation are two steps which use interpolation functions in order to make the connection between the super-particles and the fields (Birdsall and Langdon (2005); Tajima (2004)). This step is also called weighting.

The current assignation consists on calculating the current $\mathbf{j}$ (and also the density ρ) on a grid cell induced by the nearby propagating particles. On the different points of the grid i, the grid charge density ρ_i at the position x_i is calculated from the charge

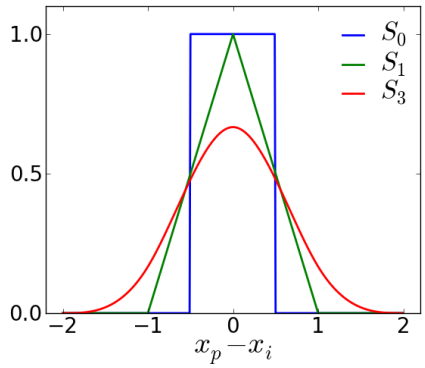

Figure 6.7: Splines of order 0, 1 and 3 used as a shape factor for the particles.

q_p and the local density n_p of each particle of number p located at position x_p

$$\rho_i = \rho(x_p) = \sum\nolimits_p q_p n_p S^k \left(|x_i - x_p|\right). \tag{6.33}$$

Similarly, the current j_i on the grid cell of number i corresponds to

$$j_i = j(x_p) = \sum\nolimits_p q_p n_p v_p S^k \left(|x_i - x_p|\right). \tag{6.34}$$

The current is then injected in Eq. 6.9 for the Maxwell calculation step.

In the motion equation, the electromagnetic fields at the position of the particle, $\mathbf{E}_p$ and $\mathbf{B}_p$, are required. These fields are determined similarly by interpolation on the discrete Maxwell grid from the fields $\mathbf{E}_i$ and $\mathbf{B}_i$ located around.

$$E_p = \sum\nolimits_i E_i S^k \left(|x_p - x_i|\right) \tag{6.35}$$
$$B_p = \sum\nolimits_i B_i S^k \left(|x_p - x_i|\right). \tag{6.36}$$

In such a method, the shape factor S characterizes the interpolation method and determines the spatial expansion of the super-particles. The shape factor can be arbitrary chosen but has to be similar during both steps or artificial forces can appear. In PIC codes, the shape functions are standard B-splines which are defined as the successive convolution products of the rectangular function by itself $S^k = (S_0 * S_0 * \cdots * S_0)_{k\ times}$ where $S_0 = 1_{[-1/2;1/2]}$. For every order, S^k satisfies the property $\sum_i S^k (x_j - x_i) = 1$ necessary to theoretically have the charge and density conservation. Shape factors of order $k = 0$ to $k = 3$ are shown in Fig. 6.7. Order $k = 0$ only affects one grid cell and the arbitrary order k affect $k - 1$ grid cells. The order $k = 3$ is written

$$S^3 = \begin{cases} \frac{1}{2}|x|^3 - x^2 + \frac{2}{3} & 0 \leq |x| \leq 1 \\ \frac{3}{4}\left(1 - \frac{1}{2}x\right)^3 & 1 < |x| \leq 2 \\ 0 & |x| > 2 \end{cases} \tag{6.37}$$

The numerical heating is an artificial increase of the energy due to the numerical approximations. This phenomenon can happen in Particle-In-Cell codes. High order shape factors play an important role to limit the numerical heating and ensure better charge and energy conservation. If we consider an initially cold, collision less (only electromagnetic interaction are taken into account) and neutral plasma, a perfect shape factor results in a perfect equilibrium so that particles remain immobile. This constitutes a possibility to test the validity of a code.

The Yee scheme ensures that the discrete Gauss equation and the discrete divergence of the magnetic field are verified in the resolution of the Ampere and the Faraday discrete equations (Eqs. 6.9) at every time step if the initial conditions respect the Gauss law and the magnetic field divergence, if the discrete operator $\nabla \cdot (\nabla \times \mathbf{B})$ of a vector field is always equal to 0 and if the charge conservation (Eq. 6.6) is always satisfied (Barthelmé (2005)).

The use of a shape factor for the current and density calculation as presented above does not enable the exact charge conservation. The field solving can therefore become unphysical as rapidly as the discretization is large. Several solutions have been developed to ensure a better charge conservation with the Yee solver.

A first possibility is the Boris correction (Boris (1970)) in which the electric field is corrected at every time after its calculation with the Ampere equation. The electric field $\mathbf{E}$ is modified by the addition of an electrostatic term so that

$$\mathbf{E}_{cor} = \mathbf{E} - \nabla\varphi \tag{6.38}$$

Where

$$\nabla^2\varphi = \nabla \cdot \mathbf{E} - \frac{\rho}{\varepsilon_0}. \tag{6.39}$$

Although it is computationally expensive due to the resolution of the Laplace operator, this method was widely used in the past before the recent apparition of more efficient techniques. It is implemented in the PIC code Calder using the conjugate gradient method.

Current projection numerical scheme can be directly derived from the continuity equation. The Villasenor-Buneman method was first developed for B-splines of order one and two (Villasenor and Buneman (1992)). An algorithm that ensures the charge conservation for any order has been published by Esirkepov (2001).

6.5 Implementation of the radiation cooling effect

The radiation radiation damping was first implemented in a PIC code in Zhidkov *et al.* (2002) using the LAD description. Recently, a significant number of PIC codes have been modified to include a radiation damping model. The LL description is one of the most considered. Epoch is one of the first codes that was improved

with this model, as described in Ridgers *et al.* (2012) and Ridgers *et al.* (2013), based on previous publications Kirk *et al.* (2009) and Duclous *et al.* (2011). In the code PICLS, the model of Sokolov has been implemented as described in Capdessus *et al.* (2012, 2013, 2014). These works have been followed by many groups (Nakamura *et al.* (2012); Green and Harvey (2015)). A detailed comparison between the different models for PIC codes has been done in Vranic *et al.* (2015).

6.5.1 Description of the continuous radiation loss implementation

In our code, we consider an approximation of the Sokolov model keeping only the term with the radiated power $P_{\rm rad}$ in the momentum equation. The equations of motion (2.38) are numerically solved using the second-order leap-frog method of J.-L. Vay (Vay (2008)) including the radiation losses.

In the classical radiative approach (Sokolov *et al.* (2009)), the motion equations with the Sokolov radiation (described in 2.1.2) damping can be numerically solved as follows. The radiation force is composed of two terms $e\left[\delta v \times \mathbf{B}\right]$ and $\mathbf{v}\gamma^2\left(\delta v \times \mathbf{f}_L\right)/c^2$ where $\mathbf{f}_L$ is the Lorentz force. At integer time, the Lorentz force corresponds to

$$\mathbf{f}_L = \frac{q_p}{m_p}\left(\mathbf{E}^n + \mathbf{v}_p^n \times \mathbf{B}^n\right) \tag{6.40}$$

The velocity at integer time corresponds to $\mathbf{v}_p^n = (\mathbf{v}_p^{n+1/2} + \mathbf{v}_p^{n-1/2})/2$. Using a Boris scheme, the average velocity becomes $v_p^n = (v_p^{n+1/2} + v_p^{n-1/2})/(2\gamma_p^n)$ where $\gamma_p^n = \sqrt{1 + (\mathbf{p}_p^{n-1/2} + q\Delta t/2\mathbf{E}^n)^2/(m_p c)^2}$. The term δv^n therefore corresponds to

$$\delta v^n = \frac{\tau_0}{m_p}\frac{\mathbf{f}_L^n - \mathbf{v}_p^n\left(\mathbf{v}_p^n \cdot \mathbf{E}^n\right)}{1 + \tau_0\left(\mathbf{v}_p^n \cdot \mathbf{E}^n\right)/m_p c} \tag{6.41}$$

The two terms in the radiation force are similarly calculated at the integer time from δv^n, f_L^n and B^n. The classical pusher is first completed providing the new radiation-less momenta of the super-particle $\mathbf{p}_p^{n+1/2} = m_p\gamma_p^{n+1/2}\mathbf{v}_p^{n+1/2}$:

$$\frac{\gamma_p^{n+1/2}\mathbf{v}_p^{n+1/2} - \gamma_p^{n-1/2}\mathbf{v}_p^{n-1/2}}{\Delta t} = \frac{q_p}{m_p}\mathbf{f}_L^n. \tag{6.42}$$

$$\tag{6.43}$$

The radiation friction terms in the calculation of the final momenta are included after the classical pusher:

$$\mathbf{p}_p^{n+1/2} = \mathbf{p}_p^{n+1/2} + q\Delta t\left(\delta v_p^n \times \mathbf{B}^n\right) - \Delta t\mathbf{v}_\mathbf{p}^\mathbf{n}\gamma_p^{n2}\left(\delta v_p^n \times \mathbf{f}_L^n\right)/c^2 \tag{6.44}$$

The velocity is consequently updated as follow:

$$\mathbf{v}_p^{n+1/2} = \frac{\mathbf{p}_p^{n+1/2}}{m_p\sqrt{1+\left(\mathbf{p}_p^{n+1/2}/m_pc\right)^2}}, \tag{6.45}$$

and the position thus determined:

$$\mathbf{x}_p^{n+1} = \mathbf{x}_p^n + \Delta t\mathbf{v}_p^{n+1/2} + \delta v^n \tag{6.46}$$

In the code Calder, we have also simplified the previous form to have an extension to the quantum regime and neglect the small terms. The radiation friction is reduced to a single term in the momentum equation depending on the radiated power $P_{\rm rad}$ that can be calculated with the quantum cross section as presented in section 2.1. By this way, the continuous description can be coupled to the discontinuous Monte-Carlo approach. First, we determine the quantum parameter χ_p^n from $\mathbf{E}^n = \mathbf{E}_\parallel^n + \mathbf{E}_\perp^n$ and $\mathbf{B}^n$ using the following relation

$$\chi_p^n = \frac{\gamma^n}{E_s}\left[(\mathbf{E}_\parallel^n/\gamma^n)^2 + (\mathbf{E}_\perp^n + \mathbf{v}_p^n \times \mathbf{B}^n)^2\right]^{1/2} \tag{6.47}$$

The radiated force therefore becomes

$$\mathbf{f}_{\rm rad}^n = -\frac{P_{\rm rad}(\chi_p^n)\mathbf{v}_p^n}{c^2} \tag{6.48}$$

Atfer the classical pusher, the velocity is updated according to

$$\mathbf{v}_p^{n+1/2} = \mathbf{v}_p^{n+1/2} - \frac{\mathbf{f}_{\rm rad}^n}{m_p\gamma^{n+1/2}} \tag{6.49}$$

This ensures that the stability of the magnetic rotation is not affected by the radiation losses.

6.5.2 Implementation of the discontinuous radiation loss description

When its quantum parameter χ_{e^-} approaches 1, an electron can emit a few photons with energies comparable to the electron kinetic energy. The radiation force acting on the particles is sufficiently high to induce a straggling effect on the trajectories. This effect corresponds to the limit of the continuous model and the intrinsic stochasticity of the photon emission has to be taken into account.

In the discontinuous model, the deterministic radiation force is replaced by the emission of a discrete photon whose energy is calculated randomly using the cross section. We use a Monte-Carlo algorithm for this process. The algorithm is very

close to what has been implemented in EPOCH (Duclous *et al.* (2011); Kirk *et al.* (2009)) and is also inspired from Timokhin (2010), Elkina *et al.* (2011) and Nerush *et al.* (2011). Similar or close implementations have also been done in particle codes in Blackburn *et al.* (2014); Harvey *et al.* (2015) and in other PIC codes in Ji *et al.* (2014),Gonoskov *et al.* (2014),Wallin *et al.* (2015) and Green and Harvey (2015).

The super-particles are assigned an optical depth τ_p evolving with time according to the fields and particle energy variations:

$$\frac{d\tau_p}{dt} = \int_0^{\chi_p} \frac{d^2 N_\gamma}{d\chi dt} d\chi. \tag{6.50}$$

The final optical depth τ_p^f at which the emission occurs is calculated via a random draw of parameter $\xi \in [0,1]$ so that $\tau_p^f = -\log(-\xi + 1)$. When $\tau_p = \tau_p^f$, a discrete photon is emitted with an energy

$$\varepsilon_\gamma = \frac{\gamma m_e c^2 \chi_\gamma}{\chi_p}. \tag{6.51}$$

The value χ_γ is calculated by inverting the equation $P(0 \to \chi_\gamma) = \xi'$ where $\xi' \in [0,1]$ is a new random parameter, the cumulative distribution function $P(0 \to \chi_\gamma)$ gives the probability for a photon emission in the range $[0, \chi_\gamma]$

$$P(0 \to \chi_\gamma) = \frac{\displaystyle\int_0^{\chi_\gamma} F(\chi_p, \chi_\gamma) d\chi_\gamma}{\displaystyle\int_0^{\chi_p} F(\chi, \chi_\gamma) d\chi}, \tag{6.52}$$

The photon is emitted parallel to the electron momentum before emission p_i. The post-emission momentum p_f thus follows from momentum conservation

$$\mathbf{p}_f = \mathbf{p}_i - \hbar\mathbf{k} \quad \hbar\mathbf{k} = \frac{\varepsilon_{ph}}{c} \frac{\mathbf{p}_i}{|\mathbf{p}_i|}. \tag{6.53}$$

The choice of the momentum conservation implies that the energy is not exactly conserved. Let us call γ_i, γ_f and γ_γ the Lorentz factor before and after emission of the emitting electron and the normalized energy of the photon. The momentum of the emitted photon corresponds to $\mathbf{p}_\gamma = \hbar\mathbf{k}$. We can evaluate the error ε on the energy as follows

$$\begin{aligned}
\gamma_f^2 &= 1 + \frac{\mathbf{p}_i - \mathbf{p}_\gamma}{m_e c^2} && (6.54)\\
&= 1 + \frac{p_i^2}{m_e c^2} - 2\gamma_\gamma \frac{p_i}{m_e c^2} + \gamma_\gamma^2 && (6.55)\\
&= (\gamma_i - \gamma_\gamma)^2 - (\gamma_i - \gamma_\gamma)^2 + \gamma_i^2 - 2\gamma_\gamma \sqrt{\gamma_i^2 - 1} + \gamma_\gamma^2 && (6.56)\\
&= (\gamma_i - \gamma_\gamma)^2 + 2\gamma_\gamma \left(\gamma_i - \sqrt{\gamma_i^2 - 1} \right) && (6.57)
\end{aligned}$$

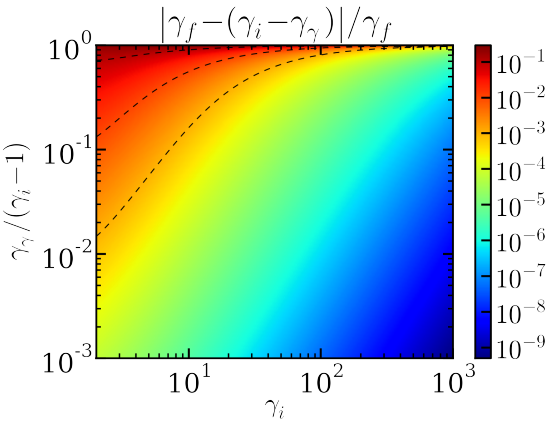

Figure 6.8: Relative error on the energy conservation using the momentum conservation for the discontinuous photon emission. The dashed line corresponds to the isocontours for 10^{-3}, 10^{-2} and 10^{-1}.

The error is consequently equal to

$$\varepsilon = 2\gamma_\gamma \left(\gamma_i - \sqrt{\gamma_i^2 - 1}\right) \underset{\gamma_i \to +\infty}{\longrightarrow} 0 \tag{6.58}$$

and tends to 0 when γ_i is extremely high. In order to get a view of the limit of this approximation, we have plotted in Fig. 6.8 the relative error defined as $\varepsilon_r = |\gamma_f - (\gamma_i - \gamma_\gamma)|/\gamma_f$. It appears that to consider that the energy relative error $\varepsilon_r \ll 1$, we should have an electron energy above $\gamma_{e^-} = 10$. The error is as high as the photon energy is close to the electron kinetic energy. This only happens in the quantum regime and fortunatly, this regime of interaction requires the electron energy to be highly relativistic. An alternative consists in giving priority to the energy conservation. In this case,

$$\gamma_f = \gamma_i - \gamma_\gamma \quad \mathbf{p}_f = \sqrt{\gamma_f^2 - 1}\frac{\mathbf{p}_i}{p_i} \tag{6.59}$$

6.5.3 Coupling between the descriptions

In order to deal with a wide range of χ values, both the continuous and discontinuous emission models are used in parallel (Duclous *et al.* (2011)) in our PIC code CALDER (Lobet *et al.* (2013)). We define $\chi_{p,s}$ the threshold value between the low and the high χ_p regions. The threshold between the classical and the quantum regime corresponds to $\chi_{p,s} \simeq 10^{-3}$.

Numerically, the algorithm makes use of a local sub-iterative method placed in the particle pusher as described in Fig. 6.9. At iteration n, let us consider a charged particle with momentum $\mathbf{p}_p^{n-1/2}$ and position $\mathbf{x}_p^n$ moving in an arbitrary field $\mathbf{E}^n$, $\mathbf{B}^n$.

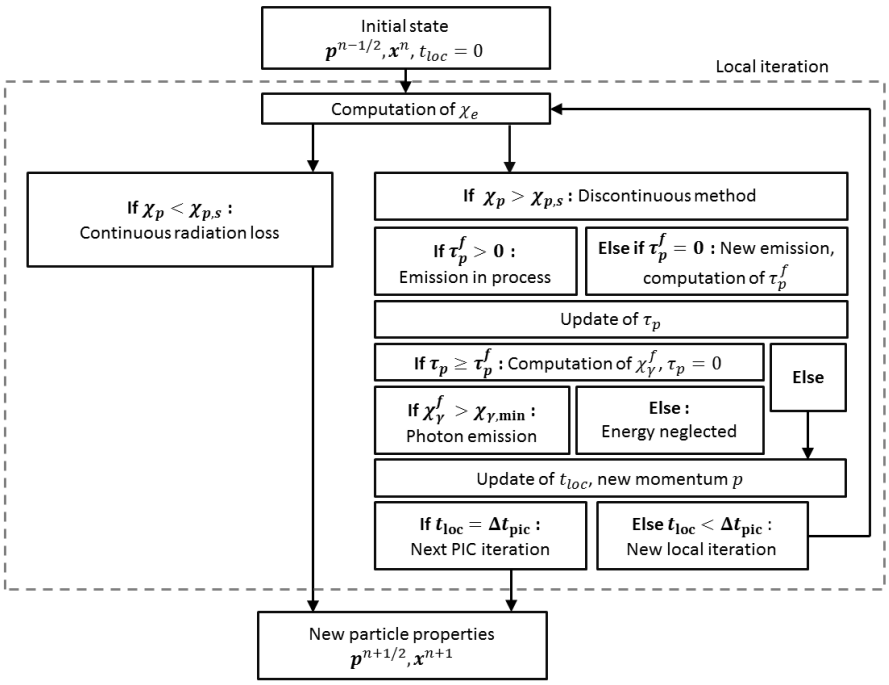

Figure 6.9: Description of the sub-iterative extension inside the particle pusher of the classical PIC iteration.

The local iteration starts by computing the quantum parameter of this particle χ_p. For $\chi_p > \chi_{p,s}$, the radiation losses are described by a Monte-Carlo algorithm. The process starts by the random calculation of a new optical depth τ_p^f. If the variable τ_p^f assigned to the particle is already calculated, it means that the process has previously started. The current optical depth τ_p initially set to zero increases as the particle propagates in a strong field. When the final optical depth is reached, the photon energy ε_γ is randomly determined using Eqs. (6.52) and (6.51). In order to eliminate the low-energy photons which weakly contribute to the physics, we use a threshold $\chi_{\min}^f$ calculated so that the radiated energy under this level is a negligible amount of the radiated energy.

$$\frac{\displaystyle\int_0^{\chi_{\min}^f} F(\chi_p, \chi_\gamma) d\chi_\gamma}{\displaystyle\int_0^{\chi_p} F(\chi_p, \chi_\gamma) d\chi_\gamma} < \epsilon. \tag{6.60}$$

The variable ϵ determines how negligible this energy is, in the code this parameter is set to 10^{-9}. If $\chi > \chi_{\min}^f$, a super-photon is emitted with the same weight, position

and propagation direction as the emitting super-particle. The local Monte-Carlo time $t_{\rm loc}$ corresponds to the time duration of the Monte-Carlo process inside the PIC iteration. It is updated after each process according to their duration $\Delta t_{\rm loc}$. If the emission duration $t_{\rm loc}$ reaches the duration of the PIC iteration $\Delta t_{\rm PIC}$, a break is made for synchronization at the end of the PIC iteration, $t_{\rm loc}$ is set to 0 but the current and final optical depths, τ_p^f and τ_p, are kept in memory to continue the emission process during the next PIC iteration. Then, the MC process goes on until the photon is emitted. The emission duration $t_{\rm emi}$ can be approximated using Eq. (6.50), assuming that the fields remain quasi-static during a PIC iteration and during the emission process:

$$\frac{d\tau_p}{dt}(\chi_p) \sim \frac{\tau_p^f}{t_{\rm emi}}. \tag{6.61}$$

Thus, the duration of a local iteration Δt_{loc} can be written:

$$\Delta t_{\rm loc} = \min\left(\beta t_{\rm emi}, \Delta t_{\rm PIC} - t_{\rm loc}\right) \tag{6.62}$$

where $\Delta t_{\rm PIC} - t_{\rm loc}$ is the remaining time before the end of the PIC iteration. Here, β is a factor chosen in $]0, 1]$ used to improve the integration accuracy. The particle momenta, and consequently χ_p, are computed after each Monte-Carlo sub-iteration whereas the fields and the particle positions are updated at the synchronization with the PIC iteration. The emitted super-photons are treated like the super-particles: they are pushed every PIC iteration and propagate ballistically without interacting with the matter.

For $\chi_p < \chi_{p,s}$, the particle is pushed until the end of the PIC iteration using the continuous radiation damping model with the quantum radiated power.

The various integrals involved in the radiative model are tabulated prior to the simulation in order to save computational time.

To summarize, we can distinguish different cases due to the decoupling between the PIC and the Monte-Carlo process. If the quantum parameter is sufficiently high, the super-particle can emit one or several photons during a PIC time step. If the super-particle loses too much energy, the emission regime can turn continuous and the PIC iteration is finished with the radiation damping model during the remaining time $\Delta t_{\rm PIC} - t_{\rm loc}$. The Monte-Carlo emission process can also last more than a PIC iteration, in this case a synchronization is made at the end of the PIC step and the super-particle properties (including the local fields) are updated classically.

6.5.4 Simulation tests

Constant magnetic field

We first consider the case of synchrotron radiation, also known as magnetic Bremsstrahlung, in which charged particles interact with a uniform and static magnetic field. Here,

χ_{e^-}	γ_0	B_z/B_0
1	3208	128
0.1	1015	40.6
0.01	320.8	12.8

Table 6.1: Synchrotron parameters. For each one, the Larmor radius is $R = 25c\omega_0^{-1}$.

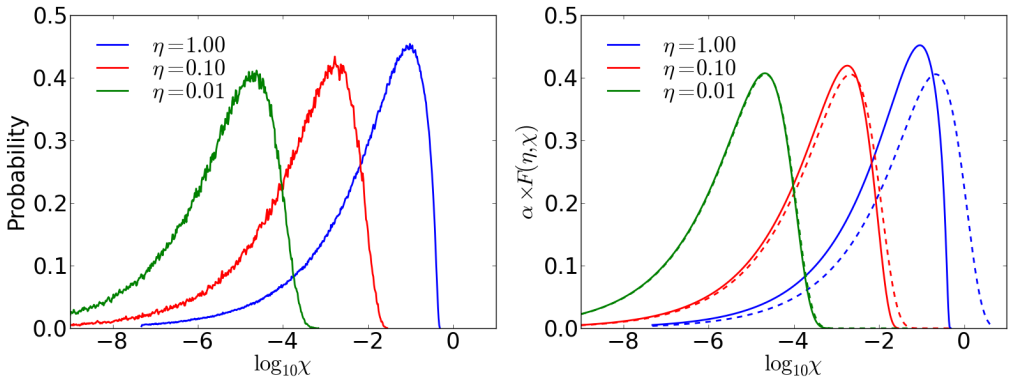

Figure 6.10: Photon distributions in $\log_{10}(\chi_\gamma^f)$: comparison between the simulations (a) and the synchrotron emissivity $F(\chi_{e^-}, \chi_\gamma)$ (b) in the classical regime (dashed lines) and the quantum regime (solid lines). The factor of normalization is $\alpha = \int_0^\infty F(\chi_{e^-}, \chi_\gamma) d\chi_\gamma$.

the particles are electrons having an initial momentum $p_{e^-,0}$ normal to the constant uniform magnetic field B_z. Without any radiation loss, the charged particles circle with a radius $R = p_{e^-,0}/|e|B_z$, an angular frequency $\omega_B = 2\pi|e|B_z/\gamma_{e^-,0}m_e$ and a quantum parameter $\chi_{e^-} = \gamma_{e^-,0}B_z/m_eE_s$.

For the different values of χ_{e^-} given in Tab. 6.1, Fig. 6.10 compares the photon distributions in $\log_{10}(\chi_\gamma^f)$ from the PIC simulations to the theoretical ones in the quantum and the classical regime. For these simulations, the particles can emit photons but they do not lose energy. The simulation starts with a group of super-electrons of low density $n_{e^-} = 10^{-4}n_c$ to avoid the electrostatic interaction. It shows that the synchrotron spectrum is correctly reproduced in both cases using the quantum correction.

For $\chi_{e^-} < 10^{-2}$, the classical emissivity is relatively close to the quantum one and thus constitutes a valid approximation. For $\chi_{e^-} = 1$, it can be seen that the classical emissivity allows emission of photons more energetic than the emitting particle. In this case, the quantum correction is necessary.

Energy balance of a single particle including the radiation reaction can be written

$$\frac{d\varepsilon}{dt} = q\mathbf{E}\cdot\mathbf{v} - P_{\text{rad}}(\chi_{e^-}). \tag{6.63}$$

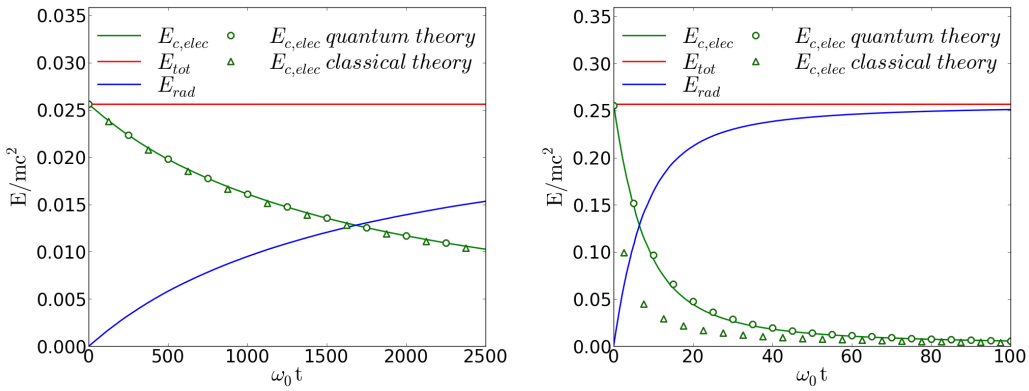

Figure 6.11: Evolution of the electron kinetic energy ε_{k,e^-}, radiated energy $\varepsilon_{\rm rad}$ and total energy $\varepsilon_{\rm tot}$ for $\chi_{e^-} = 0.01$ (a) and $\chi_{e^-} = 1$ (b). The simulation results are compared to the theory in the classical (triangle markers) and quantum regime (circle markers).

Fig. 6.11 shows the evolution of the electron energy for the simulations with χ_{e^-} initially equal to 1 and 0.01. The threshold is equal to $\chi_{e^-,s} = 10^{-3}$. The numerical solutions from Eq. (6.63) are plotted in the classical regime ($P_{\rm rad} \sim P_{\rm cl}$) and the quantum regime. For $\chi_{e^-} = 0.01$, the classical emissivity appears sufficient to approximate the radiation process. For $\chi_{e^-} \geq 1$, the classical regime underestimates the radiation losses, demonstrating that the quantum correction is required. The total energy is well conserved.

The particle energy distributions as a function of time t can be built integrating the probability functions (Sokolov *et al.* (2010)). We define f_γ and f_{e^-} the photon and the electron energy distribution respectively. The evolution of these distributions are given by the following couple of equations:

$$\frac{df_\gamma}{dt}(\gamma_\gamma, t) = \int_1^{+\infty} \frac{d^2N_\gamma}{dtd\gamma_\gamma}(\gamma_\gamma, \gamma) f_{e^-}(\gamma) d\gamma \tag{6.64}$$

$$\frac{df_{e^-}}{dtd}(\gamma_{e^-}, t) = -\int_1^{+\infty} \frac{d^2N_\gamma}{dtd\gamma_\gamma}(\gamma_\gamma, \gamma) f_{e^-}(\gamma) d\gamma + \int_{\gamma_{e^-}}^{+\infty} \frac{d^2N_\gamma}{dtd\gamma_\gamma}(\gamma_\gamma, \gamma) f_{e^-}(\gamma) d\gamma \tag{6.65}$$

Eq. 6.64 represents the total photon production rate as a function of the energy γ_γ at time t due to synchrotron radiation integrated over all the electron energies. Eq. 6.65 represents the evolution of the total electron energy distribution resulting from the radiation losses. A numerical integration of Eqs. 6.64 and 6.65 is performed using an explicit Euler method to get the time evolution of the distributions for the photons and the electrons for a quantum parameter $\chi_{e^-} = 1$. The comparison with the PIC simulation is presented in figs. 6.12 and 6.13.

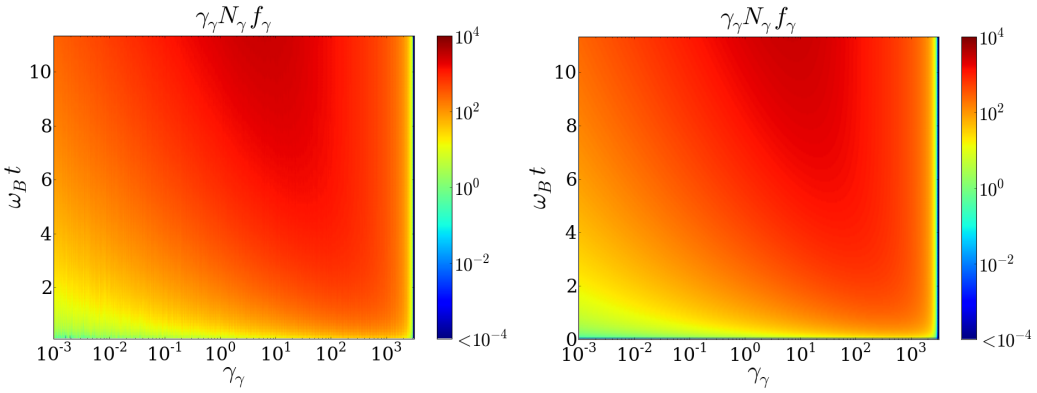

Figure 6.12: Time evolution of the photon energy distribution from the PIC simulation (a) and numerical integration of Eqs. 6.64 (b).

The distributions from the PIC simulation are well reconstituted demonstrating the correct behavior of the implemented Monte-Carlo scheme. At the beginning, high-energy electrons evolve with a quantum parameter $\chi_{e^-} \sim 1$ and the photon emission is very stochastic. Many photons are emitted with an energy of the order of the electrons resulting in the exponential decrease of the particle kinetic energy. The rapid broadening of the electron energy distribution is a consequence of the stochasticity (Fig. 6.13).

As the particles approach the classical regime $\chi_{e^-} \sim 10^{-3}$ (from $\omega_0 t \simeq 30$ corresponding to $\chi_{e^-} \sim 10^{-2}$), many photons are produced with a negligible energy $\gamma_\gamma/\gamma_{e^-} \ll 1$. The total radiated power is therefore weaker and the total particle energy stabilizes. The emission stochasticity is substantially reduced. As a consequence, the energy scattering observed in the quantum regime is reversed and the radiation reaction tends to reduce the particle energy spread (Neitz and Di Piazza (2013)).

Circularly polarized laser field

In this section, an electron beam interacts with a long duration and circularly polarized laser pulse of convention:

$$\mathbf{A} = \left(0, \frac{A_0}{\sqrt{2}}\cos(\xi), \frac{A_0}{\sqrt{2}}\sin(\xi)\right) \tag{6.66}$$

where $A_0/\sqrt{2}$ is the laser potential amplitude. Before the interaction, the electrons propagate with initial momentum $p_{\parallel,0}$ parallel to the laser propagation direction and Lorentz factor γ_0. In a plane wave, assuming a negligible radiation loss, the electron momentum and energy are related to the field vector potential according to:

$$\frac{d}{dt}\left(\gamma mc^2 - p_\parallel c\right) = 0 \quad ; \quad \frac{d}{dt}(p_\perp - eA) = 0. \tag{6.67}$$

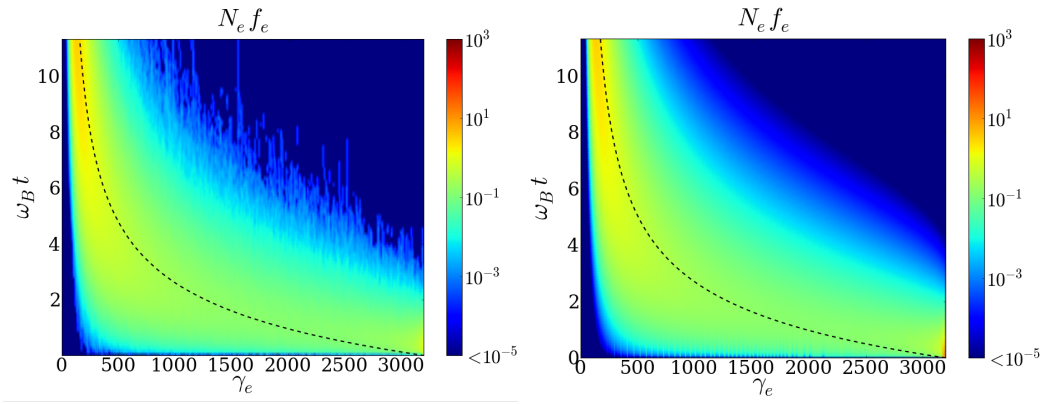

Figure 6.13: Time evolution of the electron energy distribution from the PIC simulation (a) and numerical integration of Eqs. 6.64 (b). Black curves represent the evolution of the average electron energy.

It follows:

$$\frac{p_\perp}{m_e c} = a_0/\sqrt{2} \tag{6.68}$$

$$\frac{p_\parallel}{m_e c} = \frac{1+a^2-\left(\gamma_0 - p_{\parallel,0}/m_e c\right)^2}{2\left(\gamma_0 - p_{\parallel,0}/m_e c\right)} \tag{6.69}$$

$$\gamma = \frac{1+a^2+\left(\gamma_0 - p_{\parallel,0}/m_e c\right)^2}{2\left(\gamma_0 - p_{\parallel,0}/m_e c\right)}. \tag{6.70}$$

For a counter-propagating particle with $\left|p_{\parallel,0}/m_e c\right| \gg a_0 \gg 1$, Eq. (6.69) and (6.70) can be approximated by

$$\frac{p_\parallel}{m_e c} \simeq \frac{a^2 - 4\gamma_0^2}{4\gamma_0} \quad ; \quad \gamma \simeq \frac{a^2 + 4\gamma_0^2}{4\gamma_0} \tag{6.71}$$

The parameter χ_{e^-} is then approximated by $\chi_{e^-} \simeq \gamma/E_s \left|E_0 - v_x B_0\right| \simeq 2\gamma E_0/E_s$ where E_0 and B_0 are the amplitude of the electric and the magnetic field. Simulations are performed in this configuration. A set of parameters is given in Tab. 6.2. The condition $\gamma_{e^-} \gg a_0$ ensures that the transverse momentum of the counter propagating electron beam is smaller than the longitudinal one in the plane wave. The problem is therefore reduced to a one-dimensional case. It shows that the quantum regime is reachable for a circularly polarized pulse of intensity up to 10^{22} Wcm^{-2} interacting with a 1 GeV counter-propagating electron beam. For simulations with $\chi_{e^-} = 0.1$ and $\chi_e = 1$, Fig. 6.14 shows that the electrons progressively convert their energy into photons as they interact with the electromagnetic wave. The simulation results are in good agreement with the numerical integration of the continuous model. The total energy is well conserved.

χ_{e^-}	$p_{\parallel,0}/mc$	a_0
1	-4000	72.858
0.1	-4000	7.2858
0.01	-2000	1.4572

Table 6.2: Wave parameters.

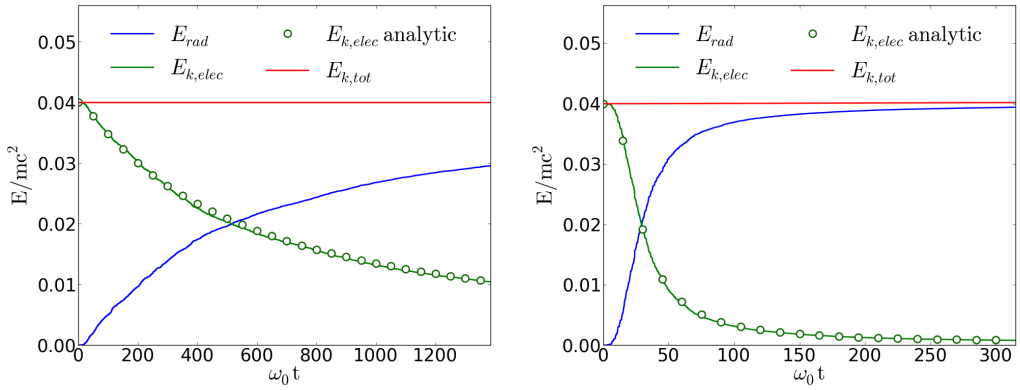

Figure 6.14: Evolution of the electron kinetic energy $E_{c,elec}$, radiated energy E_{rad} and total energy E_{tot} for $\chi_e = 0.1$ (left) and $\chi_e = 1$ (right). The continuous emission results are plotted with markers.

Again, the discontinuous description induces a straggling effect on the particle trajectories which turns out to be significant for high χ_{e^-} values. This phenomenon is clearly illustrated in Fig. 6.15: for randomly selected super-particles, the evolution of the parallel momenta is compared with the continuous emission results. Each energy jump corresponds to one emission. For $\chi_{e^-} \simeq 1$, one single photon can carry more than half of the emitting electron energy. The higher is the χ_{e^-} value, the faster is the energy damping of the particle. The straggling effect leads to the spread of the electron beam velocity.

6.6 Photon coalescence

The high emission rate of low energy super-photons can be prejudicial for the numerical efficiency of the simulations. They represent a large amount of the total number of simulated super-particles, having a costly consequence on the memory and the calculation speed. They furthermore weakly influence the simulated physics since they appear unlikely to convert into electron-positron pairs.

A method for particle merging has been proposed in Timokhin (2010) and reused

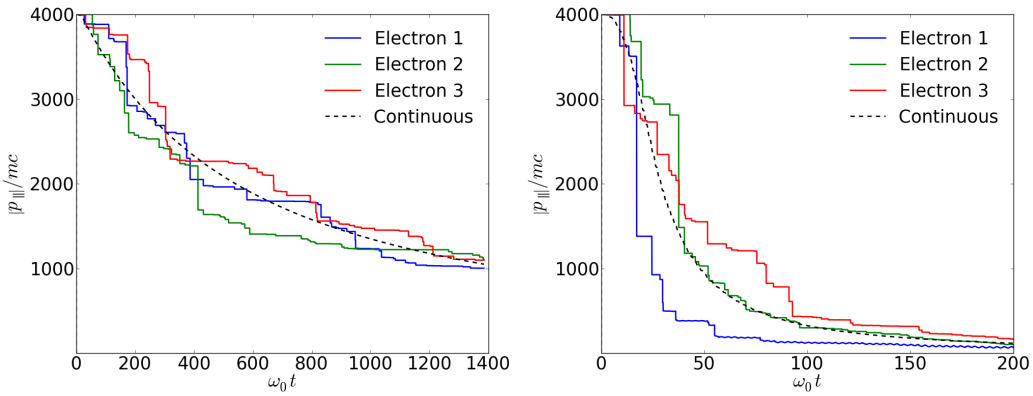

Figure 6.15: Evolution of the parallel momentum $p_\parallel$ for three electrons interacting with the circularly polarized laser field from the simulations of parameters $\chi_{e^-} = 0.1$ (a) and $\chi_{e^-} = 1$ (b). The dashed black line refers to the continuous emission.

in Nerush *et al.* (2011), as well as more recently in Luu *et al.* (2015) to prevent exponential growth of the photon number in a configuration of pair cascade. Here, an alternative method is presented. When a group of super-photons are sharing the same cell, pairs of super-photons are constituted and merge into new single one.

We consider two macro-photons of weights p_1, p_2, of energies $\hbar\omega_1$, $\hbar\omega_2$ and momenta $\hbar\mathbf{k}_1$, $\hbar\mathbf{k}_2$. Here, θ is the angle between the macro-photon trajectories so that $c^2\mathbf{k}_1 \cdot \mathbf{k}_2 = \omega_1\omega_2 \cos\theta$. After fusion, the new photon has properties p_3, $\hbar\omega_3$, $\hbar\mathbf{k}_3$. During the process, energy, momentum and weight have to be conserved :

$$p_3 = p_1 + p_2 \tag{6.72}$$

$$p_3\omega_3 = p_1\omega_1 + p_2\omega_2 \tag{6.73}$$

$$p_3\mathbf{k}_3 = p_1\mathbf{k}_1 + p_2\mathbf{k}_2. \tag{6.74}$$

However, one easily gets that Eq. 6.73 and 6.74 are not compatible when the macro-photons have different directions of propagation ($\cos\theta \neq 0$)

$$\begin{aligned} c^2\left(p_3\mathbf{k}_3\right)^2 &= \left(p_1\omega_1\right)^2 + \left(p_2\omega_2\right)^2 + 2\omega_1\omega_2\cos\theta \\ &\neq \left(p_3\omega_3\right)^2 \end{aligned} \tag{6.75}$$

In order to ensure the momentum conservation, the direction of the newly created photons is not restricted to the plane $(\mathbf{k}_1 \cdot \mathbf{k}_2)$. A transverse $\mathbf{k}_{3,\perp}$ momentum is added with amplitude

$$|k_{3,\perp}| = \frac{p}{c}\sqrt{2p_1p_2\left(\omega_1\omega_2 - c^2k_1k_2\cos\theta\right)}. \tag{6.76}$$

and the macro-photon momentum is then $\mathbf{k} = \mathbf{k}_3 + \mathbf{k}_{3,\perp}$.

Virtually, the apparition of a transverse momentum has no consequence in 1D and 2D simulations. In many configurations of laser-matter interaction, the synchrotron emission mainly occurs in a focused region of intense electromagnetic field. It results that the photons propagate outwards the target with close directions which, in consequence, tends to minimize the transverse momentum amplitude after merging. A filter can be used to match photons of only low energy, of low χ or of close propagating directions.

In practice, this particle merging is not used in the simulations presented in this thesis.

6.7 Implementation of the nonlinear Breit-Wheeler pair creation

Following the same approach as Section 6.5, pair production can be implemented numerically in a Particle-In-Cell code using a Monte-Carlo description (Kirk *et al.*, 2009; Timokhin, 2010; Duclous *et al.*, 2011; Elkina *et al.*, 2011; Gonoskov *et al.*, 2014; Green and Harvey, 2014; Harvey *et al.*, 2015) as described in Fig. 6.16. The photons are described as discrete macro-particles propagating at the speed of light c and interacting with the electromagnetic field as already considered for the discontinuous synchrotron radiation loss. The local electromagnetic field necessary to determine χ_γ is interpolated using the same shape factor as for the super-particles.

The photons are assigned an optical depth τ_{BW} evolving with time and space as they propagate in the electromagnetic field. The final optical depth at which pairs are generated corresponds to $\tau_{BW}^f = -\log(-\xi + 1)$ where ξ is randomly calculated. The crossed optical depth during the time interval dt can be computed according to the differential equation

$$\frac{d\tau_{BW}}{dt} = T_{nBW}(\chi_\gamma). \tag{6.77}$$

Inside the code, we determine from the remaining optical path and the cross-section if the time necessary to decay into pair, $t_{BW} \simeq (\tau_{BW}^f - \tau_{BW})/\frac{d\tau_{BW}}{dt}$, is longer than the PIC iteration. In this case, the photon will not be converted during the current time step. In the other case, the optical depth will be reached during the current time step, the position where the pair is created is simply computed from the current photon position and the remaining time to the pair creation. When the optical depth is reached, the photon decays into pairs. Energy of the new particles is computed using Eq. (4.6). For this purpose, we define $P(0 \to \chi_{e^-})$ the cumulative distribution function giving the probability for the electron (or the positron) to be emitted with

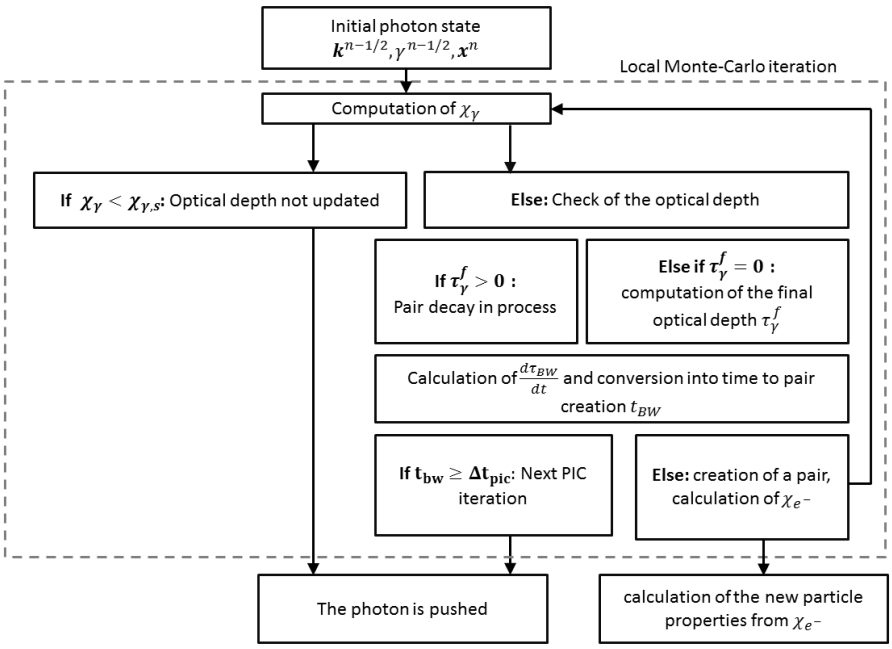

Figure 6.16: Scheme of the photon Monte-Carlo process inside the PIC code CALDER.

a quantum parameter in the range $[0; \chi_{e^-}]$:

$$P(0 \to \chi_{e^-}) = \frac{\displaystyle\int_0^{\chi_{e^-}} \frac{dN_{nBW}}{d\chi_{e^-}dt} d\chi_{e^-}}{\displaystyle\int_0^{\chi_\gamma} \frac{dN_{nBW}}{d\chi_{e^-}dt} d\chi_{e^-}}, \tag{6.78}$$

Computing a random parameter $\xi' \in [0, 1]$, emitted electron value $\chi_{e^-}^f = P^{-1}_{0\to\chi_{e^-}^f}(\xi')$ is obtained. For computational efficiency, the dimensionless function T and the cumulative distribution function P are tabulated.

Created super-particles get the weight and shape factor of the macro-photon and are thus classically treated. Obviously, the macrophoton is annihilated after pair creation. At high energies, emission direction is confined in a narrow cone of solid angle $\sim 1/\gamma$. Since photons are in the range of x-rays to gamma-rays, newly created pairs have a Lorentz factor $\gamma \gg 1$ which allows to use the approximation that the propagating direction is conserved.

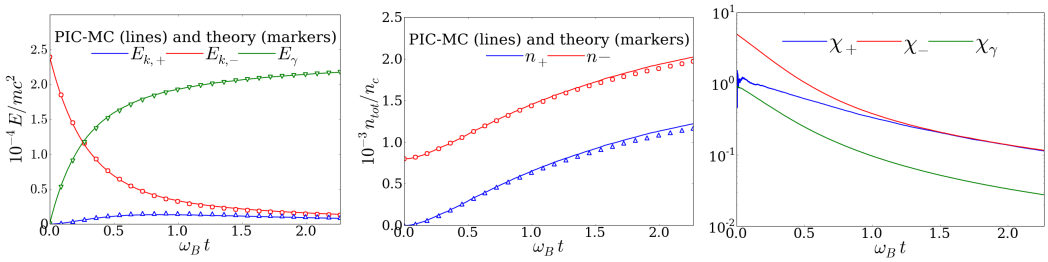

Figure 6.17: Evolution of the total kinetic energy (a), the total normalized density in the simulation domain (b) and the average quantum parameter χ (c) for each species of particles.

6.7.1 Simulation test: pair creation in a constant magnetic field

In section 6.5.4, simulations of synchrotron radiation were presented considering high energy particles interacting with a constant magnetic field. The same configuration is used here adding the mechanism of pair creation. We initially set a group of electrons of energy $\varepsilon_{e^-}/m_e c^2 = 3000$ in a uniform and constant magnetic field equal to $B/B_0 = 680$ so that the initial quantum parameter is equal to $\chi_{e^-} \simeq 5$. The initial synchrotron frequency and radius are respectively equal to $\omega_B/\omega_0 = 0.23$ and $R \simeq 4.4 c\omega_0^{-1}$.

The interaction starts in the quantum regime. The first created photons have an energy close to their emitting electrons, $\gamma_\gamma \sim 10^3$. The photon quantum parameter is therefore close to $\chi_\gamma \sim 1$ and this is favorable for the production of electron-positron pairs. Freshly generated particles in turn radiate their energy leading to the cascading creation of pairs. This regime is well illustrated in Fig. 6.17 representing the time evolution of the total particle kinetic energy and the total normalized density. During the first rotation, the total positron kinetic energy and number of particles significantly grow. Entering the semi-classical regime, the production of positrons tends to stabilize since emitted photon energy becomes non-sufficient ($\chi_\gamma < 1$) to be converted into matter. Radiation losses, originally responsible for the generation of pairs, now only acts as a cooling mechanism. The positron and electron quantum parameters tend to the same value.

As considered in section 6.5.4, we can model the interaction with the photon and electron positron pair generation using a reduced-kinetic approach. The distribution functions of the photon f_γ, of the electrons f_{e^-} and the positrons f_{e^+} are related by

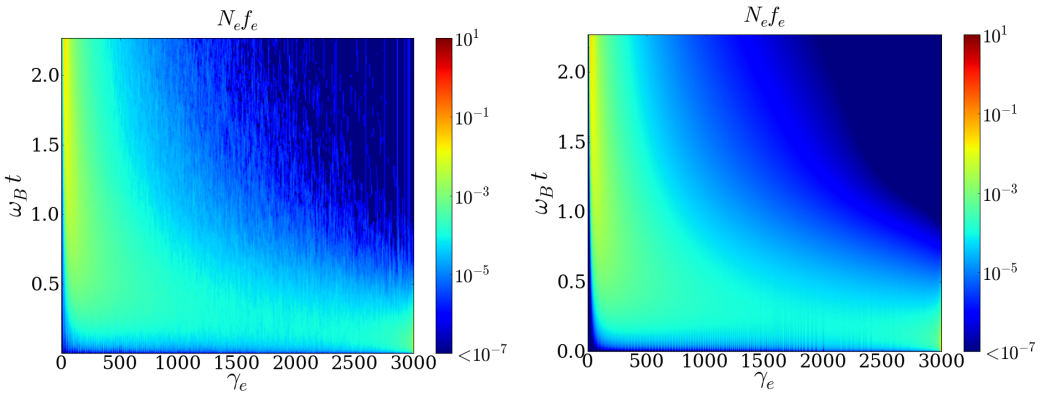

Figure 6.18: Time Evolution of the electron energy distribution from the PIC simulation (a) and the numerical solution of Eqs. (6.80) (b).

the following equations

$$\frac{df_\gamma}{dt}(\gamma_\gamma, t) = \int_1^{+\infty} \frac{d^2N_{Cs}}{dtd\gamma_\gamma}(\gamma_\gamma, \gamma) f_{e^\pm}(\gamma) d\gamma - 2\int_2^{\gamma_\gamma} \frac{d^2N_{nBW}}{dtd\gamma_{e^\pm}}(\gamma, \gamma_\gamma) f_\gamma(\gamma_\gamma) d\gamma \quad (6.79)$$

$$\begin{aligned}\frac{df_{e^\pm}}{dtd}(\gamma_{e^\pm}, t) &= -\int_0^{\gamma_{e^\pm}} \frac{d^2N_{Cs}}{dtd\gamma_\gamma}(\gamma_{e^\pm}, \gamma) f_{e^\pm}(\gamma) d\gamma + \int_{\gamma_\pm}^{+\infty} \frac{d^2N_{Cs}}{dtd\gamma_\gamma}(\gamma, \gamma - \gamma_{e^\pm}) f_{e^\pm}(\gamma) d\gamma \\ &\quad + \int_2^{+\infty} \frac{d^2N_{nBW}}{dtd\gamma_{e^\pm}}(\gamma_{e^\pm}, \gamma) f_\gamma(\gamma) d\gamma. \quad (6.80)\end{aligned}$$

Here, $f_{e^\pm}(\gamma_{e^\pm}, t)$ represents the electron or the positron energy distribution function at time t. Second integral in Eq. (6.79) represents the rate of electron-positron pairs created during dt by the photons of energy γ_γ whereas the third integral of Eq. (6.80) gives the rate of created pairs of energy $\gamma_{e^\pm}$. We also make the approximation that the pairs are created with equal energies in order to not draw them.

Evolution of the distribution functions are calculated numerically using the same parameters as in the PIC-MC simulation. Fig. 6.17 shows that the evolutions of the total number of particles and of the total kinetic energy are well reproduced by the simulation. In Figs. 6.18, 6.19 and 6.20 are respectively plotted the time evolution of the electron, positron and photon energy distributions which again confirms that the Monte-Carlo scheme is working correctly. In the high energy region, the generation of pairs is a rare event and the distribution appears consequently sparse for positrons and photons.

6.8 Conclusion

Thanks to the analysis of the cross sections made in chapter 2 for the nonlinear Compton scattering and in chapter 4 for the generation of electron-positron pairs,

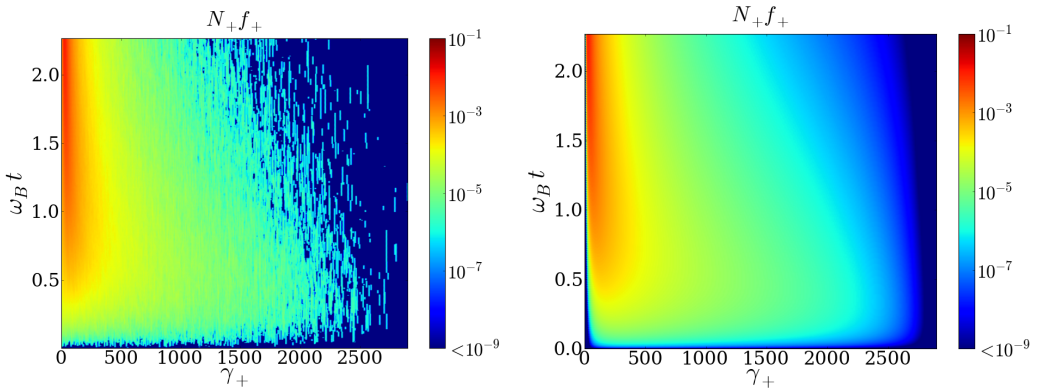

Figure 6.19: Time Evolution of the positron energy distribution from the PIC simulation (a) and the numerical solution of Eqs. (6.80) (b).

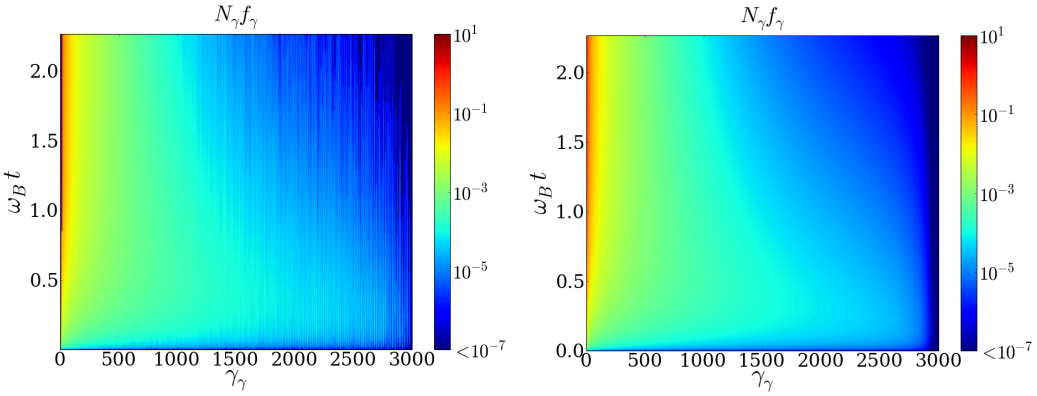

Figure 6.20: Time Evolution of the photon energy distribution from the PIC simulation (a) and the numerical simulation of Eqs. (6.80) (b).

the code CALDER has been enriched with the latter QED mechanisms. In chapter 3 and chapter 5, we have studied the Bremsstrahlung emission and the Bethe-Heitler pair generation. These chapters constitute the first step toward their future implementation. Such an implementation is essential for the simulation of laser-plasma interaction in extreme intensity if we want to anticipate the future experiments on forthcoming high-power facilities and improve our understanding of the physics in such extreme conditions. In the second part of this manuscript, different applications of the code will be presented.

Part II

Radiative and QED effects in laser-matter interaction: applications

Chapter 7

Laser-matter interaction with dense target

A target is so-characterized as overdense when the material particle density n_{e^-} overcomes the critical density n_c (depending on the laser frequency ω_0). In this case, the target is consequently opaque and the laser field can not penetrate deeply inside the target. It reduces exponentially with a typical scale length $\delta_s = c/\omega_0\sqrt{n_c/n_{e^-}}$ referred to as the skin-depth. The previous definition is valid in the linear regime of interaction when the laser is not sufficiently intense to accelerate electrons to relativistic energies. From then on, electron mass has to be corrected by the relativistic factor and the criteria roughly becomes $n_{e^-} > \gamma_{e^-} n_c$.

7.1 Collisionless laser-absorption mechanisms

An intense laser pulse ($I > 10^{18}$ W.cm^{-2}) interacting with a steep overdense plasma interface is absorbed by the media via the generation of fast electrons. The collisional absorption is negligible. The fast electrons then dilute and heat the media. Different heating mechanisms come into play depending on the laser (intensity, incidence, temporal shape, focal spot) and target (density, gradient, ion masses) properties.

7.1.1 The j $\times$ B heating mechanism

For direct incidence high-intensity lasers, electrons can be accelerated and injected in the target along the density gradient throught the combined action of the transverse electric and the magnetic fields. As a first description in a linearly polarized wave, an electron at rest gains momentum p_y via the transverse electric field E_y. This momentum is then converted to longitudinal momentum p_x via the magnetic field B_z toward the target. We consider a plane wave elliptically polarized interacting with a solid target. At modest intensity ($I \sim 10^{18}$ Wcm^{-2}), the wave is feebly absorbed. The resulting superposition of the incident and the reflected wave can consequently

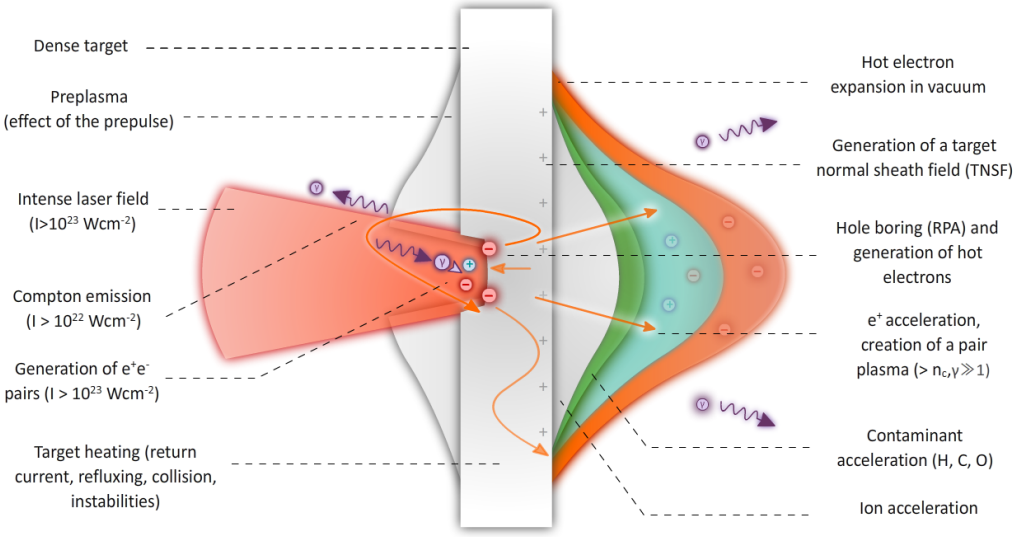

Figure 7.1: Simplified schematic of the laser-plasma interaction with thin foil in extreme intensity.

be seen as a standing wave with potential vector

$$\mathbf{A}(x,t) = \frac{A(x)}{\sqrt{1+\varepsilon^2}} \left(\cos\left(\omega_0 t\right)\mathbf{e_y} + \varepsilon \sin\left(\omega_0 t\right)\mathbf{e_z}\right) \tag{7.1}$$

where $\varepsilon \in [0,1]$, $\varepsilon = 0$ and $\varepsilon = 1$ respectively correspond to linear and circular polarization. In the hypothesis of a free electron interacting with this potential, the transverse momentum writes $p_\perp = eA$. When the electron gets near relativistic velocities, it undergoes effects of the magnetic field $B = \nabla \times \mathbf{A}$:

$$-e\mathbf{v} \times \mathbf{B} = \frac{e^2}{4m_e\gamma c^2}\partial_x A^2 \left(1 + \frac{1-\varepsilon^2}{1+\varepsilon^2}\cos\left(2\omega_0 t\right)\right)\mathbf{e_x} \tag{7.2}$$

The $-e\mathbf{v}\times\mathbf{B}$ component of the Lorentz force induces a longitudinal force pushing the electrons inward the plasma. This well-known force referred to as the relativistic ponderomotive force. In the non-relativistic regime ($I < 10^{18}$ Wcm^{-2}), the ponderomotive force is the consequence of the nonlinear effects of a smooth non-uniform oscillating electromagnetic field of which expression can be obtained from perturbative theory at first order

$$f_p = -\nabla \frac{e^2|\mathbf{E}|^2}{2m_e\omega_0} \tag{7.3}$$

In the relativistic regime, it becomes

$$f_p = -\nabla\left(\gamma - 1\right)m_e c^2 \tag{7.4}$$

where the electron Lorentz factor approximates $\gamma \sim \sqrt{1 + \langle eA/mc \rangle^2}$. For linear polarization, this force oscillates at $2\omega_0$ with amplitude ranging in $[0, 2]$. In other words, the electron heating results from the injection of bunches of hot electrons every half laser period. Electrons get a maximal energy approximated by the cycle-averaged ponderomotive energy $\varepsilon_{e^-} \sim m_{e^-}c^2 \left(\sqrt{1 + a_0^2/2} - 1\right)$. In practice, electrons interacting with the laser pulse in the target skin depth or in the vacuum can have an initial energy more or less significant gained inside the media from different mechanisms including return current, refluxing or instabilities further described later.

The non-relativistic electrons can be reflected by the skin-depth electric field without leaving the target and gain subsequent energy. However, this mechanism referred to as skin layer absorption has a relatively weak contribution compared to the $\mathbf{j} \times \mathbf{B}$, especially for high densities $n_{e^-} \gg 1$ and high intensities $a_0 > 1$ (Bauer and Mulser (2007); Gremillet (2013)). Relativistic electrons ($p_x/m_e c < a_0$) cross the skin depth weakly decelerated, enter the vacuum and are then accelerated back to the target thanks to the ponderomotive force. The deflection distance and the return momentum depend on the initial particle momentum $p_{x,0}$ and phase relative to $A(x, t)$ when escaping the target.

For circular polarization, the oscillating component of the ponderomotive force vanishes ($\varepsilon = 1$). The laser applies a steady pressure on the plasma. Electron heating, consequence of the $2\omega_0$ oscillation of the ponderomotive force, is therefore importantly reduced.

7.1.2 The Brunel effect

The Brunel heating, also referred to as the vacuum heating is an absorption mechanism based on the electrostatic description proposed by Brunel (1987). This absorption mechanism occurs when the laser electric field has a component normal to the sharp solid interface (Mulser *et al.* (2001); Macchi *et al.* (2013)). This is the case for oblique-incidence interaction at the edge of finite focal spot lasers. Under the action of the normal electric field, the electrons are dragged out of the surface during the first half oscillation of the laser. The charge separation leads to the formation of a static field that perturbs the forced oscillation of the electrons at the solid interface. The electrons are then re-accelerated back to the target and gain energy. This mechanism contrary to the $\mathbf{j} \times \mathbf{B}$ heating produces bunches of electrons every laser period.

7.1.3 Prepulses and preplasmas

The laser prepulse constitutes a long (several ns in the case of ps lasers) and a low energy preceding pedestal pulse arriving before the main one and created by leaks in energy in the amplifier chain. The energy of the prepulse is characterized by the contrast of the laser. Intensity contrast on future high-power facilities expected to

be between 10^{-10} and 10^{-12} which mean that for a laser of 10^{22} Wcm^{-2}, the prepulse is expected to have an intensity of 10^{12} Wcm^{-2}. If the prepulse is sufficiently long, this is sufficient to partially ionized the target and provoke a plasma front expansion in the vacuum. This plasma is called preplasma and has an exponential-like density profile. Due to the simulation cost to simulate an interaction in the nanosecond scale with a PIC code, the formation of the preplasma can be more easily computed with hydrodynamic codes.

In the thermal expanding sub-critical or near-critical preplasma, different absorption mechanisms take place including the so-called stochastic heating and acceleration, the Raman scattering, the laser wakefield acceleration that leads to a pre-absorption of the laser, a broadening of the electron spectrum above ponderomotive energies and a potentially reduced hot-electron density.

The effect of the preplasma on the electron acceleration was extensively studied in the framework of the fast ignition scheme of fusion target (Baton *et al.* (2008); Cai *et al.* (2010); MacPhee *et al.* (2010); Kemp *et al.* (2014)) where petawatt, multi-kJ laser are required to generate fast electrons in the direction of the core. The effects of the preplasma have been proved to be negative in this case. The laser absorption starts farther from the core of the target, the hot-electron density is reduced in the range of interesting energy (around few MeVs), the spectrum is broadened and the divergence is increased.

In short-pulse laser matter interaction, for proton and heavy ion acceleration, a tailored-preplasma can be beneficial for the target normal sheath acceleration. It has been shown that the final proton energy can be reduced with a very low contrast or with a high-contrast (Wang *et al.* (2013); Fuchs *et al.* (2006); Glinec *et al.* (2008)). In the case of a perfect contrast, the solid interface remains steep whereas for lower contrast the ablation leads to the increase of the target thickness. As a consequence a correctly-tuned preplasma can enhance the proton acceleration but a good contrast is still required to improve the cut-off energy (Zhao *et al.* (2015)). The optimal shape of the preplasma depends on the target parameters (Roth *et al.* (2002); Andreev *et al.* (2006); McKenna *et al.* (2008)). In this case, the near-critical plasma improves the absorption efficiency of the laser and increases the energy of the electrons (Sgattoni *et al.* (2012)).

Recently, a different regime of ion acceleration has been theoretically described in a strong target ablation where the TNSA is extremely weakened (Zhao *et al.* (2015)). The direct laser acceleration (DLA) of the electrons leads to an angle envelope acceleration field for the ions reducing their energy spread.

7.2 Ion acceleration

7.2.1 The target normal sheath acceleration

The target normal sheath acceleration is a positive charge acceleration mechanism which strongly occurs at the rear side of a thin dense target. In a warm collisionless plasma, for an electron temperature above the ion temperature $T_{e^-} > T_i$, electrons expand in the vacuum more rapidly than heavy ions resulting in the apparition of a charge separation field all around the solid target at the origin of the plasma spatial expansion. The charge separation field at the electron-ion interface in the early time of the expansion can be estimated by integration of the Poisson equation, supposing a Boltzmann distribution $n_e = n_{e^-,0} \exp e\Phi/k_B T_{e^-}$ where Φ is the field potential, $n_{e,0}$ the initial electron density to give $E_f = \sqrt{\frac{2n_{e^-,0}k_B T_e^-}{e\varepsilon_0}}$. Self similar solution of the fluid continuity and the motion equations predict an ion front velocity of $2c_s \ln \omega_{pi} t$ with c_s the ion acoustic velocity and ω_{pi} the ion plasma frequency. A more precise description of the plasma expansion has been given in Mora (2003). The electric field at the ion front decreases with time as $E_f \simeq 2E_0/\sqrt{\left(2e + \omega_{pi}^2 t^2\right)}$ leading to a maximum ion velocity $v_f \simeq 2c_s \ln\left(\tau + \sqrt{\tau^2 + 1}\right)$ with $\tau = \omega_{pi} t/\sqrt{2e}$.

At high-intensity laser-interaction, the electron temperature is very broad and inhomogeneous. Hot relativistic electrons are mainly forward accelerated, cross the target and escape backward to therefore induce the strongest charge separation field. The result is a significant transfer of energy from these relativistic electrons to the target positively charged ions depending on the ion mass, the thermal energy of the hot electrons and the target thickness (Mora (2005)). More sophisticated models have been developed to take into account the two-temperature electron distributions (cold electrons and escaping hot electrons) as well as two ion-species plasma (usually composed of a heavy and a light one, Tikhonchuk *et al.* (2005)). A complete history of the literature is available in Macchi *et al.* (2013). This constitutes the most efficient source of high-energy ions at moderate intensities ranging between 10^{18} and 10^{21} Wcm^{-2} in laser-plasma interaction with overdense thin targets. Solid foils are usually contaminated on its surface by organic molecules and oxids constituted of oxygen, carbons and hydrogen atoms. Light ions such as protons located on the target surface constitutes the most accelerated particles whereas heavy ions contributes to the establishment of the static electric field. The maximal ion velocity is given by the front velocity whereas the energy tail of the spectrum can be approximated by $\varepsilon_f \simeq 2Zk_B T_h \left[\ln(2\tau)\right]^2$.

7.2.2 The radiation pressure acceleration

Under the effect of the ponderomotive force, the laser applies a radiation pressure on the plasma interface. For small intensities, the radiation pressure equalizes the

pressure of the particles. For sufficiently strong intensity, the plasma interface can be pushed forward and globally accelerated. For finite transverse focal spot, the mechanism, usually referred as to hole boring, is responsible for the penetration of the laser inside the target.

The laser pushes ahead the electrons and is reflected by the consequently generated high-density spike. The ions left behind are therefore accelerated in the newly-generated charge separation cavity. In an homogeneous high-density plasma, a quasistationary two-layer structure can be generated and propagates as the laser properties remain unchanged. This structure is commonly named laser piston. The laser piston velocity $\beta_p = v_p/c$ can be determined from the momentum flux balancing between particles and the laser intensity (Macchi *et al.* (2005); Zhang *et al.* (2007); Schlegel *et al.* (2009)).

$$(1+R)\Pi'_l = \Pi'_i + \Pi'_{e^-} + \Pi'_{\gamma,x} \tag{7.5}$$

Here, R is the laser reflexion coefficient, Π_i is the ion flux, Π_e is the electron flux and $\Pi_{\gamma,x}$ the photon flux projected on the longitudinal axis. In the piston boosted frame, the laser pulse is entirely reflected ($R = 1$) and we suppose that no energy is deposited in the electrons $\Pi_{e^-} \ll \Pi_i$. Its intensity corresponds to $I' = I\left(1-\beta_p\right)/\left(1+\beta_p\right)$. The laser momentum flux reads $2I'/c$. In the comoving frame, the particle propagates to the piston velocity at v_p to be reflected back at v_p. The particle momentum flux in the moving frame therefore corresponds to $2n'_i v_p m_a \gamma_p v_p = 2n_i m_a \gamma_p^2 v_p^2 = 2\rho c^2 \gamma_p^2 \beta_p^2$ where $m_a = m_i + Zm_e \sim m_i$ is the atomic mass. By equating the momentum fluxes, we have

$$\frac{I}{\rho c^3}\frac{1-\beta_p}{1+\beta_p} = \gamma_p^2 \beta_p^2 \tag{7.6}$$

It is convenient to define $B = \sqrt{I/\rho c^3} = a_0\sqrt{n_c m_{e^-}/\alpha n_i m_a}$ where $\alpha = 1$ or 2 for respectively circular or linear polarization. The resulting piston velocity can be written

$$\frac{v_p}{c} = \frac{B}{1+B} = \frac{a_0\sqrt{n_c m_e/\alpha n_i m_a}}{1+a_0\sqrt{n_c m_e/\alpha n_i m_a}} \tag{7.7}$$

The piston velocity grows with the laser intensity a_0, decreases with the target ion density n_i and does not depend on the ion charge. Back to the laboratory frame, the reflected pulse has a lower intensity due to the double Doppler effect after reflection on the moving electron spike. The reflection coefficient $r = (1-\beta_f)/(1+\beta_f)$ characterizes the laser energy transferred to the ions.

After reflection on the electrostatic structure, ions have a velocity of $v_i = 2v_p/(1+v_p^2/c^2)$ in the laboratory frame. Therefore, the final energy by radiation pressure acceleration reads $\varepsilon_i = m_i c^2(\gamma_i - 1) = 2m_i c^2 \gamma_p^2 \beta_p^2$.

7.3 Nonlinear inverse Compton Scattering in laser-solid interaction

7.3.1 Simulation results

The first simulation using Particle-In-Cell of laser-interaction with thin foil have been performed more than 10 years ago in Zhidkov *et al.* (2002) using the radiation friction model of Lorentz-Abraham-Dirac. The simulation were performed in 1D using copper target and laser intensity between 10^{22} and 10^{23} Wcm^{-2}. Then, the PIC code used by N. Naumova (Naumova *et al.* (2005)) incorporating a continuous friction model has been considered to study the hole boring in intensity close to 10^{22} Wcm^{-2} (Naumova *et al.* (2009)). More recently, R. Capdessus *et al.* have implemented in their PIC code the radiation damping model of Sokolov. They have studies how the radiation losses influence the laser absorption and the ion acceleration depending on the ion mass, the target density and the laser properties (Capdessus *et al.* (2012, 2013, 2014); Capdessus and McKenna (2015)). In the case of a circularly polarized wave with 3D PIC simulations, the hole boring have been studied in an extreme regime of interaction (up to 9.3×10^{24} Wcm^{-2}) in Nerush and Kostyukov (2015). In the light sail regime (the thickness of the target is similar or below the laser wavelength), the effect of the radiation reaction on the laser radiation radiation pressure have been explored in Tamburini *et al.* (2010),Tamburini *et al.* (2011) and Tamburini *et al.* (2012).

Case of a plane wave

Synchrotron emission occurs at the laser-solid interface. Hot electrons returning back to the target front side can potentially radiate their energy in the front separation field between the ion and the electron layer, the skin depth layer or in the quasi-standing laser field in the vacuum. The process is schematically described in Fig. 7.1. In order to further describe the emission process, a first simulation have been performed at 10^{23} Wcm^{-2}. The space discretization is of $\Delta x = \Delta y = 0.03c/\omega_0$ and the domain is of 57 μm ($360c/\omega_0$) long and of 7 μm ($45c/\omega_0$) wide. The simulations are 2d spatially and 3d in the momentum space, with transverse periodic conditions (at the boundaries $y = \pm 3.6$ μm). The target is composed of aluminum of density $\rho = 2.7$ gcm^{-3}and is initially fully ionized (a_0 being sufficiently high to totally ionize aluminum at Al^{13+}). The normalized electron particle density is equal to $n_{e^-} = 780 n_c$. The target has a thickness of 8 μm ($50c/\omega_0$). A preplasma precedes the target in order to model the effect of a laser prepulse with a decreasing exponential profile of $12.5c/\omega_0$ (2 μm). At the rear side, a thin layer of hydrogen of thickness 5 nm has been added in order to mimic a contaminant layer. The initial configuration as well as the initial target electron density is shown in Fig. 7.2a. The laser is linearly polarized with the electric field oriented in the y direction. The wavelength

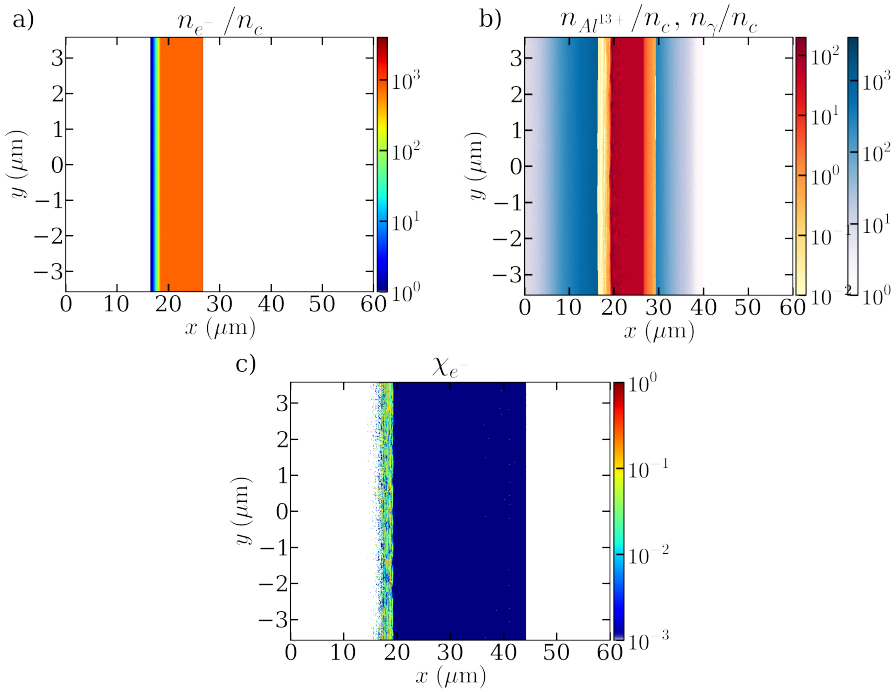

Figure 7.2: a) - Initial target configuration showing the electron density n_e/n_c. b) - Ion density $n_{\mathrm{Al}^{13+}}/n_c$ and photon density n_γ/n_c at time t = 159 fs. c) - The electron quantum parameter χ_{e^-} at time 159 fs.

is of $\lambda_l = 1$ μm. The temporal profile is composed of a growing part modeled by a hyper-Gaussian of duration at half maximum of 32 fs ($60\omega_0^{-1}$) followed by a semi-infinite plateau. The laser is injected from the left side of the computational box ($x = 0$ μm). A semi-infinite laser is considered in order to catch the stationary regime of the interaction.

The laser strikes the target at interaction time $t \simeq 55$ fs. At the laser-solid interface, the laser ponderomotive force accelerates the electrons which dilute and voluminously heat the target. The hot electrons due to their forward acceleration mainly expand at the rear side but also in a lower extent at the front side of the target. The driving of the whole electron density can be seen in Fig. 7.3b showing the time-evolution of the electron y-averaged density. The $x - p_x$ phase space of the electrons (blue colormap) is shown in Fig. 7.4 at time 159 fs and demonstrate that the electrons mainly acquire a forward longitudinal momentum of maximum close to $p_x \sim 800 m_e c$. At the target rear and front side, a charge separation field settles. At the rear side of the target, the TNSA causes the aluminium ions to be first accelerated as shown in Fig. 7.3a showing the time-evolution of the ion y-averaged density. The ion rear side evolves at velocity $v_r = 0.53c$.

At the front side, the radiation pressure accelerate the surface as a whole (see

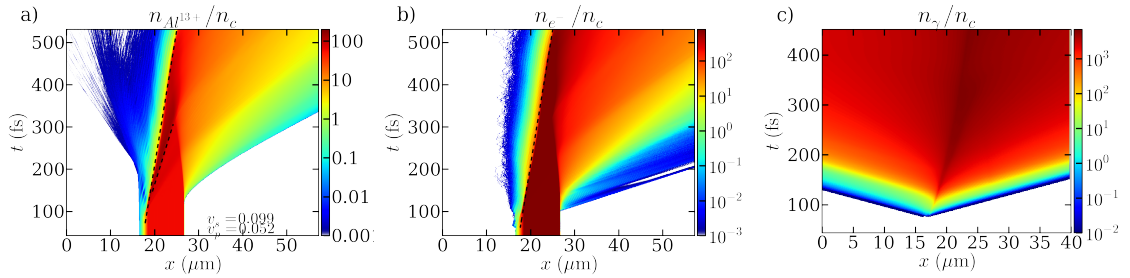

Figure 7.3: a) - Time-evolution of the y-averaged ion density $n_{Al^{13+}}/n_c$, the black dashed line corresponds to the laser-solid interface and the black to the ion front shock. b) - Time evolution of the y-averaged electron density n_{e^-}/n_c. c) - Time evolution of the y-averaged photon density n_γ/n_c.

section 7.2.2). The target front reach a constant piston velocity of $v_p = 0.052c$. The piston constitutes a reflecting wall for the inert ions of the targets. The ion shock velocity is approximated equal to $v_s \sim 0.079c$, not exactly twice the piston velocity as classically expected.

The nonlinear Compton emission takes place at the laser-solid interface and the photon expands balistically in every directions as shown in Fig. 7.2b and Fig. 7.3.

The similar case is reproduced without radiation losses. The radiation losses mainly affect electrons with high-γ values and thus cool down hot electrons generated at the laser solid-interface. The volumic heating is therefore reduced and the thermal electron expansion is diminished as demonstrated in Fig. 7.4c showing the electron phase space $x - p_x$ with (blue colormap) and without radiation losses (orange colormap). The effect is particularly obvious at the target front side where high-energy electrons escaping backward in the vacuum lose their energy in few laser periods before being re-injected forward in the target. Radiation losses also diminishes the average rear electron energy. The target normal sheath field potential is therefore reduced affecting the TNSA ion acceleration. In the non-radiative simulation, the front size is pushed at piston velocity $v_p = 0.041c$. The shock velocity reaches $v_s = 0.084c$ closer to the expected value of twice the piston velocity. The rear front propagates at $v_r = 0.44c$. Formula 7.7 gives a theoretical piston velocity of $v_{p,th} = 0.19c$. As a consequence, the radiation losses globally diminish the target temperature and confine the target front expansion as the laser irradiation is maintained. The rear target ion and proton acceleration is thus also reduced.

The energy balance of the laser-interaction in the two cases with and without radiations is shown in Fig. 7.5. The energies are normalized to the injected laser energy having interacted with the target at the final time. This means that there is a temporal shift between the injected laser energy in the domain and the amount of energy that has contributed to the particle acceleration. This shift can be estimated as $t_f - t_0 - v_p(t_f - t_0)/c$ where t_f is the final simulation time and t_0 the time when

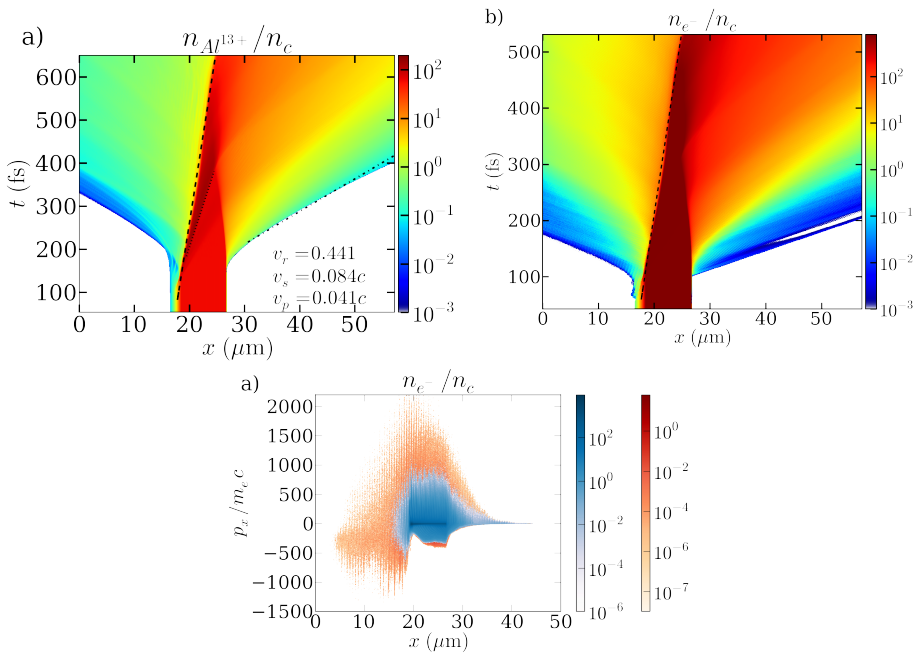

Figure 7.4: a) - Time evolution of the y-averaged ion density $n_{Al^{13+}}/n_c$ without radiation losses. The dashed black line represents the evolution of the ion front (of pistron velocity $v_p \sim 0.041c$), the dotted tile corresponds to the shock front (of velocity $v_s \sim 0.084c$) and the dash-dot line to the rear front (of velocity $v_r \sim 0.44c$). b) - Time evolution of the y-averaged electron density n_{e^-}/n_c without radiation losses. c) Phase space $x - p_x$ with (blue colormap) and without (orange colormap) radiation losses at time $t = 159$ fs ($300\omega_0^{-1}$).

the laser strikes the target. This offers an estimation since the target initially has a pre-plasma and the pulse a Gaussian feet. Not visible because of the logarithmic scale in the ordinate axis, the evolution of the radiated energy is linear from time 250 fs demonstrating that a stationary regime of emission is reached. The evolution of the particle energy is as well almost linear while the injected laser energy is constant. In the radiative case, the radiated energy represents 29 % of the laser energy at the end of the simulation corresponding to $t_f = 531$ fs ($1000\omega_0^{-1}$). The radiated power represents a dissipation of 31 % of the laser power. It first appears that the electron kinetic energy, the ion kinetic energy and the proton kinetic energy become more significant in the non-radiative case when the field is strong enough to trigger the radiation losses of the fast electrons near t = 120 fs. At the end of the simulation, the electrons have absorbed 15 % of the laser energy in the radiative case and 31 % in the non-radiative one. The aluminium ions have gained 16 % of the laser energy in the radiative case and 21 % in the non-radiative one. The energy brought by the protons is obviously low in comparison to the other species with 0.031 % in the

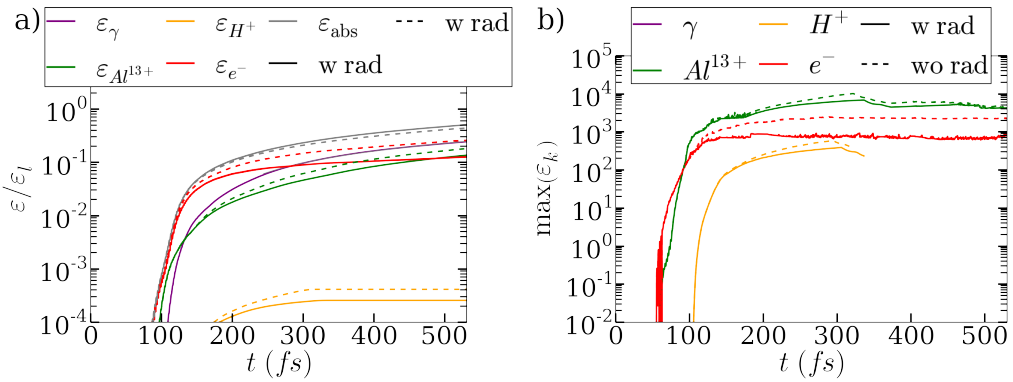

Figure 7.5: a) - Energy balance of the simulations with (solid line) and without radiation (dashed line). The photon energy is shown in purple, the aluminium ion energy in green, the protons in orange and the electron in red. The total absorbed energy is represented in grey. The energy is normalized to the laser energy. b) - Time evolution of the maximal energy of the photons, the ions, the protons and the electrons in the radiative (solid line) and the non-radiative case (dashed line).

radiative case and 0.049 % in the non-radiative one, which means a relative difference of 37 %. The total absorbed energy is estimated around 61 % in the radiative case and 52 % in the non-radiative one. In addition to the energy balance, the evolution of the maximal registered kinetic energy for all the species in the radiative and the non-radiative case is shown in Fig. 7.5. The electrons exhibit the highest difference in energy because they are directly affected by the radiation losses. This was already visible in Fig. 7.4c. The maximal kinetic energy reached by the electrons is of 933 MeV in the radiative case and 2486 in the non-radiative one. After time close to 200 fs, the plateau of the laser is reached and the maximal energies are almost constant in time which confirms that a stationary regime have been attained. The aluminium ions have a maximal energy of 6920 MeV in the radiative case and 10250 MeV in the non-radiative one. The difference is lower for the protons, of 394 MeV in the radiative case and 594 MeV in the non-radiative one. Finally, we can mention that the maximal photon energy is of 615 MeV.

In order to better understand the distribution of the radiation, the photon angular-energy radiated spectrum is shown in Fig. 7.6a at the end of the simulation. The angle θ is defined as $\theta = \arctan\left(\sqrt{p_y^2 + p_z^2}/p_x\right)$. The emission is made in every direction but is not isotropic. It is mainly forward directed and the photons with $p_x > 0$ represents 59 % of the total emission. The other part part of the emission directed backward for an average angle of 2.3 rad is mainly induced by the electron re-fluxing attempting to escape in the vacuum and the electrons oscillating at the laser-solid interface. The average emission angle is of $\langle\theta\rangle \sim 0.83$ rad and the maximum of emission is located at $\theta \sim 0.77$ rad. The emission is not maximal near $\theta = 0$.

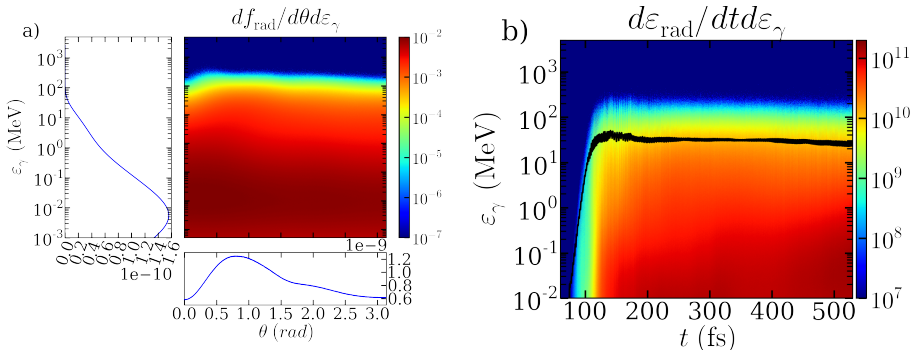

Figure 7.6: a) Radiated energy spectrum as a function of the emission angle θ (rad) and the photon energy ε_γ (MeV) taken at the end of the simulation at time 531 fs. b) Time-evolution of the radiated energy spectrum.

These typical angles of emission can be also been observed in 1d simulation and for finite focal spot sizes. The radiated energy spectrum peaks at 11 keV for an average photon energy of 32 MeV.

The time-evolution of the radiated energy spectrum is shown in Fig. 7.6b. It confirms once again that a stationary regime of emission is reached after time 200 fs. The average photon energy shown via the black line is almost constant at around 30 MeV. Nonetheless, it can be observed that the emission of photons under the MeV level increases contrary to the part above this level which is almost stabilized (the maximal emitted energy keeps constant).

7.3.2 Particle test at the laser-solid interface

In order to understand how the particles radiate at the laser solid interface, some particle trajectories are studied in a simplified configuration. We consider that the particle can evolve on a 2D plane since the laser is linearly polarized. The domain is divided into two parts: the vacuum and the solid. In the vacuum, the electromagnetic field is considered as the superimposition of an incident plane wave and its reflected wave with a reflection coefficient $\eta_{\rm r}$ so that

$$E = E_0\left(\cos\xi_i - \eta_{\rm r}\cos\xi_r\right) \qquad B = B_0\left(\cos\xi_i + \eta_{\rm r}\cos\xi_r\right). \tag{7.8}$$

Here, ξ_i and ξ_r represents the incident and reflected phase variables. We neglect the skin depth but we take into account the hole boring. Therefore, for a piston velocity $\beta_p = v_p/c$, we have $\eta_{\rm r} = \eta'_{\rm r}\frac{1-\beta_p}{1+\beta_p}$ where $\eta'_{\rm r}$ is the reflection coefficient in the reference frame of the piston. The phase of the incident wave is equal to $\xi_i = ct - {\rm kx}$ and the phase of the reflected one due to the hole boring corresponds to $\xi_r = \frac{1-\beta_p}{1+\beta_p}\left(ct + {\rm kx}\right)$. In the solid part, the particle propagates with no field and no scattering. The interface between the vacuum and the solid is initially located at

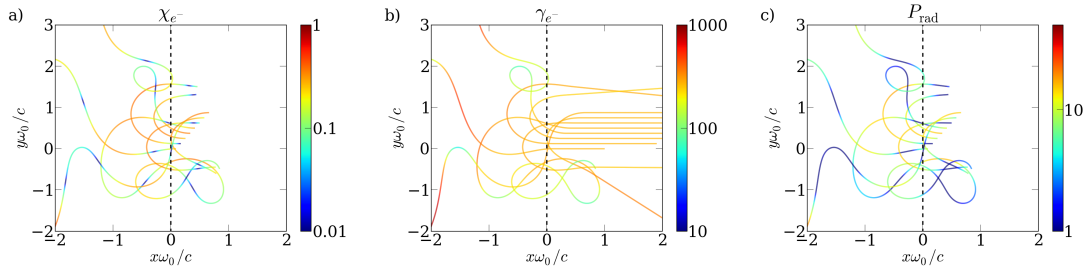

Figure 7.7: (a) - Quantum parameter, normalized energy (gamma factor) and radiated energy all along the trajectories of 8 particles initialized at different positions from c/ω_0 to $(\pi+1)c/\omega_0$ with energy $\gamma = 270$.

$x = 0$. The solid target constitutes the right part of the domain and the vacuum the left part. The configuration is similar to May *et al.* (2011) including the radiation damping.

In the first study, the electrons are initialized at different positions x in respect to the solid interface so that each particle will interact with different phases of the electromagnetic field. The particles initially have the same energy equal to $\gamma = 270$. The laser has a normalized amplitude of $a_0 = 270$ with a wavelength of 1 μm, equivalent to 10^{23} Wcm^{-2}. The movement of the particles is solved using a leap-frog pusher, here, the method of J. L. Vay is used coupled with the continuous model of I. Sokolov as for a PIC code. Eight particles are considered initialized from position $x = c/\omega_0$ to $x = (1+\pi)\, c/\omega_0$, $2\pi c/\omega_0$ being equal to $\lambda = 1$ μm, with an equal space step $dx = 2\pi/8$. The trajectories are solved a time discretization of $dt = 0.00075\omega_0^{-1}$. The electron initial transverse position y is also uniformly shifted from $y = 0$ to $y = c/\omega_0$ in order to help distinguishing all the trajectories. The particles obviously propagate initially backward. The evolution of the quantum parameter χ_{e^-}, the normalized energy γ_{e^-} and the radiated energy $P_{\rm rad}$ are plotted in Fig. 7.7.

In the second study, the initial position is the same for ten initialized particles but the energy is varied from $\gamma = 10$ to $\gamma = 1000$ with a logarithmic scale of an energy step of $\Delta\gamma = \left(\log_{10}(1000) - \log_{10}(10)\right)/9$. The evolution of the quantum parameter χ_{e^-}, the normalized energy γ_{e^-} and the radiated energy $P_{\rm rad}$ of the test electrons are plotted in Fig. 7.8.

The electrons mainly radiate when they are deflected by the standing wave. During the deflection the particles can gain energy and at the same time radiate a lot as shown both by the evolution of γ_{e^-} in fig. 7.7b and the radiated power in fig. 7.7c. As a function of the laser phase, the particle are deflected and re-accelerated toward the solid, just undergo a wiggling trajectory during their forward propagation or oscillates near the laser interface. In any case, the quantum parameter is the highest in the curve during the change in trajectories. If we analyze all the trajectories, the emission can happen during a forward or backward deflection which explain why the

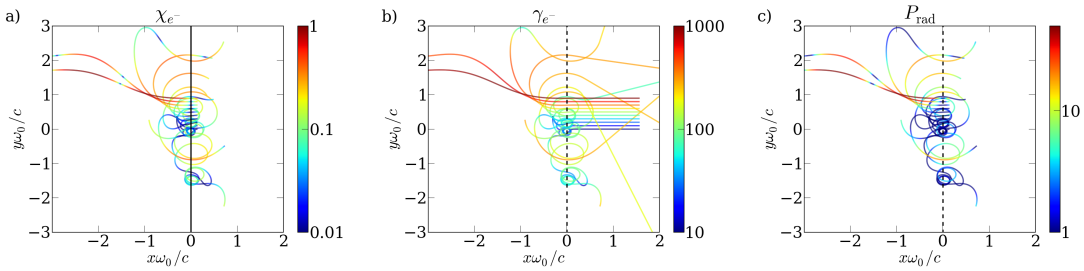

Figure 7.8: (a) - Quantum parameter, normalized energy (gamma factor) and radiated energy all along the trajectories of 10 particles initialized with different energies from $\gamma = 10$ to $\gamma = 1000$ at the same position $x = \pi/2c/\omega_0$.

emission is made in every directions. Even if this study is based on a continuous approach, the quantum parameter (Fig. 7.7a) reveals that the chance of quantum emission is maximized during the deflections. But this modeling does not take into account the straggling and therefore the sudden change of trajectory that could arise.

The radiative behavior also depends on the initial electron energy. The less energetic particles are confined near the laser-solid interface exhibiting looping trajectories. These particles gain energy during their oscillations (Fig. 7.8b) and this contributes to maintain a continuous emission as shown by the radiated power in Fig. 7.8c. When the initial electron energy is higher, the deflection curve radius increases so that the particle are not trapped anymore but are send back to the target while radiating and with a potentially higher energy than when they leaved the foil. For the highest energies $\gamma > 2a_0$, which corresponds in Fig. 7.8 to the two highest energetic electrons, the test particles keep traveling forward with wavy trajectories. With the correct phase, the particles can potentially cross several laser oscillations until they get dephased and back deflected. In the quantum regime nonetheless, a high-energy particle is unlikely to travel away far from the solid interface since the emission will bring away a significant part of the electron energy into a single or few photons and therefore instantaneously reduces the electron energy under $2a_0$. The electron will be trapped or back accelerated to the target.

Case of a finite focal spot

A simulation in the case of a finite focal spot is now reproduced. Here, the domain has a length of 48 μm ($300c/\omega_0$) and a width of 29 μm ($180c/\omega_0$) with a spatial discretization of $\Delta x = \Delta y = 0.03c/\omega_0$. All the boundary conditions are absorbing in every directions. The target is an aluminum foil ($n_{e^-} = 780n_c$) of 3 μm thickness and a transverse size of 25 μm. The front of the target is located at position 19 μm. The target has a pre-plasma of 3 μm. The laser is injected from the left side of the simulation box (boundary $x = 0$) and is focused on the target with a focal spot of 2

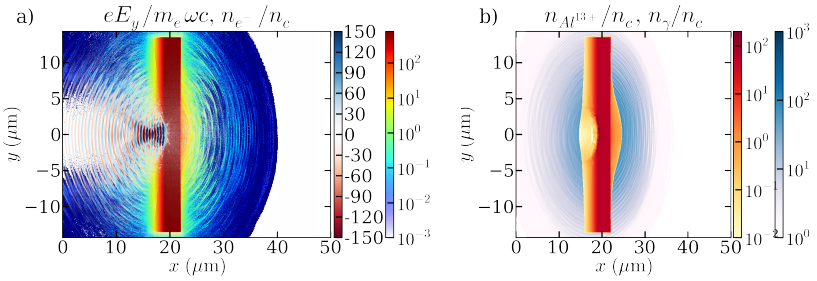

Figure 7.9: a) - Electric field $eE_y/m_e\omega_0 c$ and electron density n_e^-/n_c at time 180 fs. b) - Ion density $n_{Al^{13+}}/n_c$ and photon density n_γ/n_c at time 180 fs.

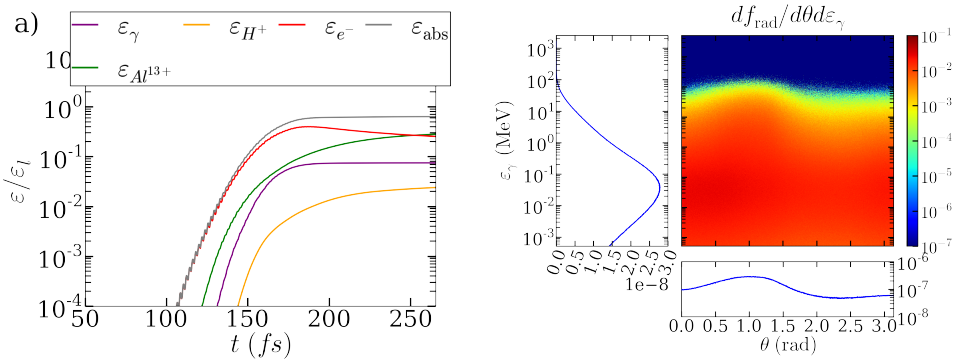

Figure 7.10: a) - Energy balance showing the time-evolution of the electron (red), the ion (green), the proton (orange), the photon (purple) and the absorbed (grey) energy. b) - Integrated radiated energy spectrum as a function of the emission angle θ (rad) and the photon energy ε_γ (MeV) taken at the end of the simulation at time 531 fs.

μm. It has a duration of 30 fs with a Gaussian profile.

The maximum of the laser arrive on the target at time 152 fs. Figure 7.9a shows the laser electric field and the electron density during the laser interaction at time 180 fs. The ion and the photon densities are shown in Fig. 7.9b. Fig. 7.9a clearly illustrates the target heating with the rear expansion of the hot electrons. The laser hole boring effect is observable in both figures. The photon density shows that in the plane $x - y$, the emission is performed in every directions.

The energy balance of the interaction is shown in Fig. 7.10a. At the end 64 % of the laser energy have been absorbed. This results is close to the results obtained with the plane wave. However, respectively 25 % and 28 % of the energy have been given to the electrons and the ions. This is more significant than in the case of a plane wave and here 7.6 % have been radiated away. The protons have acquired 2.4 % of the laser energy.

The angular energy spectrum of the photons is shown in Fig. 7.10b. The spectrum $df_{\rm rad}/d\theta d\varepsilon_\gamma$ peaks at an energy of 0.037 MeV and an angle of 1.06 rad. The average energy of the photon $\langle\varepsilon_\gamma\rangle$ is of 23 MeV and the average angle $\langle\theta_\gamma\rangle$ of 0.87 rad.

7.4 Pair generation in laser-solid interaction

7.4.1 Significance of the different mechanisms and yield estimations

The generation of pairs via the Breit-Wheeler process and the electromagnetic Trident occurs in the electromagnetic wave at the target front size, superimposition of the incident and the reflected pulses. The pairs come from the decay of the γ-photon of energy up to 1 MeV generated via the nonlinear Compton scattering. The number of pairs generated per laser period per electron can be roughly estimated as a function of the laser normalized amplitude a_0 considering the simple model already described in section 4.3.2. The number of nonlinear Breit-Wheeler pairs generated per laser period corresponds to:

$$N_{BW}^{\pm} \sim T_l \int_2^{\gamma_{e^-}-1} \frac{dN_{Cs}^2}{dtd\gamma} \times \kappa_\gamma(\chi_\gamma) d\gamma \tag{7.9}$$

where $\frac{dN_{Cs}^2}{dtd\gamma}$ is the production rate of γ-photons for an electron of normalized energy γ_{e^-} and $\kappa_\gamma(\chi_\gamma)$ is the probability for a photon of quantum parameter χ_γ to decay into pair over a laser period T_0. Here, the pair cascading is not taken into account and could further increases the production yield in the extreme intensities close to 10^{24} Wcm^{-2}. The main difference with section 4.3.2 is the approximation of the electron quantum parameter χ_{e^-}. We consider a standing wave, consequence of the reflexion of the incident one on the perfect reflecting target) of the form

$$E = E_0 \left(\sin\left(k_0 x\right)\cos\left(\omega_0 t\right)\mathbf{e_y} + \varepsilon \sin\left(k_0 x\right)\sin\left(\omega_0 t\right)\mathbf{e_z}\right) \tag{7.10}$$

$$B = B_0 \left(\cos\left(kx\right)\cos\left(\omega_0 t\right)\mathbf{e_y} + \varepsilon \cos\left(kx\right)\sin\left(\omega_0 t\right)\mathbf{e_z}\right) \tag{7.11}$$

where $E_0 = -2\omega_0 A_0/\sqrt{1+\varepsilon}$ is the electric field amplitude and $B_0 = 2A_0 k/\sqrt{1+\varepsilon}$ is the magnetic field amplitude. The quantum parameter can therefore be written

$$\chi \sim \frac{\gamma_{e^-}}{E_s}\frac{2A_0\omega_0}{\sqrt{1+\varepsilon}}\left[\cos\left(\omega_0 t\right)^2\left(\sin\left(kx\right)+\cos\left(kx\right)\right)^2 + \varepsilon^2\sin\left(\omega_0 t\right)^2\left(\cos\left(kx\right)-\sin\left(kx\right)\right)^2\right]^{1/2} \tag{7.12}$$

supposing that the electrons are propagating at c in the x direction $\mathbf{v} = c\mathbf{x}$. For a linear polarization, averaged over a laser period, the quantum parameter is maximized by

$$\chi_{e^-} \sim \frac{a_0\gamma_{e^-}E_0}{E_s} \sim \frac{a_0^2 m_e^- \omega_0 c}{eE_s} \tag{7.13}$$

where the electron energy has been approximated by $\gamma_{e^-} \sim \sqrt{1+\langle a_0 \rangle^2} \sim a_0$ The same approximation is made for the photon quantum parameter $\chi_\gamma \sim \frac{a_0 \gamma_\gamma m_e^- \omega_0 c}{e E_s}$. The prodution rate of pairs via the nonlinear Breit-Wheeler process per electron per laser period as a function of the laser intensity is shown in Fig. 7.11. The production rate of γ-photons ($\gamma_\gamma > 2$) via the nonlinear inverse Compton scattering and the electron quantum parameter are also plotted in this figure (red and blue curves respectively). For a thin foil, the Bremsstralhung emission of high-frequency photons can be neglected in comparison with the nonlinear inverse Compton scattering. We can estimate that for an electron of energy $\varepsilon_{e^-} \sim a_0 m_{e^-} c^2$, the number of γ-photons generated per laser period in an aluminium foil of thickness $l_\alpha = 10$ μm is between 10^{-3} and 10^{-4} as shown in Fig. 7.11. This estimation is calculated from the direct numerical integration of the Bremsstrahlung cross-section differential in photon energy using the Thomas-Fermi screening as described in section 3.2:

$$N_{Br}^{\gamma} \sim \int_2^{\gamma_{e^+}-1} \frac{d\sigma}{d\gamma} n_\alpha l_\alpha d\gamma, \tag{7.14}$$

where n_α and l_α are respectively the particle density and the length of the considered material. The production rate of pairs via the electromagnetic Trident $N_{Trident}^{\pm}$ is calculated by integration of Eq. 4.17 given in section 4.4. The results is shown in Fig. 7.11 (orange curve). The pairs can also be generated in the matter via the Bethe-Heitler mechanism when the γ-photons generated at the laser-solid interface interact with the nuleus field. We neglect the radiation losses and the deflection in the matter and at the laser solid interface. In order to estimate the pair production in this scenario, we consider that all the photons from the nonlinear Compton scattering can potentially decay into pairs (and we therefore forget the other effects). The pair yield is therefore obtained from the direct integration, again numerically performed, of the Bethe-Heitler energy-differential cross-section:

$$N_{BH}^{\pm} \sim \int_2^{\gamma_{e^-}-1} \frac{dN_{Cs}^2}{dt d\gamma} \left(1 - \exp\left(-\sigma_{BH}(\gamma) n_\alpha l_\alpha\right)\right) d\gamma \tag{7.15}$$

Finally, the matter Trident is also calculated supposing that Eq. 5.10 of section 5.3 is valid until energy of $\gamma_{e^-} \sim 10^3$. for an electron of given energy, a simple estimation can be obtained with the following expression

$$N_{Tr,m} = \sigma_{Tr,m} n_\alpha l_\alpha \tag{7.16}$$

The production of pairs for an aluminium target of thickness 10 μm is displayed in Fig. 7.11 (purple curve). It gives a rough estimation of the importance of the different processes of pair generation in laser-foil interaction and we can distinguish two different regimes of interaction depending on the laser intensity. At 10^{22} Wcm^{-2}, it seems that the pair production will be only created via the Bethe-Heitler process even in the case of a thin target (10 μm here). The other processes indeed appears

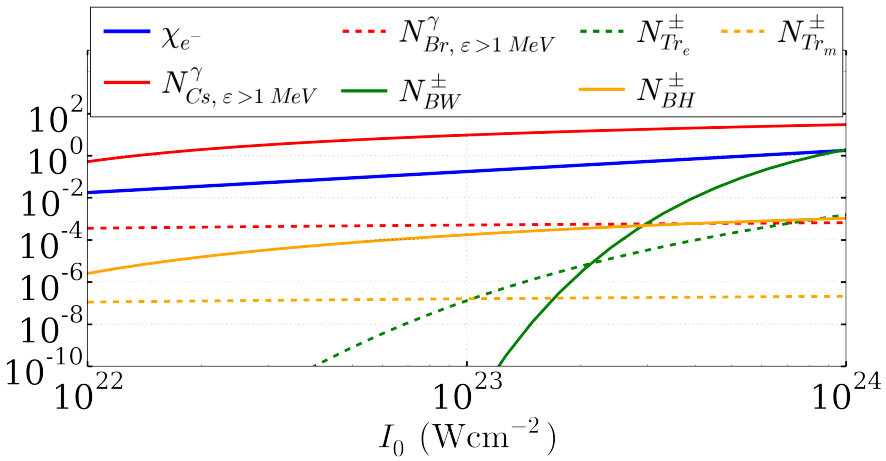

Figure 7.11: Electron quantum parameter χ_{e^-} (blue), number of γ-photons generated via the nonlinear Compton scattering N^{γ}_{Cs} (red), via the Bremsstrahlung N^{γ}_{Br} (dashed red), number of pairs generated via the nonlinear Breit-Wheeler $N^{\pm}_{BW}$ (green), via the electromagnetic Trident $N^{\pm}_{Tr,e}$ (green dashed), via the Bethe-Heitler (orange) and the matter Trident (dashed orange) during a laser period T_l from a single electron as a function of the laser normalized amplitude a_0.

completely non-significant. In this configuration, even the Trident process is lower than the Bethe-Heitler since the Compton emission is sufficiently bright (this would probably not be the case for lower intensities where the radiation is dominated by the Bremsstrahlung). However, the Bethe-Heilter pair production is relatively low per electron, around 5×10^{-4} at such an intensity and close to 10^{-3} at 10^{24} Wcm^{-2}. At intensity close to 10^{23} Wcm^{-2}, the Bethe-Heitler is still the dominant process, the Trident is 10^3 times lower and the nonlinear Breit-Wheeler is still non-significant. Note that we do not take into account the electron refluxing that could slightly raise the Bethe-Heitler and the Trident pair yield. At 10^{24} Wcm^{-2}, the nonlinear Breit-Wheeler overtakes the Trident and the Bethe-Heitler to reach a number of pairs per laser period above 1. As demonstrated in chapter 5, the emission and the pair creation processes in the matter weakly gain in efficiency as the particle and the photon energies rise in the relativistic regime. As a consequence, these processes are weakly directly dependent on the laser intensity, although the Bethe-Heitler reveals indirectly affected by the intensified γ-photons yield.

As a rough estimation of the number of hot electrons $N_{e^-,h}$ generated per laser period, we consider the ratio of the laser absorbed energy over the average electron energy. We can suppose an average electron energy of $\langle \gamma_{e^-} \rangle \sim a_0$. As for the laser absorbed energy, we consider an absorption coefficient η_{abs} that multiples the total energy equal to $\varepsilon_{las} \sim G a_0^2 T_0 \pi R_{las}^2$ where $G \sim 2.13 \times 10^{22}$ Js^{-1}m^{-2} (for $\lambda = 1$ μm), R_{las} is the focal spot radius. Therefore, we have $N_{e^-,h} = \eta_{abs} \varepsilon_{las} / \langle \varepsilon_{e^-} \rangle$. In order to

get an upper bound, let us consider half the absorption of the laser (which is the case at 10^{24} Wcm^{-2} according to the simulations), for a finite focal spot of 2 μm. At 10^{22} Wcm^{-2} ($a_0 = 85$ at 1 μm), we obtain a total number of hot electrons per laser wavelength of $N_{e^-,h} \sim 9 \times 10^{11}$ and a consequent γ-photon yield of 5×10^{11} and a Bethe-Heitler pair production of 2×10^6. At 10^{23} Wcm^{-2} ($a_0 = 600$ at 1 μm), we have $N_{e^-,h} \sim 6 \times 10^{12}$, $N_{\gamma,Cs} \sim 1.4 \times 10^{14}$ and $N_{e^\pm,BH} \sim 5 \times 10^9$. Finally, at 10^{24} Wcm^{-2} ($a_0 = 850$ at 1 μm), we have $N_{e^-,h} \sim 9 \times 10^{12}$, $N_{\gamma,Cs} \sim 2.6 \times 10^{14}$, $N_{e^\pm,BH} \sim 9 \times 10^9$ and $N_{e^\pm,nBW} \sim 1.7 \times 10^{13}$. It predicts that with extreme intensities close to 10^{24} Wcm^{-2}, over-critical pair plasmas may be created ($n_c = 1.1 \times 10^{12}$ particles per 10 μm^3)

According to Fig. 7.11, we can identify an intermediate regime of pair generation coupling the nonlinear Compton emission of γ-photons and the generation of pairs in the matter via the Bethe-Heitler process. Such a configuration would be experimentally feasible with forthcoming high-power laser facilities (Apollon, ELI...). Double-layer targets could be imagined in order to first maximize the laser absorption in γ-rays and then the pair conversion efficiency. For the first layer, a thin foil of electron density close to the transparency threshold is recommended, $n_{e^-} \sim a_0$. Then, a high-Z thick target would be preferred to a thin foil for the second layer in order to optimize the conversion efficiency. A more accurate study is required to determine the optimal thickness as a function of the intensity and the pair yield. The resulting pair flow is likely to be a highly divergent shield since the laser thin-foil interaction is a bright but short and weakly collimated photon source (of duration equivalent to the laser full width at half maximum).

7.4.2 Numerical simulation of the electron-positron pair production with a thin foil

As for the previous section, the generation of pairs during the interaction with a thin foil is now studied using 2D PIC numerical simulations. As shown in the previous subsection, the generation of pairs starts to be significant from an intensity of 5×10^{23} Wcm^{-2}. By means of PIC simulation, the problem has been first studied with EPOCH in Ridgers *et al.* (2012),Ridgers *et al.* (2013) and Brady *et al.* (2014). The effect of the pair production on the hole boring effect has been explored in Kirk *et al.* (2013). Some other teams have performed similar numerical implementation and continued this numerical study such as Ji *et al.* (2014), Ji *et al.* (2014), Nakamura and Hayakawa (2015) and Luo *et al.* (2015).

The first simulation is made in 2D in the plane wave approximation as for the previous section. The domain, the target and the numerical parameters are similar. The laser has the same properties except the intensity raised at 10^{24} Wcm^{-2} ($a_0 = 850$). For computational efficiency only the photons of energy above 1.022 MeV are created as super-particles on the grid. Under this energy threshold, the photons do not contribute to the creation of pairs. As for the previous simulation, the ions are accelerated at both the rear side of the target due to the target normal sheath

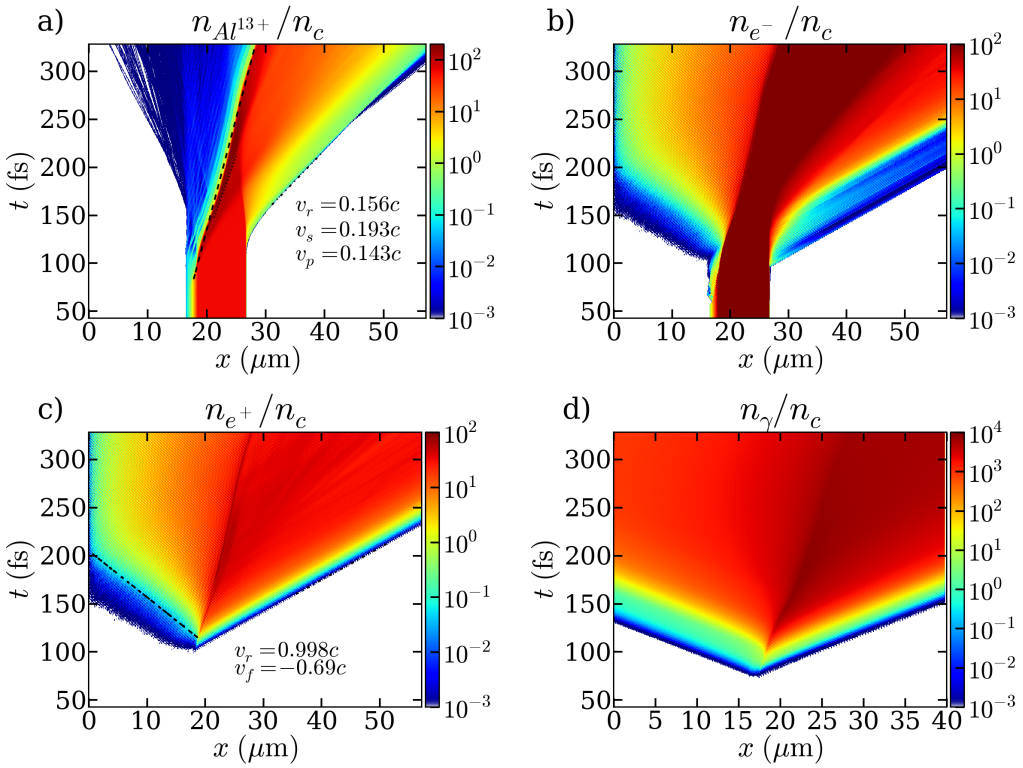

Figure 7.12: Time-evolution of the y-averaged ion $n_{Al^{13+}}/n_c$ (a), the electron n_{e^-}/n_c (b), the positron n_{e^+}/n_c (c) and the photon density n_γ/n_c (d). In (a), the dashed line corresponds to the target front (of piston velocity $v_p = 0.159c$), the dotted line to the shock front (of velocity $v_s = 0.193c$) and the dash-dot line to the rear front (of velocity $v_r = 0.156c$). In (c), the dashed line corresponds to the front of the positron cloud at density threshold $n_{e^+} \sim 0.1 n_c$ (of velocity $v_f \sim -0.69c$), the dash-dot line corresponds to the rear (with velocity $v_r \sim 0.998c$).

field and at the front side due to the radiation pressure. The time evolution of the y-averaged ion density is shown in Fig. 7.12. The linear evolution of the front side shows that there is a balance between the laser radiation pressure and the pressure of particles undergoing strong radiation losses. The numerical fitting of the ion target front gives a velocity of $v_p \sim 0.159c$ and $v_r \sim 0.156c$ for the rear side. The shock velocity is evaluated as $v_s = 0.193c$.

The γ-photons generated at the laser solid-interface are both emitted forward and backward as shown in Fig. 7.12d and Fig. 7.13 showing the phase space $x - p_x$ of the γ-photons at time 212 fs. The photons at the origin of the pair creation are propagating backward in the laser field composed of both the incident wave and the reflected one. Due to the hole boring, the reflected wave undergoes a dephasing and a Doppler effect so that the resulting wave is not standing anymore.

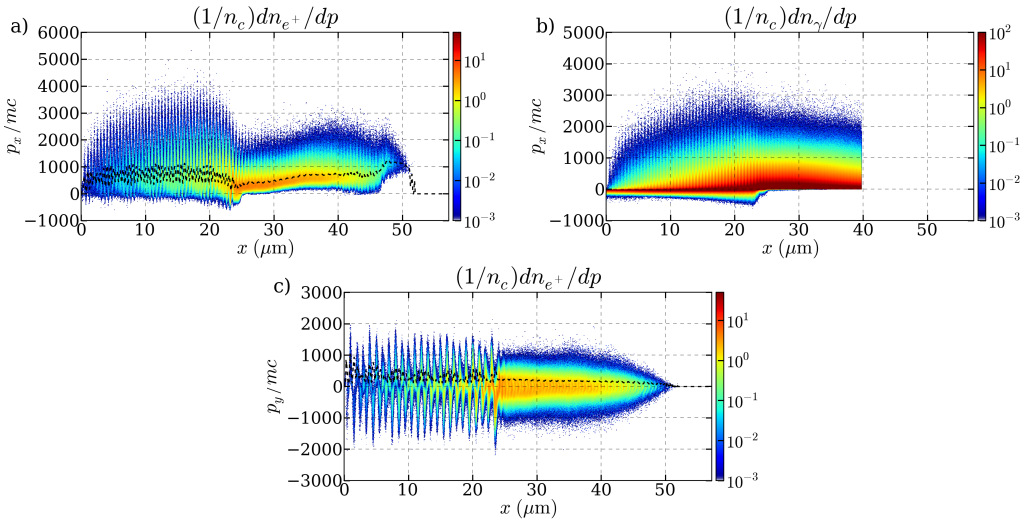

Figure 7.13: a) - Positron $x-p_x$ phase space. The dashed line represents the average p_x momentum. b) - Photon $x-p_x$ phase space. c) - Positron $x-p_y$ phase space. The dashed line represents the average p_y momentum. All the figures are plotted at $t = 212$ fs $(400\omega_0^{-1})$.

The pairs are generated in the propagation direction of the photons, which means backward. As they counter-propagate in respect to the incident laser field, they therefore lose energy by radiation cooling. They are finally deflected and forward re-accelerated by the laser toward the target. This can be observed in the phase space $x-p_x$ of the positrons in Fig. 7.13. In the vacuum in front of the target, the positrons propagating toward the target, $p_x > 0$, are the consequence of the laser re-acceleration. The momentum p_x is as strong as the the positrons approach the target interface with a maximum close to $p_x \sim 4000 m_e c$ and an average of the order of $800 m_e c$. Similarly, the positrons propagating backward, $p_x < 0$, have been recently created. In this case, the momentum is as low as the positrons are far from the target. For a photon of given energy, the chance to decay into a pair increases as they propagate farther away from the target. As a consequence, the pairs are mainly created close to the target. Finally, a pair plasma is generated at the laser-solid interface. It can be seen in Fig. 7.13a and Fig. 7.13c that the pairs oscillate driven by the laser. Entering the target, the pairs are scattered by the surface magnetic and electric fields that cause the p_x momentum to be reduced and the p_y oscillations to be diffused. Inside the target, the average momentum is equal to $p_y \sim 200 m_e c$ near the target front interface and is reduced to $135 m_e c$ near the tail of the pair plasma at $x = 45$ μm. Inside the target, some pairs can stay confined while the majority manages to cross and escape at the rear side. A pair plasma is therefore also generated at the rear side and expands with a relativistic velocity with the fastest electrons. The energy of the pairs is further enhanced at

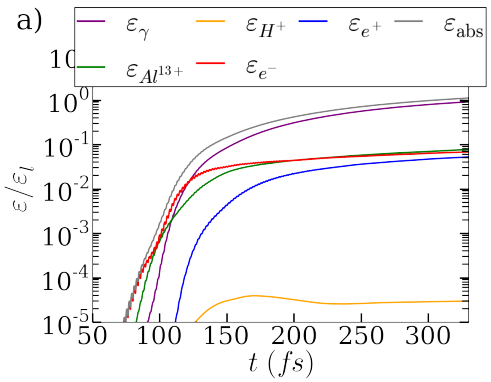

Figure 7.14: Energy balance showing the time evolution of the ion, the electron, the positron, the proton and the photon energy. The grey line corresponds to the total absorbed energy.

the exit of the target rear due to the target normal sheath field. This is shown in the time-evolution of the y-averaged positron density in Fig. 7.13. In our case, since the laser is semi-infinite and a stationary regime is reached, the pair plasma front is not confined near the target interface but it evolves with time. At the beginning of the interaction, the pairs are generated close to the solid-interface when the field is sufficiently strong via the first γ-photons. As the photons expand, then, the pair generation front also moves backward. The flow of γ-photons backward oriented increases since few photons really decay into pairs while entering in the strong laser-field. Some of them manage to leave the computational domain without decaying into pairs. By numerical fitting, the front pair generation front has an estimated velocity of $\mathbf{v_f}.\mathbf{x} = -0.69c$ and the rear front almost travels at the speed of light with $v_r \sim 0.998c$. At the end of the simulation, the front of the positron and the photon flows is outside the computational box. Since our laser is semi-infinite, from then on, the result becomes unphysical since the photons outside the box will not contribute to the creation of the pairs. Simulations are usually performed with short pulses so that this problem does not appear.

The energy balance of this simulation is shown in Fig. 7.14. The radiated energy is extremely significant accounting for almost 81 % of the laser energy having interacted with the target The absorbed electron and ion kinetic energy represent both 10 % of the laser energy. The positrons correspond to 5.6 % of the laser energy.

The angular and energy properties of the radiated photons at this intensity are shown in the spectrum of Fig. 7.15. The spectrum is integrated over the whole simulation and does not take into account the decay into pairs. The emission is mainly forward oriented ($p_x > 0$) representing 90 % of the total radiated energy. The peak in emission is located at angle $\theta = 0.38$ rad and energy 0.14 MeV. The average angular divergence is of 0.64 rad and the average photon energy of $\langle \varepsilon_\gamma \rangle \sim 166$

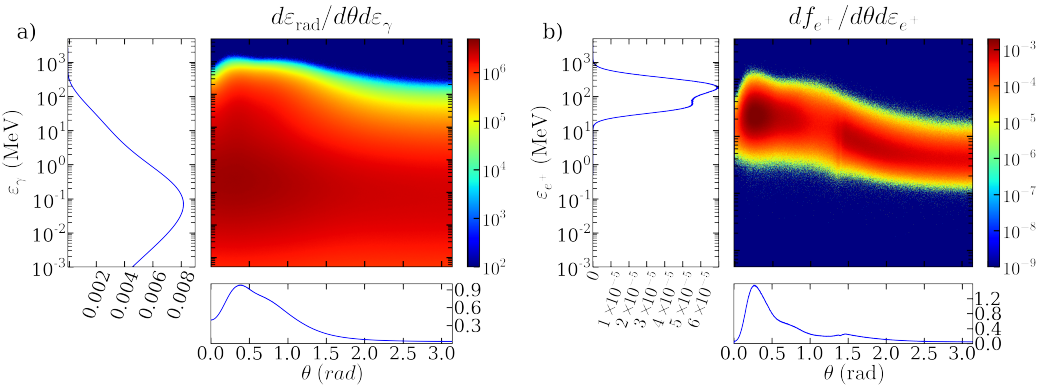

Figure 7.15: a) - Normalized angular energy spectrum $df_{\rm rad}/d\theta d\varepsilon_\gamma$ at the end of the simulation. Integration of the spectrum gives the total radiated energy. b) - Angular energy spectrum $df_{e^+}/d\theta d\varepsilon_\gamma$ of the positrons at the end of the simulation.

MeV, around 5 times higher than in the simulation at 10^{23} Wcm^{-2}.

The similar spectrum has been plotted for the pairs in Fig. 7.15. As for the photons, the positrons are mainly forward accelerated ($p_x > 0$) accounting for 84 % of the production at the end of the simulation. The peak in energy of the spectrum is located at $\theta = 0.26$ rad and 184 MeV. The average energy is equal to $\langle \varepsilon_{e^+} \rangle \sim 430$ MeV and the average angle to $\langle \theta_{e^+} \rangle \sim 0.56$ rad.

Chapter 8

Collision between a GeV electron beam and a counter-propagating extreme-intensity laser pulse

8.1 Presentation

As previously pointed out, an efficient configuration to achieve intense Compton γ-ray production (high quantum parameter χ_{e^-}) of given energy ε_{e^-} is to make it interact with a counter-propagating laser wave. The quantum parameter, χ_{e^-}, that describes how strong are the external fields compared to the Schwinger field in the electron boosted frame, can approach unity with significant electron energies and strong enough laser field amplitudes. When the fields seen by the electron approach the Schwinger field ($\chi_{e^-} \to 1$), quantum electrodynamics effects start to affect the particle motion in the laser field due to stochastic emission of high-energy photons by the inverse nonlinear Compton scattering. Similarly, the γ-photons counter-traveling in respect to the laser will encounter quantum parameter χ_γ close to one and undergo quantum electrodynamics effects. The most significant process is the pair decay via the nonlinear Breit-wheeler. In theory, the challenge is easily understandable, the stronger the laser intensity the lower the required initial electron energy, and vice-versa. As a consequence, as a unique way to test strong-field QED in the laboratory, this configuration appeared conceivable only in the 90's using linear accelerators to get sufficiently high electron energies for the interaction with the most powerful laser intensity at this time at the TW level. The experiment was first performed at SLAC in California. The linear accelerator provided a typical electron bunch of 46.6 GeV with near 10^{10} electrons in a volume of 2 mm long and a radius of around 30 μm at the laser-interaction point. The laser intensity was around 10^{18} Wcm^{-2} and duration of the order of the ps depending on the different considered configurations (Bula *et al.* (1996); Burke *et al.* (1997); Bamber *et al.* (1999)). They report the creation of 10^2 positrons after integration of the spectrum. This relatively low production is due

to the low amplitude of the field despite a quantum parameter of $\chi_{e^-} = 0.2$. This experiment is planned to be repeated at the SLAC with recent upgrades in order to measure the Compton scattering and the Breit-wheeler processes at higher precision and to study additional mass-shift, nonlinear and spin effects (Hartin *et al.* (2014)).

With the forth-coming laser facilities, we expect the laser intensities to be sufficiently important to contemplate an all-optical configuration as described in Fig. 8.1. This idea is motivated by the fact that these new laboratories will be equipped with multiple coupled beam lines. This is especially the case of Apollon that will have a PW line in addition to the multi-PW laser (Apollon (2015)) and ELI that will benefit from two multi-PW lasers (ELI (2015)). In an all-optical configuration, the electron beam is generated from the laser interaction with a gas jet in the so-called laser wakefield acceleration regime (referred to as LWFA, see Mourou *et al.* (2006) and Esarey *et al.* (2009)). The electron bunch is then sent in the second high-power laser in order to study the QED processes. Regarding the intensities between 10^{22} to 10^{23} Wcm^{-2}, reachable thanks to the forthcoming lasers the necessary electron energy to get χ values above or close to one is significantly reduced to values of the order of the GeV level that is easily achievable in LWFA with a PW laser. Such a configuration has been first considered as a source of high-frequency photons. At moderate electron energies and intensities, the emission is performed in the Thomson regime with radiation of soft X-rays. In the first experiments, the electrons were generated via small accelerators, usually able to accelerate electrons to few tens of MeV and sent to the pump-pulse (counter-propagating laser pulse). At high-intensities in the relativistic LWFA regime, the collision between an electron beam and a second laser pulse of 100 TW has been experimentally demonstrated in Chen *et al.* (2013), Powers *et al.* (2014) and Sarri *et al.* (2014). Another scenario consists of using the driver pulse as a scattering laser via the reflection on a solid foil or a plasma mirror. This has been experimentally performed in Phuoc *et al.* (2012) and Tsai *et al.* (2015). With high-intensities, this concept has been studies analytically and via numerical simulation in Hartemann *et al.* (2007). In the quantum regime, the nonlinear Compton emission could be a source of hard X-rays and γ-photons with energies close to the electron ones. With GeV electrons, the quantum regime could be approached with intensities above 10^{21} Wcm^{-2} with the present laser systems. At 10^{21} Wcm^{-2}, the laser intensity is sufficient to study the radiation reaction effect on the electronic dynamics (Vranic *et al.* (2014)). In extreme-intensity, from 10^{22} Wcm^{-2}, the concept as a source of γ-photons, has been analytically studied by different authors (Harvey *et al.* (2015); Blackburn *et al.* (2014); Blackburn (2015); Seipt *et al.* (2015)). In the framework of strong-field QED, it has also been analyzed in Mackenroth and Di Piazza (2011) and Krajewska and Kamiński (2012). The generation of pairs via the Breit-Wheeler process using γ-photons colliding with a counter-propagating laser pulse has been studied in the QED-framework in Krajewska and Kamiński (2012). The possibility to study the generation of pairs in an all-optical scheme with the future high-power lasers has been first demonstrated in Sokolov *et al.* (2010) using a

numerical integro-differential kinetic model.

When an intense laser pulse propagates in a ionized gas, it generates in its wake a driven plasma, also called Langmuir wave, that constitutes a collective response of the electrons to the perturbation created by the electromagnetic laser pulse, also referred in this case as the driver pulse. Oscillation of the electrons can be described as a modulation of the electronic density. It creates a longitudinal electric wakefield E_x traveling in the direction of the driver pulse with phase velocity v_{ph} close to the driver pulse group velocity v_g. We can distinguish different regimes of interaction in underdense plasma for the laser wakefield electron acceleration depending on the laser intensity. For non-relativistic intensities $a_0 \ll 1$, the plasma wave is a linear response of the laser perturbation. The electron density modulation, the electron fluid velocity and the longitudinal electric field are sinusoidal oscillations at the plasma frequency ω_p that can be described by the fluid equations. Inside the density cavities, the electric field is negative in the negative electron density gradients and positive in the positive ones. Electrons correctly injected in the right phase of the plasma wave can gain energy thanks to the electric field and this constitutes the basics of the laser wakefield acceleration with an external source of electrons (Tajima and Dawson (1979); Gorbunov and Kirsanov (1987)).

For stronger intensities $a_0 \geq 1$, the wakefield is no longer sinusoidal and the nonlinear effects cause a steepening of the plasma wave. This is the nonlinear regime. Electron fluid velocity v_{e^-} approaches the plasma wave phase velocity v_{ph}. In the electron density profile, spikes appear at the position where $v_{ph} \simeq v_{e^-}$. In this regime, the plasma frequency depends on the driver pulse normalized amplitude a_0. This constitutes the limit of a fluid approach and physically corresponds to the breaking of the plasma wave. Electrons oscillating out of phase can be suddenly ejected from the density spikes of the plasma wave. This mechanism enables the electrons to be self-injected in the acceleration phase of the wake field and to be therefore trapped and forward accelerated. The breaking threshold $\gamma_{e^-} = \gamma_{ph}$ gives equation (Zhidkov *et al.* (2004))

$$a^2/2 + 1 = \omega/\omega_p \sqrt[4]{1 + a^2} \tag{8.1}$$

Breaking condition on the normalized amplitude therefore yields

$$a_{br} = \begin{cases} \sqrt{2\left(\omega/\omega_p - 1\right)} & a \leq 1 \\ \left(2\omega/\omega_p\right)^{2/3} & a \gg 1 \end{cases} \tag{8.2}$$

This concept constitutes an all-optical source of high-energy electrons, released of any external source. In this case, the beam charge and energy depends on the plasma density and the laser intensity.

In the bubble acceleration regime considered here (Pukhov *et al.* (2004)) also referred to as the 3D nonlinear regime, the radiation pressure of a short-pulse intense laser expels the electrons outward so that cavities with steep gradients are created in its wake. Electrons self-injected from the rear of the bubble are forward accelerated in the first half part of the cavity thanks to the negative longitudinal electric

field E_x present in this part. In the other part of the bubble, the field changes of sign and is therefore decelerating for the electrons. Among the strong accelerating longitudinal electric field, these cavities present focusing properties brought by the created magnetic field.

Using the scaling of W. Lu *et al.* (Lu *et al.* (2007)) (other scalings exist such as Gordienko and Pukhov (2005)), we can estimate the properties of the final electron bunch as a function of the plasma (density, distance) and the laser parameters (intensity). We consider driver pulse parameters close to Apollon for the electron beam generation, that is to say, a laser of 15 J, of duration 30 fs and a waist at full width at half maximum (FWHM) of 23 μm for a wavelength $\lambda = 0.8$ μm. After propagation in an homogeneous plasma of 1 cm of electron density $n_e = 0.001 n_c$ (1.7×10^{18} cm^{-3}), we obtain a final electron beam energy of 2 GeV for a charge of 1 nC.

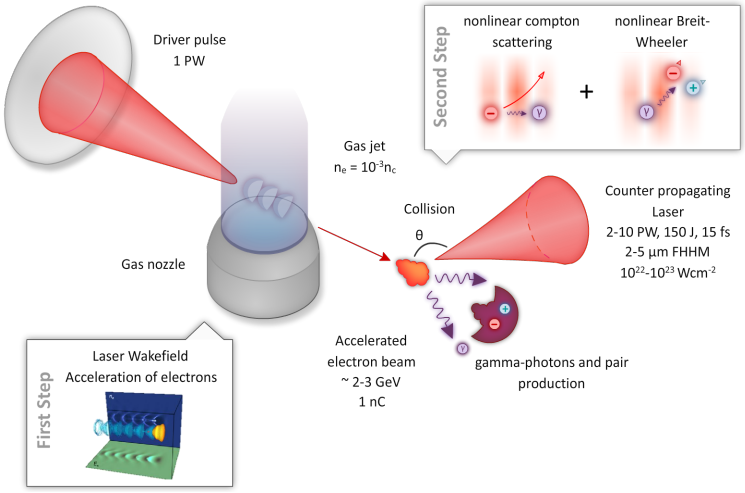

Figure 8.1: Scheme of the all-optical configuration studied in this chapter. Strong-field QED emission of γ-photons and the decay into pairs is studied in an all-optical scheme by the collision of a LWFA electron bunch with a counter-propagating extremely intense laser.

8.2 Approximation of the production rate of photons and pairs using a reduced kinetic approach

In order to estimate the production yield of γ-photons (photon of energy $\varepsilon_\gamma > m_e c^2 \sim$ 1.022 MeV) and pairs that could be generated with the previously described configuration, we use the same reduced kinetic model as described in the section 6.7.1. Here, the electron, photon and positron distributions are solved in time using the

cross-sections of the different mechanisms neglecting the advection and the electrostatic interactions and assuming an unidirectional propagation of the beam at the speed of light c. We therefore assume that the particles keep relativistic energies and that they are not reflected backward by the laser pulse. We also neglect the potential divergence of the beam, the wiggling and the deflection that could be induced by the laser pulse. The radiation losses are treated continuously despite the use of the quantum cross-sections. The result is an average behavior over a beam of electrons (the straggling effects are not included). However, the pair cascading effect is taken into account with this approach, the distribution of the electrons, the positrons and the photons are discretized logarithmically. The photon energy distribution f_γ ranges from $\gamma_\gamma = 10^{-5}$ to $\gamma_\gamma = 10^4$ for a discretization in 1000 subdivisions. The electron and positron distribution f_{e^-} and f_{e^+} ranges from $\gamma = 1$ to $\gamma = 10^4$ again for a subdivision in 1000 levels. The beam is initially located $70\omega_0^{-1}$ (~ 37 fs) before the peak in intensity and the time step is equal to $\Delta t = 0.05\omega_0^{-1}$ ($\simeq 0.008$ μm).

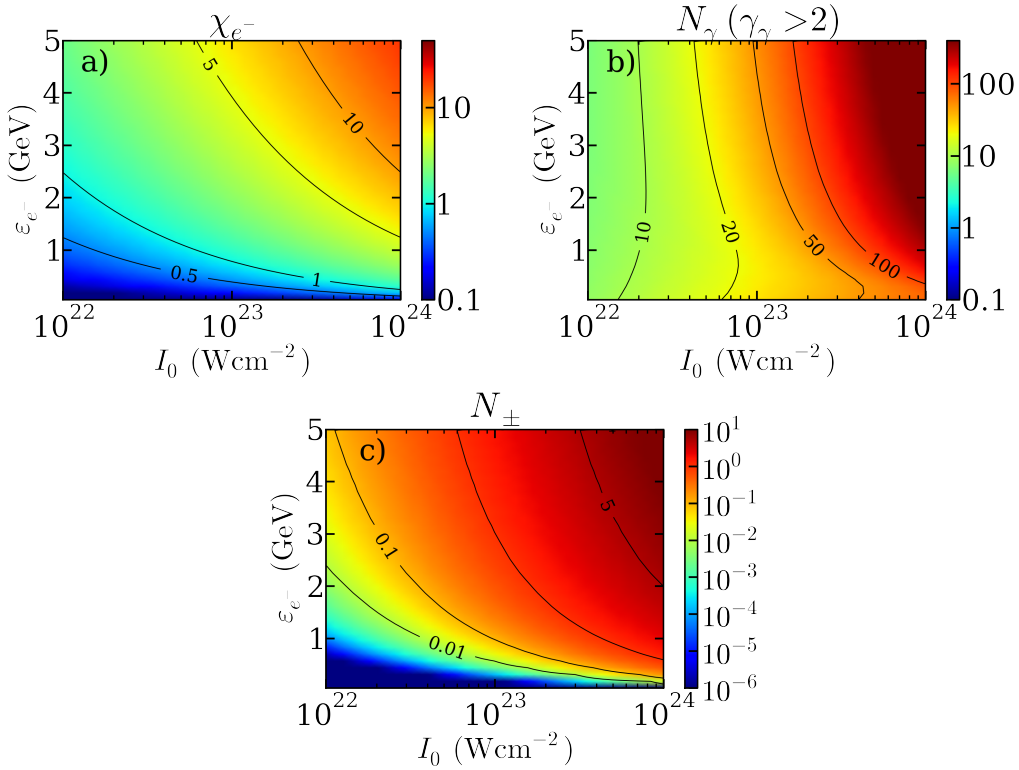

Figure 8.2: a) Maximal electron quantum parameter χ_{e^-} as a function of the laser intensity and the electron energy ε_{e^-}. Number of γ-photons (b) and number of pairs (c) generated during the interaction per electron as a function of the laser intensity and the electron energy. The black line corresponds to the iso-contour for each parameter

The laser is regarded as a plane wave and has a Gaussian profile of duration T_l

= 15 fs (FWHM). The laser interaction with a counter-traveling electron bunch is parametrically studied with different electron bunches of initial energies ε_{e^-} ranging from 100 MeV to 5 GeV (all the electrons in the bunch have the same initial energies) and different laser intensities I from 10^{22} Wcm^{-2} to 10^{23} Wcm^{-2}.

The result of the runs are shown in Fig. 8.2. The first frame, Fig 8.2a, represents the maximal quantum parameter reached during the simulations. At 10^{22} Wcm^{-2}, a quantum parameter of 1 is reachable for multi-GeV electrons, above 2 GeV. Exploring a strong QED regime is therefore already possible with present-day lasers with a GeV source of electron. Nonetheless, we see that this becomes more accessible as the intensity rises and reaches values close to 10^{23}, then one GeV electrons are sufficient. Above this intensity, reachable with the future installation ELI, the required electron energy drops to the hundred of MeV level.

As shown in section 2.1, with an important quantum parameter, an electron will travel a shorter distance in the strong field before emission of a high-energy γ-photon. After few emissions, the electron will have lost sufficient energy to leave the quantum regime. But, over a bunch of electron, the average γ-photons yield rises. This can be observed in Fig. 8.2b where the number of γ-photons increases as the field amplitude and the initial electron beam energy are high. In the range of parameters of Apollon, for an intensity $I \leq 10^{23}$ Wcm^{-2}, we expect a number of γ-photons around 10 to 20 per electrons during the interaction.

Then, Fig. 8.2c presents the nonlinear Breit-Wheeler pair yield per electron as a function of the beam energy and the laser intensity. The photon decay probability is as high as the field is strong and the pair yield as high as the number of photons is significant. In the range of parameters of Apollon, the pair yield strongly varies with the electron energy. For a 2 GeV beam, we can expect around 0.5 pairs per electron for $I \sim 10^{23}$ Wcm^{-2}.

Let us again consider the Lu's scaling. For a beam energy close to 2 GeV and a charge of 1 nC, we therefore expect 500 pC of positron in this configuration with the Apollon laser. This corresponds to the production of 3×10^9 pairs per shot. This is potentially one of the most efficient source of collimated positrons with the configuration of G. Sarri (Sarri *et al.* (2015)).

In order to make a more realistic calculation, several modelings are possible to simulate the concept. A full kinetic approach can be used where the distributions are fully described in space and momentum by the Vlasov equation. A Monte-Carlo approach can also be considered as done in Elkina *et al.* (2011) but in this case, the electromagnetic interactions between the particles should be neglected. In our case, we decide to use the PIC method both for the computation of the laser wakefield accelerated electron bunch and the study of the QED processes. To this aim, two different PIC codes are used.

The generation of the LWFA electron beam is simulated using the PIC code CALDER-CIRC (Lifschitz *et al.* (2009)). In this version, the fields are discretized using cylindrical coordinates. This scheme is particularly adapted to axisymmetric

geometry problems such as the laser wakefield acceleration (laser envelop, shape of the wake wave and the wake fields are quasi-axisymmetric). The laser oscillating field is however not axisymmetric. A Fourier decomposition is used in the poloidal direction and the first few needed modes for the physics are solved. Only the first two modes are computed. The first mode corresponds to a pure axi-symmetry with no dependence on θ. The second mode enables to described the laser field oscillations. Each mode is separately computed. Solving only the first modes also has the advantage to reduce the required computational time. The particle density and current also has to be put in the Fourier domain before projection. The cells are 3D volumes that correspond to rings characterized by the radial position, the longitudinal step dx and the radial step dr. At the end, such a simulation has almost the cost of a 2D Cartesian simulation. In fact, our whole scenario is axi-symmetric and we could have used this PIC code to describe the whole process providing that the QED effects were implemented in this version.

We prefer nonetheless to transfer the generated electron beam to the PIC code CALDER-3D (Cartesian geometry) enriched with QED effects. In any case, all the simulations are performed in 3D since the problem is not so numerically expensive to simulate (the inflation of particles and photons is limited by the short interaction duration).

8.3 Creation of a GeV electron beam in the laser-wakefield acceleration regime

In this section, we study the generation of the electron beam using CALDER-CIRC. First, we consider an homogeneous density profile as shown in Fig. 8.3a. The gas jet is composed of hydrogen of density $n_e = 10^{-3} n_c$ and the jet front is modeled with an initial linear ramp of 200 μm. The laser parameters are similar to what we give in section 8.1 (duration of 30 fs, waist of 23 μm, $\lambda = 8$ μm, energy of 15 J, intensity close to 10^{20} Wcm^{-2}). The plasma is considered as semi-infinite. This simulation was performed with a rough discretization $dx = 0.25c/\omega_0$ and $dy = 4c/\omega_0$. The evolution of the energy spectrum as a function of the propagating distance in the plasma is shown in Fig. 8.3c. We can see that all along the propagation, many bunches of electrons have been injected and forward accelerated. They form many trails at different energy levels starting at different positrons. The upper part of the spectrum culminates at 2.2 GeV. We can identify two peaks in the distribution corresponding to the head of the beam at 2 GeV and the main part at 1.2 GeV as shown in Fig. 8.3b (red curve). All electrons taken into account, the spectrum is broad with a significant part of the beam charge distributed bewteen 500 MeV and 1.5 GeV . Finally, the beam head has a charge close to 1 nC and the charge rises to 5 nC taking into consideration all the electron bunches.

Although this first simulation could be satisfactory to end up with QED effects,

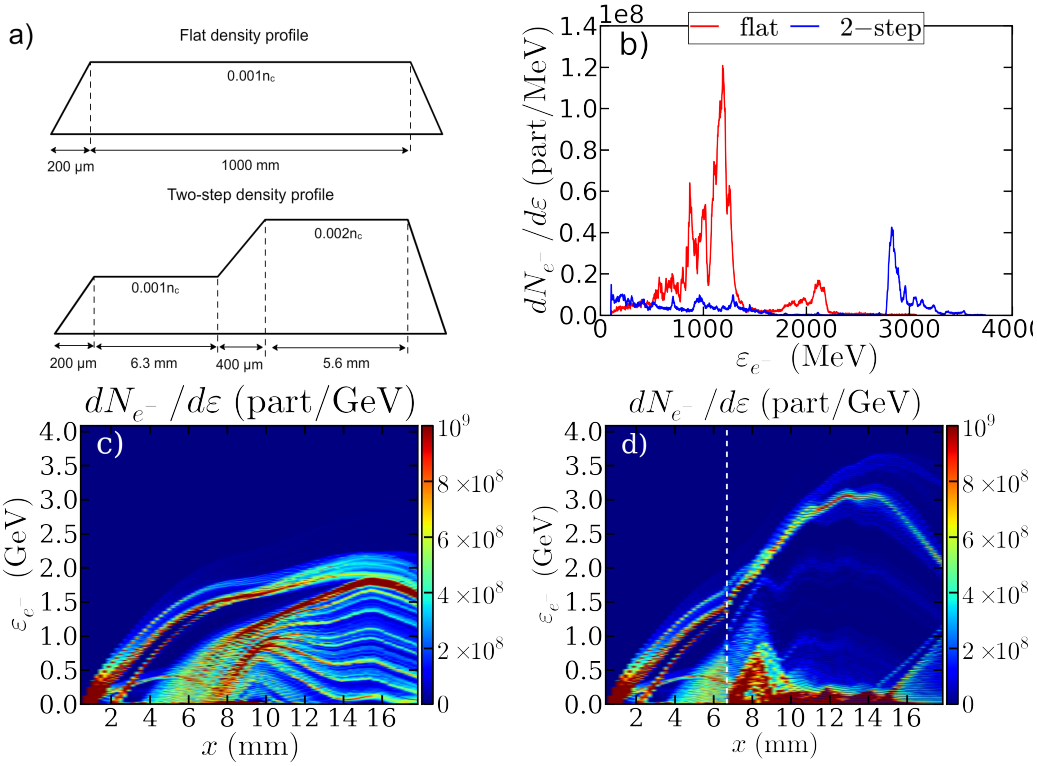

Figure 8.3: a) Scheme of the two considered density profiles. b) Comparison between the final beam energy spectra for the flat and the two-step profiles. Electron energy spectrum for the flat density profile c) and the two-step profile d) as a function of the position in the plasma. On the spectrum for the two-step profile, the dashed white line corresponds to the limit between the density levels.

we search to optimize the density profile to get the maximal electron energy. For this aim, we consider a two-step profile as described in Fig. 8.3a. The two-step profile is composed of two different homogeneous parts. The first part has a length of 6.3 mm at $n_e = 10^{-3} n_c$. The second one has a length of 5.6 mm at $n_e = 2 \times 10^{-3} n_c$. The two regions are separated by a short density ramp of 400 μm long. The jet front is simulated via a linear ramp of length 200 μm. For this simulation, the numerical parameters are similar to the previous ones with $dx = 0.25c/\omega_0$ and $dr = 4c/\omega_0$. This increasing in density leads to the reduction of the bubble size and the electron beam that was already partially dephased is relocated in the highest accelerating region of the wakefield, at the back of the bubble. This process selects the beam head and therefore reduces the total accelerated charge. As compensation, the beam gains a new acceleration distance before reaching the decelerating part of the bubble that will contribute to boost its energy. This can be appraised in Fig. 8.3d depicting the evolution of the energy spectrum all along the propagation in the plasma for this particular case. In the flat case, after a propagation of 6 mm, we can see that

the initially injected electron bunch has already reached almost its maximal energy and hardly gains a few more 500 MeV during the next 10 mm. On the other hand, the two-step profile clearly offers a second boost to the beam head thanks to the second plateau and literally doubles its energy from 1.5 GeV to 3 GeV during this second step. Moreover, the intermediate energies in the spectrum have been killed and results only in a mono-energetic beam at the maximum accessible energy as highlighted in the energy spectrum of Fig. 8.3b (blue curve). The final beam charge is of 2.2 nC, almost half of the charge obtained with flat profile.

Finally we select the electron beam from the two-step profile for its higher energy and more mono-energetic character. We consider a gas jet of finite size where the tail of the jet is modeled via a decreasing ramp of length 200 μm that contributes to focus the beam before its propagation in the vacuum. The beam is taken just at the end of the gas jet to avoid any spreading. The electrons with an energy under 100 MeV are not kept. The simulation is made with a better resolution than the previous ones with $dx = 0.125c/\omega$, $dr = 4c/\omega$, a time step of $dt = \omega_0^{-1}$ and 40 particles per cells. The super-particles space distribution of the beam with energy color dependency is plotted in Fig. 8.4. The beam is composed of three parts. The beam head is the most energetic part with a maximal electron energy of 3.8 GeV (Fig. 8.4 and Fig. 8.3b). Then, the main part of the beam has an average energy of 3 GeV. These two parts concentrate 63% of the total charge (between 2.5 and 3.8 GeV). Then, the beam has a subsequent broader part under 1.7 GeV as shown in Fig. 8.3b and 8.3d. All electrons taken into account, the average beam energy is of the order of 1.8 GeV. The beam divergence is quasi-isotropic and equal to $\theta^0_{e^-} \simeq \theta^0_{e^-,xy} \simeq \theta^0_{e^-,xz} \simeq 3$ mrad in average where $\theta^0_{e^-,xy}$ is the electron angular divergence in the laser polarization plane $x-y$ and $\theta^0_{e^-,xz}$ the divergence in the perpendicular plane x, z, both defined as

$$\theta_{xy} = \arctan\left(\frac{p_y}{p_x}\right) \qquad \theta_{xz} = \arctan\left(\frac{p_z}{p_x}\right), \tag{8.3}$$

x corresponding to the axis of propagation. The electron beam has a longitudinal length of $l_b \sim 12$ μm and transverse FWHM sizes of 4 μm and 2 μm respectively along and normal to the laser polarization direction (y-axis).

8.4 Study of the generation of high-energy photons and pairs in the interaction with a multi-PW laser

In this section, we study the interaction between the laser-wakefield accelerated electron beam and a counter-propagating mutli-PW laser using the PIC code CALDER-3D. We first consider a reference simulation in order to comprehend the physics of

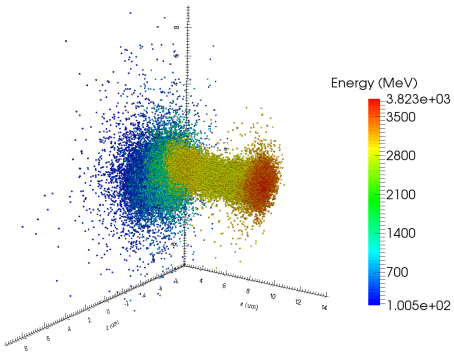

Figure 8.4: 3D view of the super-particle space and energy distribution. The color of the sphere depends on the particle energy in MeV.

the interaction. This is then followed by a parametric study to explore the impact of the laser intensity and focal spot size on the positron properties.

8.4.1 Reference simulation

The electron beam is now sent in direct incidence (head-on collision) to the counter-propagating 5-PW laser. Linearly polarized with a Gaussian temporal profile of duration $T_l = 15$ fs (FWHM), the wave is characterized by a wavelength of $\lambda_l = 0.8$ μm. It has a transverse Gaussian profile of focal spot diameter of 2 μm (FWHM). The laser parameters are chosen to reach the maximal focused intensity of 10^{23} Wcm^{-2} ($a_0 \sim 219$) on the head of the beam. Experimentally, the laser should be focused just at the exit of the gas jet to avoid the spreading of the electron beam. This is the adopted configuration in this chapter. For the Cartesian simulation, the domain has for dimensions $l_x \times l_y \times l_z = 36$ μm $(225c/\omega_0) \times 22$ μm $(140c/\omega_0) \times 22$ μm. The propagation axis corresponds to the longitudinal x-axis and the polarization direction of the wave to the y-axis. At the end of the CALDER-CIRC simulation, a file is created with all the super-particle weights, positions and kinetic properties. The beam in CALDER-3D is initialized from this external file on the left side of the simulation box ($x = 0$) and propagates toward the positive x-values. The laser is injected from the right boundary and focused on the position $x \simeq 17.5$ μm in order to synchronize the collision between the beam head with the maximal laser intensity. The beam is frozen during the laser injection until time $t = 75$ fs. The space discretization corresponds to $dx = 0.05c/\omega_0$ and $dy = dz = 0.1c/\omega_0$ for a time step $dt = 0.04\omega_0^{-1}$. All the boundaries are absorbing both for the particles and the fields. The simulations have been performed with a lower and a higher discretization. The final results appear extremely close in terms of generated photon number and positron charge and average energy, in terms of photon and particle energy spectra

as well as particle angular divergence. The current numerical settings are chosen to perform a simulation without exceeding the total available memory on 1000 cores on the Curie super-computer at CCRT in France (simulations last 7 hours in average with these parameters).

The laser-beam collision is illustrated via different figures. The evolution of the energy spectrum as a function of the relative distance to the laser peak in intensity before, during and after the collision are shown in Fig. 8.5 for the electrons, in Fig. 8.6 for the photons and in Fig. 8.9 for the positrons. We define the relative distance as $\xi = (x - x_{\text{peak}})/\lambda$ where x_{peak} is the position of the laser peak in intensity. The 3D space charge densities (isosurface) are plotted in Fig. 8.7a for the electrons, in Fig. 8.7b for the photons and in Fig. 8.7c for the positrons after the interaction at time 130 fs, around 30 fs after the interaction with the laser peak in intensity.

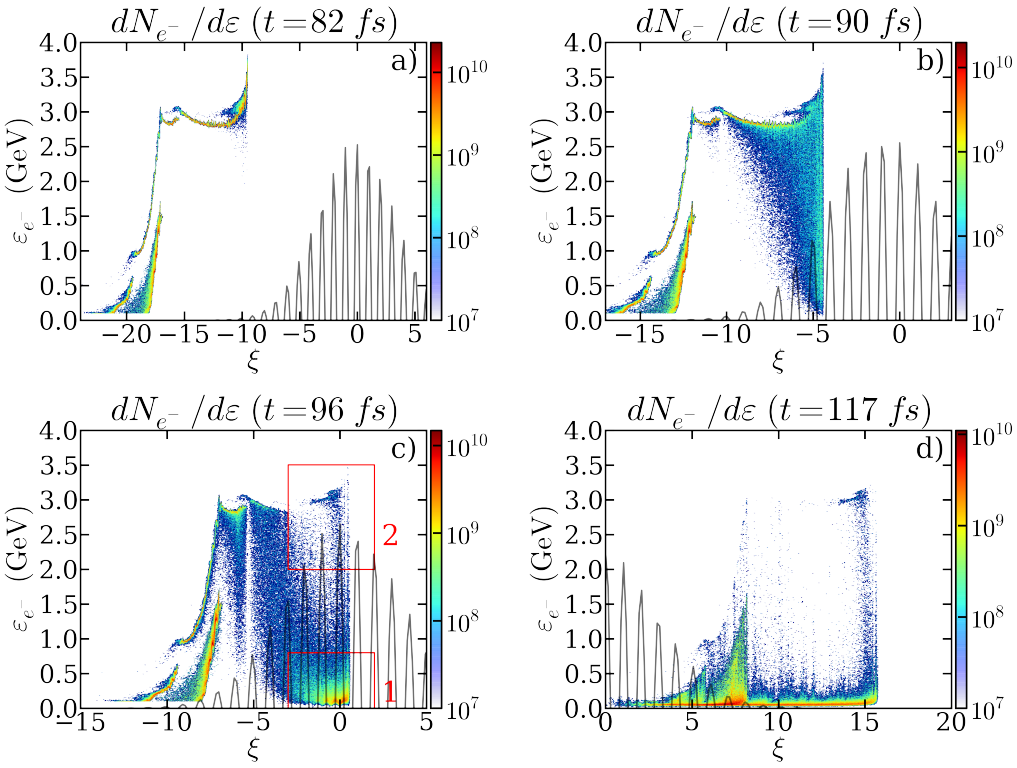

Figure 8.5: Electron energy spectrum before (t = 82 fs) (a), during (t = 90 fs and t = 96 fs) (b,c) and after (t = 117 fs) the laser-beam collision (d) as a function of the relative distance ξ to the peak x_{peak} in intensity.

The initial electron energy spectrum at the beginning of the interaction is shown in Fig. 8.5a. The beam head, located at $\xi = -10$, has already started to radiate at the foot of the laser as shown in Fig. 8.6a. At this early level, the emission occurs in the semi-quantum regime ($\chi_{e^-} \sim 0.1$, $a_0 \sim 10$). The electron energy is sufficient to lead to the emission of γ-photons. At time t = 90 fs, the beam head encounters

the required field strength to reach a quantum emission ($\chi_{e^-} \sim 1$, $a_0 \sim 70$). The γ-photons are emitted with significant energies taking away an important part of the electron kinetic one, in the GeV level, as shown in Fig. 8.6b. The radiation losses in this part are extremely strong and the electrons rapidly cool down as shown in Fig. 8.5b. At time $t = 96$ fs, the beam head highlighted by the red frame 1 in Fig. 8.5c enters the laser peak in intensity with an energy of few hundreds of MeV. The electrons have already lost the main part of their energies and the most energetic photons have been created before the laser peak. Since the laser focal spot $d_l \sim 2$ μm is smaller here than the transverse size of the electron beam $d_b = 16$ μm, some electrons do not interact and travel on the side of the laser. They correspond to the high-energy electrons highlighted by the frame 2 in Fig. 8.5c.

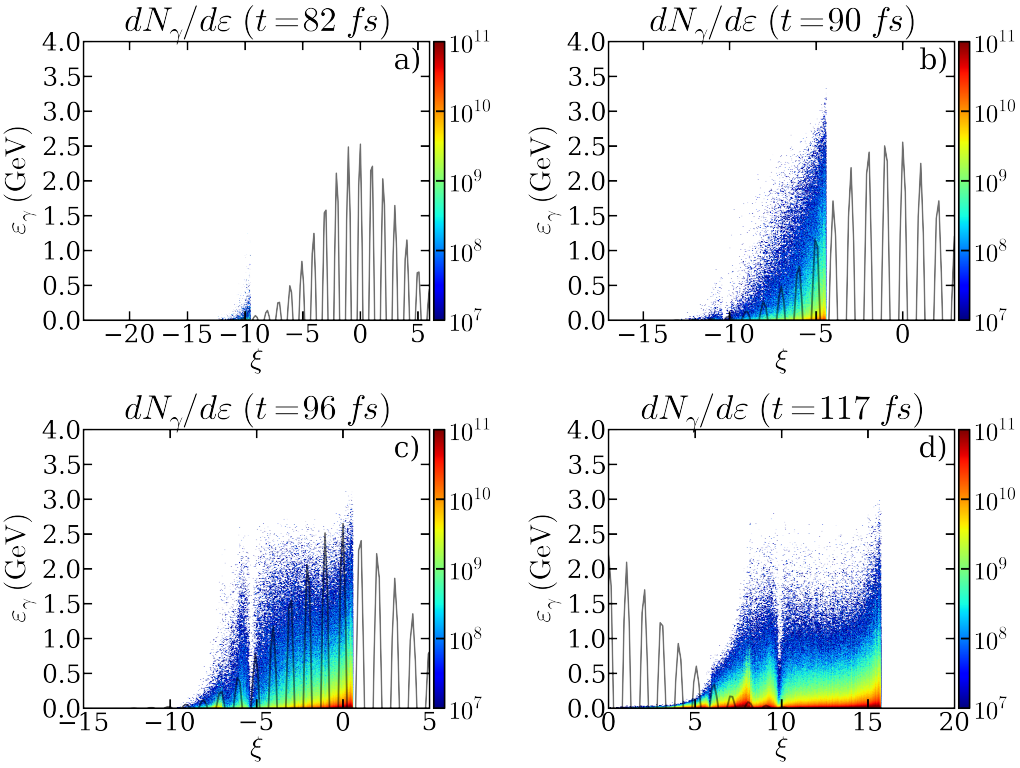

Figure 8.6: Photon energy spectrum before (a), during (b,c) and after the laser-beam collision (d) as a function of the relative distance ξ to the peak x_{peak} in intensity.

In order to understand the average behavior of an electron as a function of its initial energy, we simulate different test particles with an initial energy ranging from $\varepsilon_{e^-,0} = 100$ MeV to $\varepsilon_{e^-,0} = 10$ GeV. The radiation losses are modeled using a continuous description with a quantum correction. Fig. 8.8a represents the evolution of the quantum parameter χ_{e^-} as a function of the relative distance ξ. It shows that χ_{e^-} is not maximal in the laser peak in intensity but two laser periods before. The fact that the field is sufficiently strong to reach the quantum regime before the laser

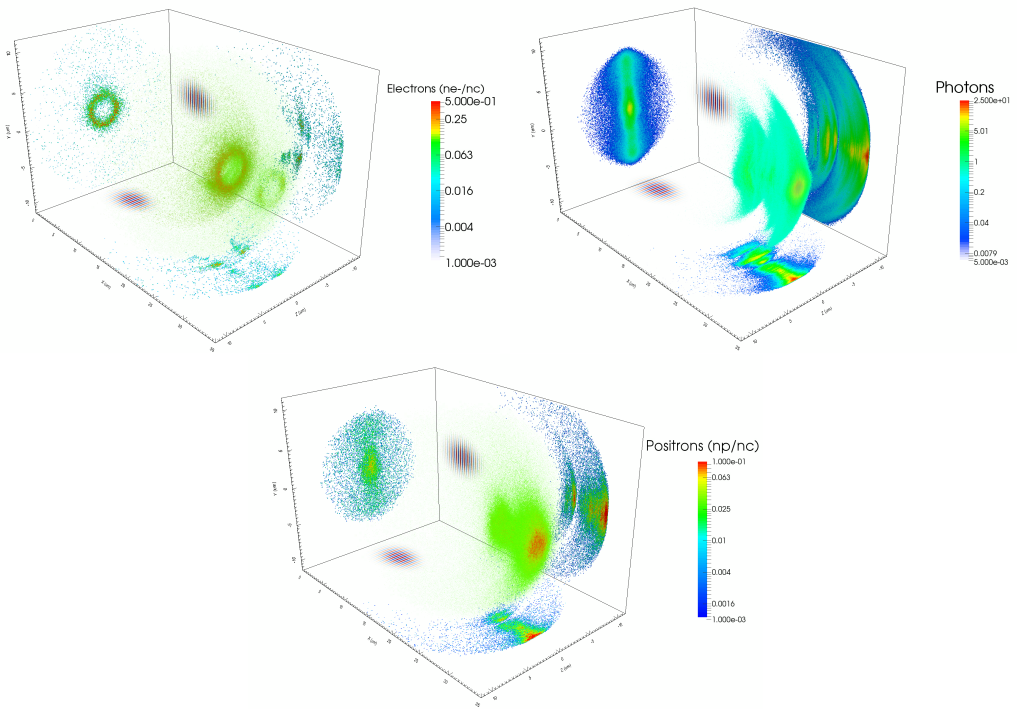

Figure 8.7: 3D view of the beam electron density via iso-surfaces at the end of the laser interaction. Density slices are projected on the domain boundaries for the planes $x = 27.5$ (denser part of the head of the beam), $y = 0$ and $z = 0$. The laser is represented through the electric field E_y for isosurfaces $a_0 = eE_y/mc\omega \sim \pm 100$.

peak causes the electrons to radiate more than 90 % of their kinetic energy when they reach $\xi = 0$ for $\varepsilon_{e^-,0} \geq 1$ GeV as shown in Fig. 8.8b which gives the evolution of the electron energy in the wave. Paradoxically, the particle that can cross the laser by loosing the less energy are the less energetic ones. Some particles in this case can eventually gain more energy in the laser wave than they had initially. The lowest energy particles can be reflected and accelerated backward. The photon energy at the maximum radiated energy of the energy spectrum $\varepsilon_{\gamma,\max}$ is plotted in Fig. 8.8c. For χ_{e^-}, $\varepsilon_{\gamma,\max}$ is calculated using the classical spectrum and the fitting function described in 2.1 in the quantum regime. As the initial particle energy is high, the most significant photon energy is observed earlier in the wave, around $\xi = -3$ for a GeV particle. The photon energy depends both on the electron energy at emission and the quantum parameter (which is proportional to the field amplitude). When the photons enter the strong field area, they are almost full of energy and consequently radiate easily GeV photons. When they approach the peak in intensity, despite an increase of the field amplitude that still leads to $\chi_{e^-} \sim 1$, most of the electrons have already lost too much energy to produce photons above the level of several hundreds of MeV.

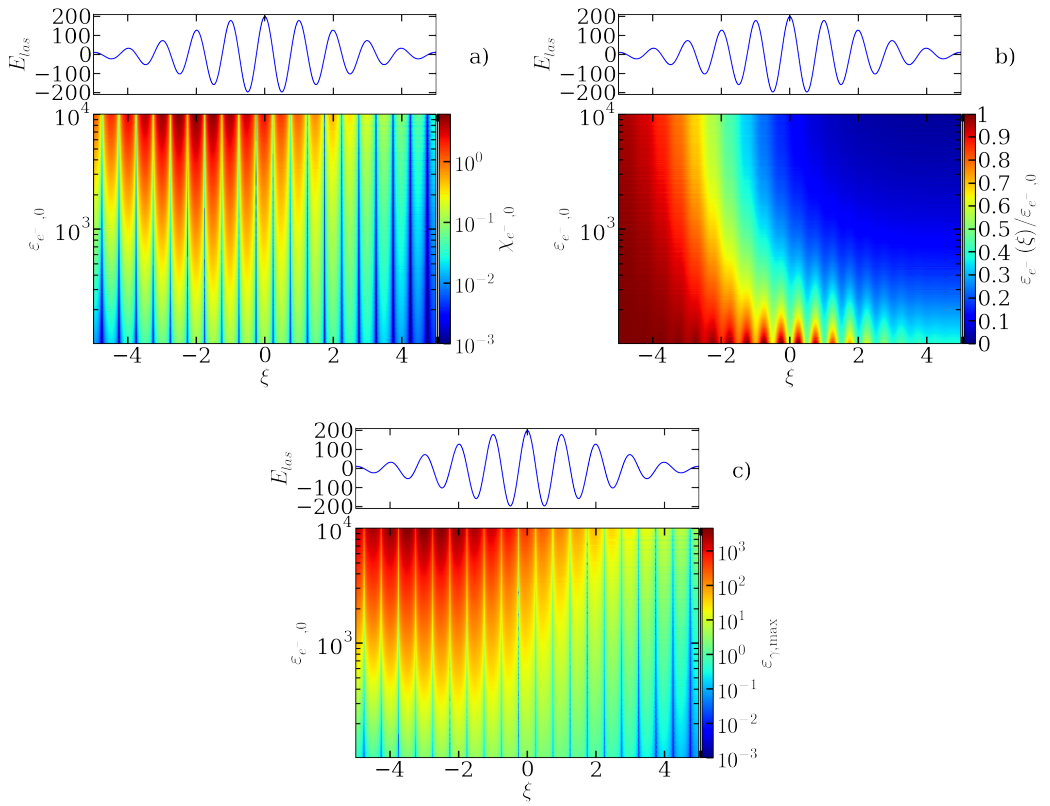

Figure 8.8: Evolution of the quantum parameter χ_{e^-} (a), of the normalized electron energy ε_{e^-} (b) and the photon energy $\gamma_{\gamma,\max}$ at the maximum of the energy spectrum (c) as a function of the initial electron energy $\varepsilon_{e^-,0}$ and the relative distance to the laser peak ξ.

At the end of the interaction, the electron and the photon energy spectrum as a function of the relative distance to the laser peak are respectively displayed in Fig. 8.5d and Fig. 8.6d. Finally, 85 % of the electron beam kinetic energy has been radiated away. The photon energy spectrum $dN^0_\gamma/d\gamma$ before the pair creation is given in Fig. 8.10 and shows that the distribution is broad ranging from the hard X-rays to γ-rays. The maximum photon energy is close to the maximal initial electron energy $\varepsilon_\gamma \sim \varepsilon_{e^-,0} \sim 3.5$ GeV. The average γ-photon energy is equal to 33 MeV (the result is very close considering all the photons of the spectrum). The 3D space-distribution of the electron beam and the γ-photon cloud after the laser interaction are respectively shown in Fig. 8.7a and Fig. 8.7b. The photon emission forms a forward-directed cone in the propagation direction of the electron beam with an emission brilliance of 3×10^{22} photons/mrad^2/mm^2/s/0.1 bandwidth close to the average energy of 33 MeV. Close to 1 MeV, we obtain 2×10^{21} photons/mrad^2/mm^2/s/0.1 bandwidth. The brilliance was calculated considering the photons emitted in a range $\gamma \pm \Delta\gamma$, with $\Delta\gamma = 2/m_e c^2$ to get a better statistic. After renormalization at 0.1 bandwidth (BW),

we have 2×10^6 photons. We assimilate the angular spectrum to a Gaussian and we use the full width at half maximum as the emission angle, close to 3 mrad here. The emission occurs in the volume of the electron beam. The photon beam is more divergent than the initial electron beam with $\theta^0_{\gamma,xy} = 0.2$ rad and $\theta^0_{\gamma,xz} = 0.017$ rad.

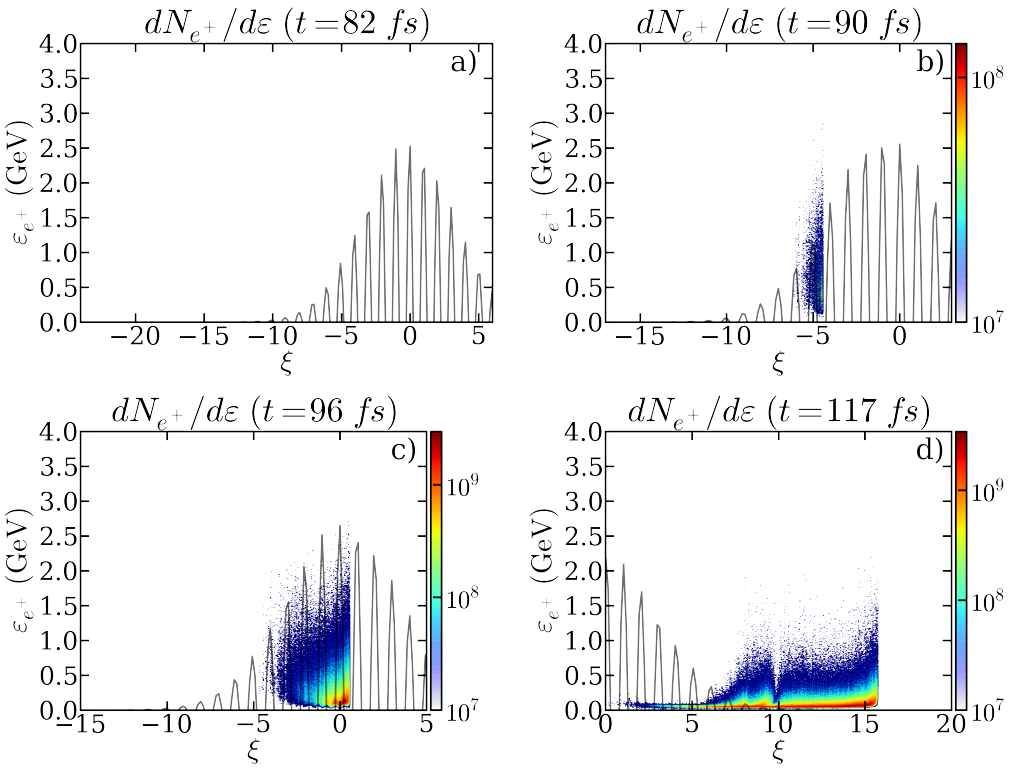

Figure 8.9: Positron energy spectrum before (a), during (b,c) and after the laser-beam collision (d) as a function of the relative distance ξ to the peak x_{peak} in intensity.

The following QED process is the pair decay via the nonlinear Breit-Wheeler of the high-energy photons. The pair generation process during the whole interaction is detailed via Fig. 8.10. The generation of pairs does not directly start at the beginning of the interaction since the photons are not sufficiently energetic and the field not strong enough, as shown in Fig. 8.9a. It begins few periods before the laser peak in intensity since the production of several hundreds of MeV photons, favorable for the pair production, is efficient at this moment. Near the peak in intensity, the photon typical optical depth to reach pair creation is of a few tens of laser periods for GeV photons, as a consequence, the main conversion into pairs really occurs near the laser peak in intensity as shown in Fig. 8.9b and Fig. 8.9c. The photon energy spectrum at creation $dN^0_\gamma/d\gamma$ (green dashed line) and after the interaction $dN^f_\gamma/d\gamma$ (green solid line) shown in Fig. 8.10 demonstrate that the photons of energies above 100 MeV mainly contribute to the pair production. The pair energy at creation ranges between 10 MeV and 3 GeV, with an average energy of 500 MeV as shown

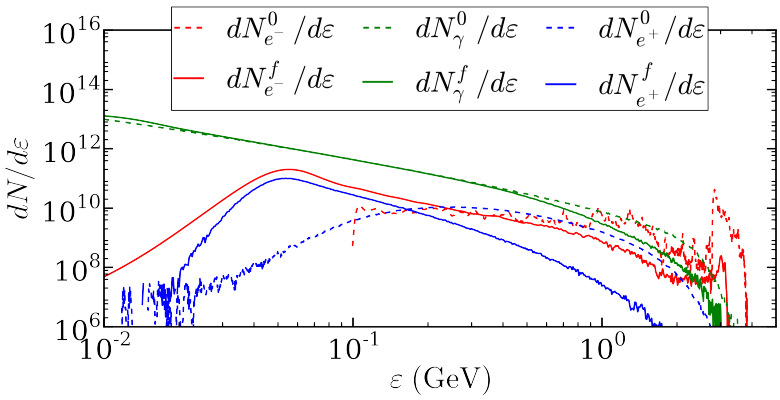

Figure 8.10: Incident electron beam (red), photon (green) and positron (blue) energy spectrum before the interaction (at creation time) $dN^0/d\gamma$ (dashed line) and after the interaction $dN^f/d\gamma$ (solid lines).

in Fig. 8.10 by the positron energy spectrum at creation $dN^0_{e^+}/d\gamma$ (blue solid line). However, while escaping the laser pulse, the positrons also undergo the radiation losses and therefore leave the field with a lower energy than in the middle of the wave as shown in Fig. 8.9d and by the final positron energy spectrum $dN^f_{e^+}/d\gamma$ (blue dashed line in Fig. 8.10). The newly created photons can in turn decay into pairs leading to a short-duration pair cascading effect. It represents 4.5 % of the total pair production. At the end of the interaction, the pairs have lost more than half of their energy to reach 110 MeV on average. The final space-distribution of the created positron beam is shown in Fig. 8.7c. The pairs represent 5.4 % of the initial electron kinetic energy. The total charge is equal to 0.93 nC (i.e. $N_{e^+} \sim 5.8 \times 10^9$ positrons). This represents 43 % of the initial beam charge. The pair production is maximal at the head of the electron beam where the electrons are the most energetic and where the laser is focused as shown in Fig. 8.7c with an average density $n_{e^+} \sim 0.5 n_c$. As predicted by the reduced kinetic approach, the laser intensity is not sufficient to reach the neutrality (production rate of more than a pair per incident electron). Due to the radiation losses, some pairs can be reaccelerated backward in the laser wave. They represent 9×10^7 positrons, namely 1.5 % of the production.

After the laser interaction, the electron beam angular divergence has increased to reach $\theta^f_{e^-,xy} = 0.29$ rad in the polarization plane of the laser $x - y$. The angular divergence of the photons and the pairs also reveals higher than the initial beam divergence although they are created in the same direction of the electrons of origin. In the polarization plane, the divergence of the positrons at creation is equal to $\theta^0_{e^+,xy} \sim 0.014$ rad. This value is lower of an order of magnitude than the photon angular divergence before pair decay in the same plane equal to $\theta^0_{\gamma,xy} = 0.2$ rad. This difference is due to the fact that the photons of highest energy are better collimated than the others and are more likely to decay into a pair. After the laser interaction,

the positron divergence deteriorates to gain an order of magnitude $\theta^f_{e^+,xy} \sim 0.33$ rad. The divergences were calculated only considering the particles and photons moving forward $p_x > 0$. The increase of the particle divergence in the laser polarization plane has three origins. First, electrons and positrons acquire a normalized transverse momentum $p_y/m_{e^-}c \sim a_0$ as a consequence of the wiggling oscillation in the laser field while the longitudinal momentum p_x is reduced due to the radiation losses (as far as $p_x \gg p_y$). Then, as we considered a tightly focused laser beam, the field gradient leads to an important radial ponderomotive force able to significantly increase the radial expansion of the positrons. In the perpendicular plane $x - z$, the electron angular divergence after the laser interaction is equal to $\theta^f_{e^-,xz} = 0.24$ rad almost equal to $\theta^f_{e^-,xy}$. The photon angular divergence at creation time, and the positron angular divergence at creation and after the interaction, are respectively equal to $\theta^0_{\gamma,xz} = 0.017$ rad, $\theta^0_{e^+,xz} = 0.001$ rad and $\theta^f_{e^+,xz} = 0.2$ rad. In the perpendicular plane $x-z$, there is no wiggling effect and the divergence is entirely the consequence of the ponderomotive force due to the laser profile and the radiation losses. The radiation losses indirectly affect the particle deflection, they diminish the particle energy and therefore modify how the particle is radially accelerated. In order to simply quantify the effect of the radiation on the angular divergence, we reproduce the simulation without activating the radiation emission of the pairs (this was also considered to estimate the pair cascading). The radiation only affects the electron beam. In this case, the positrons have a final angular divergence $\theta^f_{e^+,xy} \sim 0.01$ rad and $\theta^f_{e^+,xz} \sim 0.018$ rad. In the polarization plane $x - y$, the angular divergence is lower of an order of magnitude and two orders of magnitude in the perpendicular plane $x - z$. The divergence is more accurately studied in section 8.4.4.

In order to study the influence of the laser focal spot and intensity on the positron yield, energy and angular divergence, we have performed a parametric study with different laser parameters. First, we have varied the focal spot of the laser keeping the same energy, the same temporal profile and the same incident electron beam. We have considered 4 cases with the focal spot sizes $d_l = 2, 3, 4$ and 5 μm. The corresponding intensities are respectively $I = 10^{23},\ 4.4 \times 10^{22},\ 2.5 \times 10^{22}$ and 1.6×10^{22} Wcm^{-2}. Then, we have performed 4 cases of plane waves with different intensities corresponding to $I = 10^{23},\ 5 \times 10^{22},\ 2.5 \times 10^{22}$ and 1.25×10^{22} Wcm^{-2}. In the next sections, the consequence of the studied laser parameters on the γ-photon and positron creation are first considered. This is followed by the variation of the photon and particle energy. We finish the parametric study by the consequences on the particle angular divergences.

8.4.2 Parametric study of the electron, photon and positron charge

The evolution of the total number of created γ-photon (energy above 1.022 MeV) N_γ is shown in Fig. 8.11a for the plane wave and the finite focal spot cases. First, it obviously appears that in the case of a plane wave, the photon yield for a same intensity is higher than in the case of a finite focal spot since in a plane wave no electron has a chance to escape the laser field. In any case, the number of emitted photons during the interaction increases with the laser intensity. In the case of a plane wave, the γ-photon yield is proportional to the laser intensity in the studied range. This means that using a sufficiently large focal spot, the same behavior should be expected. The γ-photon yield calculated with the reduced kinetic approach is shown in green. It can be only compared with the case of a plane wave and appear to be lower for every intensities despite being of the same order of magnitude. Nonetheless, the relative difference between the reduced kinetic approach is constant and approximately equal to 47 %. An hypothesis to explain the difference between the simulation and the reduced kinetic approach is the wiggling effect that causes the particle to spend more time in the wave contrary to a straightly propagating particle as it is the case in the reduced kinetic approach. Moreover, the reduced kinetic approach considers the speed of all the particles equal to the speed of light even if the γ factor approaches 1.

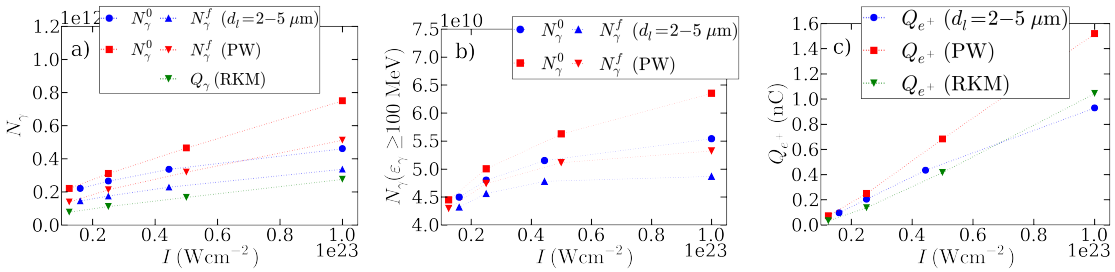

Figure 8.11: a) - Evolution of the γ-photon yield N_γ as a function of the laser intensity I in the case of a plane wave (PW, red), a finite focal spot (blue) and using the reduced kinetic approach (RKM, green) at creation time N_γ^0 and at the end of the laser interaction N_γ^f. b) - Evolution of the number of photons of energy above 100 MeV as a function of the laser intensity in the case of a plane wave (red) and a finite focal spot (blue). c) - Evolution of the positron yield as a function of the laser intensity I in the case of a plane wave (red), a finite focal spot (blue) and using the reduced kinetic approach (green).

In the previous section, we reported that the pairs are mainly created from the photons of energy above 100 MeV at 10^{23} Wcm^{-2} (photons of lower energy have a chance to decay into pairs but the probability is extremely reduced). The photon yield evolution above this threshold is presented in Fig. 8.11b. Above 100 MeV, the

photon yield carries on rising with the laser intensity but not linearly anymore for the plane wave case. It seems that the high-energy γ-photon production tends to stabilize and reaches a maximum for intensity above 10^{23} Wcm^{-2}. Furthermore, in the range of studied intensities, the production yield weakly varies and stays in the same order of magnitude between 4×10^{10} and 7×10^{10} photons above 100 MeV. This can be seen on the γ-photon spectra, displayed in Fig. 8.12a, which are slightly the same in our range of parameters at creation time for high-energy photons. Close to 10^{23} Wcm^{-2}, the emission occurs in the foot of the laser pulse. As the electrons have already lost most of their energy before reaching the intensity peak, only photons of energy lower than 10 MeV are generated near this region of the laser. For lower intensities, electrons will take longer time to radiate their energies and the γ-photon emission will eventually last until the laser tail as for $I \sim 1.25\times10^{22}$ Wcm^{-2}.

The total positron charges Q_{e^+} as a function of the laser intensity both for the plane wave and the finite focal spot cases are shown in Fig. 8.11c. As expected, the positron charge increases with the laser intensity. For the case of a plane wave, the positron yield is almost linearly proportional to the laser intensity with dependency $Q_{e^+} \propto 0.17 I_{22}$ where I_{22} is the intensity in 10^{22} Wcm^{-2} in the studied range of intensities. In the case of a finite focal spot, the positron yield is lower because some photons escape the region of strong field transversely due to their divergence. As the focal spot increases, the positron charge approaches the plane wave result. The result from the reduced kinetic approach is plotted in green. As for the photons, the positron charge is lower than the simulated results. The predicted values are nonetheless of the same order of magnitude with a relative difference of 30 % at 10^{22} Wcm^{-2} to 54 % at 10^{23} Wcm^{-2}. The photon spectra after the laser interaction is shown in Fig. 8.12b for the finite focal spot cases. It confirms the tendency of Fig. 8.11b. For intensities close to 10^{22} Wcm^{-2}, the photon spectrum above 100 MeV at the end of the interaction is weakly changed and very close to the spectrum at creation since a small fraction has lead to the creation of pairs. We can see that photons of energy close to the maximum energy $\sim$ 3.5 GeV at creation still exist. When the laser intensity increases, the photon energy threshold to efficient pair conversion decreases: more photons of lower energies can decay into pairs and the most energetic photons have a higher probability to convert.

8.4.3 Parametric study of the electron, photon and positron energy

The evolution of the electron, photon and positron energy depending on the laser intensity and the focal spot is now analyzed. We first consider the impact of the radiation losses on the initial electron beam energy. The evolution of the average electron energy $\langle \varepsilon^f_{e^-} \rangle$ at the end of the laser interaction is shown in Fig. 8.13a both for the case of a plane wave (red) and a finite focal spot (blue). It shows that as the laser field is strong, the electrons are more decelerated by the radiation friction. In

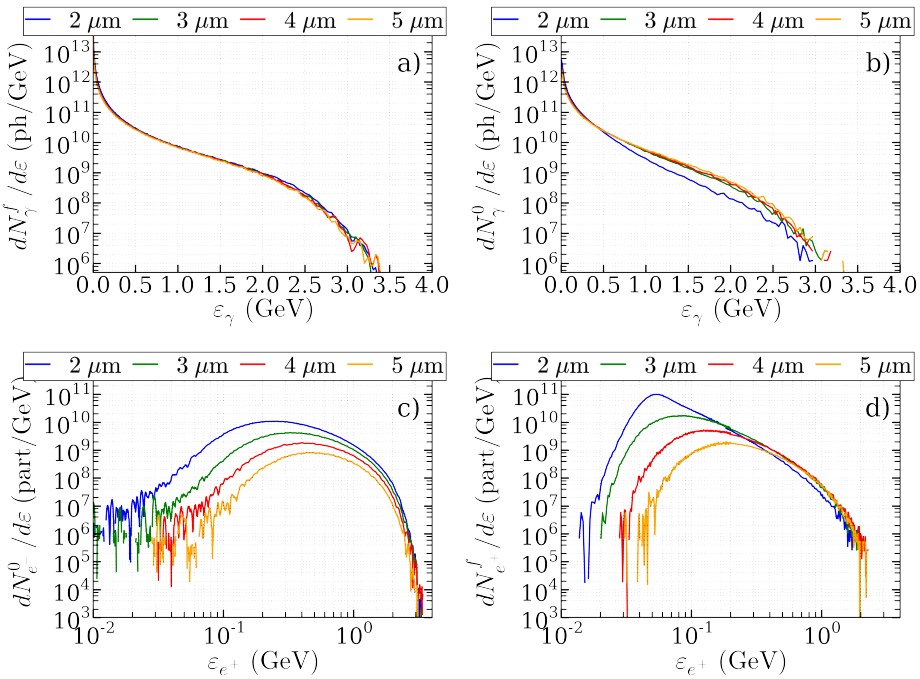

Figure 8.12: a) - Photon energy distribution at creation integrated over the whole simulation time for the cases of a finite focal spot. b) - Photon energy distribution at the end of the laser interaction for the cases of a finite focal spot. c) - Positron energy distribution at creation integrated over the whole simulation time for the cases of a finite focal spot. d) - Positron energy distribution at the end of the laser interaction for the cases of a finite focal spot.

the case of a plane wave, the average energy has dropped from 1.8 GeV to 40 MeV at 10^{23} Wcm^{-2} and to 300 MeV at 1.25×10^{22} Wcm^{-2}. The average energy is higher in the case of a finite focal spot due to two reasons. First, the electron traveling at the side of the laser and not decelerated are taken into account for the calculation of the average energy. Then, some electrons can escape transversely the strong field region and are therefore less decelerated than in a plane wave. The fact that the electrons lose more energy for high intensities means that the number of emitted photons is increased. As shown by Fig. 8.11a, Fig. 8.11b and the photon spectrum in Fig. 8.12a, the increase of the photon yield mainly contributes to energy levels under the MeV. As we noticed in the previous section, the GeV electrons when they radiate in the quantum regime lose a significant fraction of their energy extremely fast before the peak in intensity but continue to radiate after in the semi-quantum or classical regime with the emission of weak γ and hard X-photons. This phenomenon is as strong as the laser intensity is high and as a consequence the average photon energy decreases with the laser intensity as shown in Fig. 8.13b. In other words, the stronger the laser intensity, the more significant the production of sub-MeV photons but the

production of strong γ-photons due to the rapid transition to the semi-quantum regime is almost unchanged. This effect can be directly visualized on the positron energy distributions at creation displayed in Fig. 8.12c. The difference between the distributions is more important for the low-energy part under 100 MeV than for the GeV part.

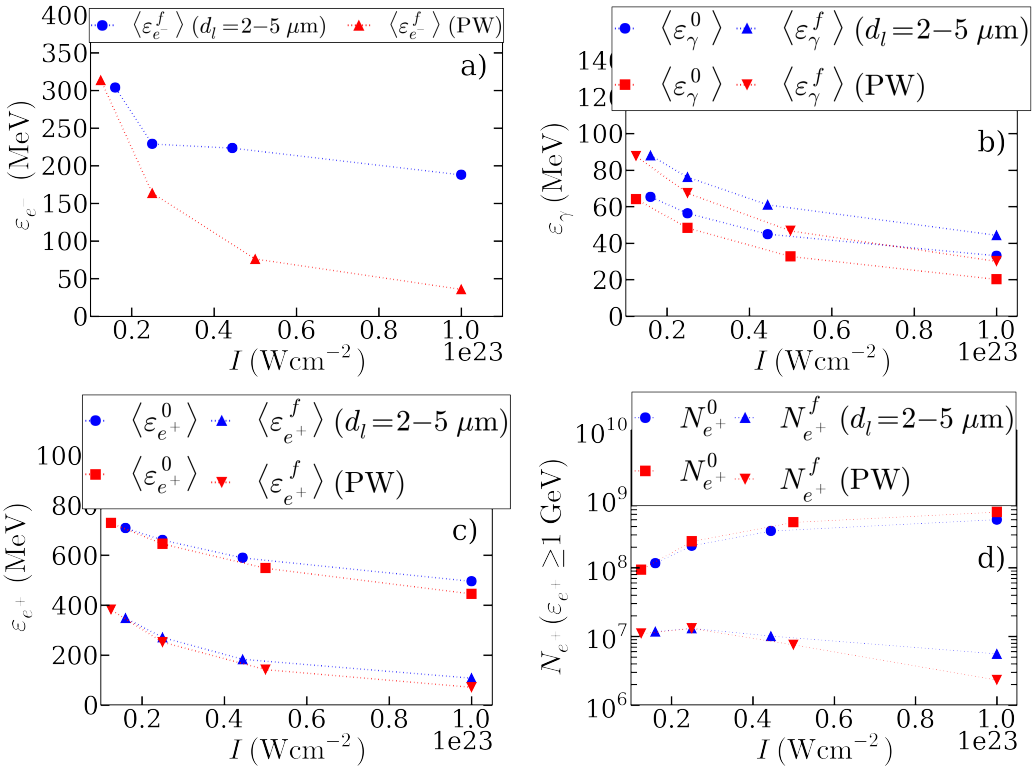

Figure 8.13: Evolution of the beam electron average energy (a), the γ-photon average energy (b) and the positron average energy $\langle \varepsilon_{e^+} \rangle$ (c) as a function of the laser intensity I in the case of a plane wave (red markers) and a finite focal spot (blue markers) at creation time (circle and square markers) and after the interaction (triangle up and down markers) for the photons and the positrons. c) - Evolution of the number of positrons of energy above 1 GeV as a function of the laser intensity I in the case of a plane wave (red markers) and a finite focal spot (blue markers) at creation time (circle and square markers) and after the laser interaction (up and down triangle markers).

The positrons just after their creation of an average energy between 600 and 800 MeV as shown in Fig. 8.13c (red square markers for a plane wave and blue circle markers for a finite focal spot). At creation, the positron energy decreases as the laser intensifies. First, this is due to the production rate of γ-photons slightly increased for higher-intensities. But the main reason is the fact that a higher intensify diminishes the energy threshold at which the photons efficiently decay into pairs. As

a consequence, the decay of more relatively low energy photons increases the positron charge but on the other hand diminishes the average energy of the created positrons by energy conservation. In the case of a plane wave, the average energy of the pairs decreases with the laser intensity according to the law $\langle \varepsilon^0_{e^+} \rangle [\text{MeV}] \sim 780 I_{22}^{-0.24}$ at creation time, where $I_{22} = 10^{22}$ Wcm^{-2}. Then, the positrons are decelerated in the laser due to the radiation friction and at the end of the interaction, their energy has significantly decreased. The energy loss is as high as the laser field is strong. At 1.25×10^{22} Wcm^{-2}, they represent 50 % of the initial energy and 70 % at 10^{23} Wcm^{-2} for the case of a finite focal spot. Therefore, the average energy scales as $\langle \varepsilon_{e^+} \rangle [\text{MeV}] \sim 490 I_{22}^{-0.81}$ after the laser interaction. Comparing the positron energy distribution at creation and after the laser interaction (Fig. 8.12b), it can be observed that the photon energy of the maxima of the distributions have been decreased of an order of magnitude in average and that this exactly depends on how strong is the laser. The number of positrons between 10 and 100 MeV have been increased at the cost of the positron above 100 MeV. Furthermore, the curve arrangement have been reversed: after the radiation losses, there are less GeV positrons at 10^{23} Wcm^{-2} than for 10^{22} Wcm^{-2}. In order to confirm this result, the evolution of the number of positrons of energy above 100 MeV is drawn in Fig. 8.13d. It appears that an optimum intensity exists to optimize the positron yield to energy ratio. In order to get the positron beam with the maximum number of positrons above the energy of 100 MeV, the intensity of 2.5×10^{22} Wcm^{-2} ($d_l = 4$ μm for a finite focal spot) gives the best results.

8.4.4 Parametric study of the electron, photon and positron angular divergence

In this section, the dependence on the angular divergence to the laser intensity and focal spot diameter is analyzed. In the laser polarization plane $x - y$, the angular deviation is the consequence of the wiggling and the radial ponderomotive force induced by the laser gradient. These two mechanisms are emphasized by the radiation losses. The electrons from the beam are the first affected particles. The divergence $\theta^f_{e^-,xy}$ after the interaction as a function of the laser intensity is plotted in Fig. 8.14a. Both for the case of a plane wave and a finite focal spot, the stronger is the laser intensity, the more significant is the electron angular divergence. At the end of the interaction, the divergence is increased by an order of magnitude at 10^{22} Wcm^{-2} and up to two orders of magnitude for 10^{23} Wcm^{-2}. The difference between the plane wave and the finite focal spot is small, less than a factor 2.

The consequence is an increase of the photon angular divergence $\theta^0_{\gamma,xy}$ at the creation with the laser intensity as shown in Fig. 8.14c and the divergence is of the same order of magnitude as for the electrons.

The positron divergence $\theta^0_{e^+,xy}$ at creation follows the same behavior but is an order of magnitude lower than the photon divergence. This is due to the fact that the

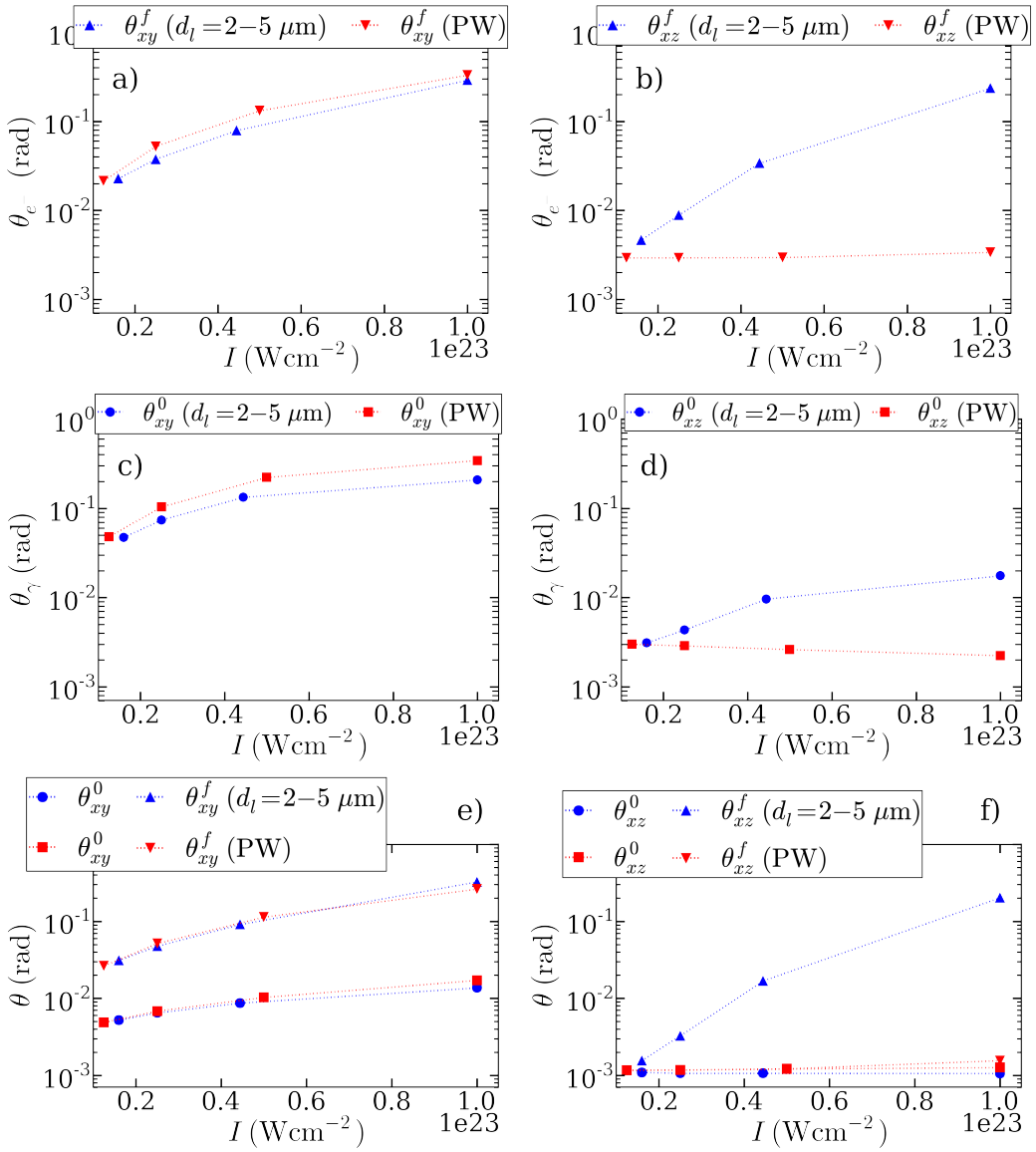

Figure 8.14: Electron angular divergence as a function of the laser intensity I for a plane wave (red curve) and a finite focal spot (blue curve) after the laser interaction in the polarization plane $x-y$ (a) and the perpendicular plane (b). Photon angular divergence as a function of the laser intensity I for a plane wave (red curve) and a finite focal spot (blue curve) at creation time in the polarization plane $x-y$ (c) and the perpendicular plane $x-z$ (d). Positron angular divergence as a function of the laser intensity I for a plane wave (red curve) and a finite focal spot (blue curve) at creation time (circle and square markers) and after the laser interaction (up and down markers) in the polarization plane $x-y$ (e) and the perpendicular plane $x-z$ (f). Only the particles propagating forward, $p_x > 0$, are taken into account.

most energetic photons that mainly contribute to the pair production are in average better collimated. During the laser interaction, the positrons undergo the wiggling, the ponderomotive force and the radiation loss and therefore gain transverse momentum so that the angular divergence is globally increased in average of an order of magnitude after the laser interaction. The divergence is nonetheless more important for strong intensities: the divergence has been multiplied by 6 near 10^{22} Wcm^{-2} and by 24 at 10^{23} Wcm^{-2} in the case of a finite focal spot wave. It appears that the positron divergence in the case of a finite focal spot wave is really close to the case of a plane wave in the studied range of intensities.

In the plane perpendicular to the laser polarization $x-z$, the wiggling disappears and only remain the ponderomotive force (in the case of a tiny focal spot) and the radiations losses. The electron beam angular divergence in this plane $\theta^f_{e^-,xz}$ after the laser interaction is shown in Fig. 8.14b. In the case of a plane wave, the beam divergence has not changed. For a finite focal spot, the divergence is as strong as the focal spot is small and the intensity high. This confirms that the transverse ponderomotive force is the main cause of the particle deviation. Close to 10^{22} Wcm^{-2}, for a focal spot diameter close to $d_l = 5$ μm, the electron divergence has weakly increased during the laser interaction. However, at 10^{23} Wcm^{-2}, for a focal spot diameter of $d_l = 2$ μm, the radial field gradients are steepened and the radiation losses stronger (due to the intensification of the field) resulting in the significant rise of the electron angular divergence. In the latter case, the divergence in both planes are almost similar.

The γ-photon angular divergence in the perpendicular plane $\theta^0_{\gamma,xz}$ is unchanged as for the electrons in the case of a plane wave as shown in Fig. 8.14d. Since the particles are not deflected, the emission is made in the same direction with an extremely low divergence. Furthermore, the fact that the most energetic electrons are in average better collimated leads to the soft decreasing of the divergence with the laser intensity. For a finite focal spot, the divergence is still growing with the laser intensity as the focal spot diameter reduces but the divergence remains lower in any case by an order of magnitude than in the polarization plane (Fig. 8.14c). For intensities close to 10^{22} Wcm^{-2} and diameter $d_l = 5$ μm, the divergence appears similar both for a plane wave and a finite focal spot.

Finally, the positron angular divergence in the perpendicular plane at creation $\theta^0_{e^+,xz}$ and after the laser interaction $\theta^f_{e^+,xz}$ are displayed in Fig. 8.14f. For the case of a plane wave, the divergence at creation and after the laser interaction are very similar and close to 0.001 rad, lower than the initial electron beam divergence close to 0.003 rad. This is also the case for a finite focal spot wave at creation. But after the laser interaction, the positron divergence rises. For an intensity close to 10^{23} Wcm^{-2}, the divergence have been multiplied by 200 due to the strong radial deflecting force in combination with the radiation friction. For intensities close to 10^{22} Wcm^{-2}, the divergence increase is moderate of the same order of magnitude.

In order to understand how the particles are deflected in a finite focal spot wave,

test particle calculations are performed in an analytical field. As we showed, in a linearly polarized wave, the particle angular divergence that increases during the interaction, is classically the consequence of two mechanisms: the wiggling and the ponderomotive acceleration due to the transverse gradients. For the analytical field, we consider a Gaussian potential polarized in the y direction, propagating backward in respect to the electrons so that $\mathbf{kx} < 0$ where $\mathbf{k}$ is the wave vector, of potential vector

$$\mathbf{A} = \begin{cases} 0 \\ A_0 \exp\left(\alpha \left(\xi - \xi_0\right)^2\right) \cos\left(\xi\right) \times g\left(y, z\right) \\ 0 \end{cases} \tag{8.4}$$

where $\alpha = -4 \log 2/(\omega T_l^2)$ and T_l the wave duration at half maximum, $\xi = \mathbf{kx} - \omega t = \omega t + kx$ since the wave is propagating backward. The function $g\left(y, z\right)$ is the transverse shape of the wave.

The electric field is therefore equal to

$$\mathbf{E} = -\frac{\partial \mathbf{A}}{\partial t} = \begin{cases} 0 \\ A_0 \omega \left(-2\alpha \left(\xi - \xi_0\right) \cos\left(\xi\right) + \sin\left(\xi\right)\right) \exp\left(\alpha \left(\xi - \xi_0\right)^2\right) g\left(y, z\right) \\ 0 \end{cases} \tag{8.5}$$

For a long enough period $T_l > 10\omega/2\sqrt{\log 2}$, we have $\alpha \ll 1$ and the electric field approaches a Gaussian profile dephased of π with the potential. The laser focal spot profile is chosen to be Gaussian depending on the radius $r = \sqrt{y^2 + z^2}$ so that $g(x, y) = \exp\left(\beta r^2\right)$ where $\beta = -4 \log\left(2\right)/d_l^2$, d_l being the focal spot diameter. The magnetic field corresponds to

$$\mathbf{B} = \nabla \times \mathbf{A} = \begin{cases} -\partial_z A \\ 0 \\ \partial_x A \end{cases} = \begin{cases} -2A_0 \exp\left(\alpha \left(\xi - \xi_0\right)^2\right) \cos\left(\xi\right) \beta z g\left(y, z\right) \\ 0 \\ A_0 k \left(2\alpha \left(\xi - \xi_0\right) \cos\left(\xi\right) - \sin\left(\xi\right)\right) \exp\left(\alpha \left(\xi - \xi_0\right)^2\right) g\left(y, z\right) \end{cases} \tag{8.6}$$

It is interesting to remark that in the potential approximation we made for a linear wave in the y direction, the magnetic field gets a component only in the $\mathbf{x}$ direction if the wave potential has a gradient in the z direction. In the opposite case, the magnetic field becomes similar to the case of a plane wave. The Lorentz force components induced by the magnetic field depend on the particle velocity $\mathbf{v}$ (of charge q) as

$$q\mathbf{v} \times \mathbf{B} = q \begin{cases} v_y \partial x A \\ -v_z \partial_z A + v_x \partial_x A \\ v_y \partial_z A \end{cases} \tag{8.7}$$

The magnetic force in the case of a finite focal spot has a component in the $\mathbf{z}$ direction which means that the electron trajectory is not confined anymore to the polarization

plane. The y-component of the force has also gained a new term showing that a slow drift is also expected in this direction. Nonetheless, any particle initially located at the position $y = z = 0$ for a Gaussian focal spot will not undergo any deflection since $\partial_z A = 0$. The acceleration in the **z** direction depends on the strength of the wiggling $v_y \sim A_0/\gamma mc$ and should be therefore enhanced with the laser intensity. Without radiation losses, the gradients are maximum at radius $r = d_l/\left(2\sqrt{2\log 2}\right)$. In this region (taking $r \sim d_l/2$), the maximal drift force could reach $2\log(2)qA_0^2/(d_l\gamma mc)$. Thus, the deflection is maximized for low energy particles, high laser intensity and tiny focal spot depending on the initial particle position entering the laser field.

In order to understand the effect of the gradient on the particle trajectories, we integrate the motion equation with or without radiation friction for a particle interacting with the previously described laser field using a leap-frog pusher.

$$\frac{d\mathbf{p}}{dt} = \mathbf{E} + \frac{\mathbf{p}}{\gamma} \times \mathbf{B} + \mathbf{F_{rad}} \tag{8.8}$$

$$\tag{8.9}$$

The radiation friction force $\mathbf{F_{rad}}$, directed in the same direction of $\mathbf{p}$ only acts as a cooling mechanism and does not contribute directly to the deflection. Nonetheless, by diminishing the particle energy $\gamma m_e c^2$, giving rise to the increase of v_y or v_z over v_x, it will increase the effect of the deflection induced by the electric and the magnetic fields.

We first start to study some particle trajectories for different particle initial energies and positions in respect to the wave. For the laser parameters, we consider a Gaussian profile of duration 15 fs ($9\pi\omega_0^{-1}$), with a focal spot diameter $d_l = 2$ μm for an intensity of $\sim 10^{23}$ Wcm^{-2} ($a_0 = 270$ at $\lambda = 1$ μm). The particles are initially located at a disatnce of 12.5 μm from the laser peak in intensity. The first group of electrons is shifted at position $y = 1$ μm and z=0 for three initial energies 100, 500 and 1000 MeV. The corresponding trajectories are shown in Fig. 8.15 with and without radiation losses. Here again, $\xi = (x - x_{\rm peak})/\lambda$ refers to the distance between the laser peak intensity and the electrons. With a shift in the y direction, there is no deflection in the plane $x - z$ ($z = 0$).

It appears that the deflection in the plane $x - y$ is as strong as the particle energy is low comparing the trajectories of the three studied particles (Fig. 8.15a). The continuous radiation losses significantly increase the deflection (dashed curve), particularly for the high energy particles (above the GeV level) that undergo a strong radiative deceleration during the field interaction. As already mentioned, Fig. 8.15b shows that the longitudinal momentum p_x is significantly reduced by the radiation losses and this reduction is as strong as the particle energy is initially high. In comparison, the transverse momentum p_y reveals to be weakly affected by the radiation losses since the trajectories are really close to the non-radiative cases as shown by Fig. 8.15c. For the most energetic particles $p_x \gg p_y$, the amplitude of the momentum oscillations are close to the laser amplitude at $y = 1$ μm, that is to say

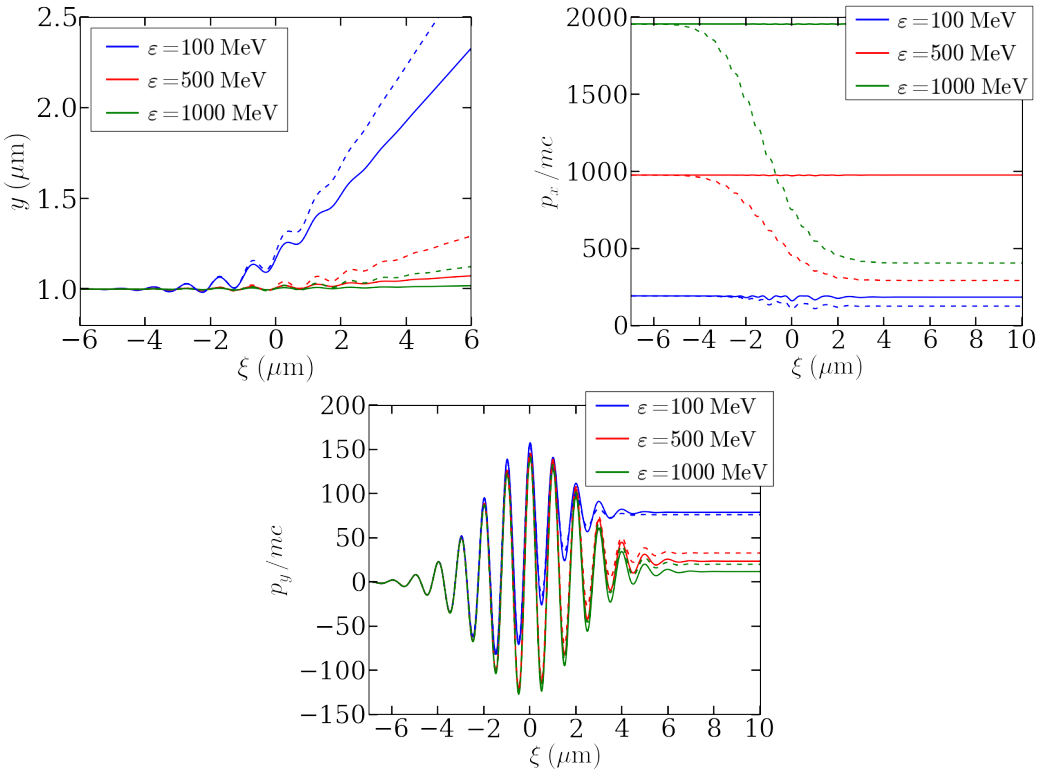

Figure 8.15: Trajectories in the polarization plane $x-y$ (a), evolution of the longitudinal momentum p_x and the transverse momentum p_y of three test electrons of initial energy 100 (blue curves), 500 (red) and 1000 MeV (green) at initial shifted position $y = 1$ μm with (solid line) and without radiation losses (dashed line).

$p_y/mc \sim a_0 \exp(\beta) \sim 135$ and the transverse momentum after the interaction is almost similar to the initial value. Fig. 8.15c also demonstrates that the ponderomotive deviation induced by the gradients is stronger for lower particle energies, with or without radiation losses. Since the radiation importantly diminishes p_x, the divergence $\sim p_y/p_x$ is increased even if p_y is not significantly modified.

For electrons initially shifted in the z direction, the trajectories are shown in Fig. 8.16. The wiggling, in the plane $x-y$, is plotted in Fig. 8.16a. The radiation losses increase the amplitude of the wiggling oscillations. As for the plane $x-y$, the radiation mainly reduces the longitudinal momentum p_x contrary to the transverse momentum p_y which is not modified by the radiations as shown in Fig. 8.16c. The γ is therefore reduced in favor of the transverse velocity $v_y = p_y/\gamma mc$, increasing the wiggling amplitude. At the end of the laser interaction, the deflection is very small in the polarization plane because the p_y momentum has gone back to 0 since the particles were initially at y=0. On the other hand, in the perpendicular plane $x-z$, the deflection is much stronger as shown in Fig. 8.16c. The deflection is as strong as the initial particle energy is high and it is enhanced by the radiation

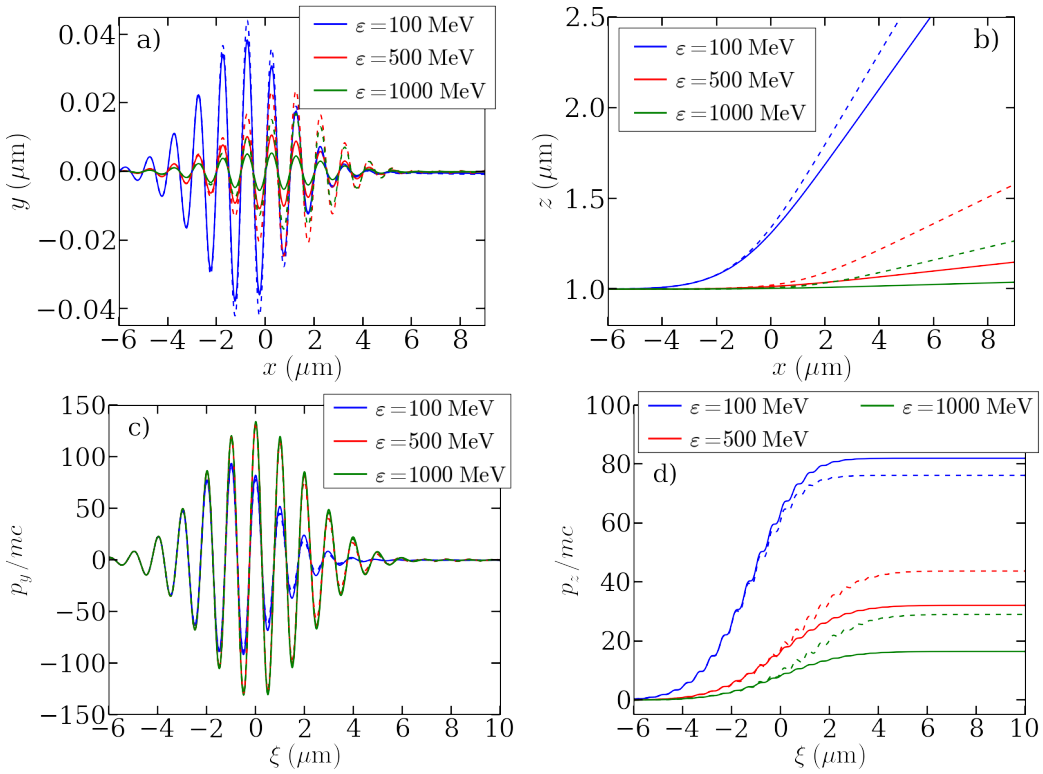

Figure 8.16: Trajectory of three electrons of initial energy 100, 500 and 1000 MeV at initial position $z = 1$ μm with (solid line) and without radiations (dashed line) in the polarization plane $x - y$ (a) and in the orthogonal one $x - z$ (b).

losses. In Fig. 8.16d displaying the p_z momentum, the transverse acceleration due to the gradient ponderomotive force is evidenced. For electrons with sufficient initial energy, the radiation losses increased the value of the final p_z momentum. This is not the case for the electron initially at 100 MeV, having a momentum close to the laser normalized amplitude $a_0 \sim 270$ where the radiation losses slightly decrease the final p_z value. Nonetheless, the reducing of the p_x momentum compensates this effect and the final divergence is still higher with radiation.

The similar process is applied on a high number of particles in order to parametrically analyze the dependence of the divergence on the particle initial energies and positions. We variate the energy between 100 MeV and 5 GeV, and we consider both a shift in the y and the z direction between 0 and 2 μm. Note that we are using a tiny focused laser ($d_l = 2$ μm) and that in this worst case the divergence is extremely high. The results are shown in Fig. 8.17 for a shift in y and in 8.18 for a shift in z with and without the radiation losses. The expected trends can be observed. The particles initially located at $y = z = 0$ are not deflected by the laser gradients. As the position is shifted in both y and z, the deflection becomes significant with a maximum under $r \sim d_l$ for the considered laser parameters. Then, the deflection

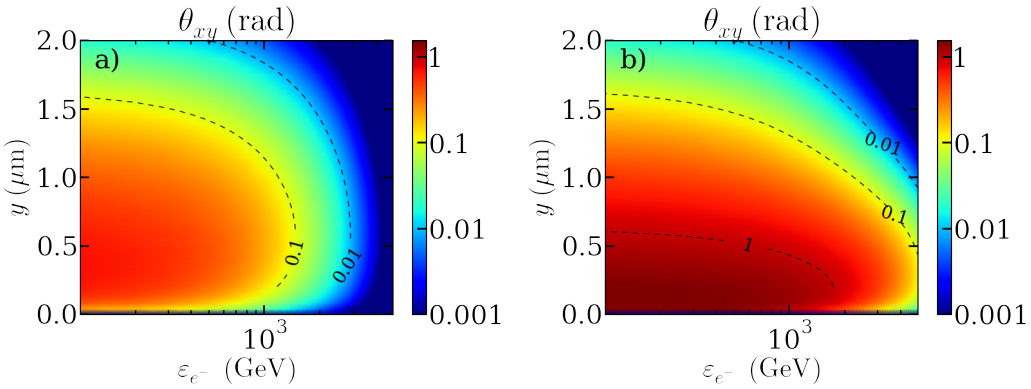

Figure 8.17: Final divergence θ_{yx} function of the initial electron energy ε_{e^-} and the initial y shifted position without (a) and with radiation losses (b).

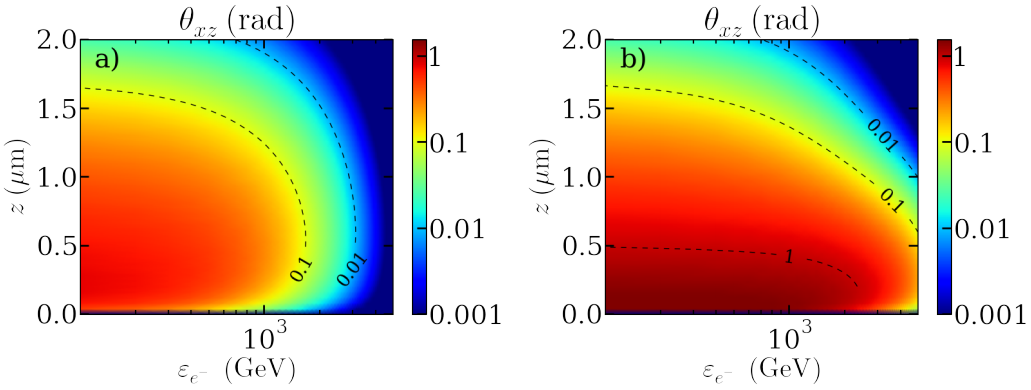

Figure 8.18: Final divergence θ_{zx} function of the initial electron energy ε_{e^-} and the initial z shifted position.

depends on the initial electron energy and here, mainly impacts the electrons under the GeV level. The radiation losses further increase this phenomenon in the region of strong field $r < d_l$.

The previous study of the continuous trajectories does not consider the discontinuous effects of the quantum emission. The quantum effects on the electron divergence and the comparison with continuous radiation cooling has been studied in Wang *et al.* (2015); Yoffe *et al.* (2015). In a plane wave, the transverse momentum p_y is conserved with the continuous radiation friction at the end of the laser interaction if the particle initially has $p_y = 0$. With $p_y \ll p_x$, the transverse momentum is weakly affected in the case of a short pulse. At the end of the laser interaction, a classical electron can not gain transverse momentum. In order to highlight the QED effects on the particle scattering, two simulations with continuous radiation cooling (with quantum correction) and discontinuous emissions are compared in the case of a plane wave at 10^{23} Wcm^{-2}. The final structure of the electron beam, after the laser interaction, is

shown in Fig. 8.19a for the Sokolov radiation friction approach and in Fig. 8.19b for the discontinuous approach. With the continuous model, the electron beam conserves the same spatial shape after interacting with the laser pulse. However, with the quantum emission, the electron beam is significantly diffused. During the laser interaction, the angular divergence in the plane $x - y$ is important due to the electron wiggling in both cases. Fig. 8.19c and 8.19d display the momentum phase space $p_x - p_y$ at the time of maximal angular divergence for the continuous approach respectively for the continuous and the discontinuous approach. The wiggling leads to the typical half-circle structure due to the electron transverse oscillations in the laser field well illustrated by Fig. 8.19c. In 8.19d, the similar structure can be observed in addition to the quantum effects that lead the particle to gain transverse momentum. After the laser interaction, the particle phase space in the continuous approach shown in Fig. 8.19e is flattened in transverse momentum p_y and significantly reduced in p_x for which the radiation losses have the most significant effect. The friction force only acts as a cooling mechanism. In the quantum discontinuous emission, the particles gain transverse momentum along the interaction as shown in Fig. 8.19f. The phase space $p_x - p_y$ is significantly reduced in longitudinal momentum p_x due the strong emission. The p_x distribution is broader than the continuous approach with higher maximal values (up to $p_x/mc \sim 500$) and some particles reaccelerated backward. Then, the particles have gained transverse momentum p_y. The final p_y distribution is broaden with higher values than the initial state. To conclude, the energy spread is enhanced with quantum-electrodynamics effects. According to Wang *et al.* (2015), they have estimated that the transverse momentum is increased of factor 0.3 with the same range of parameters as ours. This is verified in our simulations. This has been suggested as a signature to detect the transition to the quantum emission regime in laser experiments.

8.4.5 Study of the influence of the laser duration using the reduced kinetic approach

This section concerns the influence of the laser duration on the photon yield and pair decay. For this study, we only consider the reduced kinetic model. Four different laser durations are computed, equal to $T_l = 15$, 30, 60 and 90 fs. The laser is necessarly a plane wave in this description and the energy is kept constant in every cases so that the laser intensity is modified. In addition to a Gaussian profile, the cases have been run with an hyper-Gaussian of order 4. The evolution of the photon yield and the positron charge as a function of the laser intensity (i.e. laser duration) are respectively plotted in Fig. 8.20. It reveals that the production of γ-photons (again, photons of energy above 1.022 MeV), increases as the pulse duration is long. As long as the emission is in the quantum regime (or eventually the beginning of the semi-quantum regime), the emission of γ-photons is possible. When the laser intensity decreases, the χ parameter decreases as well and the emission of photons of energy

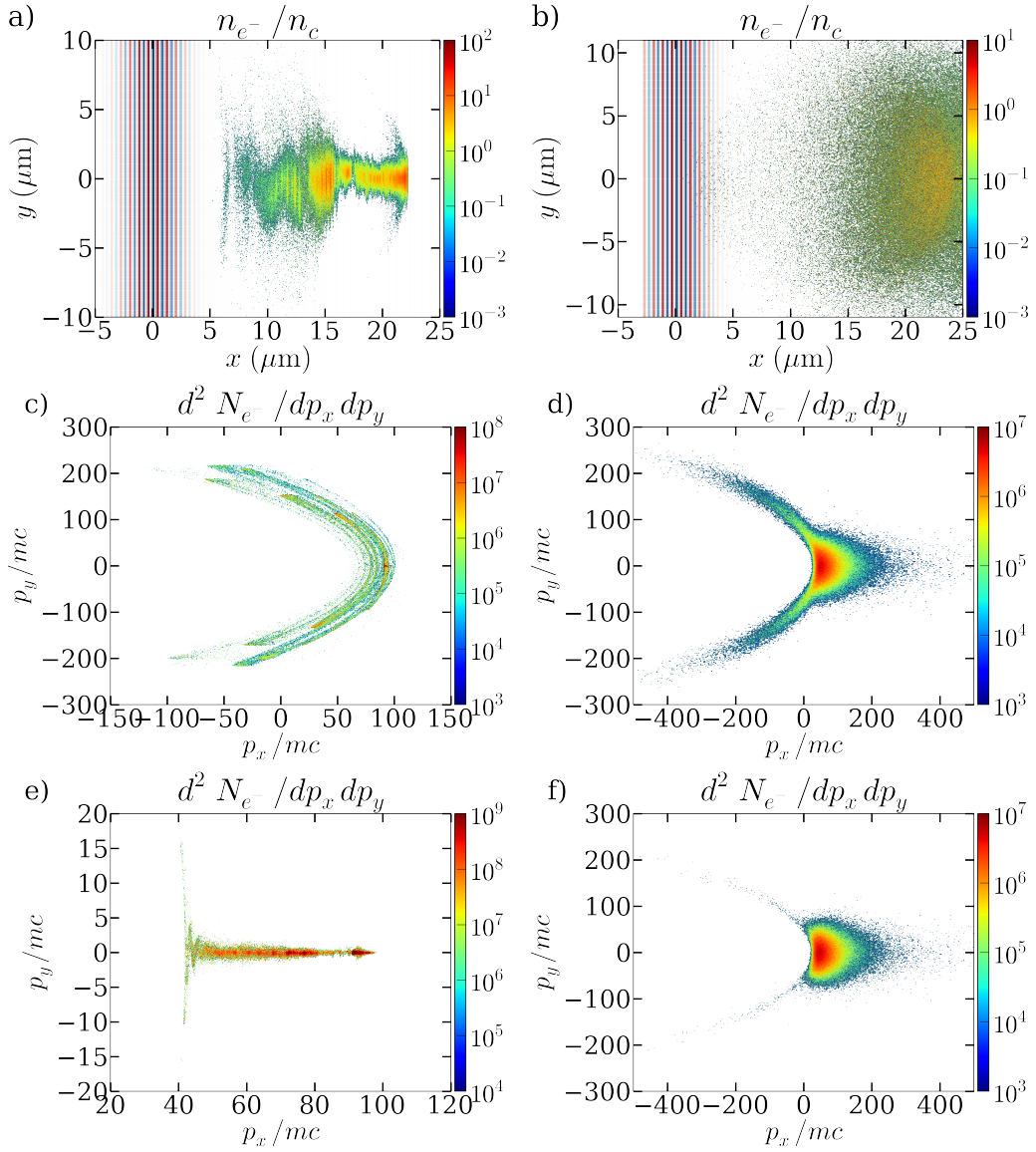

Figure 8.19: Electron density projection n_{e^-} from the initial beam on the plane $x-y$ after the laser interaction ($t = 147$ fs) with the Sokolov radiation friction model (a) and the quantum discontinuous description (b). Electron momentum phase space $p_x - p_y$ at time of the maximum average angular divergence θ_{xy} ($t = 126$ fs) with the Sokolov radiation friction model (c) and the quantum discontinuous description (d). Electron momentum phase space $p_x - p_y$ after the laser interaction with the Sokolov radiation friction model (e) and the quantum discontinuous description (f). Note that the x-axis and the colormap scales are changed in each figure.

close to the electron energy (above the GeV level) is reduced. This is in favor of the emission of lower energy photons of few MeV to few hundreds of MeV. Obviously,

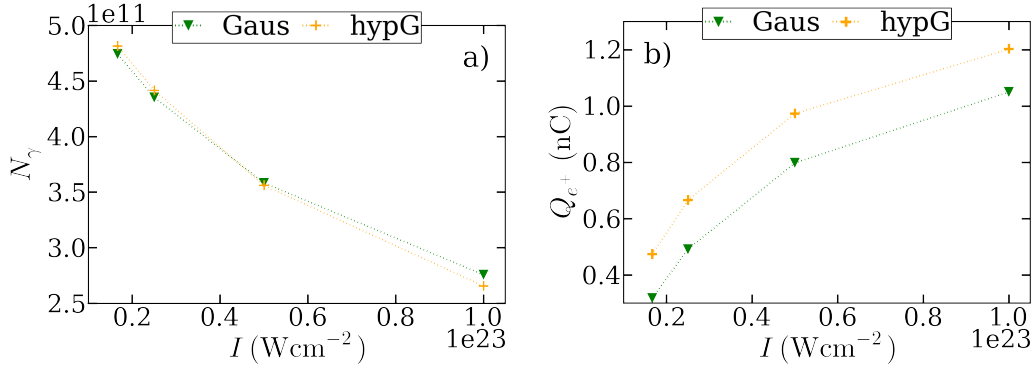

Figure 8.20: Number of γ-photons N_γ and positron charge Q_{e^+} calculated with the reduced kinetic approach as a function of the laser intensity for 4 different laser durations T_l = 15, 30, 60 and 90 fs. The laser energy is unchanged in every cases.

this has a limit when the emission enters the semi-classical regime $\chi \leq 0.1$. In this case, the photon will be emitted under the MeV level. Contrary to the photons, the total positron charge at the end of the interaction increases with the laser intensity. Back to section 4.3 about the multi-photon Breit-Wheeler process, the distance to pair decay for a photon of given energy nonlineary depends on the field amplitude. In a constant magnetic field of normalized amplitude $a_0 = eB/m\omega = 270$, equivalent to a laser intensity of 10^{23} Wcm^{-2}, a photon at 1 GeV will cross 4 μm in average before it decays into a pair, at $a_0 = 190$ ($I = 5 \times 10^{22}$ Wcm^{-2}), this distance drops to 13 μm, for $a_0 = 135$ ($I = 2.5 \times 10^{22}$ Wcm^{-2}), it further decreases to 58 μm to go up to 180 μm for $a_0 = 110$ ($I = 1.25 \times 10^{22}$ Wcm^{-2}). Clearly, it appears that for a given laser energy a short-pulse is a better choice to optimize the charge production of pairs in such a configuration.

8.4.6 Case of the oblique incidence

An oblique incidence angle is generally used in laser experimental setups to prevent the damage that could be caused by the backward reflected light. We use again the reduced kinetic model to approach parametrically the photon and positron yield for various electron beam incidence. The geometry is described in Fig. 8.21a. In spherical coordinates, φ is the polar angle and θ the azimuthal angle respectively given by

$$\varphi = \arctan -\frac{p_z}{p_x} \qquad \theta = \arctan \frac{p_y}{\sqrt{p_x^2 + p_z^2}}. \tag{8.10}$$

Physically, θ is the rotation in the orthogonal plane from the laser polarization direction so that the propagation direction of the beam and the laser polarization stay perpendicular when this angle is varied. A direct collision corresponds to $\theta = \pi$

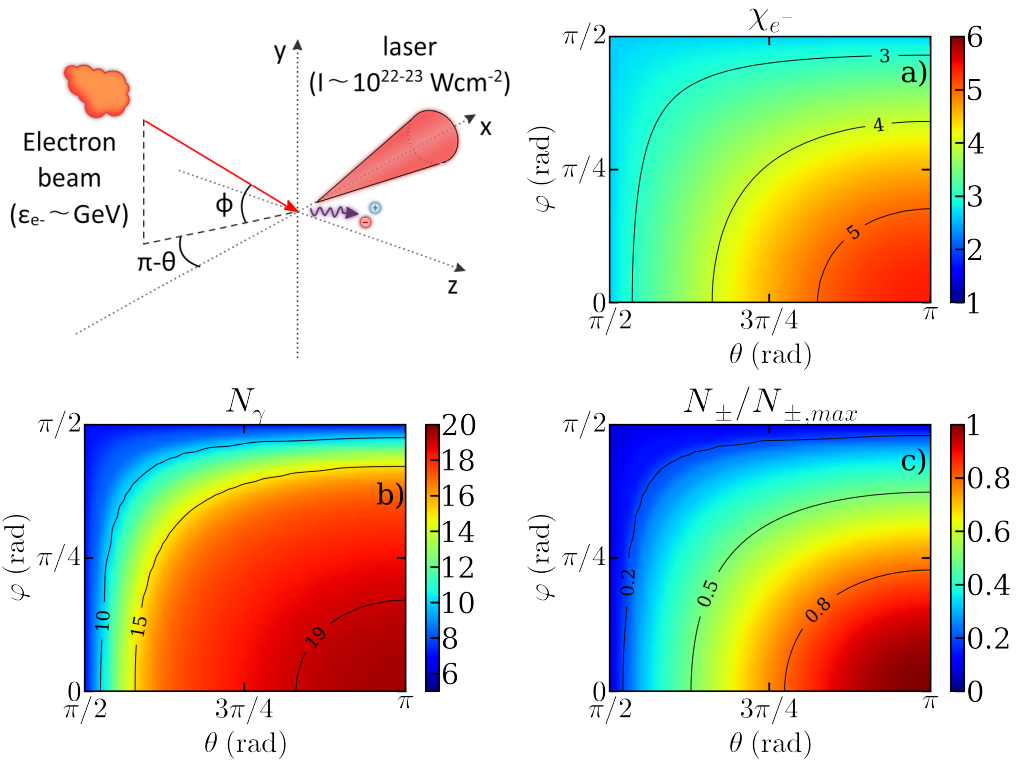

Figure 8.21: a) - Schematic of the oblique electron-laser collision. b) - Electron quantum parameter χ_{e^-} as a function of θ and φ. c) - Number of generated γ-photons as a function of θ and φ. d) - Ratio of the positron yield over the positron yield in a direct collision as a function of θ and φ ($N_{\pm,\mathrm{max}}$).

and $\varphi = 0$. The calculation of the quantum parameter and the laser phase at every time-step takes into account both angles.

The angle parametric study is performed for $\theta \in [45°, 90°]$ and $\varphi \in [0, 90°]$ for a 3 GeV electron beam interacting with a counter-propagating wave at 5×10^{22} Wcm^{-2}. The case of optimal charge production corresponds to the direct incidence. In return, the case where the charge production is the most reduced corresponds to $\theta = \varphi = 90°$. However, even in this case, the maximum electron quantum parameter is still high equal to $\chi_{e^-} \sim 2.7$ so that the photon emission is still in the quantum regime as shown in Fig. 8.21. The number of γ-photons has a low variation and varies from 20 to 10 per electrons (Fig. 8.21c). The loss in positron charge production for a 3 GeV electron is estimated to be no more than 90 % (again reached for $\theta = \varphi = 90$) as displayed in Fig. 8.21d.

For a finite focal spot, a more significant part of the beam can pass by the laser depending of the spot diameter, the angle of incidence and the beam size. In this case, PIC simulations are required. We have made three simulations with different θ angles equal to 10°, 30° and 90° and $\varphi = 0$. Here, the laser is focused on the electron

beam head. The positron charges at the end of these simulations are respectively equal to 0.42, 0.41 and 0.03 nC for a charge production of reference equal to 0.42 nC. In the case at $\theta = 90°$, the charge represents 7 % of the reference case in good agreement with the reduced kinetic approach taking into account that in the latter simulation the tail of the beam does not interact with the laser.

8.5 Conclusion and possible future studies

The study has been motivated by the possibility to test quantum electrodynamics mechanisms in an all-optical laser experiments thanks to the forth-coming high-power laser facilities, tests only accessible up to now on large-scale accelerators. We aim to provide a full-integrated numerical tool and a guideline for the experimental teams interested in such configurations. We have analyzed through 3D PIC numerical simulations and a reduced kinetic approach the properties of the γ-photon and the pair beam respectively created by the nonlinear Compton Scattering of the initial beam and the photon decay via the multiphoton Breit-Wheeler process.

It has been first confirmed that between 10^{22} Wcm^{-2} and 10^{23} Wcm^{-2}, this configuration constitutes a bright source of γ-photons forward collimated in the propagation direction of the initial electron beam. The properties of the γ-photons depend on the laser parameters and more particularly on the intensity. A typical range of values can be nonetheless estimated. Close to 10^{22} Wcm^{-2}, around 2×10^{11} γ-photon are generated, with an average energy of 65 MeV. At 10^{23} Wcm^{-2}, the number of γ-photons is equal to 4.5×10^{11}, for an average energy of 33 MeV, giving a brilliance equal to 3×10^{22} photons/mrad^2/mm^2/s 0.1% bandwidth at this level and to 2×10^{21} photons/mrad^2/mm^2/s 0.1% bandwidth at 1 MeV.

Then, we have demonstrated that the generation of pairs could be observed in this configuration. The positron yield is a rising function of the laser intensity. However, the stronger the laser field, the higher the positron divergence. The positron deflection is emphasized for tiny laser focal spot. In the polarization plane of the laser, the wiggling is also responsible for the particle deflection and is as strong as the laser intensity is high. Furthermore, the stronger the laser field, the lower the average positron energy due to the radiation losses after their creation. At 10^{22} Wcm^{-2}, we expect 5×10^{8} positrons to be produced with an average energy of 350 MeV. With a focal spot diameter of 5 μm, the divergence is on average of 0.03 rad in the laser polarization plane and 0.002 in the perpendicular plane at the end of the laser interaction. At 10^{23} Wcm^{-2}, the positron yield rises to 6×10^{9} with a lower average energy of 110 MeV. With a focal spot of 2 μm, the divergence is of 0.33 rad in the laser polarization plane and 0.2 rad in the perpendicular plane.

With the future facility Apollon, the use of an f/2 focusing parabola will enable to focus the multi-PW laser in a focal spot diameter of 5 μm, leading to an average intensity of 2×10^{22} Wcm^{-2}. With a second mirror destined to be destroyed dur-

ing the interaction, the beam could be further focused in a 2 μm to reach almost $\times 10^{23}$ Wcm^{-2}.

Once operational, this scheme could be one of the most productive way to create anti-matter with a high-repetition rate with the configurations of H. Chen *et al.* (Chen *et al.* (2009),Chen *et al.* (2010),Chen *et al.* (2011),Chen *et al.* (2015),Chen *et al.* (2015)) and Sarri *et al.* (Sarri *et al.* (2013),Sarri *et al.* (2013),Sarri *et al.* (2015)) that exploit the Bremsstrahlung, the Bethe-Heitler and the Coulombian Trident processes (see chapter 5). In the configuration of Chen *et al.*, the pair generation comes from the conversion of the fast electrons generated via the interaction of a kJ and ps laser with a high-Z target. The experimental results were obtained in different laser facilities including Titan, Omega EP and Orion giving rise to a wide range of parameters and deduced interesting scalings. They reported the production of 10^{10} to 10^{12} positrons per shots, at least an order of magnitude above our most prolific configuration. Due to the volume occupied by the pairs, of the order of the target characteristic lengths ($\sim$ mm^3), the density at the source is very low bewteen 10^{12} and 10^{13} cm^{-3}. Furthermore, the final pair beam divergence is high, of the order of 0.35 rad, of the order of what we get at 10^{23} Wcm^{-2}, due to the significant divergence of the created hot electrons. Note that the divergence depends on the strength of the target normal sheath field. Therefore, the divergence should decrease with the laser energy with scaling $\varepsilon_l^{-1/2}$. The positron average energy is between 4 and 30 MeV giving a skin depth of $l_s = c\sqrt{\langle \gamma_{e^\pm} \rangle / n_{e^\pm}} \sim 9$ mm. In the second configuration, a GeV electron beam is first generated as in our case in a gas jet via the laser wakefield acceleration regime. The beam is then directed onto different high-Z foils of different materials and different thicknesses in order to achieve the conversion into high-frequency photons and positrons. The first experimental campaign was performed at Hercules and the second at Astra-Gemini. In the second one, with a laser peak intensity of 3×10^{19} Wcm^{-2}, they reported the generation of a beam of maximal energy 1.2 GeV with maximum of the distribution around 300 MeV, charge around 0.1 nC (2×10^{19} electrons) and divergence of 2 mrad. They considered a lead thick foil of different thickness multiple of the radiation length of 0.5 cm ranging from 0.5 to 4 cm. The maximum positron yield is obtained for 1 cm at 1×10^8 pairs (with an energy above 120 MeV) but the maximal energy corresponds to the smallest thickness of 0.5 cm at 600 MeV. These results are close to our range of values for the interaction at 10^{22} Wcm^{-2}. Due to the bremsstrahlung radiation losses in the matter, the higher the target thickness, the lower the average positron energies. The maximal percentage of positron, of 50 % is reached for the longest targets which means that the beam is almost neutral. This is not the case even at 10^{23} Wcm^{-2} with 23 % of positrons in our configuration. The pair beam duration (related to the beam length) is around 15 fs for a maximum transverse size of 200 μm, well above our dimensions of an order of magnitude. The pair beam divergence of 20 mrad is comparable to the results obtained in the simulations at 10^{22} Wcm^{-2} with a focal spot of 5 μm. The consequence is a small beam density estimated around 10^{16} cm^{-3}.

In comparison, at 10^{23} Wcm^{-2}, we have a density close to 10^{20} cm^{-3} at the heart of the beam, and equal to 10^{19} cm^{-3} in average. However, the strong divergence at this intensity will lead to a rapid decreasing of the density at farther propagation distance. The configuration of Sarri *et al.* also constitutes a strong source of γ-photons with a brilliance of 2×10^{20} photons/mrad^2/mm^2/s 0.1% bandwidth around 15 MeV Sarri *et al.* (2014) that is an order of magnitude below our estimates.

The cases involving a low intensity and a bigger waist is beneficial for the generation of a high-energy and well collimated positron beam. The positron beam, segregated from the electrons using a magnet could serve as a first acceleration stage for conventional and optical accelerators. On the other hand, in order to get the maximal positron charge with the next generation of laser facilities, the maximal available intensity will be required. For the generation of dense quasi-neutral pair plasmas, higher intensities, above 10^{23} Wcm^{-2} are required to approach an electron to positron charge ratio close to 1. With present technologies, the generation of pair plasmas is currently hardly feasible. However, pair plasmas could serve a wide range of laboratory astrophysical experiments in which interstellar mechanisms are reproduced at the laboratory scale (see chapter 9). It could be used for instance to study the development of instabilities in pair plasmas. In this case, the characteristic length of the structures induced by the instability (usually dependent on the particle energy and density) should be below the width of the plasma and the beam integrity maintained longer than the instability growth rate. In Sarri *et al.* (2015), 3D PIC numerical simulations were performed in the so-called fireball configuration when an electron-positron plasma flow penetrates a cold ion plasma to demonstrate the possibility to study Weibel-like instabilities in the laboratory with the parameters of the experimentally generated pair beam. Using a neutral beam of radius close to 1.5 mm, they show that the interaction leads to the formation of current filament instability of thickness of the order of the plasma skin depth equal to $l_s = 2\pi c\sqrt{\langle\gamma_{e^\pm}\rangle/n_{e^\pm}} \sim 1$ mm for an estimated average normalized energy of $\langle\gamma_{e^\pm}\rangle \sim 15$. In our case, with an average energy $\langle\gamma_{e^\pm}\rangle \sim 100$ and $n_{e^\pm} = 10^{19}$ cm^{-3}, the filament size is estimated around 100 μm, above the current transverse size of the beam. A last application to the generation of pairs is the positron annihilation spectroscopy (PALS) that use the lifespan to pair annihilation as a diagnostic of the voids and the defects in materials and most especially metals and semi-conductors.

In order to optimize the energy to charge ratio, intermediate intensities have to be carefully chosen as shown in section 8.4.3. For the next step, the influence of the laser duration on the γ-photons and the pair generation should be addressed using numerical 3D-PIC simulations in addition to the results of the reduced kinetic model presented in section 8.4.5. The influence of the wave contrast, not really studied here, should be also analyzed. Nonetheless, we can easily think that the best contrast is preferred for the generation of pairs. The study concerning the interaction in oblique incidence should be continued addressing the influence of the laser incidence angle on the positron average energy and divergence. An experimental

challenge is the perfect synchronization and alignment between the LWFA electron beam and counter-propagating laser. The challenge becomes as difficult as the laser focal spot is small. The study could be improved with simulation of misalignment both spatially and temporally.

Finally, simulations could be continued to study the evolution of the beam at longer time, including the dilution. The fireball configuration could be also tested using futuristic and optimistic parameters (larger beam size) adapted from the current results.

Chapter 9

A laser-based scheme for studying the Weibel instability in electron-positron pair plasmas

9.1 The Weibel instability and its role in collisionless shocks

The study of plasma instabilities is a long-standing topic in laboratory and space plasma physics because they may act as major dissipation sources in non- or weakly-collisional configurations (Davidson (1983); Sudan (1983); Gary (1993)). A paradigmatic system for the investigation of plasma instabilities is the collision of plasma flows. The dominant instability is determined by the nature (electrons, positrons, ions) and parameters (mean velocities, temperatures, densities, etc.) of the interpenetrating flows, the strength and polarization of external fields (if any), as well as by the details of the interaction geometry (collision angle, gradients in velocity or density, etc.). Among the most common instabilities developing in lepton-dominated systems are the purely electrostatic, parallel[1] (or "bump-on-tail", for dilute hot beams interacting through dense plasmas) instability (Bohm and Gross (1949)), the mostly electromagnetic, Weibel-filamentation instability (Weibel (1959); Fried (1959)) and the mostly electrostatic, oblique modes (Bludman *et al.* (1960)). The respective domains of preponderance of these instabilities have been analyzed by Bret *et al.* (2008, 2010).

In this Chapter, we will focus on the Weibel-filamentation instability (Weibel (1959); Fried (1959)), which results in the spontaneous growth of coupled current and (mainly) magnetic modulations in the direction normal to the flows[2] (Fig. 9.1). The

[1]Here, "parallel", "transverse" and "oblique" refer to the angle between the unstable wave-vector and the mean flow velocity.

[2]Or the axis of the largest temperature in a single anisotropic plasma

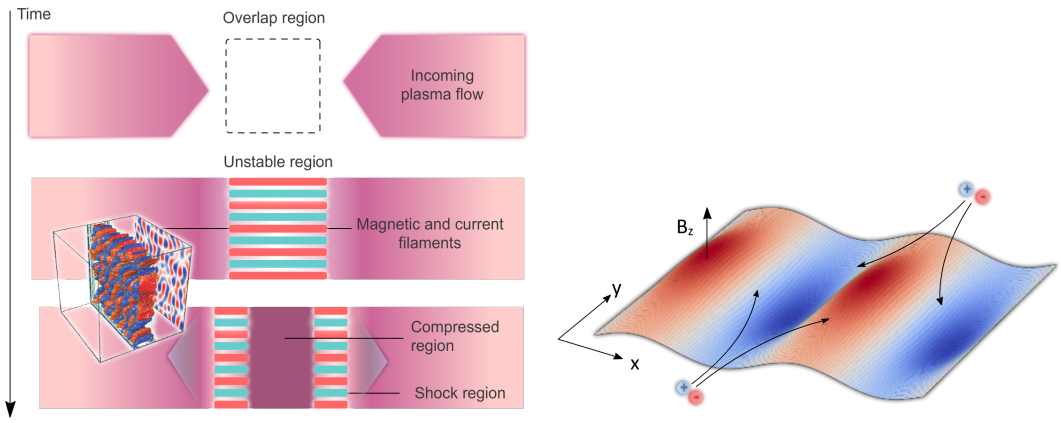

Figure 9.1: Schematic of the Weibel instability in the collision of two electron-positron pair plasmas.

buildup of the electromagnetic turbulence goes along with deceleration and transverse heating of the flow particles (Davidson *et al.* (1972); Achterberg and Wiersma (2007); Achterberg *et al.* (2007)). This instability is expected to prevail from the start in the collision of relativistic plasmas of comparable densities, but can also dominate the late-time evolution of relativistic beams interacting with much denser plasmas, following the saturation of the initially fastest-growing electrostatic modes (Bret *et al.* (2008, 2010)).

The electromagnetic turbulence produced by the Weibel instability is a good candidate for explaining the formation of collisionless turbulent shocks in non- or weakly-magnetized astrophysical systems (Sagdeev (1966); Medvedev and Loeb (1999); Gruzinov and Waxman (1999); Silva *et al.* (2003)). "Collisionless" refers to the fact that, in contrast to classical hydrodynamic shocks, these structures develop on scales much shorter than the collisional mean free path of the interacting plasmas[3]. Collisionless turbulent shocks between energetic (electron-ion or electron-positron) outflows and the ambient medium may happen in various high-energy astrophysical environments (e.g. active galaxy nuclei, pulsar wind nebulae, supernovae remnants, etc.), where they are held responsible for generating suprathermal particles and radiation through, respectively, Fermi-type acceleration (Blandford and Ostriker (1978); Drury (1983); Blandford and Eichler (1987); Jones and Ellison (1991); Malkov and O'C Drury (2001); Lemoine *et al.* (2006)) and synchrotron emission (Begelman *et al.* (1984); Piran (2005); Waxman (2006)). Both these processes require that part of the flow kinetic energy be converted into magnetic fluctuations moving at different velocities upstream and downstream of the shock front. Over the past years, impressive progress in theoretical modeling (Medvedev and Zakutnyaya (2009); Medvedev

[3]As their hydrodynamic counterparts, these turbulent shocks verify the Rankine-Hugoniot jump conditions.

and Spitkovsky (2009); Nishikawa *et al.* (2009); Lemoine and Pelletier (2011); Bret *et al.* (2014); Ruyer *et al.* (2015)) and numerical simulations (Kato (2007); Kato and Takabe (2008); Spitkovsky (2008); Spitkovsky (2008); Martins *et al.* (2009); Sironi and Spitkovsky (2011); Stockem *et al.* (2014)) has clarified the mechanisms of the micro-scale turbulence generation and shock formation. The emerging picture is that of a self-regulated structure, whereby the particles Fermi-accelerated in the turbulence and injected back into the upstream (unshocked) medium also drive the Weibel-type instabilities at the source of this turbulence. Despite these advances, the long-term evolution of the increasingly large-scale turbulence and shock structure (Chang *et al.* (2008); Keshet *et al.* (2009)) and its radiative signature (Sironi and Spitkovsky (2009)) need further understanding.

Much of this progress has been made possible by the use of massively parallel PIC simulations, which provide an *ab initio*, self-consistent description of the problem. The accuracy of these simulations, however, comes at the cost of heavy computational load, and they are usually conducted under simplified physical conditions (e.g. uniform and cold plasmas) and geometries. Even in a reduced 2D geometry, state-of-the-art simulations can only access the first stages of the shock formation, and may therefore be affected by the somewhat arbitrary choice of the initial conditions. The plasma collision is modeled either by injecting two flows from both sides of the domain or, in order to save computational time, by making a single drifting flow reflect off a boundary. In the case of electron-ion flows, artificially low ion masses are often employed to speed up shock formation and reduce the simulation domain.

The reproduction of these phenomena in the laboratory would be of great value for validating the theoretical and numerical predictions. Laser-matter interaction is likely to play a crucial role in this respect, because of the unique ability of powerful lasers to drive relatively dense plasmas at high velocities. A major difference concerns the scales at which the astrophysical and experimental phenomena take place due to the considerable disparity of the plasma densities at play (from $n_e \sim 10^{-3} - 10^3\,\mathrm{cm}^{-3}$ in astrophysical settings, to $n_e \sim 10^{18} - 10^{22}\,\mathrm{cm}^{-3}$ in laser experiments). The challenging goal will then be to create systems of similar normalized scales. According to simulations, the creation of a fully-developed, propagating shock takes place over a longitudinal length $\gtrsim 100c/\omega_p$ (where ω_p is the relativistically-corrected plasma frequency of the heavier species carried by the flows). The transverse size of the flows should be of the same order to accommodate a sufficient number of current filaments (Kato and Takabe (2008); Stockem Novo *et al.* (2015)).

It should be noted that the Weibel-filamentation instability is a naturally occurring process in relativistic laser-plasma interaction. Owing to their initial strong anisotropy, the laser-accelerated electrons penetrating the ambient plasma excite strong transverse magnetic modulations near the irradiated target surface, which tend to isotropize the hot electrons and weaken their energy coupling efficiency with the deep plasma regions. This effect severely hampers the high-energy-density applications based on laser-accelerated hot electrons, e.g. the fast ignition concept of

inertial confinement fusion or the target normal sheath acceleration (TNSA) of ion beams (Silva *et al.* (2002); Deutsch *et al.* (2005); Adam *et al.* (2006); Ren *et al.* (2006); Okada and Ogawa (2007); Robinson *et al.* (2014)). This mechanism was investigated experimentally in (Jung *et al.* (2005)) and (Mondal *et al.* (2012)).

9.1.1 Laser-based concepts for the study of the Weibel instability

The investigation of the Weibel instability using powerful lasers is challenged by the creation of unstable (beam-plasma or two-beam) systems evolving rapidly with respect to the intrinsically limited duration ($\sim$ ps $-$ ns) of the interaction. One driving goal is to attain the strongly nonlinear regime required for shock formation and, ultimately, for the start of significant particle acceleration and radiation. This objective has spurred a number of experimental and theoretical efforts over the past years. The various schemes proposed or already tested in distinct interaction regimes are summarized in Fig. 9.2 as a function of the required laser energy and intensity.

So far, the most explored route consists in making collide two ablative electron-ion plasmas issued from the irradiation of solid foils by high-energy ($> 10\,\mathrm{kJ}$) nanosecond-duration lasers (Kuramitsu *et al.* (2011); Park *et al.* (2012); Drake and Gregori (2012)). This scheme is depicted in Fig. 9.3a and represented by the red box of Fig. 9.2. Recent related experiments carried out on the OMEGA laser evidenced the growth of Weibel-type ion filamentation (Fox *et al.* (2013); Huntington *et al.* (2015)), thus indicating that shock generation should be within the reach of National Ignition Facility-class ($> 100\,\mathrm{kJ}$) systems. In this configuration, the colliding plasmas have densities of $\sim 0.01 - 0.1 n_c$ and non-relativistic velocities $\sim 100 - 1000\,\mathrm{kms}^{-1}$. The self-generated magnetic fields were probed by fast protons produced by an additional ultra-intense picosecond laser (Fox *et al.* (2013)) or a laser-imploded D^3He capsule (Huntington *et al.* (2015)).

In the relativistic regime, an alternative scheme has been recently proposed by Fiuza *et al.* (2012) and further analyzed in Ruyer *et al.* (2015) (see purple box in Fig. 9.2 and Fig. 9.3b). An ultra-intense laser of intensity $\sim 10^{20} - 10^{22}\,\mathrm{Wcm}^{-2}$ interacts with a pre-ionized plasma of density close to the relativistic transparency threshold ($n_e \sim a_0 n_c \sim 10 - 100 n_c$). The resulting hot electrons propagate into the target, where they induce a return current made of colder background electrons. Simultaneously, the laser radiation pressure pushes the target surface as a whole (up to a velocity $\sim 0.1c$). The Weibel-mediated interaction between the hot and return current electrons generates electromagnetic fluctuations that may become strong enough to scatter the ambient ions (in the laser piston frame), hence triggering a collisionless shock that propagates ahead of the laser-driven piston. Despite similarities with the standard astrophysical scenario, this configuration differs from the latter in that the shock is initially driven by the laser-accelerated hot electrons, rather than by Weibel-unstable ions (Ruyer *et al.* (2015)). Its experimental inves-

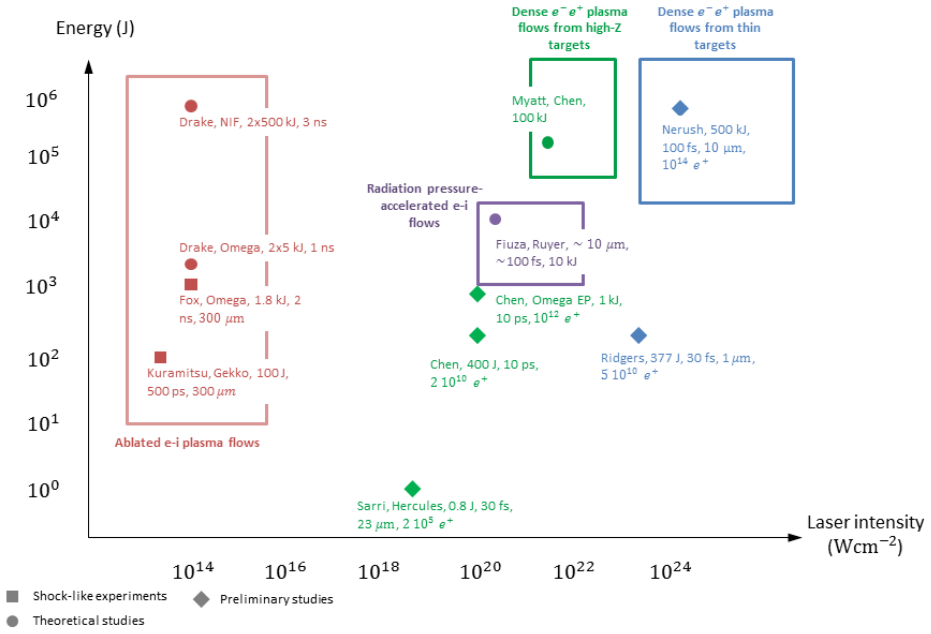

Figure 9.2: Laser-driven schemes for studying the Weibel instability and the formation of collisionless shocks. Theoretical and experimental are indicated by circlres and squares, respectively. Diamonds identify analytical and/or experimental works not directly related to collisionless shocks, but which provide results supporting the feasibility of the dedicated schemes.

tigation would require a significant laser energy ($\sim 1\,\mathrm{kJ}$), allowing of a large focal spot and sufficient interaction time. Low-Z targets below solid density should ease shock formation; this favors the use of foams, as already experimented in a similar configuration (Jung *et al.* (2005)), or of liquid hydrogen jets, as recently exploited for warm dense matter studies (Zastrau *et al.* (2014)). A further complication stems from the characterization of the turbulence profile and dynamics inside overcritical matter; the relevant spatio-temporal scales ($\sim \mu\mathrm{m}, 100\,\mathrm{fs}$) are only accessible to an ultra-short x-ray probe, as provided, for instance, by a free-electron laser (Kluge *et al.* (2014)).

The experimental study of relativistic electron-positron instabilities, which are likely to mediate the termination shocks of pulsar winds (Bykov and Treumann (2011)), appears even more challenging owing to the difficulty of creating pair plasmas dense enough so that their typical dimensions largely exceed their relativistic skin depth, $\sqrt{\gamma}c/\omega_p$ (Liang (2013)). The most advanced approach is based on the direct irradiation of thick ($\sim$ mm) high-Z targets by ultra-intense lasers. Moderately

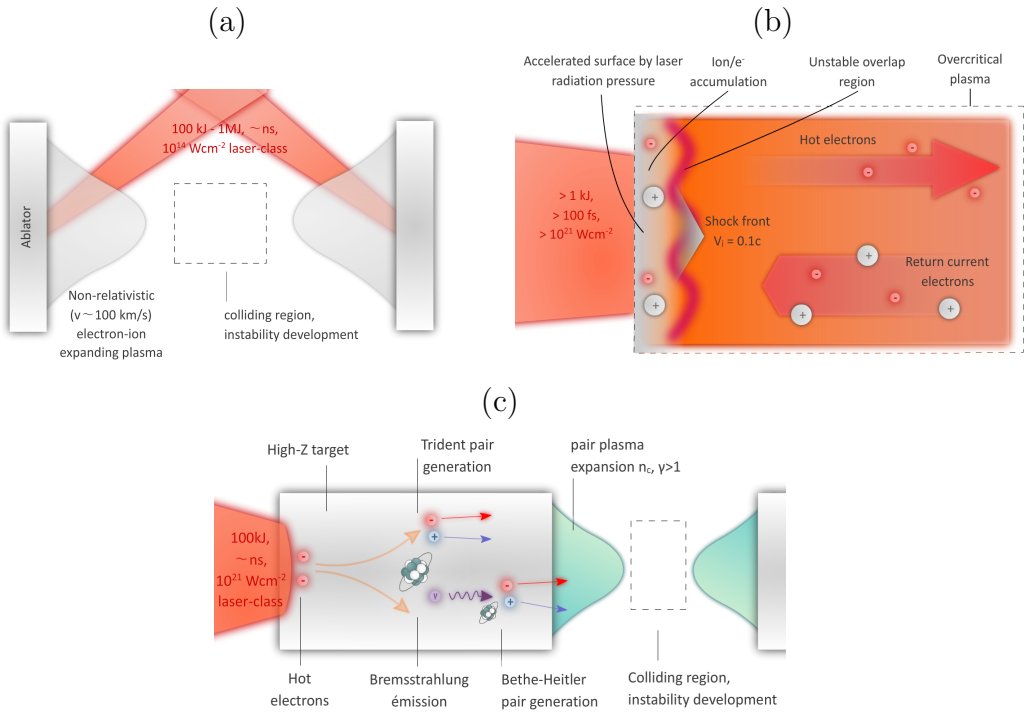

Figure 9.3: Possible schemes for laser-driven generation of collisionless shocks (a) - Collision between ablative electron-ion plasmas produced by high-energy, nanosecond-duration lasers. (b) - Interaction between a relativistic-intensity, picosecond-duration laser with an overcritical plasma (c) - Collision between e^-e^+ pair plasmas produced through Bremsstrahlung/Bethe-Hietler processes in high-Z targets irradiated at relativistic intensities.

relativistic e^-e^+ plasmas are then produced from the Bethe-Heitler annihilation of Bremsstrahlung γ rays emitted by the laser-accelerated electrons. This setup is schematized in Fig. 9.3c and identified by the green box of Fig. 9.2) (see also Sections 5.3 and 8.5). This design was studied theoretically by Myatt *et al.* (2009) and experimentally investigated on a variety of laser facilities by Chen *et al.* (Chen *et al.* (2009), Chen *et al.* (2010), Chen *et al.* (2011), Chen *et al.* (2015) and Chen *et al.* (2015)). With present-day intense laser systems, the production of up to 10^{12} positrons of $\sim$ 10-MeV mean energy has been measured per laser shot. The density and duration of the (few-mm wide) pair beam are estimated to be of $10^{15} - 10^{16}$ cm^{-3} and 10 ps, respectively, which seems insufficient for ensuring rapid instability growth. For a similar beam duration, a total positron number $> 10^{14}$ appears to be required. From extrapolation of the experimental data, an order of magnitude increase in the positron yield is expected on the upcoming 5 kJ-class laser systems (e.g. PETAL, LFEX and ARC). 2D PIC simulations then predict the generation of Weibel filaments of $\sim$ 0.5-mm wavelength and $\sim$ 40-T strength, detectable by proton radiography

(Chen *et al.* (2015)). Additional simulations indicate that longer-duration ($> 25\,\mathrm{ps}$), higher-energy ($> 20\,\mathrm{kJ}$) lasers are required to produce a fully-developed propagating shock.

The collision of counter-streaming flows is not the only configuration relevant for astrophysical purposes. In the so-called "fireball" models, high-energy ejecta from the explosion of a central engine interact with the interstellar medium (Piran (1999)). The PIC simulations of Davis *et al.* (2010) assimilate the fireball to an electron-proton plasma produced by TNSA, subsequently injected into a hydrogen gas jet. The case of an ultra-relativistic e^-e^+ fireball has been numerically investigated in (Muggli *et al.* (2013)) using the parameters of the SCLAC beam.

A variant of the Bremsstrahlung/Bethe-Heitler-based scheme for pair production has been recently explored by Sarri *et al.* (Sarri *et al.* (2013), Sarri *et al.* (2013) and Sarri *et al.* (2015)). This promising concept consists in generating a GeV electron beam by means of a laser wakefield accelerator, and injecting it into a high-Z convertor. For an optimized target thickness, one can obtain a quasi-neutral, ultra-short ($\sim 15\,\mathrm{fs}$) and highly-collimated ($\sim$ mrad) pair jet. Despite a much lower laser energy than in Chen *et al.*'s experiments ($\sim 10\,\mathrm{J}$ *vs* $> 500\,\mathrm{J}$), a similar pair density is achieved ($\sim 10^{16}\ \mathrm{cm}^{-3}$), yet with a reduced transverse size ($\sim 200\,\mu\mathrm{m}$), comparable with the relativistic skin depth ($\sqrt{\gamma_{e^+}}c/\omega_{pe^+}$) of the beam. The experimental results of Sarri *et al.* (2015) are complemented with 3D PIC simulations of the propagation of the quasi-neutral pair beam in an electron-proton plasma at rest. They indicate the onset of filamentation with magnetic field amplitude $\sim 40\,\mathrm{T}$, in stark contrast with the case of a pure electron beam, which is found to trigger plasma wakefields instead of magnetic filaments. One should notice, however, that the beam parameters in these simulations significantly differ from the actual ones: the beam density is multiplied by 10 ($10^{17}\ \mathrm{cm}^{-3}$) and its transverse size by 2.7 ($530\,\mu\mathrm{m}$), which should enhance the tendency of the beam to filament.

9.1.2 Pair plasma collision from laser-induced synchrotron/Breit-Wheeler processes

In Section 7.4, it was shown that high-density ($> n_c$), ultra-relativistic pair plasmas can result from combined synchrotron and Breit-Wheeler mechanisms in thin ($\sim \mu$m) foils driven at laser intensities $> 10^{23}\,\mathrm{Wcm}^{-2}$ (Ridgers *et al.* (2012, 2013)). One can therefore think of adapting the colliding-beam setup of Fig. 9.3b with extreme-intensity lasers, as sketched in Fig. 9.4. An important difference with the former design is that pair production mostly occurs in the laser-irradiated region (i.e., on μm scales), thereby enabling much larger positron densities. Note, however, that regarding the relativistic skin depth, which determines the efficiency of the Weibel instability, the large increase in the positron density ($> \times 10^5$) is mitigated by a much larger kinetic energy ($> \times 10$) than in the currently explored Bremsstrahlung/Bethe-Heitler concept.

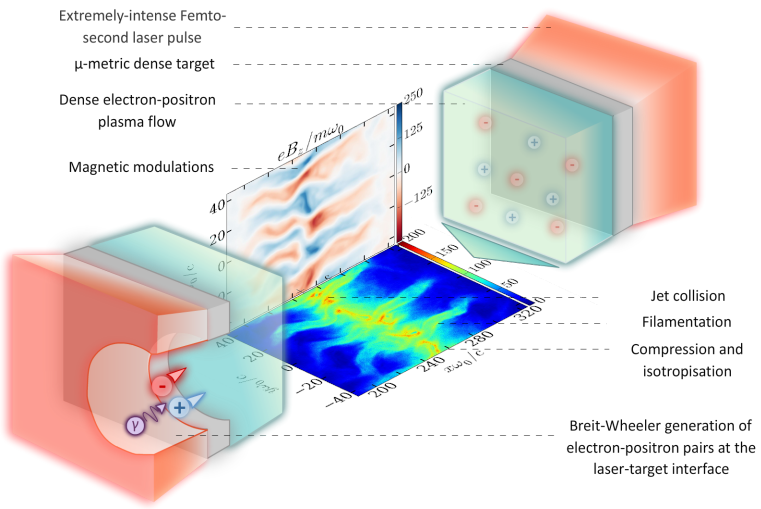

Figure 9.4: Pair beam-colliding scheme exploiting synchrotron/Breit-Wheeler processes at laser intensities exceeding $10^{23}\,\mathrm{Wcm}^{-2}$.

The physical conditions required for this scenario can be readily assessed as follows. In the cold-fluid approximation, the Weibel growth rate is given by $\Gamma_W \sim \omega_0\sqrt{n_{e^\pm}/\gamma_{e^\pm} n_c}$ (Pegoraro *et al.* (1996)). For a laser pulse focused onto a solid foil at an intensity $I_L \simeq 10^{24}\,\mathrm{Wcm}^{-2}$, we can expect the generation of an overcritical pair plasma, with $n_{e^\pm} \simeq 20 n_c$ and $\gamma_{e^\pm} \simeq 500$. This leads to a growth rate $\Gamma_W \simeq 0.2\omega_0$, corresponding to a growth time of about one laser period. The duration of the pair beam being close to that of the laser, a pulse length of a few tens of fs is therefore sufficient for several e-foldings to occur during the pair collision. The typical filament size is $\lambda_W = (2\pi c/\omega_0)\sqrt{n_c\gamma_\pm/n_\pm} \simeq 30c/\omega_0$ ($5\,\mu$m). A focal spot $L_\pm \gg \lambda_W$ is needed to obtain a number of filaments large enough for efficient wave-particle interaction. A relatively wide focal spot also helps minimize the transverse spreading of the flows exiting the target before the collision. So as to verify the above requirements, the laser energy should be then close to $E_L \simeq I_L c(10/\Gamma_W)(5\lambda_W)^2 \simeq 150\,\mathrm{kJ}$, which is outside the reach of forthcoming multi-petawatt systems. Such extreme conditions, also considered for pair cascading scenarios (Nerush *et al.* (2011)), are envisioned in a number of longer-term projects (e.g. IZEST, XCELS) aiming at compressing NIF-class lasers into sub-picosecond pulses (Mourou *et al.* (2012); Mourou and Tajima (2014); Narozhny and Fedotov (2014)). In a keynote presentation, NIF and Photon Science Chief Technology Officer Chris Barty described the "Nexawatt" Laser, an exawatt laser concept based on NIF technologies, on April 13 at the SPIE Optics + Optoelectronics 2015 Conference in Prague. Barty also gave an invited talk on "Laser-Based Nuclear Photonics" at the SPIE meeting.

9.2 Proof-of-principle numerical simulations

The feasibility of a Breit-Wheeler-based pair collision is now gauged using 2D CALDER simulations. The simulation setup consists of two 7 μm-thick foils of copper ($Z = 29$, $\rho = 8.96\,\mathrm{gcm}^{-3}$) located at positions $x \sim 24\,\mu$m ($150c/\omega_0$) and $x \sim 167\,\mu$m ($1050c/\omega_0$). The targets are taken to be fully ionized, yielding and ion density $n_{Cu} \simeq 79n_c$ and electron density $n_{e^-} \simeq 2200n_c$. To model preplasma effects, a 4-μm ($25c/\omega_0$) linear ramp is added on the front side of the targets. The targets are placed symmetrically at an approximate distance of 70 μm from the center of the domain, $x = 95\,\mu$m ($600c/\omega_0$). The domain has total longitudinal and transverse dimensions of 191 μm ($1200c/\omega_0$) and 19 μm ($120c/\omega_0$), respectively. The boundary conditions are absorbing in the longitudinal direction and periodic in the transverse direction for both the fields and the particles.

The laser pulses are modeled as plane waves injected from the left and right boundaries ($x = 0$ and $x = 191$ μm). They are linearly polarized in the z-direction with a 1-μm wavelength. Their temporal profile is a 4th-order super-Gaussian of 106-fs ($200\omega_0^{-1}$) FWHM and $8.9 \times 10^{23}\,\mathrm{Wcm}^{-2}$ ($a_0 = 800$) peak intensity.

Since optimum pair production is predicted to occur near the relativistic transparency threshold (Ridgers *et al.* (2013)), the case of Aluminium foils ($n_e \sim 780n_c$) was first considered in (Lobet *et al.* (2015)). However, as a result of the strong radiation pressure exerted by the laser, the ions are rapidly accelerated to relativistic velocities, hence limiting the life-time of the nonlinear plasma structure arising from the pair interaction. Heavier materials like copper offer the advantage of generating slower ions, which postpones their arrival in the pair overlap region.

Our simulations are limited to 2D geometries due to the important computational load required to handle the inflating numbers of particles and γ-ray photons. The discretized domain is $30000\Delta x \times 3000\Delta y$ with $\Delta x = \Delta y = 0.04c/\omega_0$. Each cell initially contains 50 super-particles per species (electrons and ions). To limit spurious Cerenkov radiations, we employ the advanced Maxwell solver developed in (Lehe *et al.* (2013)), in addition to temporal filtering of the electric field (Friedman (1990); Greenwood *et al.* (2004)). The simulations are run on 2000 cores with the Curie supercomputer at TGCC/CCRT. In order to reduce the simulation time and avoid memory overload, the following methods are used. First, the super-photons generated at the laser-solid interface are confined to a limited physically-useful area around the targets by adding photon absorbing conditions inside the computational domain. By doing so, the photons do not have to travel across the entire domain before being evacuated. Also, when the laser field is sufficiently attenuated, all the super-photons are suppressed from the grid. The photon emission occurring at later times is still simulated (using the mixed continuous-MC approach), and therefore contributes to the overall energy balance and photon spectra, but without generating super-photons.

9.2.1 Generation of the pair plasmas

The first part of the simulation concerns the generation of the e^-e^+ pair plasmas from the two targets. As described in Section 7.4, pair creation mostly occurs at the laser-plasma interfaces. This is illustrated in Figs. 9.5(a,c,e), which show the particle densities and the laser field during the laser irradiation. The γ photons emitted backwards with respect to the laser propagate through the vacuum during a few laser periods before decaying into e^-e^+ pairs. By interacting in turn with the laser, these pairs can generate high-energy photons before being returned to the target by the laser ponderomotive force. This cascading process gives rise to a pair plasma expanding through the incident laser wave. Most of the e^-e^+ pairs, however, are accelerated along the laser direction [blue curves in Fig. 9.5(e)]. At the rear side of each target, the charge separation field induced by the fast electrons at the early times of the interaction further accelerates the positrons.

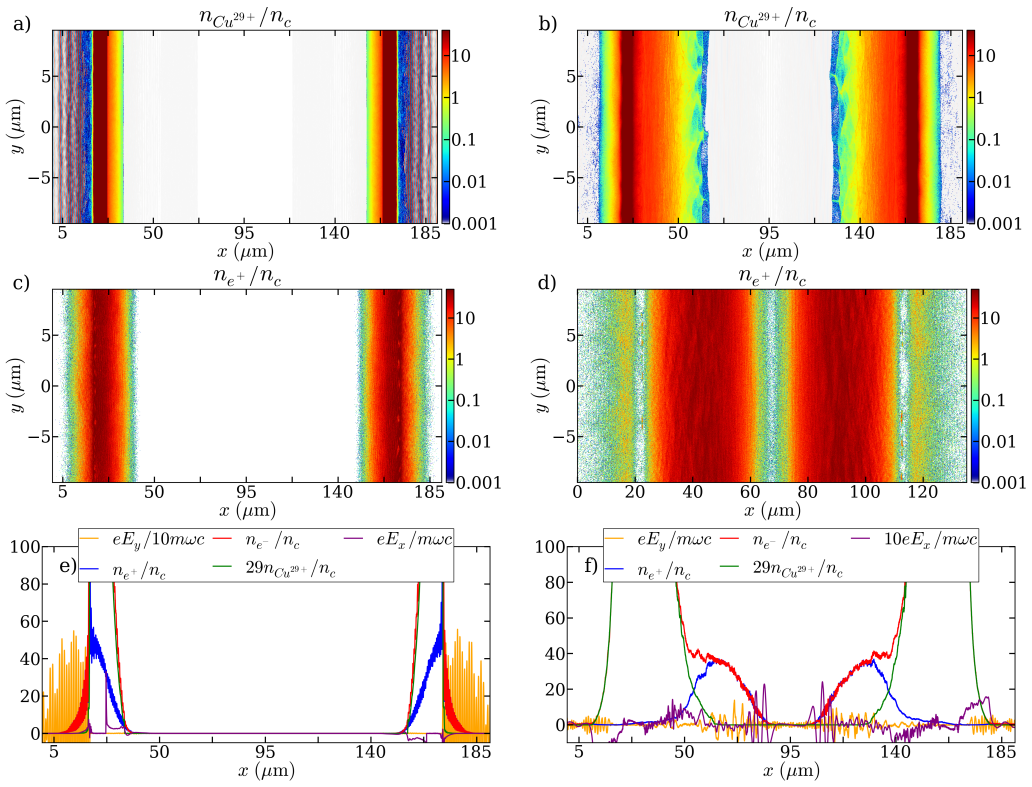

Figure 9.5: (a,b) - Ion normalized density $n_{Cu^{29+}}/n_c$ during the pair plasma creation ($t = 268\,\text{fs}$) and just before the pair plasma collision ($t = 424\,\text{fs}$). (c,d) - Positron normalized density n_{e^+}/n_c for times similar to (a,b). (e,f) - Electron (red), positron (blue) and ion (green) normalized density average over the transverse direction for times similar to (a,b). The average normalized electric field E_y (divided by 10) and E_x are also shown (respectively orange and purple).

The temporal profile of each positron jet is shaped by the laser envelope. Just after laser irradiation ($t = 424\,\mathrm{fs}$), the positrons (then still located inside the Cu target) have a super-Gaussian profile of FWHM $l_{e^+} \sim 25\,\mu\mathrm{m}$. This value is somewhat shorter than the laser length owing to the rapid drop of the e^-e^+ emission rate with decreasing laser intensity. The distance between the two targets should be large enough for allowing the pair plasmas to separate spatially from the rapidly expanding target ions. The $x - p_x$ and $x - \gamma$ ion phase spaces of Figs. 9.6(a,b) show that the TNSA ions (corresponding to the thin tail-like structure that originates from the target rear side) and the RPA ions (corresponding to the thicker tail originating from the target front side) move at velocities $v_{\mathrm{TNSA}} \simeq 0.5c$ and $v_{\mathrm{RPA}} \simeq 0.7c$, respectively. The distance needed to fully separate the pairs (moving at $\sim c$) from the ions is therefore of $\sim 300\,\mu\mathrm{m}$, considering that each pair plasma has a total length of $2l_{e^+} \sim 46\mu\mathrm{m}$. This separation distance exceeds the distance to the contact plane in the simulation. As a result, only the first half of each quasi-neutral e^-e^+ jet (from $x = 60\,\mu\mathrm{m}$ to $90\,\mu\mathrm{m}$ for the rightward-moving jet) will contribute to the "pure" pair-plasma collision (Fig. 9.5). Just before collision, the positron jet presents a maximum density of $n_{\mathrm{max}} = 36n_c$. Moreover, it has lost its super-Gaussian shape, partly because of the electrostatic repulsion exerted by the fastest ions behind the pair jet.

The $x - p_x$ and $x - \gamma$ phase spaces are plotted in Figs. 9.6(c,d) for the electrons and Figs. 9.6(e,f) for the positrons. The p_x and γ distributions of both species appear to be inhomogeneous along x. The average e^-e^+ energies (plotted as dashed curves) attain their maximum values ($\langle\gamma_{e^+}\rangle_y \sim \langle\gamma_{e^-}\rangle_y \sim 1000$) near the jet head, and exhibit spatial modulations anti-correlated between the two species. At the position of the peak pair density ($x \approx 64\,\mu\mathrm{m}$, see Fig. 9.5f), the average e^-e^+ energies are measured to be $\langle\gamma_{e^+}\rangle_y \simeq 610$ and $\langle\gamma_{e^-}\rangle_y \simeq 300$. This factor of ~ 2 difference stems from the energy boost provided by the rear-side sheath potential Φ set up by the (denser) fast electrons, particularly those accelerated in the rising phase of the laser pulse, prior to strong pair production. This sheath potential is of the order of the fast electron energy, and therefore of the laser ponderomotive potential. Consequently, the positrons can gain up to twice the energy of the fast electrons, $\langle\gamma_{e^+}\rangle \sim \langle\gamma_{e^-}\rangle + \Phi \sim 2\sqrt{1 + a_0^2/2} \sim 1100$, which is indeed observed for the first positrons reaching the target rear side. The average electron energy is maximal near the jet head and decreases when getting closer to the targets. This apparent electron cooling may result from the ponderomotive steepening of the irradiated surface, but also from the increasing contribution of the colder bulk electrons.

The $p_x - p_y$ e^-e^+ phase spaces are displayed in Figs. 9.7(a,b) at time $t = 357\,\mathrm{fs}$ and at the position of peak positron density ($x = 64\,\mu\mathrm{m}$). As already evidenced in Figs. 9.6(d,f), the pair plasma distributions present broad energy and angular spreads (with comparable p_x and p_y dispersions). Importantly, both distributions cannot be modeled by Maxwell-Jüttner functions. As discussed above, the positron distribution yields an average energy about twice larger than the electron value due

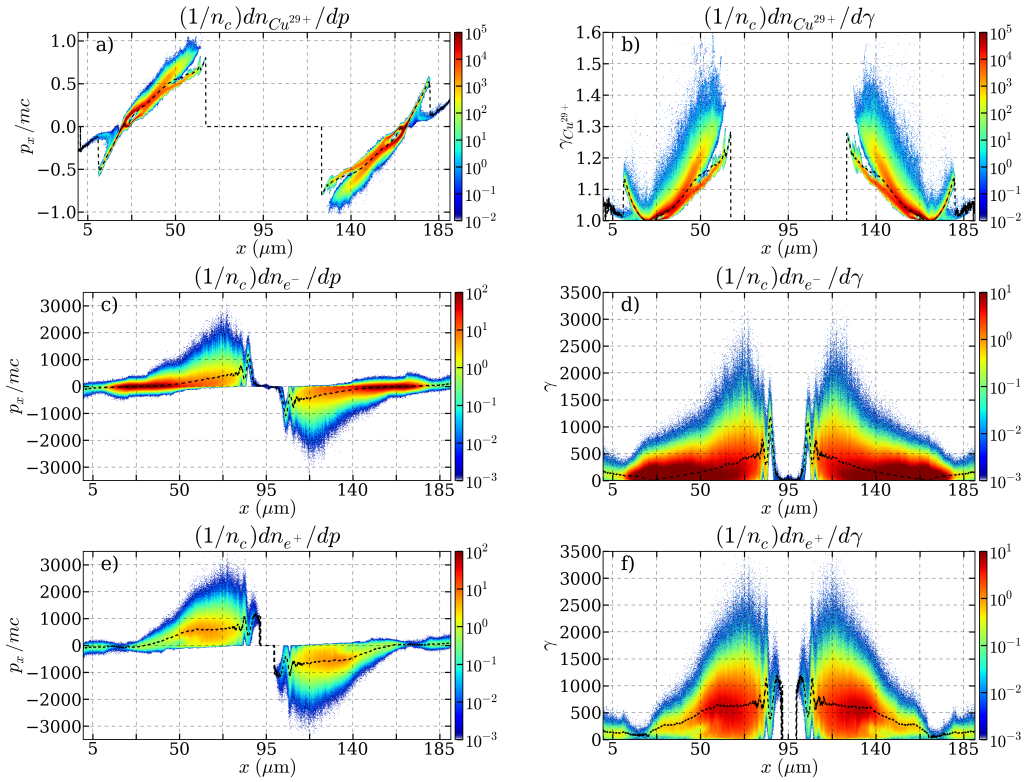

Figure 9.6: (a,c,e) - Ion, electron and positron $x-p_x$ phase spaces just before the pair plasma collision ($t = 424\,\mathrm{fs}$). (b,d,f) - Ion, electron and positron $x-\gamma$ phase spaces at $t = 424\,\mathrm{fs}$. The black dashed line represents the average values as a function of the position x.

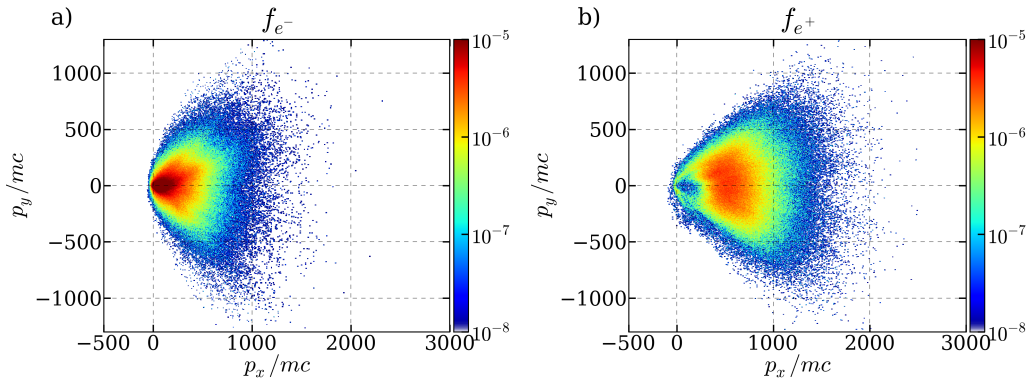

Figure 9.7: Electron and positron $p_x - p_y$ phase spaces at the center of the left pair plasma ($x = 50\ \mu\mathrm{m}$) prior to the collision at time $t = 297\,\mathrm{fs}$.

to the TNSA boost. The latter effect probably explains the deficit of positrons in the low-energy region, as well as the lower angular divergence of the positrons

($\langle\theta_{e^-}\rangle^{1/2} = 0.36$) compared to that of the electrons ($\langle\theta_{e^-}\rangle^{1/2} = 0.55$).

Just before the beam collision, the energy budget is the following: 76 % of the laser energy has been converted into high-energy radiation (71 % including pair decay), 5.2 % into positrons, 8.3 % into fast electrons and 12 % have been absorbed by the ions, yielding a total absorption fraction of 96 %.

9.2.2 Collision of the electron-positron pair plasma flows

The two electron-positron jets make contact at the center of the domain at $t \sim 390$ fs. The plasma jet overlapping is analyzed in detail in the next sections.

Generation of magnetic and density filaments

The collision leads to the formation of magnetic and density channels both for the positrons and the electrons in the interval 88 μm ($553c/\omega_0$) $< x <$ 102μm ($641c/\omega_0$). This is shown in Fig. 9.8a and 9.9b at time 424 fs corresponding to the linear phase of the instability. The maximal magnetic field amplitude is equal to $B_z \sim 1.6\times10^6$ T ($B_z \sim 149\omega_0 m_e/e$) while the filament wavelength, equal to $\lambda_W \simeq 5$ μm, is close to the theoretical value $\lambda_W = 2\pi c/\omega_0\sqrt{n_c\gamma_{e^\pm}/n_{e^\pm}} \simeq 4.1$ μm in a cold fluid model assuming $n_{e^\pm} \sim n_{\max}/2 \sim 18n_c$ and $\gamma_{e^\pm} \sim 300$. By the end of the collision ($t = 476$ fs), the particle densities and the magnetic field exhibit kink-like oscillations and the density filaments are magnetic pinched up to twice the initial density as shown in Fig. 9.9b for the magnetic field and Fig. 9.8b for the positron density. The destruction of the filament coherence contributes to the particle thermalization. The saturated magnetic amplitude, $B_{\rm sat}$, and wavelength, $\lambda_{\rm sat}$, can be understood upon assuming complete current separation inside Alfvén-limited filaments (Kato (2005)). Due to the lower relativistic inertia of the electrons, the half-width of the filaments should be close to the electron Larmor radius $\sim 2m_e c\gamma_{e^-}/eB_{\rm sat}$ (where the mean field in a filament is estimated to be $B_{\rm sat}/2$). The electron current density involved in the calculation of $B_{\rm sat}$ is estimated assuming a mean velocity $\langle v_x\rangle \sim c/2$). The saturation value reached by the magnetic field $B_{\rm sat} \simeq 206m_e\omega_0/e \simeq 2.3\times10^6$ T is of the order of the expected theoretical value with a cold fluid approach in the Alfvén limit $B_z = m_e\omega_0\sqrt{2\gamma_\pm n_\pm/n_c}/e \simeq 104m_e\omega_0/e \simeq 1.1\times10^6$ T. The corresponding wavelength at saturation is equal to $\lambda_{\rm W,sat} \simeq 5$ μm close to $\lambda_{\rm W,sat} \simeq 4c/\omega_0\sqrt{2n_c\gamma_{e^\pm}/n_{e^\pm}} \simeq 3.7$ μm.

Fig. 9.8 also exhibits magnetic modulations along the x-direction inside the traveling pair plasmas prior to the collision. These modulations, of $\sim 10^5$ T amplitude can be ascribed to a Weibel instability induced by the anisotropy of the positron $p_x - p_y$ distribution.

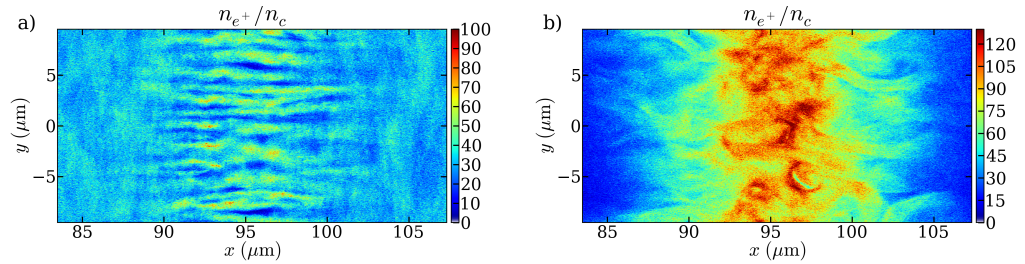

Figure 9.8: Positron density n_{e^+}/n_c during the linear growth of the filaments (a) and during the isotropization (b) at respective time $t = 424$ fs and $t = 476$ fs.

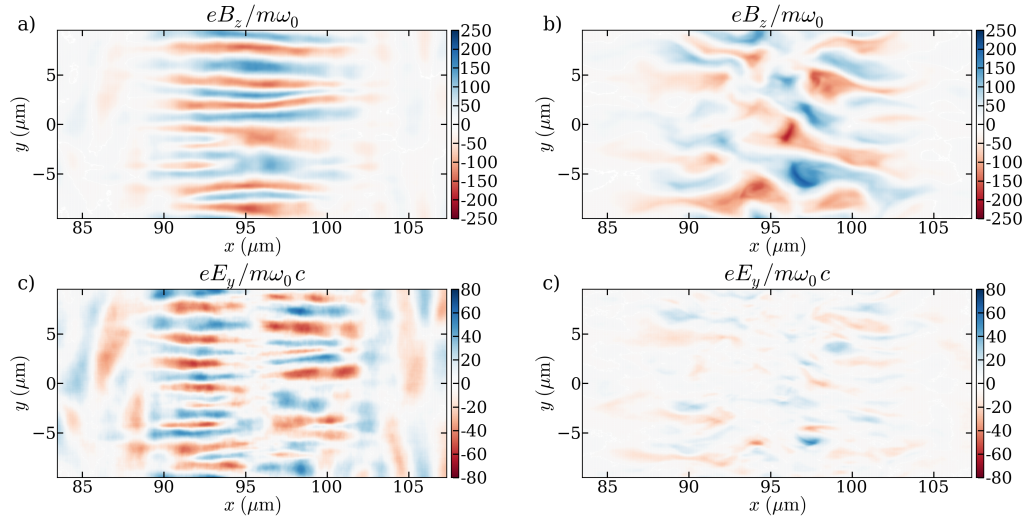

Figure 9.9: Magnetic field B_z (averaged over a laser cycle) in the overlap region (a) at times t = 424 fs at the end of the linear regime and t = 476 fs with the apparition of kink-like oscillations (b). Electric field E_y (averaged over a laser cycle) in the overlap region (c) at times t = 424 fs at the end of the linear regime and t = 476 fs (d).

Evolution of the electron-positron densities

The spatio-temporal evolution of the y-averaged electro-positron density are respectively displayed in Fig. 9.10b and Fig. 9.10c. One can observe the formation of a short-lived dense structure in the overlap region with maximal density around $110n_c$. This density is 2.7 times larger than the maximum density $n_{\max} \sim 36n_c$ of the pair flows, which demonstrates the occurrence of significant izotropization of the interacting jets. The observed compression ratio $R \sim 2.7$ is close to the Rankine-Hugoniot jump condition ($R \sim 3$) of a relativistic strong shock. This compression, however, is not sustained at later times due to the decreasing power flux carried by the jets. The evolution of the ion density is shown in Fig. 9.10a. The ions collide at $t = 570$ fs that is, 180 fs after the time of maximum compression of the pair plasmas. The effects

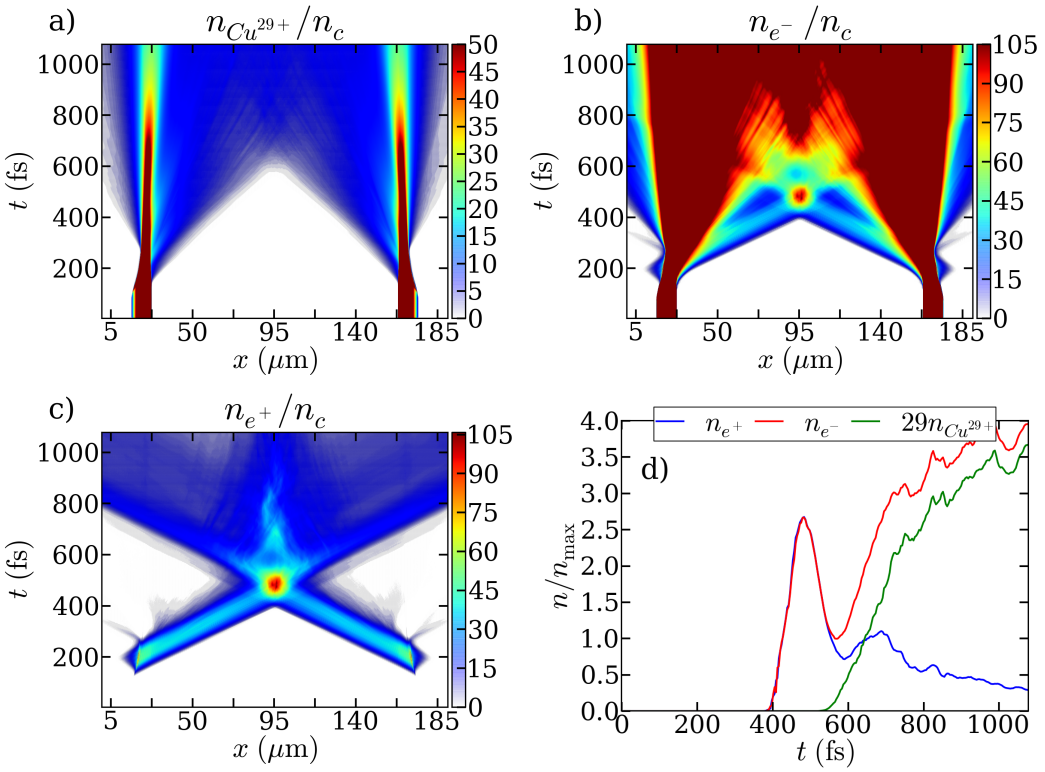

Figure 9.10: Space-time evolution of the y-averaged ion (a), electron (b) and positron density (c). (d) - Evolution of the positron, the electron and the ion density at the center of the overlapping region ($x = 95$ μm) averaged in an interval of 0.06 μm.

induced by the ions penetrating the magnetized pair plasma are described in section 9.4.

9.2.3 Evolution of the field energies and instability growth rate

The time history of the field energies in the overlap region is shown in Fig. 9.11. The magnetic field energy ε_{Bz} at the end of the instability growth is almost an order of magnitude higher than the electric field energies ε_{Ey} and ε_{Ex}. This confirms the essentially magnetic character of the instability. The first phase corresponds to the exponential growth of the magnetic and electric modes. The longitudinal and transverse electric fields, E_x and E_y, are the first to saturate at time 433 fs. The rise of the magnetic field energy stops just after at 446 fs. Fig. 9.9(c,d) shows that the maximal electric field amplitude in the overlap region is of $E_{y,\max} \simeq 64 m_e \omega_0 c/e \simeq 2 \times 10^{14}$ V/m at this time. The maximal value of the magnetic field is reached at 453 fs with a value of $240 \omega_0 m_e/e$ whereas the maximum of the electric field is reached at 433 fs for a value $103 m_e \omega_0 c/e$.

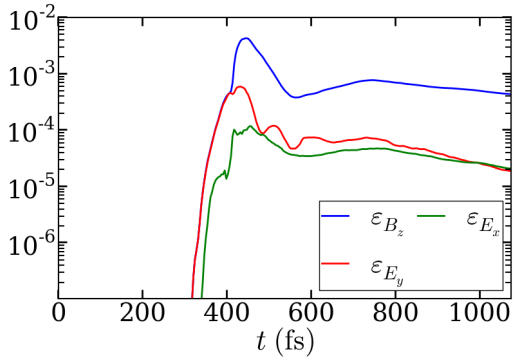

Figure 9.11: Time evolution of the electromagnetic energies ε_{E_x}, ε_{E_y}, ε_{B_z} (normalized to the laser energy) integrated in the overlap region and comparison with the theoretical growth rate (black dashed line)

The growth of the magnetic field is approximately exponential, at a rate of $\Gamma \simeq 0.12\omega_0$ (0.23s^{-1}). This values is close to the cold-fluid filamentation growth rate equal to $\Gamma_{th} \simeq 0.24\omega_0(0.45\ \text{s}^{-1})$ assuming $\gamma_{e^\pm} \sim 300$ and $n_{e^\pm} \sim 18n_c$.

A more accurate cold-fluid formula of the filamentation growth rate can be obtained by allowing for different positron and electron mean energies We consider two neutral plasma beams composed of electrons and positrons, so that $n_{e^+} = n_{e^-} = n_{e^\pm}$, counter-traveling along the x direction with respective energies $\gamma_{e^-} = \nu\gamma_{e^+}$ and γ_{e^+}. The parameter α represents the species so that $\alpha = e^+$ for the positrons and $\alpha = e^-$ for the electrons. The charge, the Lorentz facor, the momentum of the species α corresponds to q_α, γ_α and p_α. The wave-vector is taken along the transvere y axis. The magnetic modulation are directed in the z-direction.

$$p_{\alpha,x} - \frac{e}{c}A_x = p^0_{\alpha,x} \tag{9.1}$$

$$\frac{\partial p_{\alpha,y}}{\partial t} + \frac{p_{\alpha,y}}{m_e\gamma_\alpha}\frac{\partial p_{\alpha,y}}{\partial y} = q_\alpha\left(E_y - \frac{p_{\alpha,x}}{m_e\gamma_\alpha}B_z\right) \tag{9.2}$$

$$\tag{9.3}$$

The continuity equation can be written

$$\frac{\partial n_\alpha}{\partial t} + n_\alpha\frac{\partial}{\partial y}\left(\frac{p_{y,\alpha}}{m_e\gamma_\alpha}\right) = 0 \tag{9.4}$$

The Poisson equation, the Maxwell-Ampere equation and the Maxwell-Faraday equation correspond to

$$\frac{\partial E_y}{\partial y} = \frac{1}{\varepsilon_0}\left(\sum_\alpha q_\alpha n_\alpha\right).\frac{\partial B_z}{\partial y} + \frac{1}{c^2}\frac{\partial E_x}{\partial t} = \mu_0\sum_\alpha\frac{p_{x,\alpha}}{m_e\gamma_\alpha}n_\alpha\frac{\partial B_z}{\partial t} - \frac{\partial E_x}{\partial y} = 0 \tag{9.5}$$

with

$$E_x = -\frac{\partial A_x}{\partial t} \tag{9.6}$$

The linearization of the system gives the following plasma dispersion relation (Pegoraro *et al.* (1996); Gremillet (2001))

$$\left(\omega^2 - \Omega_a^2\right)\left[\omega^4 - \omega^2\left(k_z^2c^2 + \Omega_b^2\right) - k_z^2c^2\Omega_c^2\right] - k_z^2c^2\Omega_d^4 = 0 \tag{9.7}$$

Let $\omega_{e^\pm}$ be the plasma frequency associated to the density $n_{e^\pm}$.

$$\Omega_a^2 = \omega_{e^\pm}^2 \sum_\alpha \frac{n_\alpha}{n_{e^\pm}\gamma_\alpha} = 2\omega_{e^\pm}^2\left(\frac{1}{\gamma_{e^+}} + \frac{1}{\gamma_{e^-}}\right) = \frac{2\omega_\pm^2}{\gamma_{e^+}}\left(\frac{\nu+1}{\nu}\right). \tag{9.8}$$

Similarly we have

$$\Omega_b^2 = \omega_{e^\pm}^2 \sum_\alpha \frac{n_\alpha}{n_{e^\pm}\gamma_\alpha^3} = \frac{2\omega_{e^\pm}^2}{\gamma_{e^+}^3}\left(\frac{\nu^3+1}{\nu^3}\right). \tag{9.9}$$

In the ultra-relativistic limit ($\beta_\alpha \sim 1$), one obtains

$$\Omega_c^2 = \omega_{e^\pm}^2 \sum_\alpha \frac{n_\alpha}{n_{e^\pm}\gamma_\alpha^3} \sim \Omega_a^2 \qquad \Omega_d^2 = \omega_{e^\pm}^2 \sum_\alpha \frac{n_\alpha}{n_{e^\pm}\gamma_\alpha^3} \sim 0 \tag{9.10}$$

The simplified dispersion relation can be solved to obtain the growth rate of the instability Γ_W. It corresponds to the imaginary solution of the 4th order polynomial equation $\omega^4 - \omega^2\left(k_z^2c^2 + \Omega_b^2\right) - k_z^2c^2$ and we obtain

$$\Gamma_W = \sqrt{\frac{k_z^2c^2 + \Omega_b^2 - \sqrt{\left(k_z^2c^2 + \Omega_b^2\right)^2 + 4k_z^2c^2\Omega_a^2}}{2}} \tag{9.11}$$

In the cold fluid approximation, the wave vector at saturation can be evaluated as $k_z \sim \frac{\omega_{e^\pm}}{c}\sqrt{\frac{1}{\gamma_{e^+}}}$ (Bret *et al.* (2013)). For $\gamma_{e^\pm} \gg 1$, we have $\Omega_b^2 \ll k_z^2c^2$ so that

$$\Gamma_{W,\gamma_{e^\pm}\gg 1} = \frac{\omega_\pm}{\sqrt{2\gamma_{e^+}}}\sqrt{1 - \sqrt{1 + 8\frac{\nu+1}{\nu}}} \tag{9.12}$$

Using the average energy measured in the simulation $\langle\gamma_{e^+}\rangle \sim 2\langle\gamma_{e^-}\rangle \sim 600$, we get a growth rate $\Gamma_{th} \sim 0.25\omega_0$. Note that this value is consistent with a more sophisticated calculation based on a multi-waterbag fit of the e^-e^+ momentum distributions (Ruyer *et al.* (2015)).

Such a large growth rate ensures many e-foldings during the collision, and therefore a strong collective interaction between the pair jets.

Isotropization and thermalization

The $p_x - p_y$ phase spaces after the pair plasma collision at time 491 fs at the center of the domain shown in Fig. 9.12a for the electrons and Fig. 9.12b for the positrons, demonstrate that the electron and the positron populations are essentially isotropized. The deceleration experienced by the jet particles can be assessed by com-

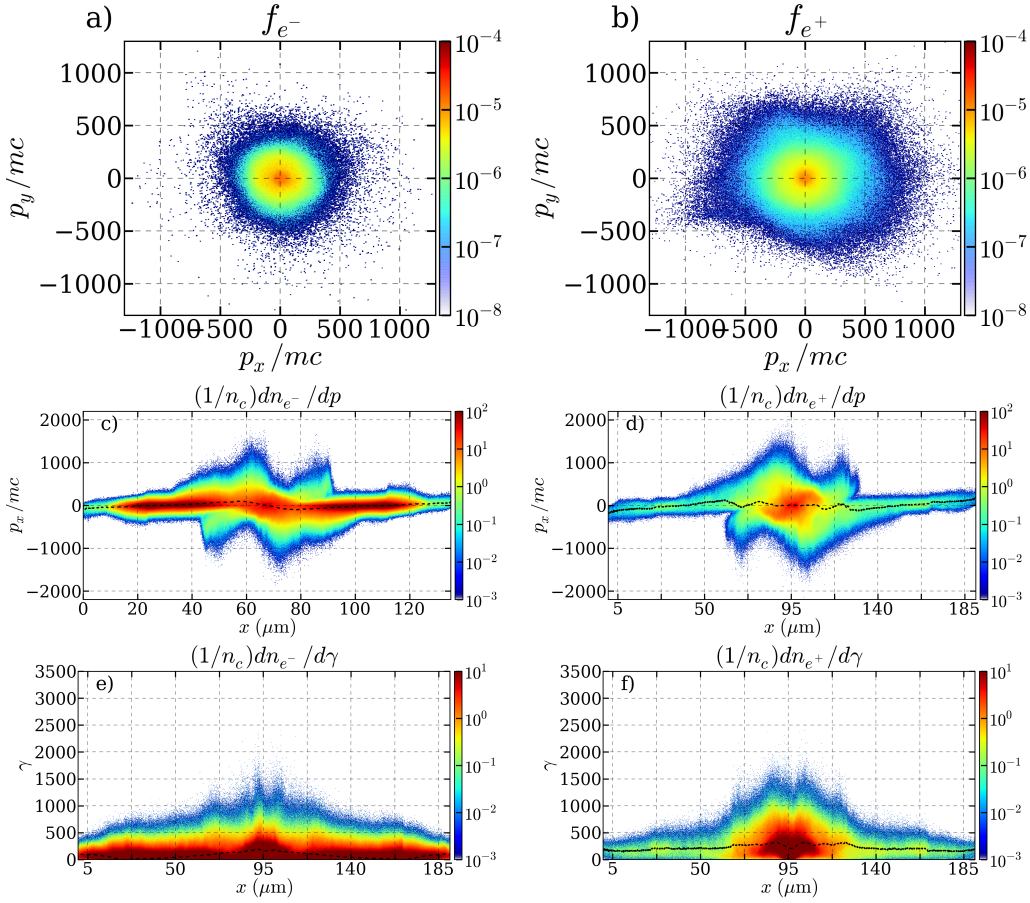

Figure 9.12: Electron (a) and positron (b) $p_x - p_y$ phase space at the end of the plasma collision at time $t = 491$ fs. Electron (c) and positron (d) $x - p_x$ phase space at the similar time $t = 491$ fs.

paring the $x - p_x$ and $x - \gamma$ phase spaces of Fig. 9.12(c-f) with the pre-collision phase spaces of Fig. 9.6(c-f). In the relativistic regime, the density compression in the overlap region mostly results from isotropization of the colliding particles. However, the isotropization is not instantaneous and total as shown by the jets that managed to cross the overlapping region. The particles at the jet head travel across the overlap region without suffering much deflection and deceleration and constitute the precursors of the instability. The space-energy phase spaces $x - \gamma$ for the positrons and the electrons are shown in Fig. 9.12(e-f) and support the previous observation. The

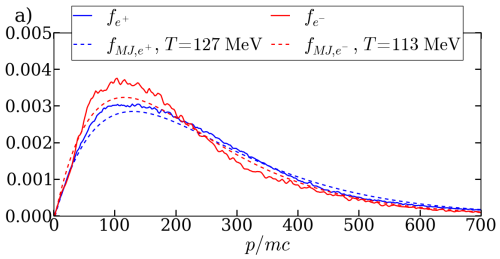

Figure 9.13: Corresponding electron f_{e^-} (red) and positron f_{e^+} (blue) distributions and comparison with the best-fitting Maxwell-Jüttner distributions f_{MJ} (dashed lines)

average energy at the middle of the overlap region is equal to $\langle \varepsilon_{e^+} \rangle \sim 228 m_e c^2$ for the positrons and $\langle \varepsilon_{e^-} \rangle \sim 180 m_e c^2$ for the electrons. These are almost 2 times lower than the incident average energy for both species demonstrating that an important part of the incoming energy has been dissipated.

The corresponding γ-distributions are well reproduced by Maxwell-Jüttner functions $f_{\mathrm{MJ}}(\gamma) \propto \gamma \exp\left(-m_e c^2 \gamma / T\right)$ with electron and positron temperatures $T_{e^-} \simeq$ 113MeV (red curve) and $T_{e^+} \simeq 127$ MeV (blue curve) as shown in Fig. 9.13. This feature shows that isotropization goes along with efficient thermalization that constitute the required conditions for the shock formation. That the inferred temperatures are significantly lower than $\gamma_{e^\pm} m_e c^2/2$ (the value expected for complete thermalization) stems from strong radiative losses during, or shortly after the turbulence buildup.

Radiation cooling in the overlapping region

The radiative behavior of the leptons is evidenced in Fig. 9.14 which display the spatial repartition of the quantum parameter both for the electrons χ_{e^-} and the positrons χ_{e^+} during the linear and saturation (isotropization) phases of the instability. Considering that the electric field E_y and the magnetic field B_z are dominant, the quantum parameter can be written $\chi \sim \gamma \| E_y - c B_z \| / E_s$ where E_s is the Schwinger electric field amplitude. The classical radiated power is related to the quantum parameter as $P = \frac{2}{3} \frac{\alpha_f m_e c^2}{\tau_c} \chi^2$ (see chapter 2). The maximal quantum parameter that can be reached corresponds to $\chi_{\max} \sim \gamma_{e^\pm,\max} B_{z,\mathrm{sat}} c / E_s \sim 1.2$ considering a saturation field $B_{z,sat} \sim 200 m_e \omega_0 / e$ reached at the center of the domain and the maximal particle energy $\gamma_{e^+,\max} \sim 2500$. Nonetheless, the particles undergo significant radiative losses as soon as they move across the magnetic filaments of average magnetic field amplitude of $100 m_e \omega_0 / e$. For an average positron energy of $\langle \gamma_{e^+} \rangle = 600$, the quantum parameter is equal to 0.15 and the radiation takes place in the semi-quantum regime. The evolutions of the radiated energy and power are plotted versus time in Fig. 9.15. The first phase corresponds to the laser-interaction, by the end of which $\sim 76\%$ of the laser energy has been dissipated in γ-rays. The

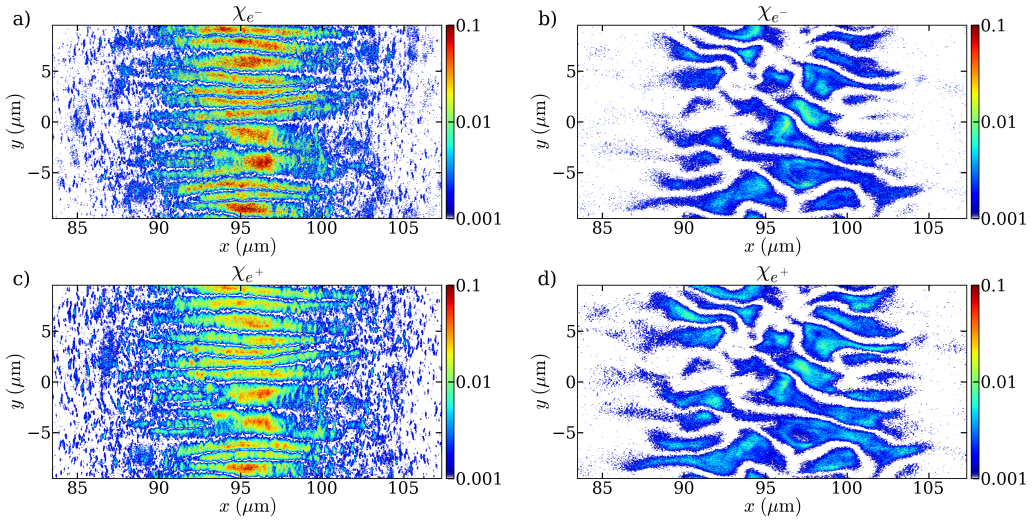

Figure 9.14: Positron χ_{e^+} and electron χ_{e^-} quantum parameter during the linear growth of the instability (a,b) at time $t = 424$ fs and during the isotropization (c,d) at time $t = 476$ fs.

second phase is associated with the pair plasma collision and leads to the dissipation of another 5% of the laser energy. The final weakly-radiating phase corresponds to the late-time interaction, affected by the ion-ion collision.

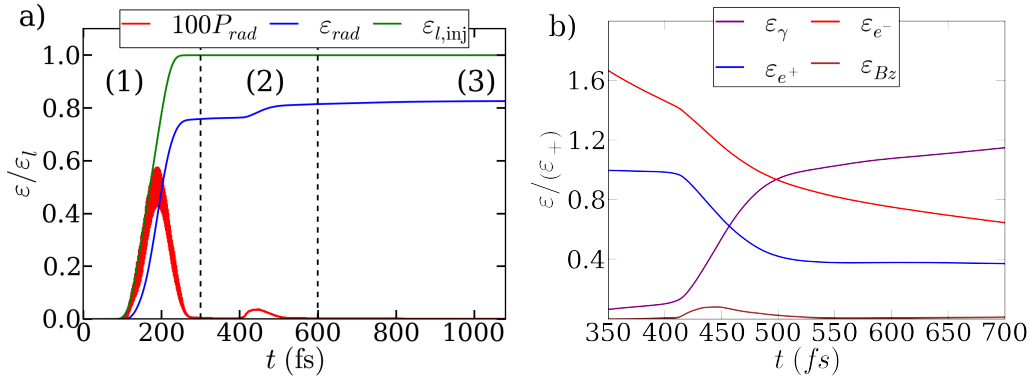

Figure 9.15: (a) - Time evolution of the total radiated energy $\varepsilon_{\mathrm{rad}}$ (blue), the radiated power P_{rad} (red) and the injected laser energy $\varepsilon_{l,\mathrm{inj}}$ (green) normalized to the total laser energy ε_l. (b) - Evolution of the particle ($\varepsilon_{e^\pm}$), photon (ε_γ) and magnetic (ε_{B_z}) energies (normalized to the total kinetic energy) in the collision region.

The overall energy balance of the collision is shown in Fig. 9.15b. The radiated energy during this phase, which is a zoom of Fig. 9.15a, represents nearly 65 % of the incoming particle energy $\varepsilon_{\mathrm{in}} = 1.5\varepsilon_{e^+}$ assuming that on the mean electron energy is half the positron energy. The positron incomiong flow has lost 41 % of its energy.

The magnetic energy amounts to 5% of the particle kinetic energy at $t = 446$ fs.

The beginning of the fast growing phase of the radiated energy between 400 fs and 425 fs is associated to the formation of the linear filaments. The spatial distribution of the quantum parameter for this period is represented in Fig. 9.14a for the electrons and in Fig. 9.14c for the positrons. The quantum parameter is at its highest value during this period. While the filaments remain parallel to the flows, the particles can reach the domain center where the magnetic field is the strongest while keeping most of their incident energy. The quantum parameter is therefore maximal at the center of the domain, where the magnetic field is the strongest, with a value close to $\chi_{e^+,\max} \sim 0.35$ for the positrons and $\chi_{e^-,\max} \sim 0.26$ for the electrons. The quantum parameters averaged along the filaments' length (from 85 μm $< x <$ 105 μm) are measured to be $\langle \chi_{e^+} \rangle \sim 0.0045$ for the positrons and $\langle \chi_{e^-} \rangle \sim 0.0026$.

The isotropization that results from the filament currents' reaching the Alfvén limit and possibly enhanced by kink-like oscillations, settles at $t \sim 440$ fs. Both the maximum and average quantum parameters then start to decrease. However, the maximal radiated power is reached during this period ($436 < t < 446$ fs). Figures 9.14b for the electrons and 9.14d for the positrons show the spatial distribution of the quantum parameter during the isotropization at $t = 476$ fs. Maximum values of $\chi_{e^+,\max} \sim 0.03$ and $\chi_{e^-,\max} \sim 0.021$ are attained in the distorted magnetic filaments as shown in Fig. 9.14b and Fig. 9.14d. On average, the quantum parameter is $\langle \chi_{e^+} \rangle \sim 0.0012$ for the positrons and $\langle \chi_{e^-} \rangle \sim 0.0006$ for the electrons. The maximal quantum parameters have diminished of an order of magnitude while the average value have been divided almost 4 times in comparison with the end of the linear growth.

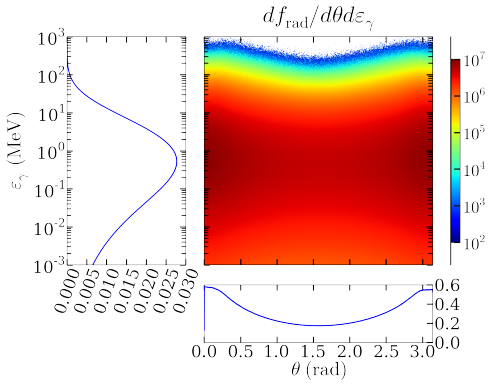

Figure 9.16: Time evolution of the electromagnetic energies ε_{E_x}, ε_{E_y}, ε_{B_z} (normalized to the laser energy) integrated in the overlap region for the pair flow collision with (dashed line) and without (solid line) radiation losses.

The synchrotron angular-energy spectrum at the end of the collision is shown in Fig. 9.16. The angular spectrum is symmetric and peaks at angles $\theta = 0$ and $\theta = \pi$ rad which corresponds to the initial propagation direction of the flows. The emission

at $\theta = \pi/2$ is nonetheless important induced by the radiation of the scattering particles. The synchrotron energy spectrum peaks around 500 keV and extends from a few keV to a few hundreds of MeV. Allowing for radiation losses, the temperatures of the distribution then prove consistent with almost complete thermalization of the jets.

9.2.4 Pair plasma collision without radiation losses

In order to better assess the impact of the radiation losses upon the two-stream interaction, the same simulation has been run with synchrotron emission switched off during the collision from $t = 372$ fs (just before the pair flow collision) to the end.

The development of the instability is first studied. Figure 9.17 compares the time evolutions of the electromagnetic energies in the overlap region with and without radiation losses. The rapid-growth phase appears to be insensitive to radiation effects. The magnetic instability also dominates. Moreover, the filaments produced

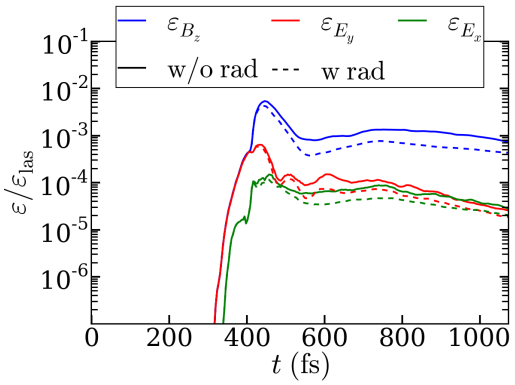

Figure 9.17: Time evolution of the electromagnetic energies ε_{E_x}, ε_{E_y}, ε_{B_z} (normalized to the laser energy) integrated in the overlap region for the pair flow collision with (dashed line) and without (solid line) radiation losses.

in the radiation-free simulation at the end of the linar phase (shown in Fig. 9.18) are similar in shape and amplitude to those generated in the radiative simulation. In the saturation phase, the distorted filaments appear to be significantly wider than with radiation (Fig. 9.9b). After the beam collision, the electromagnetic field evolve similarly.

We now study the space-time evolution of the y-average positron density in the simulation without radiation losses (Fig. 9.19a). The time evolution of the electron and the positron compression rates $n/n_{\max}$ is plotted in Fig. 9.19b with and without radiation losses. It shows that a compressed structure forms in the overlap region but with differences between the radiative and non-radiative cases (Fig. 9.10c). First, the compressed structure reaches a compression rate close to 2.1 without radiation,

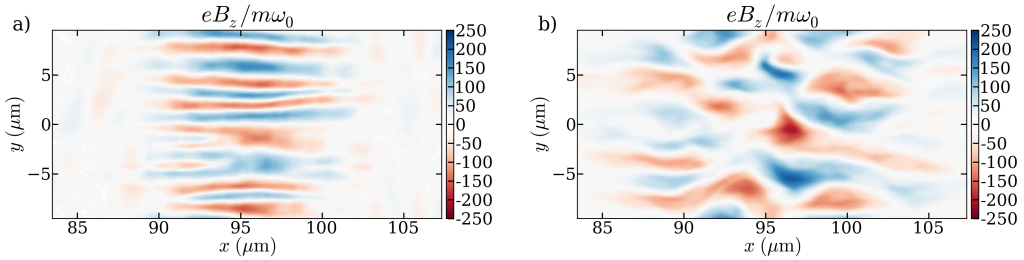

Figure 9.18: Magnetic field B_z (averaged over a laser cycle) in the overlap region (a) at times t = 424 fs at the end of the linear regime and t = 476 fs with the apparition of kink-like oscillations (b) for the pair flow collision without radiation losses.

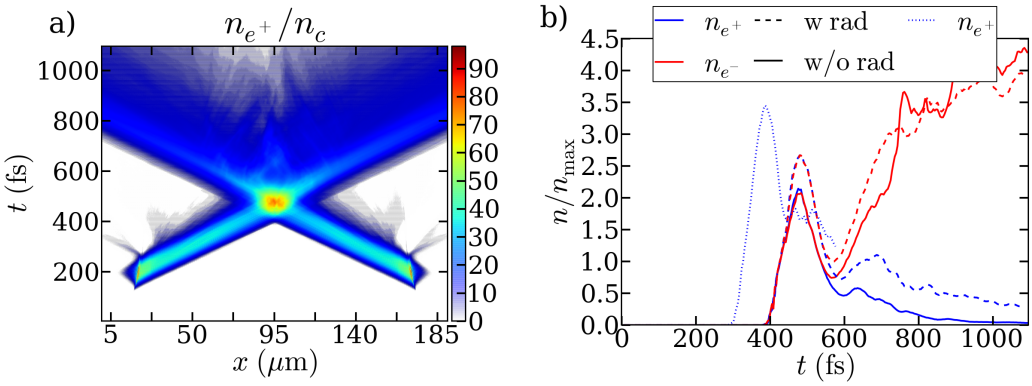

Figure 9.19: (a) - Space-time evolution of the y-averaged positron density. (b) - Evolution of the positron (blue) and the electron (red) compression rate $n/n_{\rm m}$ at the center of the overlapping region ($x = 95$ μm) averaged in an interval of 0.06 μm for the pair flow collision with (dashed line) and without (solid line) radiation losses.

lower than the value of 2.7 obtained with radiation. Second, the compressed non-radiative structure rapidly decays away, in contrast to the radiative case, where a denser compressed structure survives at latter time. It can be observed that more particles manage to escape from the overlap region. This can be explained by their higher energies, which makes them less trappable in the magnetic turbulence. Some of then conserve almost their initial direction of propagation but the magnetic field have nonetheless a visible scattering effect.

In our paper Lobet *et al.* (2015), the difference between the compressed structure with and without radiations is more pronounced. This is particularly true of the late-time evolution of the compressed structure (which was observed to survive over a time $\gtrsim$ 250 fs in the radiative case). This difference mainly comes from the ions arriving earlier in the overlap region. This can be shown by running a simulation where the distance between the two targets is decreased to 85 μm. The interaction leads to the formation of the same pair plasmas (similar size and unperturbed jet density $n_{\max} \sim 36 n_c$) but the ions arrive during the isotropization phase in the

overlap region. The time evolution of the resulting compression factor is plotted in Fig. 9.19b as a dotted line. Clearly, the curves exhibit a higher compression factor ($R \sim 3.4$), at the end of the pair collision and at later times. In fact, the ions contribute to further compress the pair plasma as it will be shown in the following section 9.4.

The fact that the compression is less efficiently maintained at later time without radiation is attributed to varying isotropization and thermalization efficiencies. The electron and positron $p_x - p_y$ phase spaces at the end of the pair plasma collision are shown in Figs. 9.20. The positrons and the electrons, albeit significantly

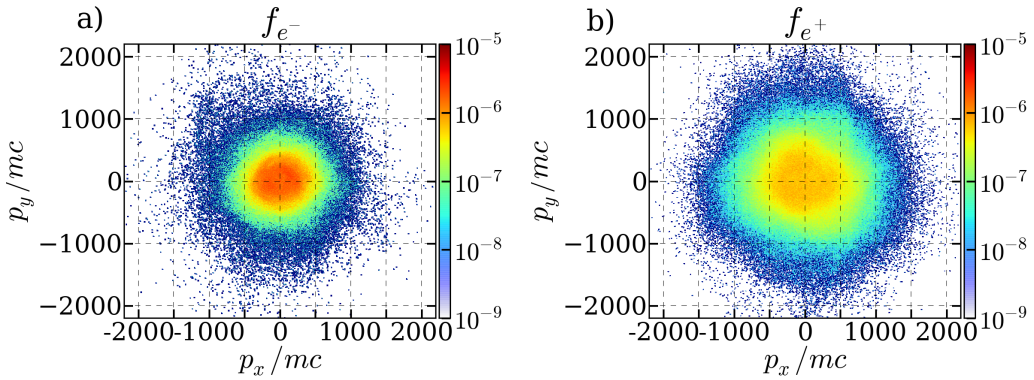

Figure 9.20: Electron (a) and positron (b) $p_x - p_y$ phase spaces at the end of the plasma collision at time $t = 491$ fs for the pair flow collision without radiation losses.

isotropized, are much less thermalized. Their momentum distributions are broader than found in the radiative simulation (Fig. 9.12). The energy distributions shown in Fig. 9.22 significantly deviate from Maxwell-Jüttner distributions, thus proving that thermalization is incomplete.

The space momentum $x-p_x$ phase diagnostics and space-energy $x-\gamma$ phase space shows that the level of isotropization is not sufficient to stop the pair flux. This is clearly seen by comparing the phase spaces of Figs. 9.21 with the pre-collision phase spaces (Figs. 9.6). Contrary to the radiative case, many of the jet head's particles have managed to come out unscathed from the overlap zone. Inside the overlap region, the average energy is equal to $\langle \varepsilon_{e^+} \rangle \sim 572 m_e c^2$ for the positrons and $\langle \varepsilon_{e^-} \rangle \sim 410 m_e c^2$ for the electrons. This is almost two time the value with radiation losses. These values are close to the average energy before the collision.

The Maxwellian fits are hardly possible due to the presence of a plateau for both species at low energies in the space $\gamma - \log\left(f_{e^\pm}(\gamma)/\gamma\right)$ (visible in Fig. 9.20(a,b)) in which the linear regression is performed. The fits in dashed lines presented in Fig. 9.22 have been performed on the linear part. The resulting temperatures are almost twice larger than with radiation effects.

We have just demonstrated that radiative losses play a critical role in enhancing the collective interaction between the counterstreaming jets. By providing an

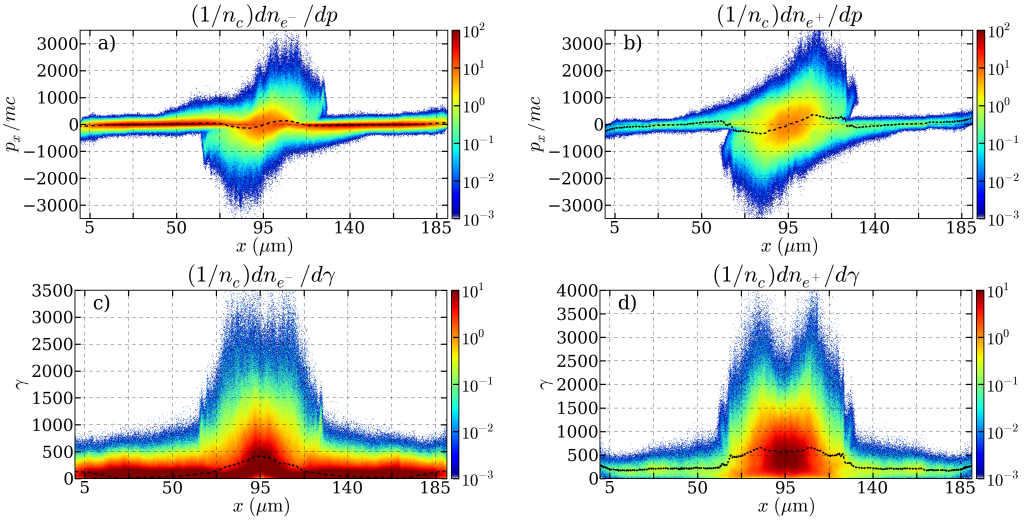

Figure 9.21: Electron (a) and positron (b) $x - p_x$ phase spaces at the time $t = 491$ fs for the pair flow collision without radiation losses. Electron (c) and positron (d) $x - \gamma$ phase space in the similar conditions.

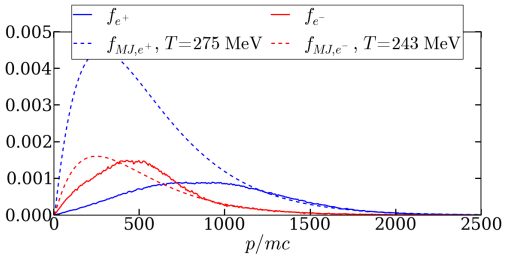

Figure 9.22: Electron f_{e^-} (red) and positron f_{e^+} (blue) distributions and comparison with the best-fitting Maxwell-Jüttner distributions f_{MJ} (dashed lines) for the pair flow collision without radiation losses.

additional dissipation channel, radiation reaction speeds up the scattering of the particles and increases the density and magnetic confinement of the resulting compressed structure.

9.3 Pair plasma collision with Maxwellian flows

In the previous integrated simulations, the interaction time of the pair flows is limited by the laser pulse duration, which proves too short for the formation of fully developed shocks. The heavy computational load of these simulations makes it difficult to consider lasers of much longer duration. Moreover, we expect that the shock generation would be affected by the intrinsically inhomogeneous profiles of the pair jets, which would thus complicate its characterization.

To examine the effects of radiative cooling upon a Weibel-instability-mediated shock, more academic simulations have been performed with two electron-positron pair plasmas injected from the x-boundaries with density $n_{\max} = 50n_c$ and longitudinal momentum $p_x = \pm 500mc$ close to those of the laser-driven plasmas. The 2D simulation box has a longitudinal length of 954 μm ($6000c/\omega_0$) and a transverse width ~ 16 μm ($100c/\omega_0$). As before, we make use of Lehe's Maxwell solver (Lehe *et al.* (2013)) and Friedman's field filtering (Friedman (1990)) to quench Cerenkov effects. The domain has a spatial discretization $dx = dy = 0.0159$ μm ($dx = dy = 0.1c/\omega_0$) and a time step $dt = 0.042$ fs ($dt = 0.08\omega_0^{-1}$). As in the integrated simulations, the boundary conditions are absorbing in x and periodic in y for both the fields and particles.

Each plasma initially occupies half of the simulation box The plasmas are uniform with a linear ramp at their front of ~ 13 μm ($80c/\omega_0$). There are initially composed of 20 particles per cells. The plasmas are Maxwellian with a drift energy of $\gamma_d \sim 500m_ec^2$ and similar temperatures for the electrons and positrons at $T_{e^\pm} \sim 0.1$ keV. A particle injector has been implemented at each boundary to maintain the particle flow despite a finite box size. The injected flow obeys the same Maxwell-Jüttner distribution as that initially contained in the box, which ensures a constant phase space at the boundaries. Two simulations, with and without radiation are run.

The Weibel instability develops rapidly with growth rate $\Gamma \sim 2.67\omega_0 \sim 1.42$ fs^{-1} (estimated from linear regression of the evolution of the magnetic field energy). The cold fluid calculation gives $\Gamma \sim 0.6$ fs^{-1}. The magnetic filaments are clearly discernible after a few femtoseconds in both the radiative and non-radiative simulations, as shown in Fig 9.23.

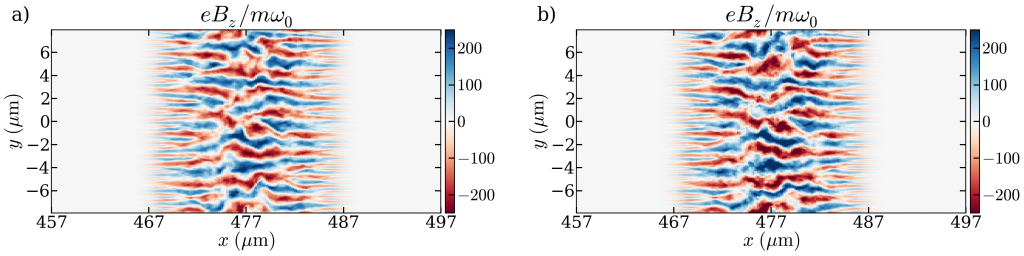

Figure 9.23: Magnetic field B_z in the overlapping region at time 42 fs in the radiative (a) and the non-radiative case (b).

The space-time evolution of the positron density is displayed in Figs. 9.24(a,b). In the non-radiative case (b), the compression ratio in the central region attains the theoretical value associated with a strong relativistic shock ($R = 3$) by ~ 80 fs ($t = 150\omega_0^{-1}$). The shock subsequently propagates at a constant velocity, $v_{sh} \sim 0.45c$ close to the theoretical value of $0.5c$. The extending shocked region presents a uniform density profile. The compression ratio at the center of the overlap region is homogeneous and close to $R = 3$ all along the simulation as shown in the time-

evolution of the y-averaged positron density in Fig. 9.24b and the time-evolution of the compression rate calculated at the center of the domain shown in Fig. 9.25a (red curve without radiation).

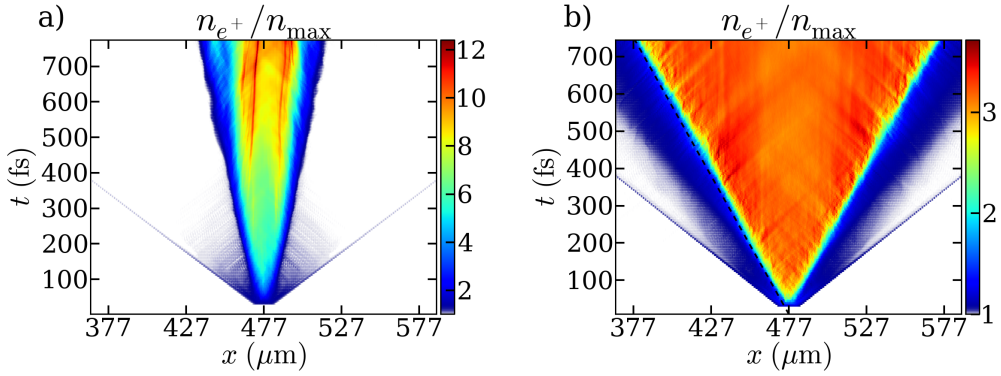

Figure 9.24: Time-evolution of the y-averaged positron density in the radiative (a) and the non radiative case (b). For the non radiative case, the black dashed line corresponds to the linear fitting of the positron of the left shock front giving a velocity close to $v_{sh} \sim 0.45c$.

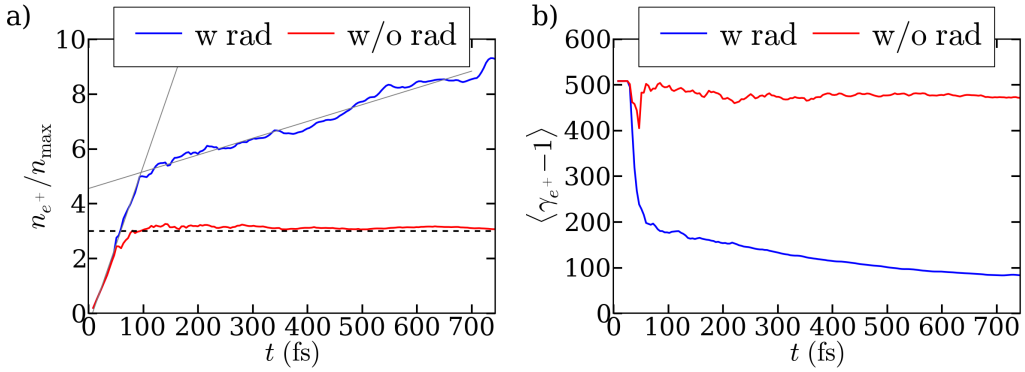

Figure 9.25: (a) - Time-evolution of the positron compression rate $R = n_{e^+}/n_{\max}$ at the center of the domain in the radiative (blue) and the non-radiative case (red). The black dashed line respresents the threshold of $R = 3$. (b) - Time-evolution of the average positron kinetic energy at the center of the domain in the radiative (blue) and the non-radiative case (red).

In the radiative, the compression in the central region attains the non-radiative 2D relativistic shock compression ratio ($R = 3$) sooner than without radiation at $t \sim 58$ fs ($t = 110\omega_0^{-1}$) as shown in Fig. 9.25a. The time-evolution of the y-averaged positron density shown in Fig. 9.24a markedly differs from that obtained without radiation, since it continues to increase. However, contrary to the case

without radiation, the compression rate continue to increase after having reached $R = 3$. At early times, the compression ratio is found to increase linearly at the same rate in both cases. In the non-radiative case, this increase slows down when reaching $R \sim 2.5$ (at $t = 50fs$) and stops when reaching $R = 3$ ($t \sim 100fs$). In the radiative case, the linear increase in R lasts until reaching $R \sim 5$ ($t = 95fs$), at which time starts a slower linear growth phase. At the end of the simulation, the compression rate has reached $R = 9$. As a result of this steady compression, the shock front behaves differently from its non-radiative counterpart Once created, the shock propagates at a velocity close to the theoretical value of $v_{sh} = 0.5c$ but the front velocity slowly diminishes with time to reach $v_{sh} \sim 0.12$ at the end of the simulation. As a consequence of the constant particle flux, the density of the downstream region steadily increases with time, well above the $R = 3$ limit. A simulation run with a lower flow density of $12.5n_c$ yields qualitatively similar results, with a maximum compression ratio of $R = 5.5$ reached at $t = 743$ fs.

The impact of radiation on the y-averaged plasma and field profiles following shock formation is clearly seen by comparing Fig. 9.26a (for the radiative case) and Fig. Fig. 9.26b (for the non radiative one). The $|B_z|$ and $|E_y|$ profiles closely coincide in the filamented region. The transverse electric field thus seems essentially motional ($E_y \sim cB_z$), and therefore should vanish in a frame (i.e., the "proper frame" of the magnetized filaments) moving at a velocity $\sim c$. The longitudinal electric field $|E_x|$, much weaker than the other field components in the filamented region, suddenly rises in a narrow transition layer preceding the downstream region.

The magnetic field modulation are shown in Fig. 9.26c for the radiative case and 9.26d for the non-radiative one. Compared with the early-time magnetic field map of Fig. 9.23(a,b), the filaments have a larger wavelength λ_W, consistent with expected value of $\lambda \simeq 3.2$ μm. The maximum field amplitude of the filaments is near 3.4×10^6 T ($307 m_e \omega_0/e$), close to the expected saturation value in the cold fluid approximation. After undergoing wiggling oscillations in the transition layer, the magnetic filaments in the shocked region evolve into clumps of amplitude ($\sim 1.1 \times 10^5$ T ($10 m_e \omega_0/e$) much weaker than in the precursor region. In the radiative simulation, the coherent character of the filament is destroyed before (near x = 335 μm) into the transition part ($x \in [435, 460]$ μm on the left and $x \in [495, 520]$ μm on the right). The boundary with the isotropization region is composed of strong magnetic clumps as for the non-radiative case. The maximal magnetic field amplitude is lower than for the non-radiative case equal to 3×10^6 T ($275 m_e \omega_0/e$). In the transition layer between the coherent filament region and the isotropized region, the magnetic field is by a factor of 2 lower than in the non-radiative case.

The corresponding behavior of the positrons is shown in Fig. 9.26e for the radiative case and Fig. 9.26f for the non-radiative one. It is observed that the filaments resulting from the pinched incoming positrons in the precursor region are anti-correlated with those formed by the incoming electrons. Moreover, the filaments made of incoming positrons (resp. electrons) are partially screened (in charge) by

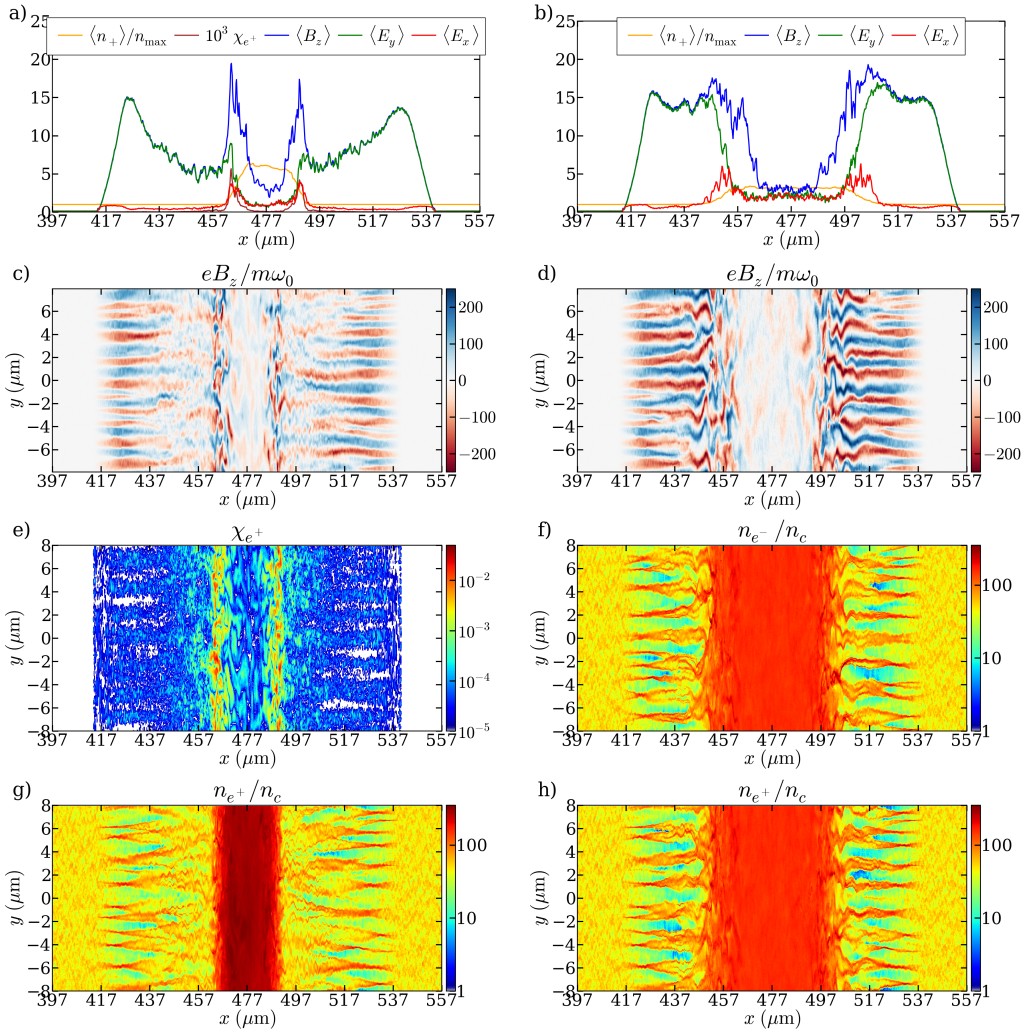

Figure 9.26: y-averaged positron density n_{e^+}, positron quantum parameter χ_{e^+}, magnetic $|B_z|$ and electric fields, $|E_x|$ and $|E_y|$, in the radiative (a) and non-radiative (b) cases. Magnetic field $|B_z|$ with (c) and without (d) radiation losses. (e) - Positron quantum parameter χ_{e^+} for the radiative case. (f) - Electron density showing the filaments and the compressed structure in the non-radiative case. Positron density in the radiative (g) and the non-radiative case (h) in the overlapping region. All of the figures correspond to time $t = 214\,\mathrm{fs}$ ($405\omega_0^{-1}$).

counterstreaming electrons (resp. positrons) originating from the shocked region.

To elucidate how the radiation losses affect the particles, the spatial distribution of the positron quantum parameter χ_{e^+} is shown in Fig. 9.26e. We can see that the strength of χ_{e^+}, and therefore the radiated power, are strongly inhomogeneous. The radiation losses are extremely weak in the region of coherent filaments with a maximal value of $\chi_{e^+} \sim 7 \times 10^{-4}$. The reason is that, as revealed above, the

magnetic force experienced by the particles is compensated for by the electric force due to the motional field ($E_y \sim cB_z$). In the transition layer, the maximal χ_{e^+} value is of 0.005, for an average of 1×10^{-4}. However, the fields are more diffused in this part and the electric field E_y close to the magnetic field B_z still propagating mainly longitudinally with relativistic particles curb the rising of the quantum parameter. In the turbulent region, where the peaks in magnetic field are localized as shown in Fig. 9.26a, the quantum parameter χ_{e^+} is the highest with a maximum value of 0.031 and an average value of 0.0014. Inside the magnetic clumps, the particles are highly deflected. The difference between the electric E_y and the magnetic field B_z amplitude, $c|B_z| \gg |E_y|$, in addition to the peak on the longitudinal electric field E_x, contribute to largely increase the quantum parameter and the radiation losses. Inside the compressed structure ($x \in [471, 484]$ μm), the isotropized particles are still radiating with a maximal quantum parameter of 0.0019 and an average value of 1.2×10^{-4}.

With an initial energy of $500 m_e c^2$ and assuming ballistic propagation, the particles lose a maximum of 5×10^{-4} % of their initial energy in the $\sim 20\,\mu$m-long filamentation region which have an average longitudinal extension of 20 μm. In the first part of the transition region, the radiative losses amount to 2%, whereas in the turbulent transition layer, they dissipate about 20% of the particle energy. In the turbulent region of smallest thickness of 10 μm, with a ballistic propagation, the loss in energy is the maximum with 20 % of the initial one. However, due to magnetic deflections, the particle motion is strongly non-ballistic: there follows an increased transit time of the particles through the turbulence, and thus larger radiative losses. Most of the radiation is therefore emitted across the turbulent layer. Note that pair annihilation and Compton scattering of energetic photons are expected to be negligible on the considered spatio-temporal scales.

The radiated power flux (averaged in the overlap region) is of $\Pi_{\rm rad} \sim 1.7 \times 10^{28}$ MeVs$^{-1}\mu$m^{-2}, i.e., $\sim 1\%$ of the kinetic energy flux. The particle kinetic energy flux is evaluated from the formulae of appendix B for a 2D Maxwellian distribution.

As the plasma cools down, magnetic trapping effects are strengthened, which weakens the turbulence damping. The magnetic layer consequently thickens with time, leading to continuous rising of the radiative losses and an increasingly dense and cold downstream plasma.

The quantum parameter observed in the central region shows that he shock's non-stationarity is accompanied by radiation cooling of the compressed plasma. Fig. 9.25b displaying the time evolution of the average energy in the overlap region confirms this observation. Two phases can be identified, which correspond to those ruling the evolution of the compression ratio (9.25a). The first one lasts until $t = 60$ fs, and leads to the kinetic energy's rapidly decreasing from $\langle \gamma_{e^+} - 1 \rangle = 500$ to 200. The second one corresponds to a slower decreasing phase with the final value $\langle \gamma_{e^+} - 1 \rangle = 80$. The average energy at the center of the overlap region without radiation is also shown in Fig. 9.25b. The difference between the time-evolution

of the average kinetic energy with and without radiations is displayed in the whole domain of interaction in Fig. 9.27. In the coherent filamentation region and the

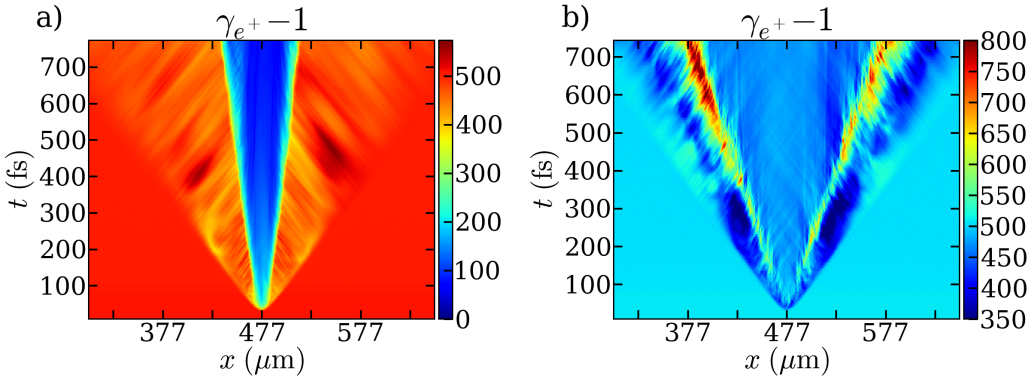

Figure 9.27: Time-evolution of the y-averaged positron kinetic energy $\langle \gamma_{e^+} - 1 \rangle$ in the simulation with radiation (a) and without (b).

first part of the transition region, the kinetic energy remains close to its initial value $\sim 500 m_e c^2$ The average kinetic energy is significantly reduced through the turbulent layer. In the non-radiative case, one observes that the weak particle deceleration ($\gamma - 1 \sim 400$) in the filamentary region is followed by a positive overshoot (up to $\gamma - 1 \sim 800$) through the turbulent layer, which subsequently relaxes to a kinetic energy close to, if slightly lower than its initial value (consistently with the assumptions underlying the Rankine-Hugoniot jump conditions). Inside the turbulent region, the particles gain energy, the average kinetic value can reach a maximum of $900 m_e c^2$. Then, inside the isotropized central region, the average kinetic energy comes back to the average value of the plasma flows. As a consequence, these losses are strong enough to quench the Fermi acceleration process (Medvedev and Spitkovsky (2009)).

The laser-driven setup involves a total laser energy of 6.3×10^5 J, assuming a focal spot $d_l = 19$ μm for each pulse. In a realistic 3D geometry, due to the radial expansion of the particles, the on-axis jet density should weakly decrease up to a distance $x_d \sim d_l / 2\sqrt{2\langle\theta^2\rangle}$ from the target. Further away, it should drop as $n(x) \sim n_{\max} (x_d/x)^2$ due to an increasing transverse size $d(x) \sim 2\sqrt{2\langle\theta^2\rangle} x$ (Debayle *et al.* (2010)). Estimating the effective dispersion angle as the γ-weighted average of the electron-positron values, one obtains $\langle\theta^2\rangle^{1/2} \sim 0.35$ and $x_d \sim 19.2$ μm. The experimental reproduction of our integrated simulation with a similar laser drive would then require a target separation below $2x_d \sim 40$ μm, yet larger than the shock width.

According to the simulations performed with Maxwellian plasmas, the clear observation of a propagating shock would imply an interaction time above 200 fs. This is two to four times larger than the results obtained with our laser parameters. For laser pulses of unchanged field amplitude ($a_0 \sim 800$) and focal spots $\sim 20\,\mu$m (equated to the transverse dimension of the simulation box), the above duration

implies a total laser energy of about 1.3×10^6 J.

9.4 Subsequent collision of the ion flows

In the laser-driven configuration, the electron-psitron energy flux is not sustained long enough to allow the compressed structure to propagate. On the contrary, the positron density starts to decrease for times > 500 fs, along with progressive dilution and weakening of the magnetic blobs. The fast ions penetrate into this decaying magnetized structure at $t \sim 570$ fs. The fastest ions, of momentum $p_x \sim 0.75 m_{Cu} c$, are located at the beam head, while the average ion beam momentum is of $p_x \sim 1.2 m_{Cu} c$. The residual magnetized fluctuations that they encounter are still strong enough to deflect them significantly, as shown by the ion density plots of Figs. 9.28(a,b), recorded at $t = 594$ fs and $t = 802$ fs. The ions therefore undergo strong scattering and pinching as shown in Fig. 9.28a and 9.29a corresponding respectively to the ion density and the magnetic field at time 594 fs. The maximal value of the magnetic is equal to 7.5×10^5 T ($68 m_e \omega_0 / e$). The electromagnetic repulsion caused by the

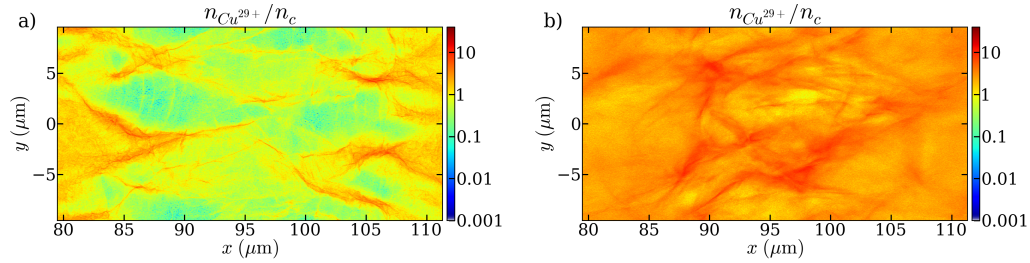

Figure 9.28: Ion density $n_{Cu^{29+}}$ in the overlapping region at $t = 594$ fs (a) and time $t = 802$ fs (b) during the ion collision.

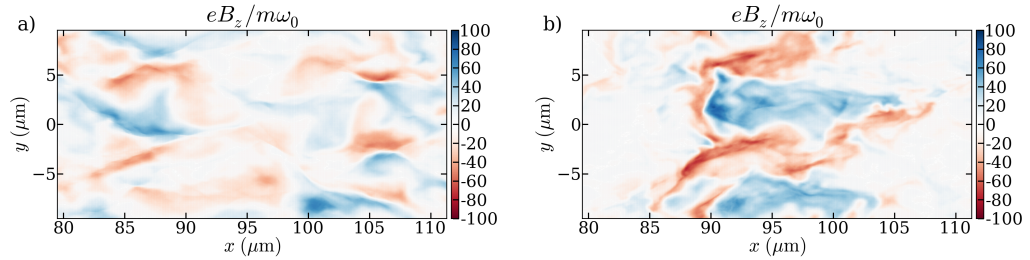

Figure 9.29: Magnetic field B_z in the overlap region $t = 594$ fs (a) and time $t = 802$ fs (b) during the ion collision.

ions arriving at later times leads to a recompression of the dense pair structure, as evidenced in Figs. 9.10(c,d) for $t > 600$ fs. At the center of the overlap region, this recompression can also be observed in Fig. 9.19 with a second grow of the positron

density from time 590 to 690 fs to the maximal value of $R = 1.2$. This goes along with a recompression of the magnetic clumps. Because the electrons are essentially magnetized, this density compression amplifies the magnetic field fluctuations. During the first part of the ion collision, it can be seen that the magnetic energy grows up again from time 550 fs until time 743 fs. The ion density n_{Cu}/n_c and the magnetic field near the second peak in magnetic energies at time 802 fs are respectively shown in Fig. 9.28a and Fig. 9.29b. In Fig. 9.29b, the maximum value of the magnetic field is equal to 9.5×10^5 T ($86 m_e \omega_0 / e$). Despite this high value, the relatively low-energy electrons only gives rise to weak synchrotron emission (phase 3 in Fig. 9.11).

The maximum ion density reached during the collisioon is of $\sim 4.3 n_c$. It is, however, difficult to asses the related compression ratio because of the strongly inhomogeneous (i.e., exponentially decreasing) ion density profiles.

The $p_x - p_y$ ion phase space at the end of the simulation is shown in Fig. 9.30. In the central region, the ion flows are almost isotropized but not thermalized. The distribution forms a ring of radius $|p| = 0.2 m_{Cu} c$, similarly to what occurs in magnetized ion-ion collisions.

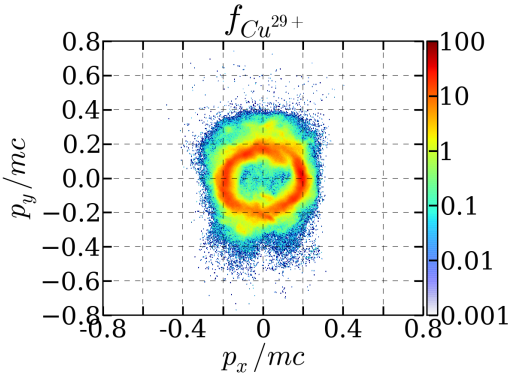

Figure 9.30: $p_x^- p_y$ ion phase space integrated over the overlap region at $t = 1490$ fs.

9.5 Conclusion

In this chapter, we have proposed and studied a visionary concept of electron-positron plasma flow collision. This concept utilizes the significant production of antimatter predicted in future experiments of laser-interaction on thin foil in extreme intensity above 5×10^{23} Wcm^{-2}. The considered laser and target simulation parameters have enabled to demonstrate, in 2D, that the collision of the generated electron-positron pair plasmas leads to the formation a short Weibel instability with formation of density and magnetic filaments as well as the isotropization, the thermalization and the compression of the overlapping jets. The predicted magnetic turbulence of few 10^6 T is extremely intense and sufficient to induce a synchrotron radiation cooling of the

incoming particles. The radiations are not without consequences on the instability development.

The simulations with initial Maxwellian distributions have demonstrated that the particle mainly radiate in the turbulent region marking the boundaries of the compressed region. The radiation losses speed up the mechanism of isotropization and thermalization. The propagation of the shock front is slowed down since the magnetic trapping effect is more efficient. As a consequence, the particles accumulate beyond the theoretical value of 3 times the incoming flow density. The rise of the compression rate has not converge at the end of our simulations despite a slowly decreasing of the shock front velocity. The particle cooling takes place even in the compressed structure. In principle, the growth of the compression rate could continue as far as the flows are maintained. The pair annihilation could be one of the limitation of the process once the compressed structure sufficiently dense and cold.

This scenario differs from the one of H. Chen presented in section 9.1.1. The plasmas generated in Chen *et al.* (2015) are closer to laser-scaling for astrophysical conditions than ours. The performed demonstration simulations in this paper considered two Maxwellian plasmas of drift energy 5 MeV and temperature 0.5 MeV. The particle flux is scaled according to the laser experiments since the pair yield depends on the square of the laser energy in average $\propto \varepsilon_l^2$. In the first case, a laser of 7 kJ, of duration of 10 ps was used, corresponding to an approximated number of pairs of $N = 10^{13}$. The simulation domain has a tansverse length of 2 mm, the final density of the plasmas is 8.3×10^{14} cm^{-3} ($7.6 \times 10^{-7} n_c$). The collisions of such plasmas leads to the formation of linear Weibel filaments as in our simulations. At saturation, the field amplitude is close to 100 T, 4 orders of magnitude below our saturation field. The filaments have a size of around 0.5 μm, which is easier to measure during an experiment with proton-imaging than our extremely tiny filaments of short duration. Another simulation have been performed with energy $\varepsilon_l = 22$ kJ and a duration of 25 ps, giving 10^{14} pairs and a corresponding density of 3×10^{15} cm^{-3}. The increase of the duration enables to study the formation of the compressed structure and the propagation of shock. The filament size has raised to almost 1 mm. In order to reach an intensity between 10^{20} to 10^{21} Wcm^{-2}, the laser should be focused on a focal spot few tens of μm. This is likely to generate a transverse inhomogeneity in the pair flow not taken into account in the simulation. Then, an important divergence have been observed in the experiments not described by the considered distributions. Pair plasma produced via the nonlinear Compton scattering and the nonlinear Breit-Wheeler will hardly accelerated below relativistic energies of $100 m_e c^2$. The intrinsic nature of the processes requires the particles to be highly-relativistic and the laser extremely intense $I > 10^{23}$ Wcm^{-2} ($a_0 = 270$ at 1 μm). With intensities close to 5×10^{23}, simulations show that the generated pair plasmas are underdense but the particles remain highly relativistics $\gamma_{e^\pm} \sim a_0 \sim 600$. As a consequence, the filament size would be larger and the instability growth longer.

In the case of the fireball configuration, as in the case of G. Sarri, our preliminary

simulations of collision between a pair plasma flow created in the same configuration with an exremely-intense laser and an inert hydrogen plasma near the same density have not given expected result with formation of current and magnetic longitudinal filaments. Further studies remain necessary.

Chapter 10

Conclusion and perspectives

This theoretical and numerical work has been motivated by the development of several multi-petawatt laser facilities in the world including Apollon, ELI and Vulcan as well as long-term projects of higher power such as the upgrade of ELI or IZEST. With an energy of the order of 100 Joules and focused on the micrometer scale, these lasers will reach intensities ranging between 10^{22} and 10^{23} Wcm^{-2} on targets. As shown in the literature and chapter 2, the radiation damping, i.e. the continuous emission of high-frequency radiation of a charged particle strongly delfected in the laser field, will start to play a significant role in the electron dynamics from 10^{22} Wcm^{-2}. Close to 10^{23} Wcm^{-2}, the classical radiation emission will turn to the quantum regime (nonlinear Compton scattering) with typical signatures including the strong recoil of the electrons by the photon emission with significant fractions of their kinetic energy and the straggling effect that will lead to the broadening of the energy distribution and scattering effects. Above this intensity, generation of electron-positron pairs from the decay of the γ-photons in the strong laser field is expected via the multiphoton Breit-Wheeler as described in chapter 4. Although the theoretical study of these mechanisms is possible in simplified situations, the complexity of the physics of the laser-plasma interaction in extreme intensity that combine strong-relativistic plasma physics, radiative and quantum electrodynamics effects requires the use of the numerical simulation with powerful numerical tools.

Numerical simulation plays an essential role at different levels. First, it enables the fundamental understanding of the different intertwined mechanisms and how they will modify our knowledge of the interaction at lower intensity. Then, numerical simulations are necessary to design and prepare future experiments. Finally, once the lasers operational, experimentalist will need further numerical explorations in order to understand their experimental results. This natural feedback between the experimental world and the theoretical one will allow us to check the models (for the radiation damping for instance) and the cross sections (for QED). We understand that the upgrade of the current simulation tools has to be anticipated well before the opening of the facilities. This thesis is a part of the worldwide effort toward this

aim.

In the first part, we have analyzed different mechanisms of high-frequency radiation and electron-positron pair generation for their implementation in the PIC code Calder. The radiation damping (classical regime) and the nonlinear Compton scattering (quantum regime) have been studied in the chapter 2 and the Bremsstrahlung emission in chapter 3. The generation of electron-positron pairs in strong laser field has been studied in chapter 4 and the pair generation in matter in chapter 5. The PIC code Calder have been first enriched with the continuous radiation damping based on the Sokolov model. The quantum γ-photon emission (nonlinear Compton Scattering) has been implemented using a Monte-Carlo algorithm. The notion of super-particles has been extended to the super-photons. A similar Monte-Carlo algorithm has been implemented on the photon species for the decay into electron-positron pairs via the nonlinear Breit-Wheeler process. The different implementations with simulations tests have been described in chapter 6. A part of these results have been published in the IFSA 2013 proceedings and is available in Lobet *et al.* (2013). Although the cross sections have been studied for their implementation, the Bremsstrahlung and the Bethe-Heitler have not been added to our code during this thesis but will constitute a base for the future developments.

In chapter 7, some scenarii of laser interaction with thin foils have been simulated. The results are close to those of the literature. For short-pulse lasers, at 10^{22} Wcm^{-2}, 2D PIC simulations forecast a conversion of few % of the laser energy into high-frequency radiations. At 10^{23} Wcm^{-2}, they predict a conversion between 10 % and 20 %. At 10^{24} Wcm^{-2}, it rises to more than 50 %. The radiations ranging from the hard X-rays to the γ-rays with an average energy around the MeV level is mainly forward oriented with an average angle of several tens of radians. Above 5×10^{23} Wcm^{-2}, the electron-positron pair production via the nonlinear Breit-Wheeler becomes significant. At 10^{24} Wcm^{-2}, 2D simulations predict the formation of an overcritical dense pair plasma expanding on the rear side of the target.

In chapter 8, using full-scale 3D PIC simulations, we have demonstrated that soon-to-be-operational, multi-PW, multi-beam lasers will enable all-optical, high-repetition-rate schemes for efficient Breit-Wheeler pair production, which was as yet only accessible to large-scale accelerators. Our scenario, already considered in Thomson scattering experiments, consists on the collision between a multi-GeV electron beam generated by LWFA with a PW-laser and a counter-traveling multi-PW focused laser. Besides providing a fully self-consistent modeling of the problem, our work presents important guidelines for future experiments. Our study thus reveals that the mean positron energy (resp. divergence) is a decreasing (resp. increasing) function of the laser intensity at fixed laser energy. In particular, we find that a high-energy ($\sim 400\,$MeV), low-divergence ($\sim 0.02\,$rad) positron beam of charge $\sim 0.5\,$nC can be achieved using a moderately-intense ($\sim 10^{22}\,$Wcm^{-2}) laser pulse focused to a $\sim 5\,\mu$m spot. Once magnetically segregated from the electrons, this beam could serve as a first acceleration stage for conventional and optical accelerators. Higher

pulse intensities ($\sim 10^{23}\,\mathrm{Wcm}^{-2}$) are required for generating dense ($\sim n_c$), quasi-neutral pair plasmas, at the expense, however, of an increased divergence ($\gtrsim 0.1\,\mathrm{rad}$) and a reduced mean energy ($\sim 100\,\mathrm{MeV}$). These results are available in Lobet *et al.* (2015).

In chapter 9, we have shown that the collective interaction of two pair jets created from solid targets by 60 fs, 120 kJ lasers is able to thermalize a significant part of the bulk jet energy, yet failing to spawn a fully-developed, propagating shock due to too short an interaction time. An important finding is that the synchrotron emission induced in the magnetic turbulence ($> 10^6\,\mathrm{T}$) dissipates $\sim 60\%$ of the kinetic energy in a few tens of fs. These losses speed up the thermalization of the jets, and enhance their magnetic confinement and compression. This novel, laser-specific interaction regime contrasts with the standard scenario of astrophysical pair shocks, where synchrotron emission mainly occurs deep into the downstream region, well after shock formation. Our results indicate that longer-duration, higher-energy ($\sim$ MJ) lasers are required for the creation of fully-formed pair shocks through nonlinear Compton/Breit-Wheeler processes. These results have been published in Lobet *et al.* (2015).

Chapter 11

List of communications

11.1 Publications

11.1.1 First author publications

Lobet, M., Kando, M., Koga, J. K., Esirkepov, T. Z., Nakamura, T., Pirozhkov, A. S., and Bulanov, S. V. (2013). Controlling the generation of high frequency electromagnetic pulses with relativistic flying mirrors using an inhomogeneous plasma. *Physics Letters A*, 377(15), 1114-1118.

Lobet, M., d'Humires, E., Grech, M., Ruyer, C., Davoine, X., and Gremillet, L. (2013). Modeling of radiative and quantum electrodynamics effects in PIC simulations of ultra-relativistic laser-plasma interaction. *arXiv preprint arXiv:1311.1107*, Proceeding of the IFSA conference.

Lobet, M., Ruyer, C., Debayle, A., d'Humiéres, E., Grech, M., Lemoine, M. and Gremillet, L. (2015). Ultra-fast, synchrotron-enhanced thermalization of laser-driven colliding pair plasmas. *Physical Review Letter*.

Lobet, M., Davoine, X., d'Humires, E. and Gremillet, L. (2015). Generation of high-energy electron-positron beams in the collision of a laser-accelerated electron beam and a multi-petawatt laser. *arXiv preprint arXiv:1510.02301*. Sumitted to PRL.

11.1.2 Other publications

Capdessus, R., **Lobet, M.**, d'Humiéres, E. and Tikhonchuk, V. T. (2014). γ-ray generation enhancement by the charge separation field in laser-target interaction in the radiation dominated regime. *Physics of Plasmas (1994-present)*, 21(12), 123120.

Cros, B., Paradkar, B. S., Davoine, X., Chanc, A., Desforges, F. G., Dobosz-Dufrnoy, S., Delerue N., Ju J., Audet T. L., Maynard G., **Lobet M.**, Gremillet L., Mora P., Schwindling J., Delferrire O., Bruni C., Rimbault C., Vinatier T., Di Piazza A., Grech M., Riconda C., Marqus J. R., Beck A., Specka A., Martin Ph., Monot P., Normand

D., Mathieu F., Audebert P., Amiranoff, F. (2014). Laser plasma acceleration of electrons with multi-PW laser beams in the frame of CILEX. *Nuclear Instruments and Methods in Physics Research Section A: Accelerators, Spectrometers, Detectors and Associated Equipment*, 740, 27-33.

Ribeyre, X., **Lobet, M.**, D'Humires, E., Jequier, S., and Tikhonchuk, V. T. (2015). Pair creation in collision of γ-ray beams produced with high intensity lasers. *arXiv preprint arXiv:1504.07868*.

E. dHumires, S. Chen, P. Antici, M. Bailly-Grandvaux, T. Gangolf, **M. Lobet** et al., Longitudinal laser ion acceleration in gas jets: experimental optimization on the Titan laser facility and numerical investigation of the ultra-high intensity limit, *42th EPS Conference proceedings*, P2.154 (2015).

E. dHumires, S. Chen, **M. Lobet** et al., Longitudinal laser ion acceleration in gas jets: experimental optimization on the Titan laser facility and numerical investigation of the ultra-high intensity limit, *Proceedings of SPIE* Vol. 9514, 95140B (2015).

11.2 Conferences, workshops and seminars

11.2.1 Oral presentation

Event and presentation title	Place	Date
IFSA International conference on Inertial Fusion Sciences and Applications - *Radiative and quantum electrodynamics effects in extremely intense laser-matter interaction*	Nara, Japan	September 2013
Forum ILP Lasers et Plasmas - *Radiative and quantum Electrodynamic effects in extremely intense laser-matter interaction*	Orcière, France	February 2014
HEDLA International Conference on High Energy Density Laboratory Astrophysics - *Ultra-fast thermalization of laser-driven relativistic plasma jets: towards the generation of collisionless electron-positron shocks in the laboratory*	Bordeaux, France	May 2014
Workshop on astrophysical shocks - *Weibel instability in laser-driven colliding pair plasma flows*	Bordeaux	May 2014
LULI Seminar - *Weibel instability in laser-driven colliding electron-positron pair plasma flows*	LULI, Palaiseau	July 2014

ECLIM 33rd conference on Laser Interaction with Matter - *Weibel instability in the collision of laser-induced dense relativistic pair plasmas in extreme intensity*	Paris	September 2014
Workshop Astro - *Weibel instability in laser-driven colliding electron-positron pair plasma flows*	UPMC, Paris	October 2014
HIRSCHEGG 35th Internationnal Workshop on High Energy Density physics with intense Ion and laser beams - *Toward Quantum Electrodynamics experiments on forthcoming high-power laser facilities*	Hirschegg, Autria	January 2015
Seminar at the GSI - Application to radiative and Quantum electrodynamics effects in extreme-intensity laser-matter interaction	GSI, Darmstadt	April 2015
NLIGHT - *γ-ray emission and electron-positron pair production in extreme intensity laser-matter interaction*	Dresden, Germany	April 2015
FORUM ILP 2015 - *Application to radiative and Quantum electrodynamics effects in extreme-intensity laser-matter interaction*	Porquerolle, France	June 2015
PhD day of the CEA - *Effets radiatifs et d'électrodynamique quantique en interaction laser-matière à ultra-haute intensité*	Bruyères-le-Châtel	June 2015
Seminar at the NERSC - *Numerical and Computational aspects of the laser-matter interaction in extreme intensity*	Berkeley	August 2015
Seminar at BELLA - *A few applications of the radiative and quantum electrodynamics effects in future extreme-intensity laser-matter experiments*	Berkeley	August 2015
Apollon SAC meeting - *Electron beam-laser collision: Compton scattering and Pair production on Apollon*	LULI, Palaiseau	November 2015

11.2.2 Poster presentation

Event and poster title	Place	Date
UK-France Workshop on PIC for Laser Plasma Interaction - *Controlling the generation of high-frequency electromagnetic pulses with relativistic flying mirrors using an inhomogeneous plasma*	LULI, Palaiseau	November 2012

PhD student day of the CEA	TGCC, Bruyères-le-Châtel	May 2013
Erice International School of Quantum electronics - *Radiative and quantum electrodynamics effects in extremely intense laser-matter interaction*	Erice, Sicile	July 2013
Seminar on plasma modelling and simulation - *Radiative and quantum electrodynamics effects in extremely intense laser-matter interaction*	IMB, Bordeaux	November 2013
PhD student day of Bordeaux - *Radiative and QED effects in extreme laser-matter interaction*	Bordeaux	Mars 2014
CEA visiting comittee on plasma physics and lasers - *Radiative and QED effects in extremely intense laser-matter interaction*	Saclay	June 2014
Ecole d'aquitaine onde et matière, les phénomènes de transport - *Weibel instability in the collision of laser-induced dense relativistic pair plasmas in extreme intensity*	Gradignan	October 2014

Appendices

Appendix A

The laser normalization

Parameters	Normalization	Values at $\lambda = 1\mu$m
Distance	c/ω	0.159 μm
Time	ω^{-1}	0.531 fs
Particle density	$n_c = \dfrac{\varepsilon_0 m_e \omega^2}{e^2}$	1.1×10^{21} cm^{-3}
Mass	m_e	9.1×10^{-31} kg
Speed	c	3×10^{8} ms^{-1}
Momentum	$m_e c$	27.3×10^{-23} kgms^{-1}
Energy	$m_e c^2$	511 keV
Current density	$n_c e c$	4.8×10^{6} Am^{-2}
Potential	$m_e c/e$	1.7×10^{-3}Vsm^{-1}
Electric field	$m_e \omega c/e$	3.2×10^{12}V/m
Magnetic field	$m_e \omega/e$	1.1×10^{4}T, 110MG

Appendix B

Maxwell-Jüttner ditribution

In this section, we remind for the reader the usefull physical values related to the Maxwell-Jüttner distribution in the different dimensions. For the sake of generality, the distributions have a drift velocity β_d in the x direction associated to the Lorentz factor γ_d. In the reference frame isotropic with respect to the distribution, we have $\beta_d = 1$ and $\gamma_d = 0$. The Lorentz transformations for the momentum energy p_x and the Lorentz factor γ correspond to

$$\begin{aligned} p_x &= \gamma_d \left(p'_x + \beta_d \gamma'\right) && \text{(B.1)} \\ dp &= \gamma_d \left(1 + \frac{\beta_d p}{\gamma}\right) dp'_x && \text{(B.2)} \\ \gamma &= \gamma_d \left(\gamma' + \beta_d p'\right) && \text{(B.3)} \\ p_y &= p'_y && \text{(B.4)} \end{aligned}$$

B.0.3 Maxwell-Jüttner 3d

The Maxwell-Jüttner distribution with drift velocity β_d (and γ_d the drift Lorentz factor) in the x direction can be written

$$f = C \exp\left(-\mu \left(\gamma - \beta_d p_x\right)\right) \qquad \text{(B.5)}$$

The normalization factor can be deduced from the following equation.

$$\int_{-\infty}^{+\infty} f dp^3 = 1 \tag{B.6}$$

$$\Leftrightarrow \quad C \int_{-\infty}^{+\infty} \exp\left(-\mu\left(\gamma - \beta_d p_x\right)\right) dp^3 = 1 \tag{B.7}$$

$$\Leftrightarrow \quad 4\pi\gamma_d C \int_0^{+\infty} p'^2 \exp\left(-\mu\frac{\gamma'}{\gamma_d}\right) dp' = 1 \tag{B.8}$$

$$\Leftrightarrow \quad 4\pi\gamma_d C \int_0^{+\infty} \cosh\theta \sinh\theta^2 \exp\left(-\mu\frac{\cosh\theta}{\gamma_d}\right) d\theta = 1 \tag{B.9}$$

$$\Leftrightarrow \quad C = \frac{\mu}{4\pi\gamma_d^2 K_2(\mu/\gamma_d)} \tag{B.10}$$

With no drift velocity $\gamma = 1$, $\beta_d = 0$, we obtain the well-known result $C = \dfrac{\mu}{4\pi K_2(\mu/\gamma_d)}$

The current corresponds to

$$\begin{aligned} J_x &= C \int_{-\infty}^{+\infty} \beta_x f dp^3 && \text{(B.11)}\\ &= C \int_{-\infty}^{+\infty} \frac{p_x}{\gamma} \exp\left(-\mu\left(\gamma - \beta_d p_x\right)\right) dp^3 && \text{(B.12)}\\ &= 4\pi C \gamma_d^2 \beta_d \int_0^{+\infty} p'^2 \exp\left(-\mu\frac{\gamma'}{\gamma_d}\right) dp' && \text{(B.13)}\\ &= \beta_d && \text{(B.14)} \end{aligned}$$

B.0.4 Maxwell-Jüttner 2d

Normalization

$$\int_{-\infty}^{+\infty} f dp^2 = 1 \tag{B.15}$$

$$\Leftrightarrow \quad C \int_{-\infty}^{+\infty} \gamma_d \left(1 + \frac{\beta_d p'_x}{\gamma'}\right) \exp\left(-\mu\left(\gamma - \beta_d p_x\right)\right) dp'^2 = 1 \tag{B.16}$$

$$\Leftrightarrow \quad C \int_{-\infty}^{+\infty} \gamma_d \exp\left(-\mu\frac{\gamma'}{\gamma_d}\right) dp'^2 = 1 \tag{B.17}$$

$$\tag{B.18}$$

Because by symmetry

$$\int_{-\infty}^{+\infty} \left(\frac{\beta_d p'_x}{\gamma'}\right) \exp\left(-\mu\frac{\gamma'}{\gamma_d}\right) dp'^2 = 0 \tag{B.19}$$

So, we have using the integration by substitution $p' = \sinh\theta$, $\gamma' = \cosh\theta$ and $dp' = \cosh\theta d\theta$

$$\int_{-\infty}^{+\infty} f dp^2 = 1 \tag{B.20}$$

$$\Leftrightarrow \quad 2\pi C \int_0^{+\infty} \gamma_d p' \exp\left(-\mu\frac{\gamma'}{\gamma_d}\right) dp' = 1 \tag{B.21}$$

$$\Leftrightarrow \quad 2\pi C \int \gamma_d \sinh\theta \exp\left(-\mu\frac{\cosh\theta}{\gamma_d}\right) \cosh\theta d\theta = 1 \tag{B.22}$$

$$\tag{B.23}$$

So finally, the normalization factor is equal to

$$C = \frac{\exp\frac{\gamma_d}{\mu}}{2\pi\gamma_d\left(\frac{\gamma_d}{\mu} + \frac{\gamma_d^2}{\mu^2}\right)} \tag{B.24}$$

In the boosted frame of the plasma, $\beta_d = 0$ and $\gamma_d = 1$, as a consequence

$$C = \frac{\exp(\mu)}{2\pi}\frac{\mu^2}{\mu+1} \tag{B.25}$$

Current in the x direction

$$J_x = \int_0^{+\infty} f(p) v_x dp^2 \tag{B.26}$$

$$= C\int_0^{+\infty} \frac{p_x}{\gamma} \exp\left(-\mu\left(\gamma - \beta_d p_x\right)\right) dp^2 \tag{B.27}$$

$$= \beta_d \tag{B.28}$$

Energy flux in the x-direction

$$\Sigma_x = \int \gamma\beta_x f dp^2 \tag{B.29}$$

$$= C\int p_x \exp\left(-\mu\left(\gamma - \beta_d p_x\right)\right) dp^2 \tag{B.30}$$

$$= C\int \gamma_d\left(p'_x + \beta_d\gamma'\right)\gamma_d\left(1 + \frac{\beta_d p'_x}{\gamma'}\right)\exp\left(-\mu\frac{\gamma'}{\gamma_d}\right) dp'^2 \tag{B.31}$$

$$= 2\pi\gamma_d^2\beta_d C\int\left(\frac{p'^2}{2\gamma'} + \gamma'\right)\exp\left(-\mu\frac{\gamma'}{\gamma_d}\right) p' dp' \tag{B.32}$$

$$= 2\pi\gamma_d^2\beta_d C\left(A + B\right) \tag{B.33}$$

We have

$$A = \int \gamma' p' \exp\left(-\mu\frac{\gamma'}{\gamma_d}\right) dp' \tag{B.34}$$

$$= \int \cosh^2\theta \sinh\theta \exp\left(-\mu\frac{\cosh\theta}{\gamma_d}\right) d\theta. \tag{B.35}$$

The result of the integral is given in the section B.0.5. Then, we have

$$B = \int \frac{p'^3}{2\gamma'} \exp\left(-\mu\frac{\gamma'}{\gamma_d}\right) dp' \tag{B.36}$$

$$= \frac{1}{2}\int \sinh^3\theta \exp\left(-\mu\frac{\cosh\theta}{\gamma_d}\right) d\theta \tag{B.37}$$

$$= \frac{1}{2}\int \left(\sinh\theta\cosh^2\theta - \sinh\theta\right) \exp\left(-\mu\frac{\cosh\theta}{\gamma_d}\right) d\theta \tag{B.38}$$

$$= \frac{1}{2}(A - D) \tag{B.39}$$

The integration of D can in be found in section B.0.5. Finally, the energy flux can be written

$$\Sigma_x = \int \gamma\beta_x f dp^2 \tag{B.40}$$

$$= 2\pi\gamma_d^2\beta_d C\left(\frac{3}{2}A - \frac{1}{2}D\right) \tag{B.41}$$

Kinetic energy flux in the x-direction

The kinetic energy flux corresponds to

$$\Sigma_{k,x} = \int (\gamma - 1)\beta_x f dp^2 \tag{B.42}$$

$$= \Sigma_x - J_x \tag{B.43}$$

B.0.5 Useful relations

- $$\int_0^{+\infty} \sinh\theta \exp\left(-\mu\frac{\cosh\theta}{\gamma_d}\right) d\theta = \frac{\gamma_d}{\mu}\exp\left(-\frac{\mu}{\gamma_d}\right) \tag{B.44}$$

- $$\int_0^{+\infty} \cosh^2\theta \sinh\theta \exp\left(-\mu\frac{\cosh\theta}{\gamma_d}\right) d\theta \tag{B.45}$$

$$= \left(\frac{\gamma_d}{\mu} + 2\frac{\gamma_d^2}{\mu^2} + 2\frac{\gamma_d^3}{\mu^3}\right)\exp\left(-\frac{\mu}{\gamma_d}\right) \tag{B.46}$$

Bibliography

Abraham M., and A. Föppl (1908), *Theorie der Elektrizität: Bd. Elektromagnetische Theorie der Strahlung*, Theorie der Elektrizität (B. G. Teubner).

Achterberg A., and J. Wiersma (2007), Astronomy and Astrophysics, **475**, 1.

Achterberg A., J. Wiersma, and C. A. Norman (2007), Astronomy and Astrophysics, **475**, 19.

Adam J. C., A. Héron, and G. Laval (2006), Phys. Rev. Lett., **97**, 205006.

Allen M., P. K. Patel, A. Mackinnon, D. Price, S. Wilks, and E. Morse (2004), Physical Review Letters, **93**, 265004.

Amaldi U., and G. Kraft (2005), Reports on progress in physics, **68** (8), 1861.

Amsden A. A. (1969), "The particle-in-cell method for the calculation of the dynamics of compressible fluids," .

Anderson C. D. (1932), Physical Review, **41** (4), 405.

Anderson C. D. (1933), Physical Review, **43** (6), 491.

Andreev A. A., R. Sonobe, S. Kawata, S. Miyazaki, K. Sakai, K. Miyauchi, T. Kikuchi, K. Platonov, and K. Nemoto (2006), Plasma Physics and Controlled Fusion, **48** (11), 1605.

Apollon (2015), "Cilex, centre interdisciplinaire lumière extrême," `http://cilexsaclay.fr`, accessed: 2015-07-04.

Avdonina N., and R. Pratt (1993), Journal of Quantitative Spectroscopy and Radiative Transfer, **50** (4), 349 , ISSN 0022-4073.

Bamber C., S. J. Boege, T. Koffas, T. Kotseroglou, A. C. Melissinos, D. D. Meyerhofer, D. A. Reis, W. Ragg, C. Bula, K. T. McDonald, E. J. Prebys, D. L. Burke, R. C. Field, G. Horton-Smith, J. E. Spencer, D. Walz, S. C. Berridge, W. M. Bugg, K. Shmakov, and A. W. Weidemann (1999), Physical Review D, **60**, 092004.

Barthelmé R. (2005), *Le probleme de conservation de la charge dans le couplage des équations de Vlasov et de Maxwell*, Tech. Rep. (Strabourg 1. Inst. Rech. Math. Appl.).

Bashinov A., A. Gonoskov, A. Kim, G. Mourou, and A. Sergeev (2014), The European Physical Journal Special Topics, **223** (6), 1105.

Bastrakov S., R. Donchenko, A. Gonoskov, E. Efimenko, A. Malyshev, I. Meyerov, and I. Surmin (2012), Journal of Computational Science, **3** (6), 474.

Batani D., C. Joachain, S. Martellucci, and A. Chester (2012), *Atoms, Solids, and Plasmas in Super-Intense Laser Fields* (Springer US) ISBN 9781461513513.

Baton S. D., M. Koenig, J. Fuchs, A. Benuzzi-Mounaix, P. Guillou, B. Loupias, T. Vinci, L. Gremillet, C. Rousseaux, M. Drouin, E. Lefebvre, F. Dorchies, C. Fourment, J. J. Santos, D. Batani, A. Morace, R. Redaelli, M. Nakatsutsumi, R. Kodama, A. Nishida, N. Ozaki, T. Norimatsu, Y. Aglitskiy, S. Atzeni, and A. Schiavi (2008), Physics of Plasmas, **15** (4), 042706.

Bauer D., and P. Mulser (2007), Physics of Plasmas (1994-present), **14** (2), 023301.

Baĭer V. N., and V. S. Fadin (1971), Zhurnal Eksperimentalnoi i Teoreticheskoi Fiziki, **61**, 476.

Becker W. (1991), Laser and Particle Beams, **9**, 603, ISSN 1469-803X.

Beg F. N., A. R. Bell, A. E. Dangor, C. N. Danson, A. P. Fews, M. E. Glinsky, B. A. Hammel, P. Lee, P. A. Norreys, and M. Tatarakis (1997), Physics of Plasmas, **4** (2), 447.

Begelman M. C., R. D. Blandford, and M. J. Rees (1984), Reviews of Modern Physics, **56**, 255.

Bell A. R., and J. G. Kirk (2008), Physical Review Letters, **101**, 200403.

Benedetti C., A. Sgattoni, G. Turchetti, and P. Londrillo (2008), Plasma Science, IEEE Transactions on, **36** (4), 1790.

Bennett K. (2015), *Users Manual for the EPOCH PIC codes*, Tech. Rep. (University Of Warwick).

Bethe H., and W. Heitler (1934), in *Proceedings of the Royal Society of London A: Mathematical, Physical and Engineering Sciences*, Vol. 146 (The Royal Society) pp. 83–112.

Bewilogua L. (1931), Physik Zeitschrift, **32**, 740.

Bhabha H. J. (1935), in *Proceedings of the Royal Society of London A: Mathematical, Physical and Engineering Sciences*, Vol. 152 (The Royal Society) ISSN 0080-4630, pp. 559–586.

Birdsall C., and A. Langdon (2005), *Plasma Physics Via Computer Simulation*, Series in plasma physics (Taylor & Francis) ISBN 9780750310253.

Blackburn T. G. (2015), Plasma Physics and Controlled Fusion, **57** (7), 075012.

Blackburn T. G., C. P. Ridgers, J. G. Kirk, and A. R. Bell (2014), Physical Review Letters, **112**, 015001.

Blandford R., and D. Eichler (1987), Physics Reports, **154** (1), 1 , ISSN 0370-1573.

Blandford R. D., and J. P. Ostriker (1978), Astrophysical Journal, **221**, L29.

Bludman S. A., K. M. Watson, and M. N. Rosenbluth (1960), Physics of Fluids, **3**, 747.

Blue B. E., C. E. Clayton, C. L. O'Connell, F.-J. Decker, M. J. Hogan, C. Huang, R. Iverson, C. Joshi, T. C. Katsouleas, W. Lu, K. A. Marsh, W. B. Mori, P. Muggli, R. Siemann, and D. Walz (2003), Physical Review Letters, **90**, 214801.

Blumenthal G. R., and R. J. Gould (1970), Reviews of Modern Physics, **42**, 237.

Bohm D., and E. P. Gross (1949), Physical Review, **75**, 1851.

Borghesi M., D. H. Campbell, A. Schiavi, M. G. Haines, O. Willi, A. J. MacKinnon, P. Patel, L. A. Gizzi, M. Galimberti, R. J. Clarke, F. Pegoraro, H. Ruhl, and S. Bulanov (2002), Physics of Plasmas, **9** (5), 2214.

Boris J. P. (1970a), Plasma Physics Laboratory.

Boris J. P. (1970b), Proceedings of the 4th Conference on Numerical Simulation of Plasmas, 3.

Borsellino A. (1947), Review of Universidad Nacional de Tucumán, **A6**, 7.

Bouquet S., E. Falize, C. Michaut, C. Gregory, B. Loupias, T. Vinci, and M. Koenig (2010), High Energy Density Physics, **6** (4), 368 , ISSN 1574-1818.

Bowers K. J., B. Albright, L. Yin, B. Bergen, and T. Kwan (2008), Physics of Plasmas (1994-present), **15** (5), 055703.

Brady C. S., C. P. Ridgers, T. D. Arber, and A. R. Bell (2014), Physics of Plasmas, **21** (3), 033108.

Brady C. S., C. P. Ridgers, T. D. Arber, A. R. Bell, and J. G. Kirk (2012), Physical Review Letters, **109** (24), 245006.

Breit G., and J. A. Wheeler (1934), Physical Review, **46**, 1087.

Bret A., L. Gremillet, D. Bénisti, and E. Lefebvre (2008), Physical Review Letters, **100**, 205008.

Bret A., L. Gremillet, and M. E. Dieckmann (2010), Physics of Plasmas, **17** (12), 120501.

Bret A., A. Stockem, F. Fiuza, C. Ruyer, L. Gremillet, R. Narayan, and L. O. Silva (2013), Physics of Plasmas, **20** (4), 042102.

Bret A., A. Stockem, R. Narayan, and L. O. Silva (2014), Physics of Plasmas, **21** (7), 072301, arXiv:1406.4144 .

Brunel F. (1987), Physical Review Letters, **59**, 52.

Bula C., K. T. McDonald, E. J. Prebys, C. Bamber, S. Boege, T. Kotseroglou, A. C. Melissinos, D. D. Meyerhofer, W. Ragg, D. L. Burke, R. C. Field, G. Horton-Smith, A. C. Odian, J. E. Spencer, D. Walz, S. C. Berridge, W. M. Bugg, K. Shmakov, and A. W. Weidemann (1996), Physical Review Letters, **76**, 3116.

Bulanov S., E. Y. Echkina, T. Z. Esirkepov, I. Inovenkov, M. Kando, F. Pegoraro, and G. Korn (2010a), Physical Review Letters, **104** (13), 135003.

Bulanov S., T. Z. Esirkepov, Y. Hayashi, M. Kando, H. Kiriyama, J. Koga, K. Kondo, H. Kotaki, A. Pirozhkov, S. Bulanov, *et al.* (2011a), Nuclear Instruments and Methods in Physics Research Section A: Accelerators, Spectrometers, Detectors and Associated Equipment, **660** (1), 31.

Bulanov S., C. Schroeder, E. Esarey, and W. Leemans (2013), Physical Review A, **87** (6), 062110.

Bulanov S. S., T. Z. Esirkepov, A. G. Thomas, J. K. Koga, and S. V. Bulanov (2010b), Physical Review Letters, **105** (22), 220407.

Bulanov S. V., T. Z. Esirkepov, M. Kando, J. K. Koga, and S. S. Bulanov (2011b), Physical Review E, **84**, 056605.

Bulanov S. V., T. Z. Esirkepov, M. Kando, J. K. Koga, T. Nakamura, S. S. Bulanov, A. G. Zhidkov, Y. Kato, and G. Korn (2013), in *Society of Photo-Optical Instrumentation Engineers (SPIE) Conference Series*, Society of Photo-Optical Instrumentation Engineers (SPIE) Conference Series, Vol. 8780, p. 878015, arXiv:1304.6519 [physics.plasm-ph] .

Bunaciu D., V. Florescu, R. Pratt, and Y. S. Kim (1980), Nuclear Physics A, **339** (2), 329 , ISSN 0375-9474.

Buneman O. (1993), Simulation Techniques and Software, 67.

Burau H., R. Widera, W. Hönig, G. Juckeland, A. Debus, T. Kluge, U. Schramm, T. E. Cowan, R. Sauerbrey, and M. Bussmann (2010), Plasma Science, IEEE Transactions on, **38** (10), 2831.

Burke D. L., R. C. Field, G. Horton-Smith, J. E. Spencer, D. Walz, S. C. Berridge, W. M. Bugg, K. Shmakov, A. W. Weidemann, C. Bula, K. T. McDonald, E. J. Prebys, C. Bamber, S. J. Boege, T. Koffas, T. Kotseroglou, A. C. Melissinos, D. D. Meyerhofer, D. A. Reis, and W. Ragg (1997), Physical Review Letters, **79**, 1626.

Bykov A. M., and R. A. Treumann (2011), Astronomy and Astrophysics Review, **19**, 42.

Cai H.-b., K. Mima, A. Sunahara, T. Johzaki, H. Nagatomo, S.-p. Zhu, and X. T. He (2010), Physics of Plasmas, **17** (2), 023106.

Capdessus R., E. dHumieres, and V. Tikhonchuk (2013), Physical Review Letters, **110** (21), 215003.

Capdessus R., E. d'Humières, and V. T. Tikhonchuk (2012), Physical Review E, **86** (3), 036401.

Capdessus R., M. Lobet, E. d'Humières, and V. Tikhonchuk (2014), Physics of Plasmas (1994-present), **21** (12), 123120.

Capdessus R., and P. McKenna (2015), Physical Review E, **91**, 053105.

CEA-DAM (2015), *LMJ-Petal User Guide*, Tech. Rep. (CEA-DAM).

CERN F. (2009), "LHC the guide," .

Chang P., A. Spitkovsky, and J. Arons (2008), The Astrophysical Journal, **674** (1), 378.

Chapman H. N., A. Barty, M. J. Bogan, S. Boutet, M. Frank, S. P. Hau-Riege, S. Marchesini, B. W. Woods, S. Bajt, W. H. Benner, *et al.* (2006), Nature Physics, **2** (12), 839.

Chen H., F. Fiuza, A. Link, A. Hazi, M. Hill, D. Hoarty, S. James, S. Kerr, D. D. Meyerhofer, J. Myatt, J. Park, Y. Sentoku, and G. J. Williams (2015a), Physical Review Letters, **114**, 215001.

Chen H., A. Link, Y. Sentoku, P. Audebert, F. Fiuza, A. Hazi, R. F. Heeter, M. Hill, L. Hobbs, A. J. Kemp, G. E. Kemp, S. Kerr, D. D. Meyerhofer, J. Myatt, S. R. Nagel, J. Park, R. Tommasini, and G. J. Williams (2015b), Physics of Plasmas, **22** (5), 056705.

Chen H., D. Meyerhofer, S. Wilks, R. Cauble, F. Dollar, K. Falk, G. Gregori, A. Hazi, E. Moses, C. Murphy, J. Myatt, J. Park, J. Seely, R. Shepherd, A. Spitkovsky, C. Stoeckl, C. Szabo, R. Tommasini, C. Zulick, and P. Beiersdorfer (2011), High Energy Density Physics, **7** (4), 225 , ISSN 1574-1818.

Chen H., S. C. Wilks, J. D. Bonlie, E. P. Liang, J. Myatt, D. F. Price, D. D. Meyerhofer, and P. Beiersdorfer (2009), Physical Review Letters, **102** (10), 105001.

Chen H., S. C. Wilks, D. D. Meyerhofer, J. Bonlie, C. D. Chen, S. N. Chen, C. Courtois, L. Elberson, G. Gregori, W. Kruer, O. Landoas, J. Mithen, J. Myatt, C. D. Murphy, P. Nilson, D. Price, M. Schneider, R. Shepherd, C. Stoeckl, M. Tabak, R. Tommasini, and P. Beiersdorfer (2010), Physical Review Letters, **105**, 015003.

Chen S., N. Powers, I. Ghebregziabher, C. Maharjan, C. Liu, G. Golovin, S. Banerjee, J. Zhang, N. Cunningham, A. Moorti, *et al.* (2013), Physical Review Letters, **110** (15), 155003.

Chu Y., X. Liang, L. Yu, Y. Xu, L. Xu, L. Ma, X. Lu, Y. Liu, Y. Leng, R. Li, and Z. Xu (2013), Optics Express, **21** (24), 29231.

Corde S., K. Ta Phuoc, G. Lambert, R. Fitour, V. Malka, A. Rousse, A. Beck, and E. Lefebvre (2013), Reviews of Modern Physics, **85**, 1.

Cowan B. M., D. L. Bruhwiler, J. R. Cary, E. Cormier-Michel, and C. G. Geddes (2013), Physical Review Special Topics-Accelerators and Beams, **16** (4), 041303.

Davidson R. C. (1983), *Basic Plasma Physics: Selected Chapters, Handbook of Plasma Physics, Volume 1*, edited by A. A. Galeev and R. N. Sudan (North-Holland Publishing Company, Amsterdam).

Davidson R. C., D. A. Hammer, I. Haber, and C. E. Wagner (1972), Physics of Fluids, **15** (2), 317.

Davies H., H. A. Bethe, and L. C. Maximon (1954), Physical Review, **93**, 788.

Davis S., V. Tikhonchuk, E. d'Humières, and S. Weber (2010), Journal of Physics: Conference Series, **244** (4), 042006.

Dawson J. M. (1983), Reviews of Modern Physics, **55**, 403.

Debayle A., J. J. Honrubia, E. d'Humières, and V. T. Tikhonchuk (2010), Physical Review E, **82** (3), 036405.

Debayle A., J. Sanz, L. Gremillet, and K. Mima (2013), Physics of Plasmas, **20** (5), 053107.

Deutsch C., A. Bret, M.-C. Firpo, and P. Fromy (2005), Physical Review E, **72**, 026402.

d'Humières E., S. Chen, M. Lobet, M. Sciscio, P. Antici, M. Bailly-Grandvaux, T. Gangolf, G. Revet, J. Santos, A.-M. Schroer, *et al.* (2015), in *SPIE Optics+ Optoelectronics* (International Society for Optics and Photonics) pp. 95140B–95140B.

d'Humières E., E. Lefebvre, L. Gremillet, and V. Malka (2005), Physics of Plasmas (1994-present), **12** (6), 062704.

Di Piazza A., C. Müller, K. Z. Hatsagortsyan, and C. H. Keitel (2012), Reviews of Modern Physics, **84**, 1177.

Dirac P. A. (1928a), in *Proceedings of the Royal Society of London A: Mathematical, Physical and Engineering Sciences*, Vol. 117 (The Royal Society) pp. 610–624.

Dirac P. A. (1928b), in *Proceedings of the Royal Society of London A: Mathematical, Physical and Engineering Sciences*, Vol. 118 (The Royal Society) pp. 351–361.

Dirac P. A. M. (1930), Mathematical Proceedings of the Cambridge Philosophical Society, **26**, 361, ISSN 1469-8064.

Dirac P. A. M. (1938), in *Proceedings of the Royal Society of London A: Mathematical, Physical and Engineering Sciences*, Vol. 167 (The Royal Society) ISSN 0080-4630, pp. 148–169, http://rspa.royalsocietypublishing.org/content/167/929/148.full.pdf .

Domínguez S., R. Mares, and G. Ares de Parga (2006), Revista Mexicana de Física, **52** (002).

Drake R. P., and G. Gregori (2012), The Astrophysical Journal, **749**, 171.

Drouin M. (2009), *Vers la simulation particulaire réaliste de l'interaction laser-plasma surcritique: conception d'un schéma implicite avec amortissement ajustable et fonctions de forme d'ordre élevé*, Ph.D. thesis (École normale supérieure de Cachan-ENS Cachan).

Drury L. O. (1983), Reports on Progress in Physics, **46**, 973.

Duclous R., J. G. Kirk, and A. R. Bell (2011), Plasma Physics and Controlled Fusion, **53** (1), 015009.

ELI (2015), "Eli, extreme light infrastructure," `http://www.eli-beams.eu`, accessed: 2015-07-04.

Elkina N. V., A. M. Fedotov, I. Y. Kostyukov, M. V. Legkov, N. B. Narozhny, E. N. Nerush, and H. Ruhl (2011), Physical Review Accelerators and Beam, **14**, 054401.

Erber T. (1966), Reviews of Modern Physics, **38**, 626.

Esarey E., C. Schroeder, and W. Leemans (2009), Reviews of Modern Physics, **81** (3), 1229.

Esirkepov T. (2001), Computer Physics Communications, **135** (2), 144 , ISSN 0010-4655.

Esirkepov T., M. Borghesi, S. Bulanov, G. Mourou, and T. Tajima (2004), Physical Review Letters, **92** (17), 175003.

Falize ., B. Loupias, A. Ravasio, C. Gregory, A. Dizire, M. Koenig, C. Michaut, C. Cavet, P. Barroso, J.-P. Leidinger, X. Ribeyre, J. Breil, H. Takabe, Y. Sakawa, Y. Kuramitsu, T. Morita, N. Woolsey, W. Nazarov, and S. Pikuz (2011), Astrophysics and Space Science, **336** (1), 81, ISSN 0004-640X.

Fishman G. J., and C. A. Meegan (1995), Annual Review of Astronomy and Astrophysics, **33**, 415.

Fiuza F., R. A. Fonseca, J. Tonge, W. B. Mori, and L. O. Silva (2012), Physical Review Letters, **108**, 235004.

Fochesato C., and D. Bouche (2006), *Evaluation de différents solveurs Maxwell pour la résolution de Maxwell-Vlasov par une méthode PIC*, Tech. Rep. (LRC MESO).

Fonseca R. A., L. O. Silva, F. S. Tsung, V. K. Decyk, W. Lu, C. Ren, W. B. Mori, S. Deng, S. Lee, T. Katsouleas, *et al.* (2002), in *Computational ScienceICCS 2002* (Springer) pp. 342–351.

Fonseca R. A., J. Vieira, F. Fiúza, A. Davidson, F. S. Tsung, W. B. Mori, and L. O. Silva (2013), Plasma Physics and Controlled Fusion, **55** (12), 124011.

Ford G., and R. O'Connell (1991), Physics Letters A, **157** (4), 217 , ISSN 0375-9601.

Ford G., and R. O'Connell (1993), Physics Letters A, **174** (3), 182 , ISSN 0375-9601.

Fox W., G. Fiksel, A. Bhattacharjee, P.-Y. Chang, K. Germaschewski, S. X. Hu, and P. M. Nilson (2013), Physical Review Letters, **111** (22), 225002.

Fried B. D. (1959), Physics of Fluids, **2** (3), 337.

Friedman A. (1990), Journal of Computational Physics, **90** (2), 292.

Fuchs J., P. Antici, E. d'Humières, E. Lefebvre, M. Borghesi, E. Brambrink, C. Cecchetti, T. Toncian, H. Pépin, and P. Audebert (2006), in *Journal de Physique IV (Proceedings)*, Vol. 133 (EDP sciences) pp. 1151–1153.

Gahn C., G. D. Tsakiris, G. Pretzler, K. J. Witte, C. Delfin, C.-G. Wahlstrm, and D. Habs (2000), Applied Physics Letters, **77** (17), 2662.

Gahn C., G. D. Tsakiris, G. Pretzler, K. J. Witte, P. Thirolf, D. Habs, C. Delfin, and C.-G. Wahlstrm (2002), Physics of Plasmas, **9** (3), 987.

Galy J., M. Maučec, D. Hamilton, R. Edwards, and J. Magill (2007), New journal of Physics, **9** (2), 23.

Gary S. P. (1993), *Theory of Space Plasma Microinstabilities* (Cambridge University Press, Cambridge).

Geant4 (2012), *Physics reference manual*, Vol. 9.6.

Gelfer E. G., A. A. Mironov, A. M. Fedotov, V. F. Bashmakov, E. N. Nerush, I. Y. Kostyukov, and N. B. Narozhny (2015), Physical Review A, **92**, 022113.

Germaschewski K., W. Fox, N. Ahmadi, L. Wang, S. Abbott, H. Ruhl, and A. Bhattacharjee (2013), arXiv preprint arXiv:1310.7866.

Ghizzetti A. G. (1947), Review of Universidad Nacional de Tucumán, **A6**, 37.

Glinec Y., G. Genoud, O. Lundh, A. Persson, and C.-G. Wahlstrm (2008), Applied Physics B, **93** (2-3), 317, ISSN 0946-2171.

Gonoskov A. (2013), *Ultra-intense laser-plasma interaction for applied and fundamental physics*, Ph.D. thesis (Ume University, Department of Physics).

Gonoskov A., S. Bastrakov, E. Efimenko, A. Ilderton, M. Marklund, I. Meyerov, A. Muraviev, I. Surmin, and E. Wallin (2014), arXiv preprint arXiv:1412.6426.

Gorbunov L. M., and V. I. Kirsanov (1987), Journal of Experimental and Theoretical Physics, **93**, 509.

Gordienko S., and A. Pukhov (2005), Physics of Plasmas (1994-present), **12** (4), 043109.

Gould R. J., and G. Schréder (1966), Physical Review Letters, **16** (6), 252.

Gould R. J., and G. P. Schréder (1967), Physical Review, **155** (5), 1404.

Green D., and C. Harvey (2014a), arXiv preprint arXiv:1410.4055.

Green D., and C. Harvey (2015), Computer Physics Communications, **192**, 313 , ISSN 0010-4655.

Green D. G., and C. N. Harvey (2014b), Physical Review Letters, **112**, 164801.

Greenwood A., K. Cartwright, E. Baca, and J. Luginsland (2002), in *Antennas and Propagation Society International Symposium, 2002. IEEE*, Vol. 3, pp. 268–271.

Greenwood A. D., K. L. Cartwright, J. W. Luginsland, and E. A. Baca (2004), Journal of Computational Physics, **201** (2), 665 , ISSN 0021-9991.

Gremillet L. (2001), *Etude théorique et expérimentale du transport des électrons rapides dans l'interaction laser-solide à très haut flux*, Ph.D. thesis.

Gremillet L. (2013), "Introduction a l'interaction laser-plasma relativiste," .

Gruzinov A., and E. Waxman (1999), The Astrophysical Journal, **511** (2), 852.

Gryaznykh D., Y. Kandiev, and V. Lykov (1998), Journal of Experimental and Theoretical Physics Letters, **67**, 257.

Harlow F. H., and M. W. Evans (1955), "A machine calculation method for hydrodynamics problems," .

Hartemann F. V., D. J. Gibson, W. J. Brown, A. Rousse, K. T. Phuoc, V. Mallka, J. Faure, and A. Pukhov (2007), Physical Review Accelerators and Beam, **10**, 011301.

Hartin A., S. Porto, and G. Moortgat-Pick (2014), arXiv preprint arXiv:1404.0810.

Harvey C., A. Ilderton, and B. King (2015a), Physical Review A, **91** (1), 013822.

Harvey C., M. Marklund, and E. Wallin (2015b), in *SPIE Optics+ Optoelectronics* (International Society for Optics and Photonics) pp. 950908–950908.

Hatchett S. P., C. G. Brown, T. E. Cowan, E. A. Henry, J. S. Johnson, M. H. Key, J. A. Koch, A. B. Langdon, B. F. Lasinski, R. W. Lee, A. J. Mackinnon, D. M. Pennington, M. D. Perry, T. W. Phillips, M. Roth, T. C. Sangster, M. S. Singh, R. A. Snavely, M. A. Stoyer, S. C. Wilks, and K. Yasuike (2000), Physics of Plasmas, **7** (5), 2076.

Haug E. (1975), Zeitschrift fuer Naturforschung, Teil a, **30**, 1099.

Haug E. (2004), Astronomy & Astrophysics, **416** (2), 437.

Hegelich B. M. (2011), Bulletin of the American Physical Society, **56**, 322.

Hegelich M., S. Karsch, G. Pretzler, D. Habs, K. Witte, W. Guenther, M. Allen, A. Blazevic, J. Fuchs, J. C. Gauthier, M. Geissel, P. Audebert, T. Cowan, and M. Roth (2002), Physical Review Letters, **89**, 085002.

Heinzl T., and A. Ilderton (2009), The European Physical Journal D, **55** (2), 359.

Heisenberg W. (1931), Physik Zeitschrift, **32**, 737.

Heitler W. (1954), *The Quantum Theory of Radiation*, Dover Books on Physics and Chemistry (Dover Publications) ISBN 9780486645582.

Heitler W., and F. Sauter (1933), Nature, **132**, 892.

Henderson A., E. Liang, N. Riley, P. Yepes, G. Dyer, K. Serratto, and P. Shagin (2014), High Energy Density Physics, **12**, 46.

Hockney R. W., and J. W. Eastwood (1988), *Computer simulation using particles* (CRC Press).

Hogan M. J., T. O. Raubenheimer, A. Seryi, P. Muggli, T. Katsouleas, C. Huang, W. Lu, W. An, K. A. Marsh, W. B. Mori, C. E. Clayton, and C. Joshi (2010), New Journal of Physics, **12** (5), 055030.

Hönig W., F. Schmitt, R. Widera, H. Burau, G. Juckeland, M. S. Müller, and M. Bussmann (2010), in *Symposium on Application Accelerators in High-Performance Computing 2012, SAAHC'12, Argonne National Laboratory*, pp. 1–3.

Hubbell J. (2006a), Radiation Physics and Chemistry, **75** (6), 614.

Hubbell J., H. A. Gimm, *et al.* (1980), Journal of physical and chemical reference data, **9** (4), 1023.

Hubbell J., W. J. Veigele, E. Briggs, R. Brown, D. Cromer, and R. Howerton (1975), Journal of physical and chemical reference data, **4** (3), 471.

Hubbell J. H. (2006b), Physics in medicine and biology, **51** (13), R245.

Huntington C. M., F. Fiuza, J. S. Ross, A. B. Zylstra, R. P. Drake, D. H. Froula, G. Gregori, N. L. Kugland, C. C. Kuranz, M. C. Levy, C. K. Li, J. Meinecke, T. Morita, R. Petrasso, C. Plechaty, B. A. Remington, D. D. Ryutov, Y. Sakawa, A. Spitkovsky, H. Takabe, and H.-S. Park (2015), Nat. Phys., **11**, 173.

IZEST (2013), "www.izest.polytechnique.edu/izest-home/," .

Jauch J. M., and F. Rohrlich (1955), *The theory of photons and electrons* (Addison-Wesley).

Ji L., A. Pukhov, I. Y. Kostyukov, B. Shen, and K. Akli (2014a), Physical Review Letters, **112** (14), 145003.

Ji L., A. Pukhov, E. Nerush, I. Y. Kostyukov, K. Akli, and B. Shen (2014b), The European Physical Journal Special Topics, **223** (6), 1069.

Ji L. L., A. Pukhov, E. N. Nerush, I. Y. Kostyukov, B. F. Shen, and K. U. Akli (2014c), Physics of Plasmas (1994-present), **21** (2), 023109.

Jones F., and D. Ellison (1991), Space Science Reviews, **58** (1), 259, ISSN 0038-6308.

Jost R., J. M. Luttinger, and M. Slotnick (1950), Physical Review, **80**, 189.

Jung R., J. Osterholz, K. Löwenbrück, S. Kiselev, G. Pretzler, A. Pukhov, O. Willi, S. Kar, M. Borghesi, W. Nazarov, S. Karsch, R. Clarke, and D. Neely (2005), Physical Review Letters, **94**, 195001.

Juntunen J. S., and T. D. Tsiboukis (2000), Microwave Theory and Techniques, IEEE Transactions on, **48** (4), 582.

Kato T. N. (2005), Physics of Plasmas, **12** (8), 080705.

Kato T. N. (2007), The Astrophysical Journal, **668**, 974.

Kato T. N., and H. Takabe (2008), The Astrophysical Journal Letters, **681** (2), L93.

Kemp A., F. Fiuza, A. Debayle, T. Johzaki, W. Mori, P. Patel, Y. Sentoku, and L. Silva (2014), Nuclear Fusion, **54** (5), 054002.

Keshet U., B. Katz, A. Spitkovsky, and E. Waxman (2009), The Astrophysical Journal Letters, **693**, L127.

Kim H. T., K. H. Pae, H. J. Cha, I. J. Kim, T. J. Yu, J. H. Sung, S. K. Lee, T. M. Jeong, and J. Lee (2013), Physical Review Letters, **111**, 165002.

Kirk J. G., A. R. Bell, and I. Arka (2009), Plasma Physics and Controlled Fusion, **51** (8), 085008.

Kirk J. G., A. R. Bell, and C. P. Ridgers (2013), Plasma Physics and Controlled Fusion, **55** (9), 095016.

Kiselev S., A. Pukhov, and I. Kostyukov (2004), Physical Review Letters, **93**, 135004.

Kluge T., C. Gutt, L. G. Huang, J. Metzkes, U. Schramm, M. Bussmann, and T. E. Cowan (2014), Physics of Plasmas, **21** (3), 033110.

Kmetec J. D., C. L. Gordon, J. J. Macklin, B. E. Lemoff, G. S. Brown, and S. E. Harris (1992), Physical Review Letters, **68**, 1527.

Koch H. W., and J. W. Motz (1959), Reviews of Modern Physics, **31**, 920.

Korzhimanov A. V., A. A. Gonoskov, E. A. Khazanov, and A. M. Sergeev (2011), Physics-Uspekhi, **54** (1), 9.

Krajewska K., and J. Z. Kamiński (2012a), Physical Review A, **86**, 052104.

Krajewska K., and J. Z. Kamiński (2012b), Physical Review A, **85**, 062102.

Krausz F., and M. Ivanov (2009), Reviews of Modern Physics, **81**, 163.

Kuramitsu Y., Y. Sakawa, T. Morita, C. D. Gregory, J. N. Waugh, S. Dono, H. Aoki, H. Tanji, M. Koenig, N. Woolsey, and H. Takabe (2011), Physical Review Letters, **106**, 175002.

Lamoureux M., and N. Avdonina (1997), Physical Review E, **55**, 912.

Landau L., and E. M. Lifshitz (2012), *Physique théorique - Electrodynamique quantique* (Ellipses).

Landau L. D., and E. M. Lifshitz (1975), *The classical theory of fields*, Vol. 2 (Butterworth-Heinemann).

Lebedev V., and V. Shiltsev (2014), *Accelerator Physics at the Tevatron Collider*, Particle Acceleration and Detection (Springer New York) ISBN 9781493908851.

Lee C. M., L. Kissel, R. H. Pratt, and H. K. Tseng (1976), Physical Review A, **13**, 1714.

Leemans W., R. Duarte, E. Esarey, S. Fournier, C. Geddes, D. Lockhart, C. Schroeder, C. Toth, J. Vay, S. Zimmermann, *et al.* (2010), in *AIP Conference Proceedings*, Vol. 1299, p. 3.

Leemans W. P., A. J. Gonsalves, H.-S. Mao, K. Nakamura, C. Benedetti, C. B. Schroeder, C. Tóth, J. Daniels, D. E. Mittelberger, S. S. Bulanov, J.-L. Vay, C. G. R. Geddes, and E. Esarey (2014), Physical Review Letters, **113**, 245002.

Lefebvre E., N. Cochet, S. Fritzler, V. Malka, M.-M. Alonard, J.-F. Chemin, S. Darbon, L. Disdier, J. Faure, A. Fedotoff, O. Landoas, G. Malka, V. Mot, P. Morel, M. R. L. Gloahec, A. Rouyer, C. Rubbelynck, V. Tikhonchuk, R. Wrobel, P. Audebert, and C. Rousseaux (2003), Nuclear Fusion, **43** (7), 629.

Lehe R., A. Lifschitz, C. Thaury, V. Malka, and X. Davoine (2013), Physical Review Accelerators and Beam, **16**, 021301.

Lemoine M., and G. Pelletier (2011), Monthly Notices of the Royal Astronomical Society, **417**, 1148.

Lemoine M., G. Pelletier, and B. Revenu (2006), The Astrophysical Journal Letters, **645**, L129.

Liang E. (2013), High Energy Density Physics, **9** (3), 425 , ISSN 1574-1818.

Lifschitz A., X. Davoine, E. Lefebvre, J. Faure, C. Rechatin, and V. Malka (2009), Journal of Computational Physics, **228** (5), 1803 , ISSN 0021-9991.

Liu B., H. Wang, D. Wu, J. Liu, C. Chen, X. Yan, and X. He (2013), arXiv preprint arXiv:1310.6164.

Lobet M., X. Davoine, E. d'Humières, and L. Gremillet (2015a), arXiv preprint arXiv:1510.02301.

Lobet M., E. d'Humières, M. Grech, C. Ruyer, X. Davoine, and L. Gremillet (2013), arXiv preprint arXiv:1311.1107.

Lobet M., C. Ruyer, A. Debayle, E. d'Humières, M. Grech, M. Lemoine, and L. Gremillet (2015b), Physical Review Letters, **115**, 215003.

Lorentz A. (1909), *The Theory of Electrons* (B. G. Teubner).

Lu W., M. Tzoufras, C. Joshi, F. S. Tsung, W. B. Mori, J. Vieira, R. A. Fonseca, and L. O. Silva (2007), Physical Review Accelerators and Beam, **10**, 061301.

Luo W., Y.-B. Zhu, H.-B. Zhuo, Y.-Y. Ma, Y.-M. Song, Z.-C. Zhu, X.-D. Wang, X.-H. Li, I. C. E. Turcu, and M. Chen (2015), Physics of Plasmas, **22** (6), 063112.

Luu P. T., T. Tückmantel, and A. Pukhov (2015), arXiv preprint arXiv:1504.00636.

Ma C., and T. Lomax (2012), *Proton and Carbon Ion Therapy*, Imaging in medical diagnosis and therapy (Taylor & Francis) ISBN 9781439816073.

Macchi A., M. Borghesi, and M. Passoni (2013), Reviews of Modern Physics, **85**, 751.

Macchi A., F. Cattani, T. V. Liseykina, and F. Cornolti (2005), Physical Review Letters, **94**, 165003.

Mackenroth F., and A. Di Piazza (2011), Physical Review A, **83**, 032106.

MacPhee A. G., L. Divol, A. J. Kemp, K. U. Akli, F. N. Beg, C. D. Chen, H. Chen, D. S. Hey, R. J. Fedosejevs, R. R. Freeman, M. Henesian, M. H. Key, S. Le Pape, A. Link, T. Ma, A. J. Mackinnon, V. M. Ovchinnikov, P. K. Patel, T. W. Phillips, R. B. Stephens, M. Tabak, R. Town, Y. Y. Tsui, L. D. Van Woerkom, M. S. Wei, and S. C. Wilks (2010), Physical Review Letters, **104**, 055002.

Madau P., and C. Thompson (2000), The Astrophysical Journal, **534** (1), 239.

Maiman T. H. (1960), Nature, **187**, 493.

Maine P., and G. Mourou (1988), Optics Letters, **13** (6), 467.

Maine P., D. Strickland, P. Bado, M. Pessot, and G. Mourou (1988), Quantum electronics, IEEE Journal of, **24** (2), 398.

Malka V., J. Faure, Y. A. Gauduel, E. Lefebvre, A. Rousse, and K. T. Phuoc (2008), Nature Physics, **4** (6), 447.

Malkov M. A., and L. O'C Drury (2001), Reports on Progress in Physics, **64**, 429.

Martins S. F., R. A. Fonseca, L. O. Silva, and W. B. Mori (2009), The Astrophysical Journal Letters, **695**, 189.

May J., J. Tonge, F. Fiuza, R. Fonseca, L. Silva, C. Ren, and W. Mori (2011), Physical Review E, **84** (2), 025401.

McKenna P., D. Carroll, O. Lundh, F. Nürnberg, K. Markey, S. Bandyopadhyay, D. Batani, R. Evans, R. Jafer, S. Kar, *et al.* (2008), Laser and Particle Beams, **26** (04), 591.

McNeil B. W., and N. R. Thompson (2010), Nature photonics, **4** (12), 814.

Medvedev M. V., and A. Loeb (1999), The Astrophysical Journal Letters, **526**, 697.

Medvedev M. V., and A. Spitkovsky (2009), The Astrophysical Journal, **700**, 956.

Medvedev M. V., and O. V. Zakutnyaya (2009), The Astrophysical Journal, **696** (2), 2269.

Mironov A., N. Narozhny, and A. Fedotov (2014), Physics Letters A, **378** (44), 3254.

Mo T. C., and C. H. Papas (1971), Physical Review D, **4**, 3566.

Moliere G. (1947), Zeitschrift für Naturforschung A, **2** (3), 133.

Mondal S., V. Narayanan, W. J. Ding, A. D. Lad, B. Hao, S. Ahmad, W. M. Wang, Z. M. Sheng, S. Sengupta, P. Kaw, A. Das, and G. R. Kumar (2012), Proceedings of the National Academy of Sciences, **109** (21), 8011, http://www.pnas.org/content/109/21/8011.full.pdf .

Mora P. (2003), Physical Review Letters, **90**, 185002.

Mora P. (2005), Physical Review E, **72**, 056401.

More R. (1985), Advances in Atomic and Molecular Physics, **21**, 305 , ISSN 0065-2199.

Mork K. (1967), Physical Review, **160** (5), 1065.

Motz J., H. A. Olsen, and H. Koch (1969), Reviews of Modern Physics, **41** (4), 581.

Mourou G., N. Fisch, V. Malkin, Z. Toroker, E. Khazanov, A. Sergeev, T. Tajima, and B. L. Garrec (2012), Optics Communications, **285** (5), 720 , ISSN 0030-4018.

Mourou G., and T. Tajima (2014), The European Physical Journal Special Topics, **223** (6), 979, ISSN 1951-6355.

Mourou G. A., T. Tajima, and S. V. Bulanov (2006), Reviews of Modern Physics, **78** (2), 309.

Muggli P., S. F. Martins, J. Vieira, and L. O. Silva (2013), ArXiv e-prints, arXiv:1306.4380 [physics.plasm-ph] .

Mulser P., H. Ruhl, and J. Steinmetz (2001), Laser and Particle Beams, **19** (01), 23.

Murota T., A. Ueda, and H. Tanaka (1956), Progress of Theoretical Physics, **16** (5), 482, http://ptp.oxfordjournals.org/content/16/5/482.full.pdf+html .

Myatt J., J. A. Delettrez, A. V. Maximov, D. D. Meyerhofer, R. W. Short, C. Stoeckl, and M. Storm (2009), Physical Review E, **79**, 066409.

Nakamura T., and T. Hayakawa (2015), Laser and Particle Beams, **33** (02), 151.

Nakamura T., J. K. Koga, T. Z. Esirkepov, M. Kando, G. Korn, and S. V. Bulanov (2012), Physical Review Letters, **108**, 195001.

Nakashima H. (2015), Computers & Electrical Engineering.

Nardi E., Y. Maron, and D. Hoffmann (2007), Laser and Particle Beams, **25** (03), 489.

Nardi E., and Z. Zinamon (1978), Physical Review A, **18** (3), 1246.

Narozhny N., S. Bulanov, V. Mur, and V. Popov (2004), Journal of Experimental and Theoretical Physics Letters, **80** (6), 382.

Narozhny N., and A. Fedotov (2014), The European Physical Journal Special Topics, **223** (6), 1083, ISSN 1951-6355.

Narozhny N. B., and A. M. Fedotov (2014), The European Physical Journal Special Topics, **223**, 1083, arXiv:1312.4705 [physics.plasm-ph] .

Naumova N., T. Schlegel, V. Tikhonchuk, C. Labaune, I. Sokolov, and G. Mourou (2009a), The European Physical Journal D, **55** (2), 393.

Naumova N., T. Schlegel, V. T. Tikhonchuk, C. Labaune, I. V. Sokolov, and G. Mourou (2009b), Physical Review Letters, **102**, 025002.

Naumova N. M., J. A. Nees, and G. A. Mourou (2005), Physics of Plasmas, **12** (5), 056707.

Neitz N., and A. Di Piazza (2013a), Physical Review Letters, **111** (5), 054802.

Neitz N., and A. Di Piazza (2013b), Physical Review Letters, **111**, 054802.

Neitz N., and A. Di Piazza (2013), ArXiv e-prints, arXiv:1301.5524 [physics.plasm-ph] .

Nelson W. R., H. Hirayama, and D. W. Rogers (1985), *EGS4 code system*.

Nerush E., and I. Y. Kostyukov (2015), Plasma Physics and Controlled Fusion, **57** (3), 035007.

Nerush E. N., I. Y. Kostyukov, A. M. Fedotov, N. B. Narozhny, N. V. Elkina, and H. Ruhl (2011), Physical Review Letters, **106**, 035001.

Nieter C., and J. R. Cary (2004), Journal of Computational Physics, **196** (2), 448.

NIF (2015), *National Ignition Facility User Guide*, Tech. Rep. (LLNL).

Nikishov A. I. (1964), Journal of Experimental and Theoretical Physics, **14**, 549.

Nikishov A. I., and V. I. Ritus (1964), Journal of Experimental and Theoretical Physics, **19**, 529.

Nikishov A. I., and V. I. Ritus (1967), Journal of Experimental and Theoretical Physics, **25**, 1135.

Nishikawa K.-I., J. Niemiec, P. E. Hardee, M. Medvedev, H. Sol, Y. Mizuno, B. Zhang, M. Pohl, M. Oka, and D. H. Hartmann (2009), The Astrophysical Journal Letters, **698**, L10.

Nishina Y., and S. Tomonaga (1933), Proceedings of the Physico-Mathematical Society of Japan, **15**, 248.

Nunes M. (2015), *Protontherapy Versus Carbon Ion Therapy: Advantages, Disadvantages and Similarities*, Biological and Medical Physics, Biomedical Engineering (Springer International Publishing) ISBN 9783319189833.

Okada T., and K. Ogawa (2007), Physics of Plasmas, **14** (7), 072702.

Oppenheimer J. R., and M. S. Plesset (1933), Physical Review, **44** (1), 53.

Park H.-S., D. D. Ryutov, J. S. Ross, N. L. Kugland, S. H. Glenzer, C. Plechaty, S. M. Pollaine, B. A. Remington, A. Spitkovsky, L. Gargate, G. Gregori, A. Bell, C. Murphy, Y. Sakawa, Y. Kuramitsu, T. Morita, H. Takabe, D. H. Froula, G. Fiksel, F. Miniati, M. Koenig, A. Ravasio, A. Pelka, E. Liang, N. Woolsey, C. C. Kuranz, R. P. Drake, and M. J. Grosskopf (2012), High Energy Density Physics, **8**, 38.

Paschotta R. (2008), *Encyclopedia of laser physics and technology*, Vol. 1 (Wiley-vch Berlin).

Pegoraro F., S. Bulanov, F. Califano, and M. Lontano (1996a), Physica Scripta, **1996** (T63), 262.

Pegoraro F., S. V. Bulanov, F. Califano, and M. Lontano (1996b), Physica Scripta, **T63**, 262.

Phuoc K. T., S. Corde, C. Thaury, V. Malka, A. Tafzi, J. Goddet, R. Shah, S. Sebban, and A. Rousse (2012), Nature photonics, **6** (5), 308.

Pike O., F. Mackenroth, E. Hill, and S. Rose (2014), Nature Photonics, **8** (6), 434.

Piran T. (1999), Physics Reports, **314**, 575, astro-ph/9810256 .

Piran T. (2005), Reviews of Modern Physics, **76**, 1143.

Piskarskas A., A. Stabinis, and A. Yankauskas (1986), Soviet Physics Uspekhi, **29** (9), 869.

Powers N. D., I. Ghebregziabher, G. Golovin, C. Liu, S. Chen, S. Banerjee, J. Zhang, and D. P. Umstadter (2014), Nature Photonics, **8** (1), 28.

Pratt R., H. Tseng, C. Lee, L. Kissel, C. MacCallum, and M. Riley (1977), Atomic Data and Nuclear Data Tables, **20** (2), 175 , ISSN 0092-640X.

Pukhov A. (1999), Journal of Plasma Physics, **61** (03), 425.

Pukhov A., S. Gordienko, S. Kiselev, and I. Kostyukov (2004), Plasma Physics and Controlled Fusion, **46** (12B), B179.

Quinn K., L. Romagnani, B. Ramakrishna, G. Sarri, M. E. Dieckmann, P. A. Wilson, J. Fuchs, L. Lancia, A. Pipahl, T. Toncian, O. Willi, R. J. Clarke, M. Notley, A. Macchi, and M. Borghesi (2012), Physical Review Letters, **108**, 135001.

Rax J. (2005), *Physique des plasmas - Cours et applications: Cours et applications*, Physique (Dunod) ISBN 9782100527878.

Reiss H. R. (1962), Journal of Mathematical Physics, **3** (1), 59.

Ren C., M. Tzoufras, J. Tonge, W. B. Mori, F. S. Tsung, M. Fiore, R. A. Fonseca, L. O. Silva, J. C. Adam, and A. Héron (2006), Physics of Plasmas, **13**, 056308.

Ribeyre X., M. Lobet, E. D'Humières, S. Jequier, and V. Tikhonchuk (2015), arXiv preprint arXiv:1504.07868.

Ridgers C. P., C. S. Brady, R. Duclous, J. G. Kirk, K. Bennett, T. D. Arber, and A. R. Bell (2013), Physics of Plasmas, **20** (5), 056701.

Ridgers C. P., C. S. Brady, R. Duclous, J. G. Kirk, K. Bennett, T. D. Arber, A. P. L. Robinson, and A. R. Bell (2012), Physical Review Letters, **108**, 165006.

Ritus V. (1985), Journal of Soviet Laser Research, **6**, 497, ISSN 0270-2010.

Rivera R., and D. Villarroel (2002), Physical Review E, **66**, 046618.

Robinson A. (2011), Physics of Plasmas (1994-present), **18** (5), 056701.

Robinson A., D. Kwon, and K. Lancaster (2009), Plasma Physics and Controlled Fusion, **51** (9), 095006.

Robinson A., D. Strozzi, J. Davies, L. Gremillet, J. Honrubia, T. Johzaki, R. Kingham, M. Sherlock, and A. Solodov (2014), Nuclear Fusion, **54** (5), 054003.

Rohrlich F. (1997), American journal of Physics, **65** (11), 1051.

Rohrlich F. (2000), American Journal of Physics, **68** (12), 1109.

Rohrlich F. (2001), Physics Letters A, **283** (5), 276.

Romagnani L., J. Fuchs, M. Borghesi, P. Antici, P. Audebert, F. Ceccherini, T. Cowan, T. Grismayer, S. Kar, A. Macchi, P. Mora, G. Pretzler, A. Schiavi, T. Toncian, and O. Willi (2005), Physical Review Letters, **95**, 195001.

Roth M., A. Blazevic, M. Geissel, T. Schlegel, T. E. Cowan, M. Allen, J.-C. Gauthier, P. Audebert, J. Fuchs, J. Meyer-ter Vehn, M. Hegelich, S. Karsch, and A. Pukhov (2002), Physical Review Accelerators and Beams, **5**, 061301.

Rousse A., K. Ta Phuoc, R. Shah, A. Pukhov, E. Lefebvre, V. Malka, S. Kiselev, F. Burgy, J.-P. Rousseau, D. Umstadter, and D. Hulin (2004), Physical Review Letters, **93**, 135005.

Rousse A., C. Rischel, and J. Gauthier (2001), Reviews of Modern Physics, **73**, 17.

Rozsnyai B. F. (1979), Journal of Quantitative Spectroscopy and Radiative Transfer, **22** (4), 337 , ISSN 0022-4073.

Rp-photonics (2015a), "Neodymium-doped gain media," `https://www.rp-photonics.com/neodymium_doped_gain_media.html`, accessed: 2015-10-04.

Rp-photonics (2015b), "Titanium-sapphire lasers," `https://www.rp-photonics.com/titanium_sapphire_lasers.html`, accessed: 2015-10-04.

Rp-photonics (2015c), "Ytterbium-doped gain media," `https://www.rp-photonics.com/ytterbium_doped_gain_media.html`, accessed: 2015-10-04.

Ruffini R., G. Vereshchagin, and S.-S. Xue (2010), Physics Reports, **487** (1), 1 , ISSN 0370-1573.

Ruhl H. (2005), "Classical particle simulations with the psc code," .

Ruyer C., L. Gremillet, and G. Bonnaud (2015a), Physics of Plasmas, **22**, 082107.

Ruyer C., L. Gremillet, A. Debayle, and G. Bonnaud (2015b), Physics of Plasmas, **22** (3), 032102.

Ryutov D., and B. Remington (2007), in *High Energy Density Laboratory Astrophysics* (Springer) pp. 291–296.

Sagdeev R. Z. (1966), Reviews of Plasma Physics, **4**, 23.

Sarri G., D. J. Corvan, W. Schumaker, J. M. Cole, A. Di Piazza, H. Ahmed, C. Harvey, C. H. Keitel, K. Krushelnick, S. P. D. Mangles, Z. Najmudin, D. Symes, A. G. R. Thomas, M. Yeung, Z. Zhao, and M. Zepf (2014), Physical Review Letters, **113**, 224801.

Sarri G., K. Poder, J. Cole, W. Schumaker, A. Di Piazza, B. Reville, T. Dzelzainis, D. Doria, L. Gizzi, G. Grittani, *et al.* (2015), Nature communications, **6**.

Sarri G., W. Schumaker, A. Di Piazza, M. Vargas, B. Dromey, M. E. Dieckmann, V. Chvykov, A. Maksimchuk, V. Yanovsky, Z. H. He, B. X. Hou, J. A. Nees, A. G. R. Thomas, C. H. Keitel, M. Zepf, and K. Krushelnick (2013a), Physical Review Letters, **110**, 255002.

Sarri G., W. Schumaker, A. D. Piazza, K. Poder, J. M. Cole, M. Vargas, D. Doria, S. Kushel, B. Dromey, G. Grittani, L. Gizzi, M. E. Dieckmann, A. Green, V. Chvykov, A. Maksimchuk, V. Yanovsky, Z. H. He, B. X. Hou, J. A. Nees, S. Kar, Z. Najmudin, A. G. R. Thomas, C. H. Keitel, K. Krushelnick, and M. Zepf (2013b), Plasma Physics and Controlled Fusion, **55** (12), 124017.

Sauter F. (1931), Zeitschrift fr Physik, **69** (11-12), 742, ISSN 0044-3328.

Schawlow A. L., and C. H. Townes (1958), Physical Review, **112**, 1940.

Schlegel T., N. Naumova, V. T. Tikhonchuk, C. Labaune, I. V. Sokolov, and G. Mourou (2009), Physics of Plasmas (1994-present), **16** (8), 083103.

Schumaker W., G. Sarri, M. Vargas, Z. Zhao, K. Behm, V. Chvykov, B. Dromey, B. Hou, A. Maksimchuk, J. Nees, *et al.* (2014), Physics of Plasmas (1994-present), **21** (5), 056704.

Schwinger J. (1951), Physical Review, **82**, 664.

Seipt D., A. Surzhykov, S. Fritzsche, and B. Kampfer (2015), arXiv preprint arXiv:1507.08868.

Seltzer S. M., and M. J. Berger (1985), Nuclear Instruments and Methods in Physics Research Section B: Beam Interactions with Materials and Atoms, **12** (1), 95.

Seltzer S. M., and M. J. Berger (1986), Atomic Data and Nuclear Data Tables, **35** (3), 345 , ISSN 0092-640X.

Sgattoni A., L. Fedeli, S. Sinigardi, A. Marocchino, A. Macchi, V. Weinberg, and A. Karmakar (2015), arXiv preprint arXiv:1503.02464.

Sgattoni A., P. Londrillo, A. Macchi, and M. Passoni (2012), Physical Review E, **85**, 036405.

Shearer J. W., J. Garrison, J. Wong, and J. E. Swain (1973), Physical Review A, **8**, 1582.

Shen C. S., and D. White (1972), Physical Review Letters, **28**, 455.

Silva L. O., R. A. Fonseca, J. W. Tonge, J. M. Dawson, W. B. Mori, and M. V. Medvedev (2003), The Astrophysical Journal Letters, **596** (1), L121.

Silva L. O., R. A. Fonseca, J. W. Tonge, W. B. Mori, and J. M. Dawson (2002), Physics of Plasmas, **9**, 2458.

Sironi L., and A. Spitkovsky (2009), The Astrophysical Journal Letters, **707** (1), L92.

Sironi L., and A. Spitkovsky (2011), The Astrophysical Journal, 75.

Snavely R. A., M. H. Key, S. P. Hatchett, T. E. Cowan, M. Roth, T. W. Phillips, M. A. Stoyer, E. A. Henry, T. C. Sangster, M. S. Singh, S. C. Wilks, A. MacKinnon, A. Offenberger, D. M. Pennington, K. Yasuike, A. B. Langdon, B. F. Lasinski, J. Johnson, M. D. Perry, and E. M. Campbell (2000), Physical Review Letters, **85**, 2945.

Sokolov I. (2009), Journal of Experimental and Theoretical Physics, **109** (2), 207.

Sokolov I. V., N. M. Naumova, J. A. Nees, and G. A. Mourou (2010a), Physical Review Letters, **105**, 195005.

Sokolov I. V., N. M. Naumova, J. A. Nees, G. A. Mourou, and V. P. Yanovsky (2009), Physics of Plasma, **16** (9), 093115.

Sokolov I. V., J. A. Nees, V. P. Yanovsky, N. M. Naumova, and G. A. Mourou (2010b), Physical Review E, **81** (3), 036412.

Spitkovsky A. (2008), The Astrophysical Journal Letters, **673**, L39.

Spitkovsky A. (2008), The Astrophysical Journal Letters, **682** (1), L5.

Spohn H. (2000), Europhysics Letters, **50** (3), 287.

Stockem A., F. Fiuza, A. Bret, R. A. Fonseca, and L. O. Silva (2014), Scientific Reports, **4**, 3934, ISSN 2045-2322.

Stockem Novo A., A. Bret, R. A. Fonseca, and L. O. Silva (2015), The Astrophysical Journal Letters, **803**, L29, arXiv:1504.00468 [astro-ph.HE] .

Strickland D., and G. Mourou (1985), Optics Communications, **55** (6), 447 , ISSN 0030-4018.

Sudan R. C. (1983), *Basic Plasma Physics: Selected Chapters, Handbook of Plasma Physics, Volume 2*, edited by A. A. Galeev and R. N. Sudan (North-Holland Publishing Company, Amsterdam).

Surmin I., S. Bastrakov, E. Efimenko, A. Gonoskov, A. Korzhimanov, and I. Meyerov (2015), arXiv preprint arXiv:1505.07271.

Svensson R. (1982), apj, **258**, 321.

Tajima T. (2004), *Computational Plasma Physics: With Applications To Fusion And Astrophysics*, Frontiers in Physics (Westview Press) ISBN 9780813342115.

Tajima T., and J. M. Dawson (1979), Physical Review Letters, **43**, 267.

Tamburini M., T. Liseykina, F. Pegoraro, and A. Macchi (2012), Physical Review E, **85** (1), 016407.

Tamburini M., F. Pegoraro, A. Di Piazza, C. H. Keitel, T. V. Liseykina, and A. Macchi (2011), Nuclear Instruments and Methods in Physics Research Section A: Accelerators, Spectrometers, Detectors and Associated Equipment, **653** (1), 181.

Tamburini M., F. Pegoraro, A. Di Piazza, C. H. Keitel, and A. Macchi (2010), New Journal of Physics, **12** (12), 123005.

Tang S., M. A. Bake, H.-Y. Wang, and B.-S. Xie (2014), Physical Review A, **89** (2), 022105.

Teubner U., and P. Gibbon (2009), Reviews of Modern Physics, **81**, 445.

Bella (2015), "Bella laser," `http://loasis.lbl.gov/facilities_BELLA.html`, accessed: 2015-10-04.

Thomas A. (2014), Nature Photonics, **8** (6), 429.

Tikhonchuk V. T., A. A. Andreev, S. G. Bochkarev, and V. Y. Bychenkov (2005), Plasma Physics and Controlled Fusion, **47** (12B), B869.

Timokhin A. N. (2010), Monthly Notices of the Royal Astronomical Society, **408** (4), 2092, ISSN 1365-2966.

Tsai H.-E., X. Wang, J. M. Shaw, Z. Li, A. V. Arefiev, X. Zhang, R. Zgadzaj, W. Henderson, V. Khudik, G. Shvets, *et al.* (2015), Physics of Plasmas (1994-present), **22** (2), 023106.

Tseng H. K., and R. H. Pratt (1971), Physical Review A, **3**, 100.

Tskhakaya D., K. Matyash, R. Schneider, and F. Taccogna (2007), Contributions to Plasma Physics, **47** (8-9), 563.

Vay J.-L. (2008), Physics of Plasmas (1994-present), **15** (5), 056701.

Vay J.-L., C. Geddes, E. Cormier-Michel, and D. Grote (2011), Journal of Computational Physics, **230** (15), 5908 , ISSN 0021-9991.

Vieira J., and J. T. Mendonça (2014), Physical Review Letters, **112**, 215001.

Villasenor J., and O. Buneman (1992), Computer Physics Communications, **69** (2), 306 , ISSN 0010-4655.

Votruba V. (1948), Physical Review, **73**, 1468.

Vranic M., J. L. Martins, R. A. Fonseca, and L. O. Silva (2015), arXiv preprint arXiv:1502.02432.

Vranic M., J. L. Martins, J. Vieira, R. A. Fonseca, and L. O. Silva (2014), Physical Review Letters, **113**, 134801.

Vulcan (2015), "The vulcan 10 petawatt project," `http://www.clf.stfc.ac.uk/CLF/Facilities/Vulcan/The+Vulcan+10+Petawatt+Project/14684.aspx`, accessed: 2015-11-04.

Wallin E., A. Gonoskov, and M. Marklund (2015), Physics of Plasmas (1994-present), **22** (3), 033117.

Wang H. Y., X. Q. Yan, and M. Zepf (2015), Physics of Plasmas, **22** (9), 093103.

Wang W., W. Li, J. Liu, C. Wang, Q. Chen, Z. Zhang, R. Qi, Y. Leng, X. Liang, Y. Liu, X. Lu, C. Wang, R. Li, and Z. Xu (2013a), Applied Physics Letters, **103** (24), 243501.

Wang W., B. Shen, H. Zhang, Y. Xu, Y. Li, X. Lu, C. Wang, Y. Liu, J. Lu, Y. Shi, *et al.* (2013b), Applied Physics Letters, **102** (22), 224101.

Waxman E. (2006), Plasma Physics and Controlled Fusion, **48** (12B), B137.

Weibel E. S. (1959), Physical Review Letters, **2**, 83.

West D., and A. Sherwood (1972), Nature, **239**, doi:http://dx.doi.org/10.1038/239157b0.

Wilks S. C., W. L. Kruer, M. Tabak, and A. B. Langdon (1992), Physical Review Letters, **69**, 1383.

Winterfeldt C., C. Spielmann, and G. Gerber (2008), Reviews of Modern Physics, **80**, 117.

Wu Y.-B., and S.-S. Xue (2014), Physical Review D, **90** (1), 013009.

XCELS (2015), "Exawatt center for extreme light studies," `http://www.xcels.iapras.ru/img/site-xcels.pdf`, accessed: 2015-11-04.

Yanovsky V., V. Chvykov, G. Kalinchenko, P. Rousseau, T. Planchon, T. Matsuoka, A. Maksimchuk, J. Nees, G. Cheriaux, G. Mourou, and K. Krushelnick (2008), Optics Express, **16** (3), 2109.

Yee K. S., *et al.* (1966), IEEE Transactions on Antennas and Propagation, **14** (3), 302.

Yi L., B. Shen, L. Ji, K. Lotov, A. Sosedkin, W. Wang, J. Xu, Y. Shi, L. Zhang, Z. Xu, *et al.* (2014), Scientific Reports, **4**.

Yin L., B. J. ALBRIGHT, B. M. HEGELICH, and J. C. FERNANDEZ (2006), Laser and Particle Beams, **24**, 291, ISSN 1469-803X.

Yoffe S. R., Y. Kravets, A. Noble, and D. A. Jaroszynski (2015), New Journal of Physics, **17** (5), 053025.

Zagorodnov I., R. Schuhmann, and T. Weiland (2003), Journal of Computational Physics, **191** (2), 525 , ISSN 0021-9991.

Zagorodnov I., and T. Weiland (2005), Physical Review Accelerators and Beam, **8**, 042001.

Zampieri L., R. Turolla, L. Foschini, and A. Treves (2003), The Astrophysical Journal, **592** (1), 368.

Zastrau U., P. Sperling, M. Harmand, A. Becker, T. Bornath, R. Bredow, S. Dziarzhytski, T. Fennel, L. B. Fletcher, E. Förster, S. Göde, G. Gregori, V. Hilbert, D. Hochhaus, B. Holst, T. Laarmann, H. J. Lee, T. Ma, J. P. Mithen, R. Mitzner, C. D. Murphy, M. Nakatsutsumi, P. Neumayer, A. Przystawik, S. Roling, M. Schulz, B. Siemer, S. Skruszewicz, J. Tiggesbäumker, S. Toleikis, T. Tschentscher, T. White, M. Wöstmann, H. Zacharias, T. Döppner, S. H. Glenzer, and R. Redmer (2014), Physical Review Letters, **112** (10), 105002.

Zhang X., B. Shen, X. Li, Z. Jin, F. Wang, and M. Wen (2007), Physics of Plasmas (1994-present), **14** (12), 123108.

Zhao S., C. Lin, J. Chen, and X. Yan (2015a), arXiv preprint arXiv:1510.04765.

Zhao S., C. Lin, H. Y. Wang, H. Y. Lu, X. T. He, J. E. Chen, T. E. Cowan, and X. Q. Yan (2015b), Physics of Plasmas, **22** (7), 073106.

Zhidkov A., J. Koga, T. Hosokai, K. Kinoshita, and M. Uesaka (2004), Physics of Plasmas, **11** (12), 5379.

Zhidkov A., J. Koga, A. Sasaki, and M. Uesaka (2002), Physical Review Letters, **88**, 185002.

Zhou J., D. Liu, C. Liao, and Z. Li (2009), Plasma Science, IEEE Transactions on, **37** (10), 2002.

Zhu X.-L., Y. Yin, T.-P. Yu, F.-Q. Shao, Z.-Y. Ge, W.-Q. Wang, and J.-J. Liu (2015), New Journal of Physics, **17** (5), 053039.

Résumé

Cette thèse a pour objet l'étude de l'interaction laser-matière dans un régime d'éclairement extrême que visent à atteindre plusieurs installations multi-pétawatt en cours de développement (CILEX-Apollon, ELI, IZEST, etc.). Pour un éclairement supérieur à $10^{22}\,\mathrm{Wcm}^{-2}$, la dynamique relativiste des électrons accélérés dans l'onde laser est modifiée par un important rayonnement Compton inverse non-linéaire. Au-delà de $10^{23}\,\mathrm{Wcm}^{-2}$, les photons γ ainsi produits peuvent, en interagissant à leur tour avec le champ laser, se désintégrer en paires électron-positron via le mécanisme de Breit-Wheeler non-linéaire. Ces mécanismes d'électrodynamique quantique, dont l'étude expérimentale était jusqu'ici l'apanage des grands accélérateurs de particles, peuvent grandement affecter les mécanismes "usuels" d'interaction laser-plasma, notamment ceux régissant l'accélération de particules chargées et, par conséquent, le bilan global de l'interaction. Afin de modéliser ce régime inédit d'interaction, qui combine processus collectifs, relativistes et d'électrodynamique quantique, nous avons enrichi des mécanismes précédents le code de simulation *particle-in-cell* CALDER développé de longue date au CEA/DIF. L'influence de ces mécanismes est d'abord explorée dans le cas d'une impulsion laser interagissant avec une cible dense de taille micrométrique. Un rendement de conversion de l'énergie laser en photons γ supérieur à 10% est observé au-dessus de $10^{23}\,\mathrm{Wcm}^{-2}$, tandis que la production d'anti-matière s'emballe, via un mécanisme de cascade, à partir de $10^{24}\,\mathrm{Wcm}^{-2}$. Dans un second temps, nous étudions la génération de positrons lors de la collision frontale entre un faisceau d'électrons ultra-relativistes issu d'un accélérateur plasma et une impulsion laser ultra-intense. Dans une dernière partie, nous considérons un scénario prospectif d'intérêt astrophysique, à savoir la collision de plasmas de paires issus de cibles solides irradiées à $10^{24}\,\mathrm{Wcm}^{-2}$ montrant la croissance rapide d'une instabilité de filamentation magnétique combinée à d'intenses effets radiatifs.

Mots-clés : interaction laser-matière, plasma, électrodynamique quantique, positron, particle-in-cell, Compton inverse non linéaire, Breit-Wheeler non linéaire, Apollon, radiation friction, Monte-Carlo, Bremsstrahlung, Bethe-Heitler, Trident

Abstract

This PhD thesis is concerned with the regime of extreme-intensity laser-matter interaction that should be accessed on upcoming multi-petawatt facilities (e.g. CILEX-Apollon, ELI, IZEST). At intensities $I_L > 10^{22}\,\mathrm{Wcm}^{-2}$, the relativistic dynamics of the laser-driven electrons becomes significantly modified by high-energy radiation emission through nonlinear inverse Compton scattering. For $I_L > 10^{23}\,\mathrm{Wcm}^{-2}$, the emitted γ-ray photons can, in turn, interact with the laser field and decay into electron-positron pairs via the nonlinear Breit-Wheeler process. These quantum electrodynamic processes, which until recently could only be explored on large-scale particle accelerators, can greatly alter the "standard" mechanisms of laser-plasma interaction, and therefore its overall energy budget. In order to model their intricate interplay with the laser-induced plasma processes, they have been implemented within the particle-in-cell code CALDER developed at CEA. In a first part, we study these QED processes in the interaction of an ultra-intense laser with a micrometric overdense target. It is found that the laser-to-γ-ray energy conversion efficiency can by far exceed 10% for intensities $I_L > 10^{23}\,\mathrm{Wcm}^{-2}$, while copious pair production (through pair cascading) kicks in for $I_L > 10^{24}\,\mathrm{Wcm}^{-2}$. In a second part, we consider positron generation in the collision between a GeV electron bunch issued from a laser-wakefield accelerator and a counterpropagating laser pulse. In a third part, we analyze a prospective scheme of astrophysical interest, consisting in the collision between two dense pair plasmas produced from solid targets irradiated at $10^{24}\,\mathrm{Wcm}^{-2}$ showing a fast-growing magnetic filamentation instability amplified by intense synchrotron emission.

keywords: laser-matter interaction, plasma, quantum electrodynamics, positron, particle-In-cell, nonlinear inverse Compton, nonlinear Breit-Wheeler, Apollon, radiation friction, Monte-Carlo, Bremsstrahlung, Bethe-Heitler, Trident

---

CEA, DAM, DIF, F-91297, Arpajon, France

CELIA, UMR 5107, Université de Bordeaux-CNRS-CEA, 33405, Talence, France

---